


Spring 5-13-2017

AN EXPERIMENTAL AND NUMERICAL STUDY OF NANOMECHANICAL BEHAVIOR OF HARD/SOFT MULTILAYERED COATINGS

Benigno Sandoval
University of New Mexico

Follow this and additional works at: https://digitalrepository.unm.edu/me_etds

 Part of the [Mechanical Engineering Commons](#), and the [Other Materials Science and Engineering Commons](#)

Recommended Citation

Sandoval, Benigno. "AN EXPERIMENTAL AND NUMERICAL STUDY OF NANOMECHANICAL BEHAVIOR OF HARD/SOFT MULTILAYERED COATINGS." (2017). https://digitalrepository.unm.edu/me_etds/126

This Thesis is brought to you for free and open access by the Engineering ETDs at UNM Digital Repository. It has been accepted for inclusion in Mechanical Engineering ETDs by an authorized administrator of UNM Digital Repository. For more information, please contact disc@unm.edu.

Benigno Francisco Sandoval

Candidate

Mechanical Engineering

Department

This thesis is approved, and it is acceptable in quality and form for publication:

Approved by the Thesis Committee:

Mehran Tehrani, Chairperson

Yu-Lin Shen

William Mook

**AN EXPERIMENTAL AND NUMERICAL STUDY OF NANOMECHANICAL
BEHAVIOR OF HARD/SOFT MULTILAYERED COATINGS**

by

**BENIGNO FRANCISCO SANDOVAL
B.S. MECHANICAL ENGINEERING,
UNIVERSITY OF NOTRE DAME, 2013**

THESIS

Submitted in Partial Fulfillment of the
Requirements for the Degree of

**Master of Science
Mechanical Engineering**

The University of New Mexico
Albuquerque, New Mexico

May 2017

Dedication

To my Mom and Dad:

All that I am and all that I have done is because of the care, guidance, and
mentorship you have endlessly supplied.

This thesis is dedicated to my family, and especially to my loving parents who have
supported me unconditionally at every turn and every obstacle of my life.

Acknowledgements

I would first like to thank Professors Mehran Tehrani and Yu-Lin Shen of the University of New Mexico for their support in all aspects of the conception, execution, and understanding of this thesis. These two professors have guided and aided me while always allowing this to be my own exploration and work. They have faithfully taught me and provided support and resources beginning as professors, continuing as collaborators, and finally culminating in service as members of my thesis committee.

I would also like to thank the personnel at both the Core and Gate Facilities of the Center for Integrated Nanotechnologies. In particular I would like to thank William Mook, John Kevin Baldwin, and Doug Pete. These three have been instrumental in the fabrication and characterization of physical samples. I would like to thank them both for their professional contributions to the research as well as their patience and generosity while training and teaching me. It has been a pleasure and a unique opportunity to observe and participate in all the aspects of this research that has been made possible through the combined efforts of these collaborators.

Finally I would like to thank the members and staff of the Advanced Structural and Energy Materials Lab, the Mechanical Engineering Department at UNM, and the Center for Micro-Engineered Materials at the Advanced Materials Laboratory. In particular I would like to mention Nekoda VanDerWerken, Ali Nematollahi, and Pouria Khanboluki, Rochelle Piatt, Ronald McKinstry, and Cindi Santistevan for their contributions and general support while I was completing this thesis.

This work was performed, in part, at the Center for Integrated Nanotechnologies, an Office of Science User Facility operated for the U.S. Department of Energy (DOE) Office of Science by Los Alamos National Laboratory (Contract DE-AC52-06NA25396) and Sandia National Laboratories (Contract DE-AC04-94AL85000).

**AN EXPERIMENTAL AND NUMERICAL STUDY OF NANOMECHANICAL
BEHAVIOR OF HARD/SOFT MULTILAYERED COATINGS**

by

Benigno Francisco Sandoval

B.S. Mechanical Engineering, University of Notre Dame, 2013

M.S. Mechanical Engineering, University of New Mexico, 2017

Abstract

Multilayer thin film composites, sometimes referred to as nanolaminates, have emerged as an important subset of materials with novel, and often tunable, properties such as high strength, high toughness, and resistance to wear or corrosion. Often fabricated using alternating layers of two or more materials, these multilayer thin film coatings are typically expensive and time intensive to fabricate and characterize and exhibit novel responses to nanomechanical testing such as plasticity during unloading. This thesis explores the nanoindentation response of hard/soft multilayer coatings through examination of the optical coating Al/SiC and similar coating Al/SiO₂. Instrumented indentation was used to study single layer films of aluminum, silicon carbide, and silicon dioxide with thicknesses 40nm to 4 μ m. Results from individual and cyclic indentation load cycles provided insight into film mechanical properties. Additionally alternating 51 layers hard/soft multilayers on silicon and quartz substrates were studied with spherical and Berkovich indenters. These multilayer films were fabricated with bilayer thickness of 160nm but variable thickness ratio to achieve 25, 50, and 75% aluminum by volume. Further microstructural characterization is necessary to fully explain the indentation behavior, however an accurate prediction of indentation derived modulus for the nanolaminate based upon monolayer properties was found. Furthermore, cyclic indentation of the nanolaminates along with post-indentation TEM led to the conclusion that unloading plasticity was not occurring within the multilayer structure or the effect was not significantly altering the indentation response.

Finite element simulations were created to model individual load cycles for each combination of indenter, thickness ratio, film material, and substrate using ABAQUS. Single layer and multilayer simulations exhibited plastic deformation increasing within the aluminum layers during the unloading phase of indentation for all cases. Further simulation was conducted focusing on the cyclic indentation of aluminum thin films and Al/SiC nanolaminates. It was concluded that the simulation adequately represented the single material film responses but were unable to predict the indentation-derived properties for the Al/SiC multilayer. Further investigation would benefit from knowledge of the ceramic microstructure and viscous properties.

TABLE OF CONTENTS

Dedication	iii
Acknowledgements	iv
Abstract	v
LIST OF FIGURES	ix
LIST OF TABLES	xiv
Chapter 1. Introduction	1
1.1. <i>Overview</i>	1
1.2. <i>Importance of Materials in History</i>	1
1.3. <i>Multilayer Structures</i>	3
1.4. <i>Al/SiC Multilayers</i>	7
1.5. <i>Motivation</i>	10
Chapter 2. Fabrication and Characterization of Multilayered Coatings	14
2.1. <i>Physical Vapor Deposition: Sputtering</i>	14
2.2. <i>Fabrication Conditions and Characterization</i>	20
2.3. <i>Scanning and Transmission Electron Microscope Characterization</i>	21
2.4. <i>Micropillar Creation</i>	26
Chapter 3. Nanoindentation	28
3.1. <i>Theory of Nanoindentation</i>	28
3.2. <i>Calculations for Instrumented Indentation</i>	33
3.3. <i>Indentation of Thin Films</i>	36
3.4. <i>The NanoTest System</i>	40
3.5. <i>Sample Specimen Mounting</i>	43
3.6. <i>Indentation Results</i>	49
3.7. <i>Substrates and Reference</i>	51
3.8. <i>Single Layer Thin Films</i>	56
3.9. <i>Multilayered Thin Films</i>	67
Chapter 4. FEM: Modeling and Simulation	83
4.1. <i>Introduction</i>	83

4.2. Simulation Set Up	89
4.3. Individual Indentations.....	95
4.4. Cyclic Indentations.....	97
Chapter 5. Conclusions and Future Work.....	109
5.1. Conclusions.....	109
5.2. Introduction to Micropillar Compression	111
5.3. Micropillars and FIB with Ga Ions.....	113
5.4. Microstructural Characterization.....	114
5.5. Adapted Simulations and Comparison to Indentation.....	115
5.6. Spherical indentations.....	116
5.7. SiC and SiO ₂ viscosity and Al/SiO ₂ cyclic simulations.....	116
5.8. Delamination concerns/void growth.....	117
APPENDIX A: Sample Code - Berkovich Indentation of 80nm Al/80nm SiC....	120
APPENDIX B: Sample Code - Spherical Indenter Geometry	135
APPENDIX C: Sample Code - 120nm/40nm Nanolaminate Geometry.....	138
APPENDIX D: Sample Code - 40nm/120nm Nanolaminate Geometry	146
LIST OF REFERENCES.....	154

LIST OF FIGURES

<i>Figure 1.1 Illustration and SEM image of the “brick and mortar” structure of nacre[38, 39]</i>	<i>2</i>
<i>Figure 2.1 Schematic of a sputter gun setup showing the glow plasma creation of argon ions, collision of Ar⁺ with the target material, resultant sputtered atoms traveling to the substrate, and the adatom impact.[85].....</i>	<i>15</i>
<i>Figure 2.2 Sputtering target showing characteristic erosion pattern</i>	<i>17</i>
<i>Figure 2.3 Inside of DC Magnetron Chamber (CINT Gateway Facility) showing plasma glow of four sputter guns with open shutters and rotating sample stage for even deposition.</i>	<i>18</i>
<i>Figure 2.4 DC Magnetron System (CINT Gateway Facility) showing the vacuum chamber with sputter guns mounted above, load lock system and the computer control system. Not labeled is the e-beam evaporation system that extends on the right side of the picture.</i>	<i>19</i>
<i>Figure 2.5 Berkovich indentation to extreme depth upon multilayer nanolaminate. Image under SEM shows relative surface roughness top 80nm Aluminum layer.....</i>	<i>22</i>
<i>Figure 2.6 Berkovich indent of 51 layer Al/SiO₂ nanolaminate with layers approximately 80nm thickness. (left) Same indent with platinum deposited in preparation for the FIB milling and subsequent lift-out process for preparing a TEM sample. (right).....</i>	<i>23</i>
<i>Figure 2.7 TEM sample of Berkovich indented 51 layer 80nm-Al/80nm-SiO₂ nanolaminate. From left to right pictures show the sample after liftout but prior to thinning , post thinning from SEM view, and during thinning view from the ion beam.....</i>	<i>23</i>
<i>Figure 2.8 Post indentation cross section TEM: 51 layer nanolaminate of 80nm Al/80 nm SiO₂ films upon a Si wafer substrate. Berkovich indentation much deeper than regular max depth</i>	<i>24</i>
<i>Figure 2.9 TEM of 80nm Al/ 80nm SiO₂ nanolaminate near substrate. Si wafer and thin oxide layer can be seen clearly, as can the structure of the Al layers. Note the growth of layer undulation as more layers are added</i>	<i>25</i>
<i>Figure 2.10 Composite of multiple TEM images near indentation site for greater clarity of indentation effects. Note no delamination within layers or at interface with substrate.....</i>	<i>25</i>
<i>Figure 2.11 TEM expansion of 80nm Al/ 80nm SiO₂ near indentation site under extreme indentation stress. Findings are inconclusive.</i>	<i>26</i>
<i>Figure 2.12 Preparation of a micropillar of 51 layer 80nm Al/80 nm SiO₂ nanolaminate.....</i>	<i>26</i>
<i>Figure 2.13 Micropillar of 51 alternating ~80nm layers Al/SiO₂ nanolaminate.....</i>	<i>27</i>
<i>Figure 3.1 Berkovich indenter (left) and geometry and SEM image of a Berkovich indenter tip (right).[96, 97].....</i>	<i>29</i>
<i>Figure 3.2 (a) Typical load vs. displacement curve for an elastic-plastic specimen loaded using a conical indenter. (b) Cross-sectional geometry of a conical indenter trace in the sample. Shows sample surface under full load and no load.....</i>	<i>30</i>

Figure 3.3 (a) Typical load vs. displacement curve for an elastic-plastic specimen loaded using a spherical indenter. (b) Cross sectional geometry for loading using spherical indenter of radius R_i , shows residual impression radius, R_r , 32

Figure 3.4 Load vs. Displacement curves for the indentations of fused silica which were used to develop the DAF file applied for analyses of all Berkovich indentations..... 34

Figure 3.5 Diamond Area Function coefficients determined using fifth order polynomial. Resulting polynomial is used within Equation 4.11 for all subsequent analyses to determine contact area which is critical for calculations of hardness and elastic modulus..... 35

Figure 3.6 Scaling parameter a/t used to remove substrate effect when finding the Young's modulus for a thin film. 37

Figure 3.7 (left) Schematic of film delamination and separation from substrate under spherical indentation. (right) Characteristic shape and features of load-displacement curve typical to samples that are well-adhered and delaminated..... 38

Figure 3.8 Cross sectional view showing delamination in 41 layer Al/SiC nanolaminate with approximately 50nm layers. Delamination shown by white arrows on either side of indentation between layers and at layer and substrate interface.[55]..... 39

Figure 3.9 Simulated load-displacement curve during indentation unloading. Contour plots of the equivalent plastic strain as indenter retracts from full load for an indentation of 0.5 μm . Images adapted from Tang[54] and show only the material close to the indentation site. The scale is the same for both images and the blue arrow at left shows the interface between silicon substrate and the first layer of the Al/SiC nanolaminate..... 40

Figure 3.10 Schematic and Picture of NanoTest 600 components..... 41

Figure 3.11 Indentation response of glued (left series) and taped (right series) SiC specimen under extreme loading with a spherical indenter..... 44

Figure 3.12 Modulus vs. Depth of Taped and Glued SiC Specimen 46

Figure 3.13 Hardness vs. Depth of Taped and Glued SiC Specimen..... 46

Figure 3.14 Berkovich indentation response of alternating 80nm Al/80nm SiC multilayer on Si wafer glued to sample stub..... 48

Figure 3.15 Berkovich indentation response of alternating 80nm Al/80nm SiC multilayer on Si wafer glued to sample stub (left) and taped to sample stub (right) 49

Figure 3.16 Reduced modulus and hardness against maximum indentation depth for reference sample, fused silica. The modulus indentations were used in creation of the DAF..... 53

Figure 3.17 Reduced modulus and hardness vs. indentation depth for the silicon substrate. Resulting modulus of 124 GPa and hardness of 7.3 after substrate effect removed..... 54

Figure 3.18 Reduced modulus and hardness vs. indentation depth for the quartz substrate. Resulting modulus of 67 GPa after substrate effect removed. 55

<i>Figure 3.19 Reduced modulus and hardness against the indentation depth for aluminum samples. Resulting modulus of 150 GPa after substrate effect removed likely due to the effect of oxide growth....</i>	<i>60</i>
<i>Figure 3.20 Reduced modulus and hardness against the indentation depth for silicon carbide samples. Resulting modulus of 213 GPa and hardness of 16.3 after substrate effect removed.....</i>	<i>61</i>
<i>Figure 3.21 Reduced modulus and hardness against the indentation depth for silicon dioxide samples. Resulting modulus of 60 GPa after substrate effect removed.....</i>	<i>62</i>
<i>Figure 3.22 Cyclic indentation reduced modulus for Al on Si wafer samples against depth and cycle.....</i>	<i>63</i>
<i>Figure 3.23 Cyclic indentation reduced modulus for SiC on Si wafer samples against depth and cycle. .</i>	<i>64</i>
<i>Figure 3.24 Cyclic indentation reduced modulus for SiO₂ on Si wafer samples against depth and cycle.</i>	<i>65</i>
<i>Figure 3.25 Loading information for selected single cycle indentations upon a 1000nm thick aluminum film upon silicon wafer substrate. Used as part of the investigation into the extreme stiffness found for the aluminum thin films. Shows the load vs. displacement curves both before and after the thermal drift correction was applied.</i>	<i>66</i>
<i>Figure 3.26 Reduced modulus and hardness for 40/120 Al-SiC nanolaminate. Resulting modulus of 190 GPa and hardness of 10.9 after substrate effect removed.....</i>	<i>71</i>
<i>Figure 3.27 Reduced modulus and hardness for 40/120 Al-SiO₂ nanolaminate. Resulting modulus of 77 GPa and hardness of 5.7 GPa after substrate effect removed.....</i>	<i>72</i>
<i>Figure 3.28 Reduced modulus and hardness for 80/80 Al-SiC nanolaminate Resulting modulus of 175 GPa and hardness of 11.6 GPa after substrate effect removed.</i>	<i>73</i>
<i>Figure 3.29 Reduced modulus and hardness for 80/80 Al-SiO₂ nanolaminate. Resulting modulus of 95 GPa and hardness of 5.0 GPa after substrate effect removed.....</i>	<i>74</i>
<i>Figure 3.30 Reduced modulus and hardness for 120/40 Al-SiC nanolaminate. Resulting modulus of 156 GPa and hardness of 9.7 GPa after substrate effect removed.....</i>	<i>75</i>
<i>Figure 3.31 Reduced modulus and hardness for 120/40 Al-SiO₂ nanolaminate. Resulting modulus of 115 GPa and hardness of 3.0 GPa after substrate effect removed and consideration for alumina.</i>	<i>76</i>
<i>Figure 3.32 Reduced modulus and hardness against max depth for Al-SiC nanolaminate individual cycle indentations, for reference on the effect of modulation ratio on properties.</i>	<i>77</i>
<i>Figure 3.33 Reduced modulus and hardness against max depth for Al-SiO₂ nanolaminates.....</i>	<i>78</i>
<i>Figure 3.34 Cyclic indentation results for Al-SiC nanolaminates on Si wafer vs. depth and cycle number</i>	<i>79</i>
<i>Figure 3.35 Cyclic indentation results for Al-SiC nanolaminates on quartz substrate vs. depth and cycle number</i>	<i>80</i>
<i>Figure 3.36 Cyclic indentation results for Al-SiO₂ nanolaminates on Si wafer vs. depth and cycle number</i>	<i>81</i>
<i>Figure 3.37 Cyclic indentation results for Al-SiO₂ nanolaminates on quartz substrate</i>	<i>82</i>
<i>Figure 4.1 Schematic of geometric setup for preliminary simulations[48].....</i>	<i>84</i>
<i>Figure 4.2 Load Displacement Data for 41 Layer Tests.....</i>	<i>85</i>

<i>Figure 4.3 Snapshots of simulations showing unloading plasticity. From left to right samples are Al/SiO₂ on SiO₂, Al/SiO₂ on Si, and Al/SiC on Si. As indenter is retracted from full load (top to bottom) plastic deformation within the aluminum layers developing to the right side of the indenter, highlighted in the area of the yellow circle.</i>	88
<i>Figure 4.4 Post Compression Samples of 25%, 50%, and 75% Aluminum used in determination of the Poisson's Ratio, ν, for multilayer structure</i>	89
<i>Figure 4.5 Basic Spherical Indenter Design</i>	91
<i>Figure 4.6 Spherical and Conical Indenter Geometries</i>	91
<i>Figure 4.7 Schematic of simulation general geometry</i>	92
<i>Figure 4.8 Model Geometry Sections and Seize Reference</i>	93
<i>Figure 4.9 Element Structure of Multilayer Structure upon Substrate</i>	94
<i>Figure 4.10 Simulated single indentations of an aluminum and silicon carbide nanolaminate. Results in hardness of 3.5 GPa and Young's modulus of 97 GPa.</i>	96
<i>Figure 4.11 Load vs. displacement results from a cyclic indentation of 4.08μm thick Al layer upon a Si substrate. Modeled from 51 layer geometry but with all layers defined as Al with no viscous effects. First indentation cycle (unloading to 10% of full load) is shown in solid red while the second indentation cycle is shown in dashed blue. Second cycle follows first cycle unload perfectly.</i>	100
<i>Figure 4.12 Cyclic load vs. displacement for a 4.08μm Al film including viscous properties upon Si substrate.</i>	101
<i>Figure 4.13 Cyclic load vs. displacement for a 51 layer nanolaminate with 26x purely elastic-plastic 80nm thick Al layers and 25x80nm thick SiC layers film upon Si substrate. Final unloading is not pictured, each cycle is depicted with a different color so as to better follow the hysteresis loops.</i>	102
<i>Figure 4.14 Cyclic load vs. displacement for a 51 layer nanolaminate with 26x80nm thick Al layers including viscous properties and 25x80nm thick SiC layers film upon Si substrate. Final unloading is not pictured, each cycle is depicted with a different color so as to better follow the hysteresis loops.</i>	103
<i>Figure 4.15 Modulus and hardness results against cycle number for the Al and Al/SiC cyclic simulations. Note the similarity in shape of trends and the final modulus value.</i>	104
<i>Figure 4.16 Unloading to 10% of full load for cycle 1 of simulated Berkovich indentation of 51 layer Al-SiC 80nm/80nm nanolaminate. Note increased PEEQ throughout the laminate as a whole, especially the aluminum layers 9-25 layer deep.</i>	105
<i>Figure 4.17 Unloading to 10% of full load for cycle 2 of simulated Berkovich indentation of 51 layer Al-SiC 80nm/80nm nanolaminate. Note increased PEEQ throughout the laminate as a whole, especially the aluminum layers 9-25 layer deep.</i>	105
<i>Figure 4.18 Unloading to 10% of full load for cycle 8 of simulated Berkovich indentation of 51 layer Al-SiC 80nm/80nm nanolaminate. Note that increased plasticity is largely localized close to the indenter rather than throughout the laminate structure.</i>	106

Figure 4.19 Cyclic indentation of 51 layer 80nm Al/80nm SiC nanolaminate with a Berkovich tip. Although difficult to see the hysteresis loop is similar to that seen in the simulations with less overlap and less curve due to the hold at max hold to take up the creep effects. 107

Figure 4.20 Sample curve of determination for the depth corresponding to a specific max load for a cycle within the Al/SiC multilayer simulation with viscous properties. Note the curve shows little consistency in slope and is not even monotonic as would be expected. 108

Figure 5.1 Micropillar and Dogbone Cantilever (from [127, 128]). 112

Figure 5.2 Load vs. displacement curves for many indents on the nanolaminate structures all of which show a significant and abrupt change in the loading rate at about 75nm of indentation depth. 118

Figure 5.3 Load vs. displacement curves for a specific SiC sample that did not show the loading rate change during one set of indentations (left) but did in another (right). 118

Figure 5.4 Load vs. displacement curves for fused silica. At left are the original indentations used to create the DAF file, at right are tests completed after all other indentation were completed that show the exact same loading curve shape. Neither of these sets of indentations exhibited the loading rate change discussed. 119

LIST OF TABLES

<i>Table 2-1 Single material thin film coatings</i>	<i>20</i>
<i>Table 2-2 Multilayer thin film coatings. The intended thickness was $4.08 \pm 0.1 \mu\text{m}$</i>	<i>21</i>
<i>Table 3-1 Properties from single material thin film and bare substrate indentations.....</i>	<i>50</i>
<i>Table 3-2 Indentation derived modulus and hardness with reference Poisson's ratio</i>	<i>67</i>
<i>Table 3-3 Measured and calculated moduli for comparison</i>	<i>68</i>
<i>Table 4-1 Results of 41 Layer Verification Test.....</i>	<i>86</i>
<i>Table 4-2 Poisson's Ratio (Simulation Results).....</i>	<i>90</i>

Chapter 1. Introduction

1.1. Overview

Multilayer thin film coatings have been studied extensively for enhanced mechanical properties such as high strength, high toughness, wear and corrosion resistance, and novel optical properties.[1-32] Their potential has expanded immensely from an academic pursuit to common commercial applications and as such the mechanical characterization of these films has been the subject of intense research with the primary form of experimental testing being instrumented nanoindentation.[33-37] Although indentation has been widely refined and is well understood for bulk materials and monolayers, the introduction of multilayered composites, especially those of alternating hard/soft layers, on the nano and micro scales has added significant complexity. This is primarily due to the large amount of interfacial area between layers and the commonly used alternating hard/soft nature of materials used in these films. This thesis, therefore, aims to understand the nanoindentation response of multilayered composite coatings through an integration of experiments and simulations.

1.2. Importance of Materials in History

Throughout the history of civilization the advancement of human society has been directly driven by advancements in materials. Technological advancements such as the ability to create tools and weapons in the early Bronze Age, construct buildings and vehicles during the steel age, and develop electronics and telecommunication devices throughout the silicon age. Each of these technological advancements marks immense growth and development of human civilization, and each can be attributed directly to advancements in knowledge, processing, or development of materials. It is this connection that has driven humans to strive to investigate and experiment with materials in mixtures, alloys, and pure elemental forms. We have learned to classify materials into ceramics, metals, and plastics, developing each as our ability to process and utilize these advanced. Driven by the need to contain and hold, ceramics were developed independently by many early civilizations in the form of jars and pitchers. Similarly metals were explored for the creation of tools for agriculture and weapons for protection. Finally polymers were widely

explored following the World War I as a cheap and lightweight replacement for metals and ceramics. Each material classification has produced astounding capabilities that are used simply in most human lives on a daily basis whether for dishes, electronics, or car tires. However, while each classification spans a huge range of specific materials with distinct properties and functionalities, humans have continued to push for more: better, novel or multifunctional mechanical, physical, chemical, and/or optical properties. While this often lead to research of a specific material and the processing or machinability of said material, a whole new field of materials has arisen from the desire to improve beyond simple bulk materials, composites. In a composite material two or more materials of differing properties are combined with each other to create a new material with properties varying from any of the constituents. For example, carbon fiber reinforced polymer composites have enabled strong and lightweight parts for Aerospace and Automotive industries, which are not possible to achieve by conventional materials. Moreover, the use of nanomaterials in composites has opened new avenues for tailoring material properties. At the nanoscale quantum effects become significant and surface area (thus surface energy) becomes significantly large, hence novel properties/functionalities become possible. As the pursuit of more advanced materials continues, humans must look to other sources for inspiration One tried and true method of discovering systems beyond our knowledge is to look into the realm of nature for the capabilities or structures that have arisen via evolution over the estimated 3.8 billion years of life upon the earth. Many fields have taken advantage of naturally occurring compounds, processes, and mechanisms. Of particular interest here are the micro- or nano-scale material science advances made by study of natural systems such as the thin film coatings and multilayer structure of mother-of-pearl, nacre.[17]

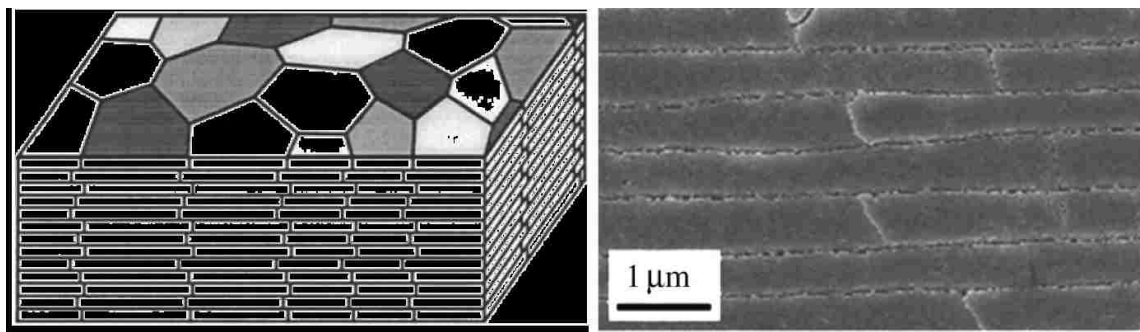


Figure 1.1 Illustration and SEM image of the “brick and mortar” structure of nacre[38, 39]

This multilayer structure is where the term nanolaminate is derived, a term first coined in a paper on the structure of nacre.[40] Nacre, created by the abalone and used in the shell is said to have a “bricks and mortar” structure of aragonite crystal platelets (CaCO_3) held together by organic layers of conchiolin. This can be seen in Figure 1.1 and is a classic example of a naturally occurring increase in the mechanical properties of a material based on a composite structure. The impressive toughness and strength of nacre can be attributed to several specialized features that go beyond the nanolaminate structure itself such as the “hidden length” displayed by the specialized bio-macromolecules present between the aragonite platelets, the orderly interlocking of those platelets, the nanoasperities on their surfaces, and the inclusion of protein within the platelets themselves.[41] Nevertheless, the composite ideology based on a large volume of individually small and stiff (but brittle) ceramic components cemented together by a small quantity of a soft (but tough) polymeric phase represents an important material model. A model followed by many man-made nanolaminates consisting of a stiff but brittle material for strength with a softer, more ductile material to accommodate strain.[42] The goal of most research and fabrication of nanolaminates is to improve one or more material properties, be they mechanical or otherwise. The nacre found in abalone shells is a nanolaminate focused on creating a material that is stiff, strong, and tough. [42-47]

1.3. Multilayer Structures

In an amazing natural system, the high strength and toughness of the mollusk shell can be attributed to the multilayer structure of ceramic layers bonded together with a soft organic glue.[1-32, 48-56] The basic mechanism behind such material property enhancement is apparent in the commonly used laminate wood beams that can be found in a regular hardware store. These beams rely on the interfacial compression and tension fields between each layer of the beam to provide significantly better load bearing ability perpendicular to the layers than a similar sized beam of bulk material could have. On a related note, steel shows remarkable strength and toughness due to the microscale laminar structure of α ferrite/ Fe_3C cementite. Therefore the advantages of a simple structural composite and the small-scale advantages can be seen across many systems which provides explanation for why these multilayer structures have been the subject of

extensive study [2]. This research on multilayered materials covers a wide range of materials, deposition methods, treatments, and characterization techniques, not to mention computational research. Multilayer structures can be a variety of materials but typically can be classified into one of three categories: metal-metal, metal-ceramic, and ceramic-ceramic, where this refers to the type of materials used in the alternating layer structure. Universal terminology has yet to be adopted for these multilayer thin films but they are predominantly referred to as nanolaminates in the metal-ceramic literature, nanoscale multilayers in the metal-metal literature, and superlattices in some of the early ceramic-ceramic literature.[57] Most multilayered structures are fabricated through thin film deposition techniques allowing for tuning properties based on the deposition method and parameters.[20] Common methods for deposition include chemical methods (plating, chemical solution deposition, spin coating, chemical vapor deposition, plasma enhanced chemical vapor deposition, and atomic layer deposition)[58-63], physical methods (thermal evaporation, e-beam evaporation, molecular beam epitaxy, pulsed laser deposition, cathodic arc deposition, electrohydrodynamic deposition, and sputtering)[64-69].[70] The samples used in our investigation were fabricated using the physical vapor sputtering method and as such this method will be discussed more extensively in Chapter 2. Chemical deposition methods involve a fluid or gaseous precursor which, when in contact with a solid surface, undergoes a chemical reaction resulting in the formation of a new solid layer on the surface. The chemical reaction here leads to the distinction of chemical deposition as opposed to physical deposition, which involves mechanical, electrical, or thermodynamic processes to create the new solid layer. Physical deposition techniques use high-energy methods such as ion bombardment or electrical heating to excite atoms off of one surface or material toward the deposition surface, growing until the excitement is ceased. It should be noted that most of these reactions occur at low pressures. In particular, a vacuum deposition chamber should be used to enable free movement of atoms or molecules to the deposition surface, which is often held at a lower temperature to attract particles. In some methods an electromagnetic field is induced to attract ions in a particular direction, this will also be discussed in Chapter 2. Whether within a vacuum chamber or a chemical solution, depositions are intended to leave perfect stoichiometry without contaminants. This is not always the case particularly with ceramics,

which undergo changes as they form on the deposition surface. Selection of deposition process and parameters are important to achieving desired structure and thus properties in the final coatings. Post-processing procedures are often used to resolve issues that arise during deposition. For example, thermal annealing has been used in diamond-like carbon (DLC) films as a means of relieving the internal compressive stresses that develop during deposition and limit film thickness, or cause debonding, delamination, or cracking.[30] In this regard, however, annealing can lead to undesirable graphitization. Therefore, a more reliable method of alleviating the internal compressive stresses while maintaining the surface is to use a multilayer DLC structure rather than a single layer film. This method has proven successful in various applications, especially for wear protection.[30] Another method often employed is heat treatment during deposition leading to improved crystalline structures. While this can sometimes be highly desirable in laminates of DLC they are antithetical for applications requiring an amorphous or nano-crystalline structure. One example of this would be tungsten nitride films in nanolayered CrN/WN coatings where properties based on fracture and failure mechanics benefit from the amorphous structure of the layers.[28] Another advantage of thin films is the extremely shallow depth of deposition (a few to hundreds of nanometers) that, in many cases, leads to lower defect density, thus better properties. This is similar to the process of defects moving through a stressed grain until they reach a grain boundary at which point they will be forced to stack up in a favorable manner. With the nanoscale thickness of the layers, stacking of defects occurs at the edge of each individual layer therefore leading to an impressive increase in strength.[71]

It is clear that the multilayered structure itself provides benefits both from thin film advantages and stacking advantages as exhibited in DLC layers. Going further, many groups have demonstrated the value of introducing layers of a second (or third) [1-5, 7, 14, 20, 21, 25, 28, 30, 31] material to the multilayer structure. For example, deposition of graphene oxide (GO) nanocomposites have been shown to improve mechanical properties of polyelectrolyte multilayer (PEM) films. It was demonstrated that the elastic modulus of multilayered polyelectrolytes could be improved by up to 181% through the addition of a single graphene oxide layer after ten bilayers of polyelectrolyte.[20] In the same study, the hardness of the PEM increased from 0.295 GPa to 2.79 GPa. Furthermore and most

encouraging is that results from this study support the idea that mechanical properties of the film could be tuned by varying the number of GO layers in the multilayer architecture.[20] In other researches, multilayers of TiN/Metal have been widely explored.[10, 14, 15, 23, 30, 31, 45, 72, 73] TiN is commonly used as coatings in drilling and cutting tools to improve hardness, friction, and corrosion resistance[23, 74] However, being a brittle material, TiN films are susceptible to fracture and spalling from the substrate. A multilayer system of TiN with titanium introduces toughness to the coating while maintaining a considerable hardness and wear resistance, making it an attractive candidate for erosion resistant applications.[15] Often the hardness increase in a TiN/metal multilayer is attributed to the alternating crystal structure which prevents dislocations from moving from one layer to another; this is widely disputed however, and it is indeterminate whether the increase in hardness can truly be attributed to dislocations being pinned or if this comes from other layer effects.[31] Similarly if two hard metals of the same crystal structure are used in a multilayered structure, the hardness should increase according to the Hall-Petch model where mobility of dislocations always increases with decreasing periodicity as the dislocations accumulate at the interfaces. However, this was found not to be the case for TiN/TiC or NbN/VN. Instead the difference of shear stiffness values represents the major cause of the increase in the hardness of nitride superlattices. This difference decides how much energy is required to move a dislocation from one position to another. The higher the energy requirement, the more difficult the dislocation movement and the higher the hardness will be.[13] The reason for mentioning this is to demonstrate that the mechanism behind mechanical property changes in systems that have been widely studied is not yet understood and requires more investigation. Even though fracture toughness is one of the most critical parameters for brittle-ductile multilayers, the literature on the micro-mechanics of damage initiation and accumulation in Ti-TiN coatings is limited to a few fracture and fatigue studies. Furthermore, it is important to note that most of these studies do not test the coating alone, but the coating-substrate system, which implies that the mechanical behavior of the coating is influenced by the contribution from the substrate.[15] There are methods of analyzing indentation data such that the substrate effect can be removed as will be done in Chapter 3 Nanoindentation and Chapter 4 FEM: Modeling and Simulation while the micropillar compression test's results

should be inherently free of any substrate effect due to filtering of said effects by the digital image correlation procedure.

1.4. Al/SiC Multilayers

Aluminum and silicon carbide multilayered films have been studied and implemented in extreme ultraviolet and x-ray reflection applications. These applications require high performance for high-energy x-ray application, lithography, spectroscopy, passivation, satellites, and space based solar physics among many others. These coatings are reportedly common for normal incidence high reflectance of specific spectral lines that can originate from the sun while having relatively low reflectance of nearby bright wavelengths thereby avoiding spectral contamination.[16, 19, 25-27, 32, 42] Due to the applicability of these films they are studied and improvements in the understanding of the film properties or improvement in the ability to design specific films can be of significant value.

In thin film coating applications there are many variables leading to increased functionality or improved properties. So far we have focused primarily on the geometry and the idea of a multilayer structure for improvement of properties. When looking to characterize mechanical properties via indentation we know that not only does geometry affect the response but also the material selection.[48] Many thin film composites are made up of alternating hard and soft material layers such as a brittle ceramic for the hard layer and a more ductile metal for the soft. The resultant strengthening of metal-ceramic multilayers can be attributed to three main considerations: the metal layer response, the interface response, and the constraint of the ceramics.[57]

With large metal layer thickness dislocations would be able to pile up as expected in bulk materials. However as thin layers would be only one grain thick, the strength versus layer thickness in the pile up regime follows the relation that would be expected when considering Hall-Petch strengthening.[57] As the layer thickness decreases, dislocations pile up disappears.

At intermediate thicknesses ranging from a few nanometers to around 50 nm, deformation is able to occur through confined layer slip. Confined layer slip occurs when force is applied to a threading dislocation (one which is pinned on two adjacent interfaces) that causes the dislocation to bow between the layers. When the resolved shear stress

exceeds the energy for increasing the dislocation line length on the interface, the dislocations propagate through the layers leaving dislocation lines along the interface.[18, 57] Furthermore, dislocations crossing interfaces would not be applicable, as dislocation motion in ceramics is exceptionally unfavorable, the metal ceramic interface is therefore effectively impenetrable for dislocations. Theoretically, the only other deformation pathways available for the ceramic layers are brittle fracture and the formation of shear bands. In addition to impeding dislocation motion in the metal layer, the interface acts as a barrier to brittle fracture largely due to the crack blunting effect when passing through the ductile metal layers.[57] Thus the multilayer structure and resultant material interface acts as a barrier to both dislocation movement and brittle crack propagation through the material as a whole.

The third contribution to the strength is supplied by the ceramic layers and in the form of constraint. Constraint of deformation occurs when stresses are applied to adjacent materials with different stress strain behavior. In order to keep the interface between the two intact, hydrostatic stresses build up,[12] which delays the onset of plasticity in the weaker layer. As the metal and ceramic phases generally have very different elastic properties and strong interfaces,[2] this constraint helps to increase the apparent strength of the ductile layers. Additionally, once plastic strain begins to develop, the buildup of hydrostatic stresses greatly increases the strain hardening rate, as shown by studies using FEM simulations of laminate structures.[55, 57, 75]

In this thesis, Al is used as the soft metallic layer and SiC is used as the hard ceramic layer. Al/SiC nanolaminates have been explored using a variety of methods in order to understand this system better.[2, 48-57, 76] Findings include that as the layer thickness decreases the hardness grows due to increased plastic constraint on individual Al layers. However, layer thickness does not affect the elastic modulus as this is controlled by the relative volume fraction of materials.[2] Logically, however, the modulus does increase with increasing the amount of SiC and as indentation depth increases.[56] It has also been found that although damage is clearly present post-indentation, analysis by FIB showed that damage took place by localized cracking of SiC, plasticity and void nucleation and growth in aluminum layers. The voids were confined to the Al layers, indicating that the interface strength between Al-SiC and Al-Si substrate was higher than that of the fracture

strength of Al[2] leading to the conclusion in future work that delamination is not a top concern.

Another important aspect of the multilayered hard/soft coatings is their unloading induced plasticity during an indentation experiment.[52, 54, 56] Nanoindentation remains the major technique for assessing the mechanical performance of coatings and thin films. This technique is used to extract surface mechanical properties of materials by simultaneously measuring force (with a micro newton resolution) and displacement (with a nanometers resolution) during a full indentation cycle (penetration and withdrawal) usually using a sharp indenter. Response of material is assumed to be largely elastic during the unloading phase and hence the modulus of elasticity can be extracted from an indentation experiment following the Oliver-Pharr analysis.[35-37, 77-80] For multilayered hard/soft coatings, however, there is plastic deformation within the Al layers during the unloading phase of indentation (i.e., the unloading induced plasticity) making it difficult to measure the modulus.

The viscoplastic behavior of Al/SiC nanolaminates has been compared to deformation in Al thin films. With the observation that hold time during indentation has a pronounced effect of “creep” on unloading in pure Al. With zero hold time there is viscoplasticity during unloading due to a displacement lag. This is less predominant at larger hold times since the stresses are relaxed. This effect is minimal in the multilayered material because of the constraint from SiC which is encouraging for our efforts to determine properties via nanoindentation. However, the constraint also showed significant effect during thermal drift measurement at low load. The material experiences “negative creep” due to pushback from the sample upon removal of the indenter.[52] It is known that aluminum has a columnar growth pattern and so most recently the presence of undulating layers has been looked into and determined that it affects the mechanical properties of the multilayered thin films. Furthermore, in a multilayered coating with undulating layers, the variation hardness and modulus is dependent on the indentation depth and the phase of the waveform.[48, 50] The indentation-derived Young’s modulus becomes less sensitive to wavelength as wavelength decreases, which is good for small load indentations. However, it has been shown via finite element simulations that there is little correlation between indentation derived properties and those derived from uniaxial compression tests.[50]

Researchers have been looking into the comparison of micro/nano mechanical testing techniques common in literature and newer methodologies.[57] One commonly explored technique is that of micropillar compression which will be discussed with its drawbacks and benefits later in this thesis.[51, 75, 76, 81-84] Many other investigations have been conducted on this material system such as the effect of high temperature upon the loading response. These will not be discussed but are all important for moving toward ultimately understanding the indentation mechanics and response of multilayered hard/soft coatings.

The characterization of multilayered thin films and explanation of demonstrated property changes is a difficulty facing those researching multilayers. Although there are many advantages to multilayer structures there are also many challenges including delamination of layers, inconsistent deposition conditions, damage from processing techniques, and difficulty in imaging and mechanically characterizing these materials.

1.5. Motivation

Mechanical characterization of thin films and coatings is essential for their reliable design, research and development (R&D), and quality control (QC). Nanoindentation is the most commonly employed technique for this purpose. The effect of material heterogeneity (in this case the distinct hard/soft layer structure) on indentation response, and thus the measurement and interpretation of effective properties extracted from the indentation tests are, however, not well understood. As an example, previous analyses have implied an error of over 30% in indentation-derived elastic modulus.[55] More recently the effect of layer undulation within multilayers was studied in a numerical simulation and determined that the indentation derived modulus and hardness are directly influenced by the depth of indentation and the waveform of the undulations.[48-50] Although some believe that methods for performing measurements of hardness and elastic modulus were fully developed and the limitations of exactly what could be measured were established in the first two decades of nanoindentation research,[37] this is proved not to be fully correct. And, although since then the focus has shifted to a variety of other properties that can be measured at the sub-micron and nanoscales such as creep, viscoelasticity, and fracture, the fundamental research to determine methods of characterization for multilayered thin films is still highly important. Similarly despite much research being devoted to improving

systems to allow for measurements at extremes of temperature or environment, the theory for standard conditions must persist. Research should continue in these other areas, however, it cannot simply move on from fundamental mechanical properties of high importance in design of materials; namely, the hardness, H , a simple but important measure of the material's resistance to plastic deformation, and the elastic modulus, E , the most fundamental measure of a material's elastic behavior. Yes, models address how substrates influence the measurements so that the properties of very thin films could be unambiguously determined independent of their substrates, however, the effect of unloading inelasticity in multilayered thin films has not been addressed definitively.[37] This is the primary motivation for the research that will be conducted in this study. Furthermore, although modulation ratios have been studied for other systems and modulation period has been studied,[30] there has yet to be an investigation of the effect of the layer thickness ratio. Moreover, the effect of geometry on unloading plasticity has yet to be defined and as such it will be another parameter of investigation.

The purpose of this thesis is to address the questions pertaining to the dependence of mechanical properties, Young's modulus and hardness, upon certain variables and to further understand the role that unloading plasticity plays upon the indentation derived properties. Furthermore, we are hoping to provide a modeling structure to forecast these properties for a system of ductile/brittle multilayers on the nanoscale such that future development can use computational modeling to design a multilayered thin film, anticipating the resultant mechanical properties, before beginning fabrication of said film. The plan for achieving these goals is to first fabricate a series of test samples by sputtering aluminum, silicon carbide, and silicon dioxide monolayers and multilayers onto standard silicon and quartz substrates. The full list of fabricated samples can be found in Chapter 2 Fabrication and Characterization of Multilayered Coatings. These samples will then be subjected to nanoindentation testing and analysis with a Berkovich indenter to determine the properties of individual thin layers of each material over a range of thicknesses from 40nm to 1 μ m. Following monolayer indentation we will use the derived mechanical properties within computational simulations to determine the expected indentation derived moduli and hardness for samples of 51 alternating layers of Al/ceramic where the ceramics used will be SiC and SiO₂. Materials were selected based on prior study of the

Al/SiC system and potential informational yield from the Al/SiO₂ system as the bulk materials show a similar Young's modulus and therefore if the monolayer moduli are also matched it can be expected that the indentation derived modulus from a multilayer of these two materials would be also similar. Therefore any deviation between the multilayer modulus and the monolayer moduli can be determined to be a direct result of the multilayered structure. Both systems will undergo expansive testing beyond what has previously been studied. Furthermore the effect of modulation or thickness ratio will be studied where 25%, 50%, and 75% percent of material by volume will be aluminum while the ceramic layers will be 75%, 50%, and 25%, respectively. Each of these monolayer and multilayered samples, Al/SiC and Al/SiO₂, silicon or quartz substrate, and the three thickness ratios will be tested to multiple indentation depths. Similar depths will be used in the simulations of the multilayers to verify the validity of any depth dependent findings. Multilayered samples will be subjected to cyclic indentation to account for time dependent effects such as creep, thereby accounting for the viscoplasticity of the multilayer. This is driven largely by the plasticity of aluminum within the multilayer[48-56] and our intention of refining a reliable indentation technique, improving on the widely accepted indentation method proposed by Oliver and Pharr.[35, 36, 80] During indentation analysis it is important to note that monolayer indentation should show no dependence on unloading plasticity while the multilayers will.[49] Other characterization of the systems includes SEM and TEM imaging. Samples will be viewed under SEM to evaluate thin film thickness and surface roughness. Multilayer samples will be subjected to TEM imaging so as to investigate the structure of each layer, layer thickness and modulation ratio, consistency of deposition vertically and horizontally, and finally for layer undulation. Layer undulation is a result we are aware of due to the columnar growth of aluminum and the nature of waviness in multilayers to grow as more layers are deposited. Previous research shows that the undulation of layers does affect modulus and hardness in simulations based on depth of indentation and waveform[48, 50] therefore we would expect it to affect indentation derived modulus. Additional characterization by micropillar compression was planned initially but was reevaluated and will be attempted in future research. Micropillars were to be constructed from the multilayers using focused-ion beam and then

compressed while SEM and digital image correlation were used to extract the Young's modulus free of substrate effect by directly analyzing the stain field.

In this thesis we will cover the fabrication of samples, instrumented indentation of those samples, FEM modeling for better understanding of indentation mechanics and indentation derived properties, and finally discuss the results of our investigation and suggest future investigations to be conducted. Within Chapter 2 we will cover the basics of fabrication techniques for thin film coatings, discuss the specifics of the deposition process used to create our samples, and outline the measurement and imaging used to investigate the specimens. Chapter 3 includes an overview of nanoindentation theory, explains the concerns and practices for the system used and experiments conducted, and reports the results of our instrumented indentation experiments. Finite element simulations are discussed in Chapter 4 and cover previous work, model verification, and the results of some simulations specifically intending to bring light to physical indentation results. Finally, we will review our findings and discuss potential future work in Chapter 5.

Chapter 2. Fabrication and Characterization of Multilayered Coatings

2.1. Physical Vapor Deposition: Sputtering

Many materials can be layered onto to a substrate to form thin films and nanolaminates and this can be accomplished through a variety of manufacturing methods. Solid material can be deposited from solid, liquid, or even gaseous and plasma forms of the material. Often the deposition of materials is followed by a thermal treatment to derive certain properties or improve adhesion.

As outlined in the introduction, the key differentiation between physical (PVD) and chemical (CVD) vapor deposition is that there is a chemical reaction within the process of CVD where constituents of a vapor phase react at the surface of a hot surface and the reactants are absorbed onto the heated surface. The gaseous byproducts are then desorbed and removed from the reaction chamber. It should be noted that homogeneous reactions lead to gas phase cluster deposition and result in poor adhesion, low density, and high defect films.[71] Furthermore, the deposition rate of chemical vapor deposition is particularly difficult to calculate as it is determined by the slowest step of the process. Mass and heat transfer models are required to estimate the rate while knowledge of the sample surface chemistry, its temperature, and thermodynamics can be used to determine the compound deposited. Thereby this makes it difficult to deposit a thin film of proper stoichiometry let alone the correct depth. This difficulty makes CVD unmanageable for most of our needs and specifically for multilayered thin films this is an unrealistic option for deposition.

The most common methods for thin film deposition, particularly in integrated circuitry and micromechanics, are evaporation and sputtering, both of which are examples of physical vapor deposition. PVD reactors may use solid, liquid, or vapor for raw material based on the source configuration. More complex compound material deposition can be accomplished through other PVD techniques such as molecular beam epitaxy and laser ablation. Further methods such as ion plating and cluster deposition will combine advantages from multiple PVD techniques.[71] The most distinguishable feature of PVD is that deposition is line-of-site impingement type. This is a particular advantage in the low

pressure environments often employed in PVD that help the vaporized material to deposit upon the substrate with relatively few intermolecular collisions while traveling. This direct deposition characteristic allows for the simple calculation of deposition rates through geometric calculations. We will not discuss or review more deposition techniques in this thesis but rather give a brief overview of the method and system used; sputtering with a RF and DC magnetron, and its particular characteristics.

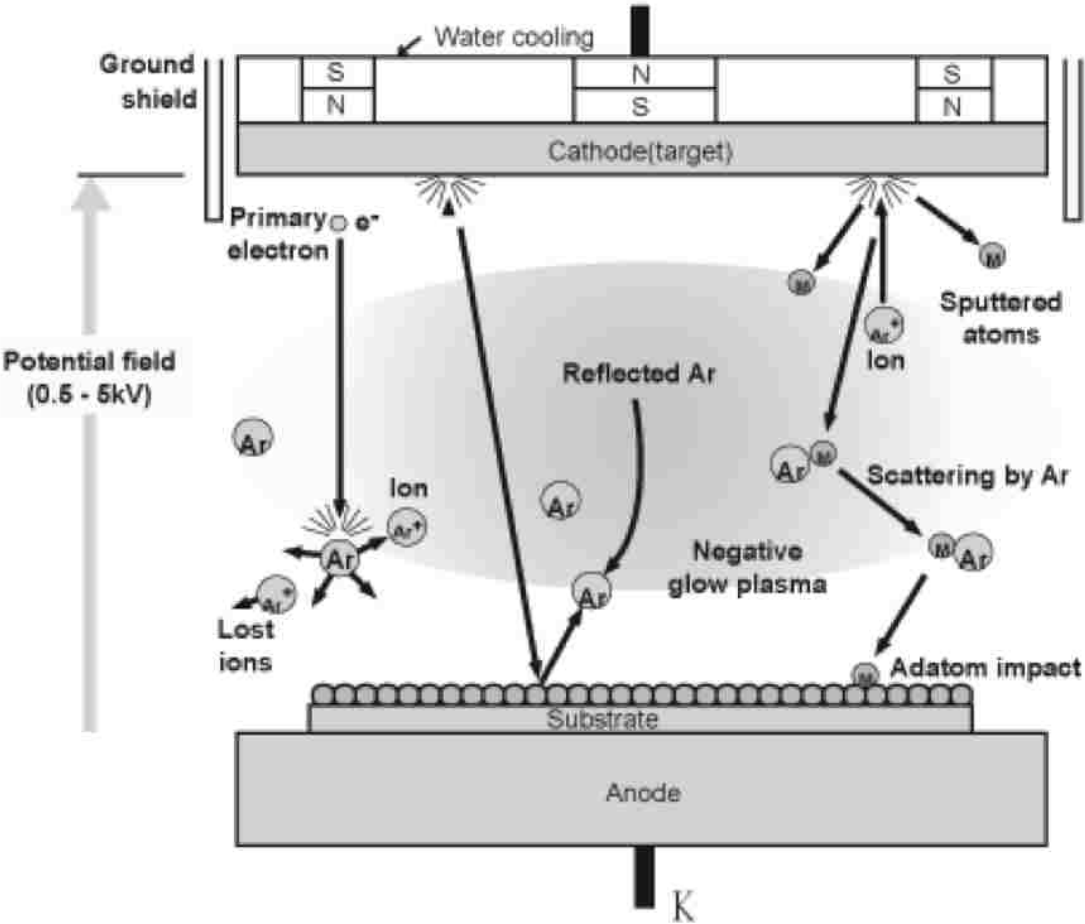


Figure 2.1 Schematic of a sputter gun setup showing the glow plasma creation of argon ions, collision of Ar^+ with the target material, resultant sputtered atoms traveling to the substrate, and the adatom impact.[85]

As a brief overview, sputtering has many advantages such as: material choice is nearly unlimited, *in situ* cleaning is easily accomplished, alloy composition can be tightly controlled, material decomposition is low, material uniformity is easy over large areas and

scaling up is simple. Furthermore, substrate adhesion is excellent, shadowing effect is small, many depositions may be carried out from a single target, and control of thickness and film properties can be controlled in many ways. However, there are drawbacks as well: the deposition rate is usually slow, impurities are possible based on the low to medium vacuum range, the surface can be damaged by ion bombardment or radiation, and substrate heating can be significant. Also from a financial perspective, the initial startup in capital equipment is expensive and the time required to change targets causes source material changes to be of significant expense.[71] This can be of particular problem for multilayer deposition as it requires different materials and therefore equipment able to switch between sources without removing vacuum. Fortunately the chamber used for this thesis has four sputter guns and can therefore accommodate large scale multilayer depositions efficiently while retaining a constant deposition environment.

During the sputtering process, a disc of the material to be deposited (called the target) is held at a high negative potential and bombarded with positively charged noble gas ions that are created within a plasma (glow discharge) as can be seen in Figure 2.1. The most commonly used gas, and that used in our fabrication, is argon.[71]



Figure 2.2 Sputtering target showing characteristic erosion pattern

The target is sputtered away as atoms are ejected from the surface and deposit upon the substrate or growing film. Due to the configuration of the magnetic field the target is eroded in a characteristic circular pattern shown in Figure 2.2 where collision is likely to occur. The magnets seen in Figure 2.1 and the collision locations shown lead to the circular erosion pattern when this cross sectional view is rotated around the central axis. Also visible in Figure 2.1 are the Ar^+ ions contacting the surface of the target and causing sputtered neutrals and free electrons to be ejected. Figure 2.1 shows a complete schematic of the DC magnetron making note of the water-cooling behind the target and making it is clear to see that as the pressure in the chamber drops the collisions between the sputtered atoms and Argon ions decrease in frequency.

There are significant drawbacks to the sputtering process that can be seen from these images, particularly the complexity of the sputtering process compared to a simple evaporative deposition process where the glow, Argon ions, and magnetic field are all absent. Furthermore, sputtering causes excessive heating of the substrate due to secondary electron bombardment. The water cooling and magnetron are therefore highly

important and can be used to help regulate the substrate temperature which has an effect on the material properties of the deposition. The other major drawback to sputtering is that the deposition rate is very slow, on the rate of one atomic layer per second rather than the thousands typical in an evaporative process.[71]

As mentioned before the sputtering chamber used for fabrication of samples in this study contained four sputter guns and can be seen in Figure 2.3

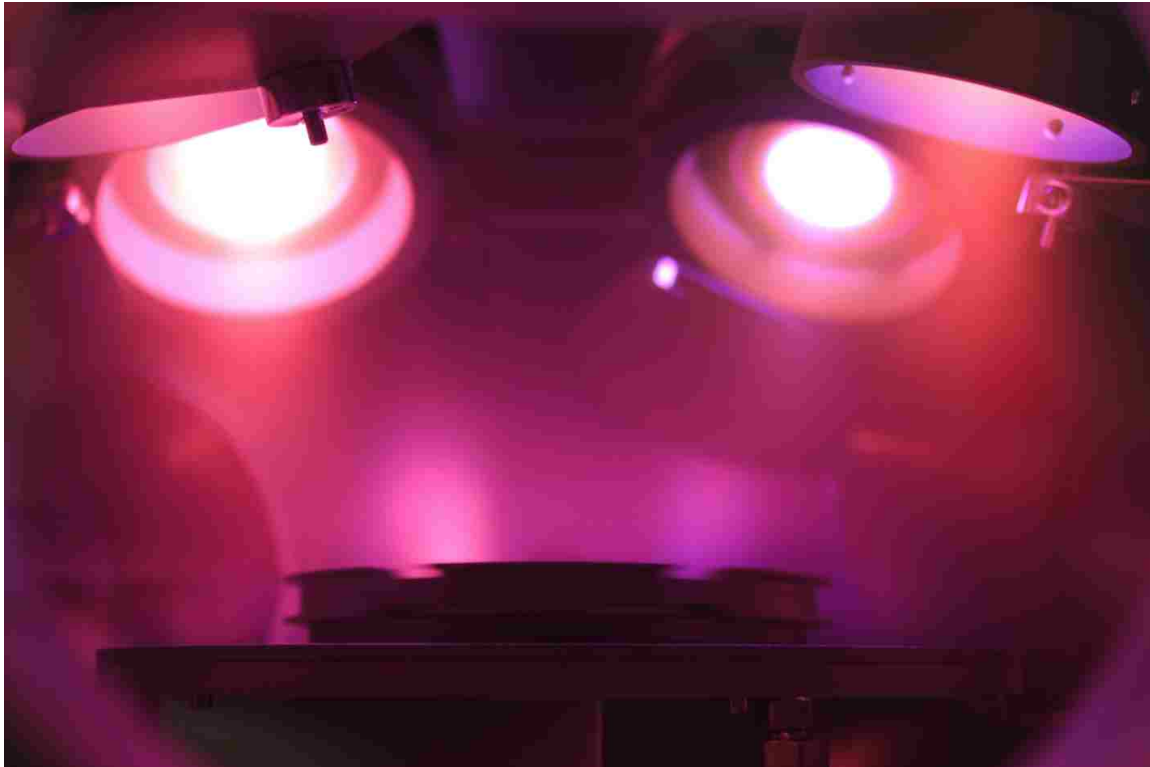


Figure 2.3 Inside of DC Magnetron Chamber (CINT Gateway Facility) showing plasma glow of four sputter guns with open shutters and rotating sample stage for even deposition.

This system (which can be seen in Figure 2.4) has a typical deposition rate of 0.5 - 5 nm/s, base pressure $\approx 2 \times 10^{-7}$ Torr, 4 magnetron guns with shutters and can accommodate 2" sputtering targets, 1.5kW DC or RF power and 5Kw Pulsed DC, a load-lock for inserting samples into the main chamber, and computer controlled processes. At this point it is prudent to note that the system used can produce either a DC or RF plasma. The theory of plasma physics will not be explained here except to note that when sputtering conductors a DC plasma can be used however when sputtering an insulator an RF plasma must be used. This is particularly important for us as both methods are required for the materials used in

this research. The Al and SiC layers can be deposited with the DC magnetron but the SiO₂ requires RF plasma.

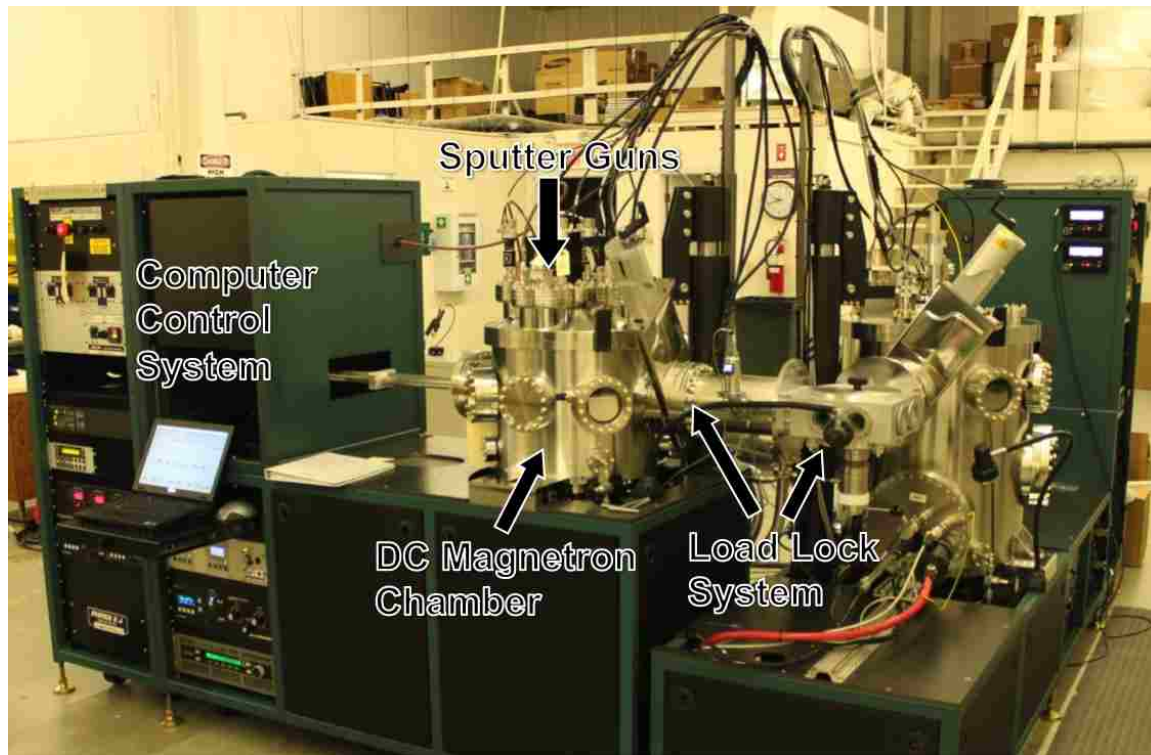


Figure 2.4 DC Magnetron System (CINT Gateway Facility) showing the vacuum chamber with sputter guns mounted above, load lock system and the computer control system. Not labeled is the e-beam evaporation system that extends on the right side of the picture.

The deposition is affected by several parameters controllable by the system: argon gas flow, nitrogen gas flow, chamber pressure, target power, substrate bias, substrate rotation, and substrate temperature. These parameters have significant effect on the deposited thin film such as when chamber pressure is decreased the number of contaminants decrease leading to a more pure film and often fewer nucleation sites. These must be carefully monitored because each change has multiple effects, continuing the example, as the pressure decreases mean free path increases and the kinetic energy of particles increases as well. This in turn has an effect of increasing the film stress and density. Films with a compressive or tensile stress are more likely to warp and are of particular concern in multilayered structures where the effect will grow with each new layer. This change in film stress and density could be compensated for by modulating the target power, however, that will also alter the rate of deposition. Similarly the compressive stress increases when

substrate bias is increased but doing so will also increase the density.[71, 85] As with most bottom up fabrication processes the parameters are closely related and connected in many ways. Samples for this study were carefully fabricated to minimize the undulation and maximize crystallinity and uniformity of the layers at the nanoscale. The samples created are listed in Table 2-1 and Table 2-2.

2.2. Fabrication Conditions and Characterization

Specimens were fabricated at the CINT Gateway facility in Los Alamos, NM within the RF/DC Magnetron chamber that can be seen in Figure 2.4. Initial depositions were conducted to tune the deposition chamber with the proper conditions and initial deposition depth was measured using a profilometer in order to determine a deposition rate for each material. The deposition rates calculated were 0.1 nm/sec for SiC, 0.03 nm/sec for SiO₂, and ~0.3 nm/sec for Al. These were general estimates for the deposition rate and were not constant; in particular the aluminum deposition rate was highly variable as can be seen in Table 2-1 and Table 2-2. Unless otherwise noted all depositions were conducted with the chamber pressure at 3 mT and an Argon flow rate of 30 sccm. SiC and Al films were deposited using 300 W of DC power while the SiO₂ required 150 W for an RF plasma.

Table 2-1 Single material thin film coatings

Substrate	Intended Deposition	Profilometer Reading and Deposition Time
Si	40nm SiC	40nm, 400 sec
Si	80nm SiC	80nm, 800 sec
Si	120nm SiC	120nm, 1200 sec
Si	500nm SiC	506nm, 5000 sec
Si	1000nm SiC	1.09 μm, 10000 sec
Si and Quartz	4000nm SiC	4.3 μm, 40000 sec
Si	40nm SiO ₂	40.9 nm, 1212 sec
Si	80nm SiO ₂	73.4 nm, 2424 sec
Si	120nm SiO ₂	115nm, 3000 sec
Si	500nm SiO ₂	733nm, 15152 sec
Si	1000nm SiO ₂	1484nm, 33333 sec
Si and Quartz	4000nm SiO ₂	4.4 μm, 99999 sec
Si	40nm Al	37 nm, 150 sec

Si	80nm Al	73 nm, 275 sec
Si	120nm Al	124 nm, 425 sec
Si	500nm Al	494 nm, 1667 sec
Si	1000nm Al	975 nm, 3125 sec
Si and Quartz	4000nm Al	4.6 μm , 13800 sec

Nanolaminate coatings fabricated consisted of 51 alternating layers beginning and ending with an aluminum layer. The intended thickness of each layer can be found in the following table and the thickness ratios were intended to deliver 25, 50, and 75 volume percent of aluminum, respectively. Layer thickness within the nanolaminates was a concern as deposition takes a significant amount of time and resources and *in situ* measurement of deposition growth is not accurate enough. As such, these specimens were deposited last for the highest level of confidence in deposition rates.

Table 2-2 Multilayer thin film coatings. The intended thickness was $4.08 \pm 0.1 \mu\text{m}$

Substrate	Deposition	Profilometer reading
Si and Quartz	40nm Al/120nm SiC	4.5 μm total height
Si and Quartz	80nm Al/80nm SiC	4.6 μm total height
Si and Quartz	120nm Al/40nm SiC	4.4 μm total height
Si and Quartz	40nm Al/120nm SiO ₂	6.8 μm , 4mT vacuum
Si and Quartz	80nm Al/80nm SiO ₂	4.9 μm , 4mT vacuum
Si and Quartz	120nm Al/40nm SiO ₂	4.8 μm , 4mT vacuum

2.3. Scanning and Transmission Electron Microscope Characterization

Specimens were viewed under SEM and TEM for quality control and microstructural characterization. First, samples were viewed under SEM in order to view the surface roughness and verify the thicknesses measured using the profilometer. The thicknesses of multilayer samples were confirmed by viewing samples at an angle and measuring height along a wall. The edges of samples give no useful information on layer thickness or quality, as they are grown during the deposition and not cut using FIB. A sample edge can be seen in Figure 2.12 for reference. In Figure 2.5, a Berkovich indentation of an Al/SiO₂ nanolaminate is shown with the top layer of aluminum and the surface of the nanolaminate. As expected, there is some roughness due to the columnar growth of

aluminum layers, which can affect indentation derived results for shallow indentations. This roughness does not appear to be significant and therefore deeper indentations should show little variation due to surface effects. The indentation shown is also explored under TEM through Figure 2.11.

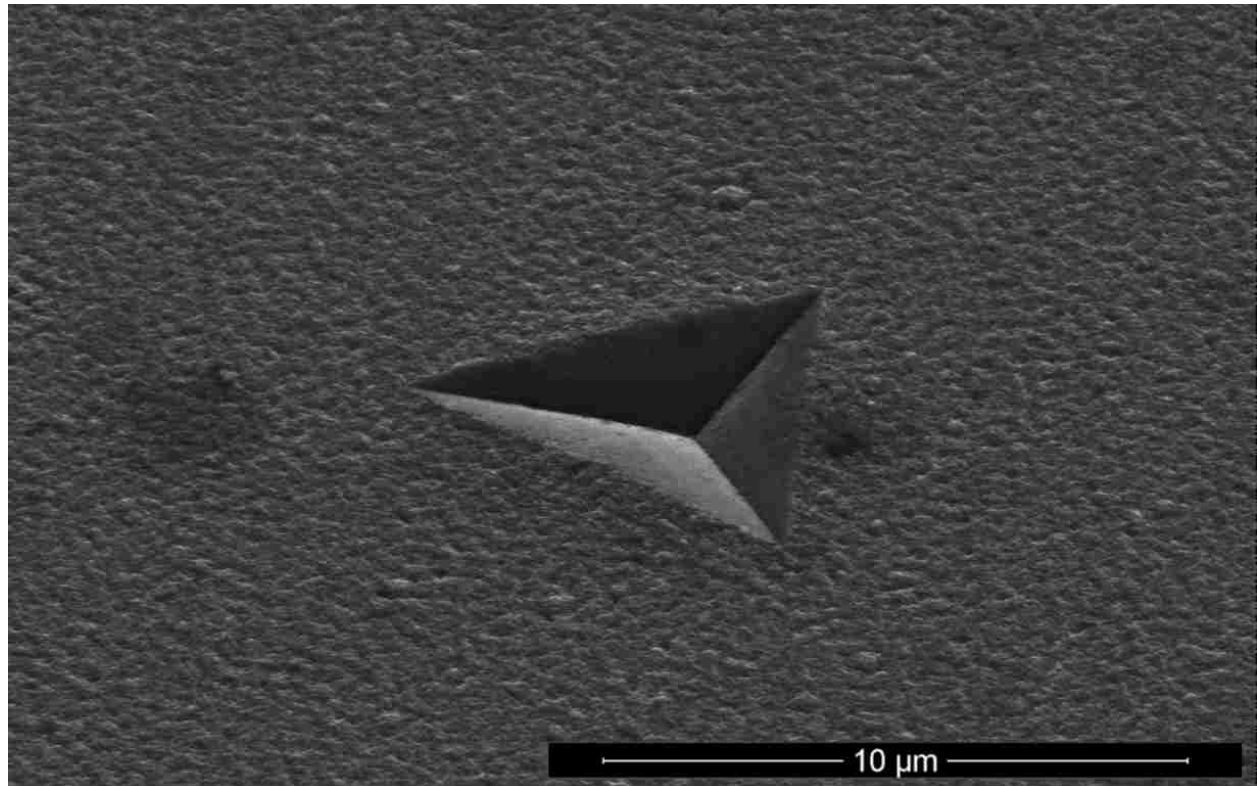


Figure 2.5 Berkovich indentation to extreme depth upon multilayer nanolaminate. Image under SEM shows relative surface roughness top 80nm Aluminum layer

TEM was used to further explore the nano-structure of the nanolaminates and to investigate the effect of indentation upon the multilayer itself. TEM samples were created through a process of platinum deposition over the indentation site as a shield and then FIB milling with gallium ions to create a stepped channel on either side of the indentation leaving a thin wall of nanolaminate under the protective platinum. FIB is then used to cut this wall free and platinum is used to secure the wall to a probe for liftout. This wall is then transferred to a TEM grid that can be moved from the SEM chamber to the TEM chamber. Full explanation of the liftout procedure is not covered here. Further thinning of the sample is conducted and can be seen in Figure 2.7. For this sample the thinning process

warped the sample due to large amounts of residual stress in the layers most likely due to stresses developed during deposition or induced stresses during indentation.

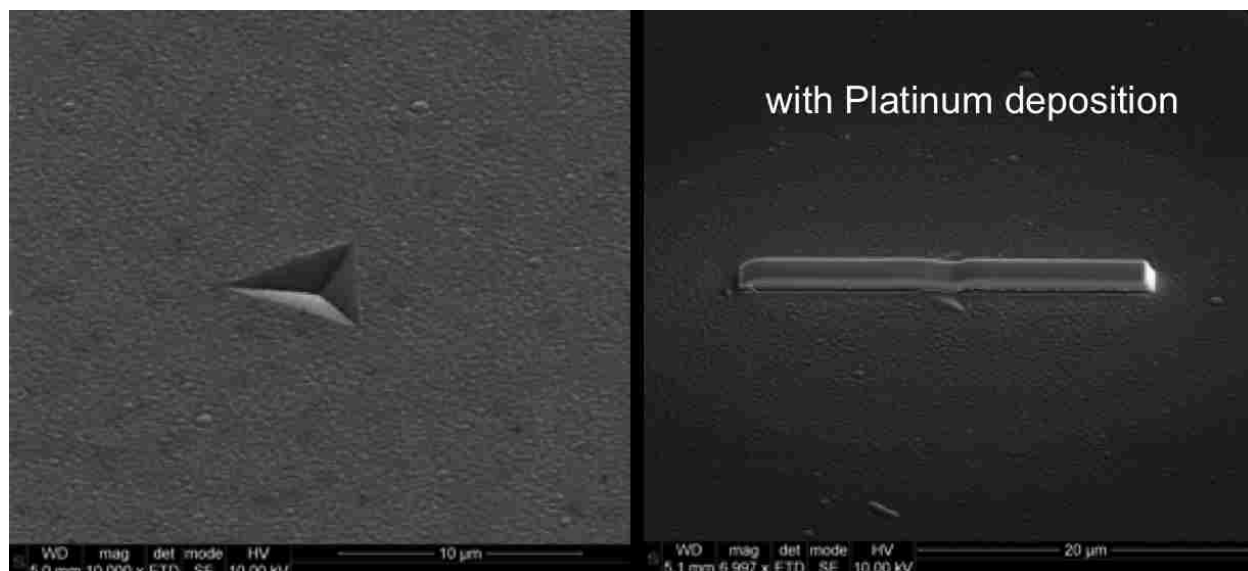


Figure 2.6 Berkovich indent of 51 layer Al/SiO₂ nanolaminate with layers approximately 80nm thickness. (left) Same indent with platinum deposited in preparation for the FIB milling and subsequent lift-out process for preparing a TEM sample. (right)

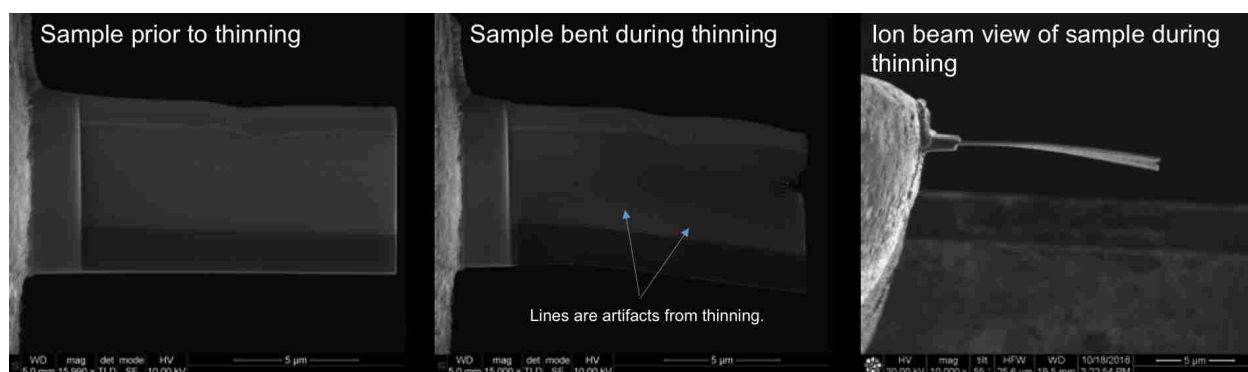


Figure 2.7 TEM sample of Berkovich indented 51 layer 80nm-Al/80nm-SiO₂ nanolaminate. From left to right pictures show the sample after liftout but prior to thinning , post thinning from SEM view, and during thinning view from the ion beam.

Bending of the sample was unfortunate as further thinning would be ideal, however, this is acceptable and yielded TEM images as below. Under TEM it is easy to see the layer undulation increasing from a nearly flat first layer. In Figure 2.9 the deposition near the Si wafer is shown and it is clear to see this increase within the first several layers. In these TEM images the columnar grain structure of the Al depositions can be seen along with

oxide layers that develop on exposed surfaces. One particularly important finding from these images is that there is no evidence of delamination with the multilayer structure or at the interface with the substrate. Similarly there is no void creation or crack propagation within the layers themselves, these are both positive findings as these are common the methods of failure found, such as can be seen in Figure 3.8. Investigation of the nanolaminate structure led to discovery of some areas of concern such as the one found in Figure 2.11 however in depth examination was inconclusive. Other findings of the TEM are simply the layer thickness was fairly consistent and no major concerns were identified. Near the end of TEM imaging the TEM camera was replaced with an upgraded imager however this system has had technical difficulties and as of yet is not operational. We regret that this problem continues to persist and so we are unable to deliver any more of the TEM results at this point.

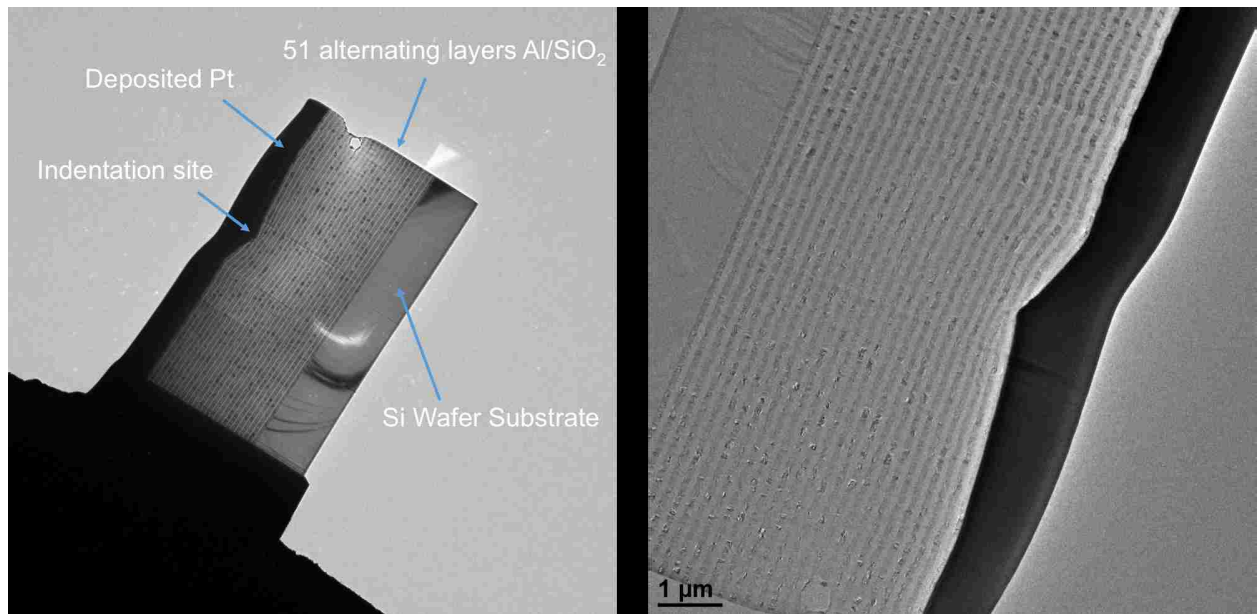


Figure 2.8 Post indentation cross section TEM: 51 layer nanolaminate of 80nm Al/80 nm SiO₂ films upon a Si wafer substrate. Berkovich indentation much deeper than regular max depth

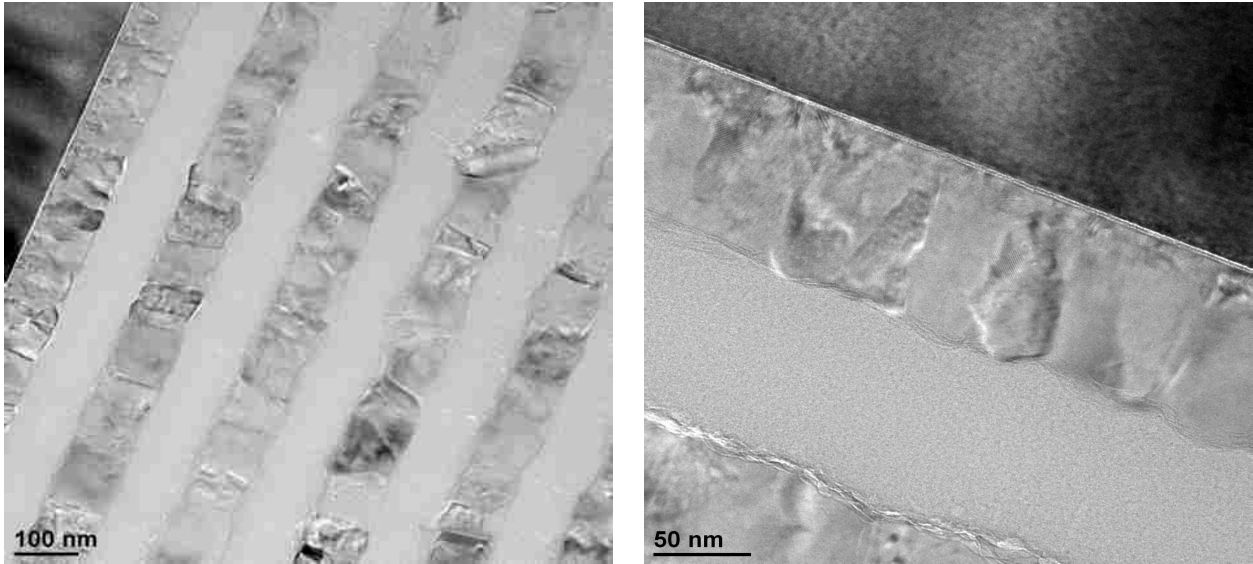


Figure 2.9 TEM of 80nm Al/ 80nm SiO₂ nanolaminate near substrate. Si wafer and thin oxide layer can be seen clearly, as can the structure of the Al layers. Note the growth of layer undulation as more layers are added.

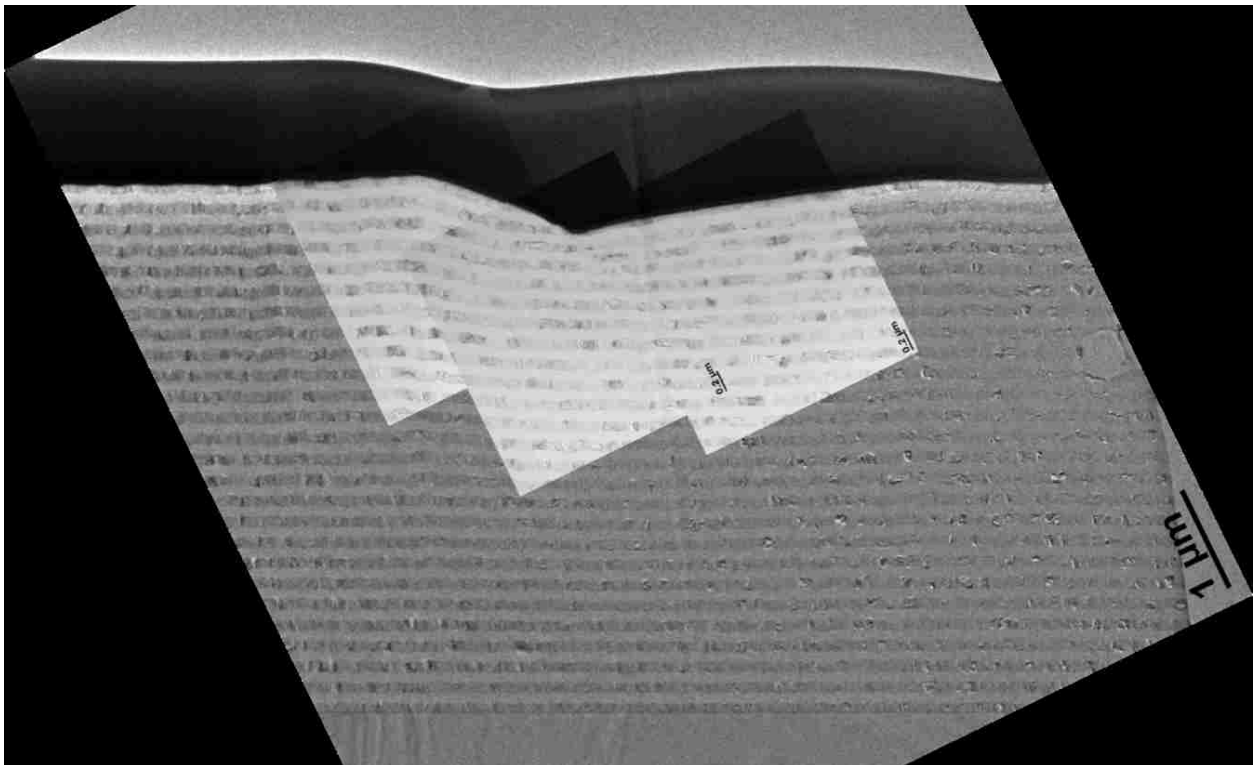


Figure 2.10 Composite of multiple TEM images near indentation site for greater clarity of indentation effects. Note no delamination within layers or at interface with substrate.

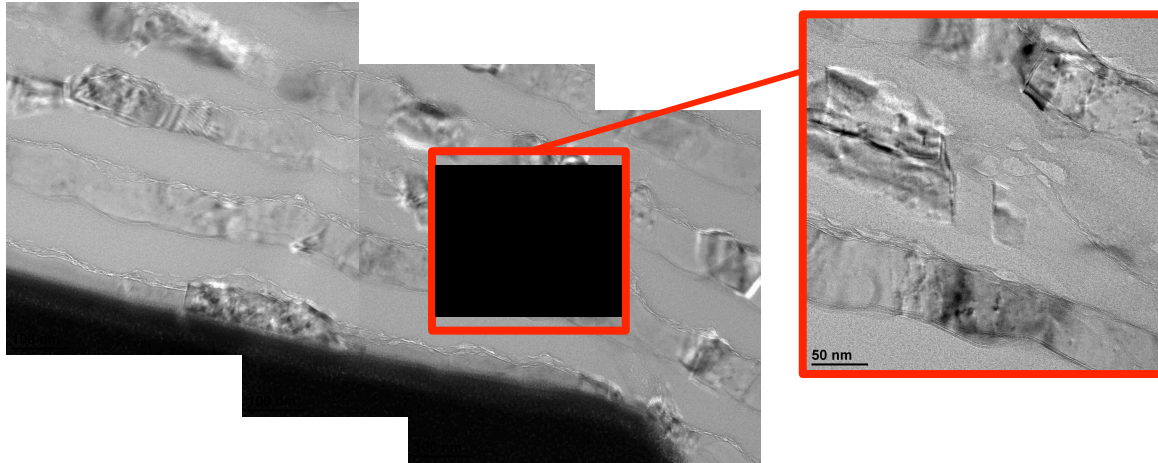


Figure 2.11 TEM expansion of 80nm Al/ 80nm SiO₂ near indentation site under extreme indentation stress. Findings are inconclusive.

2.4. Micropillar Creation

Micropillars and micropillar compression with digital image correlation procedure (DIC) will be discussed in Chapter 5. We include this section here as micropillar compression tests were intended to be performed, however, we encountered difficulties in the process as described here and opted to postpone micropillar testing. Micropillars were fabricated at the CINT Core facility in Albuquerque, NM within the SEM/FIB chamber. Milling was conducted using focused ion beam using the following parameters and can be seen in Figure 2.12:

Step 1. High current milling: 30keV, 20nA, mill annular ring OD = 40mm, ID = 10mm

Step 2. Pillar shaping: 30keV, 5nA, mill annular ring, OD = 9.5mm, ID = 5mm

Step 3. Pillar shaping: 30 keV, 1 nA, mill annular ring, OD = 5 mm, ID = 2.5 mm

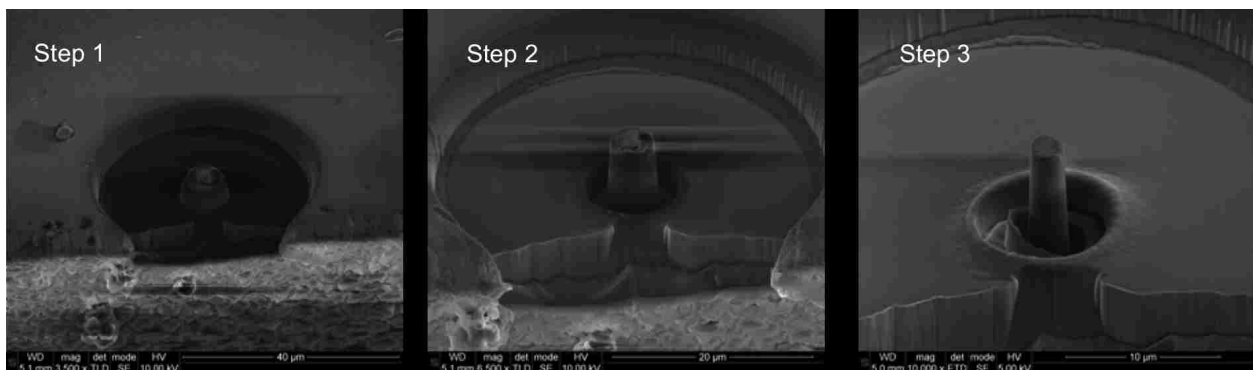


Figure 2.12 Preparation of a micropillar of 51 layer 80nm Al/80 nm SiO₂ nanolaminate.

Several pillars needed to be made for each decent pillar result, even considering this the taper was evident and imaging was difficult as can be seen in Figure 2.13.

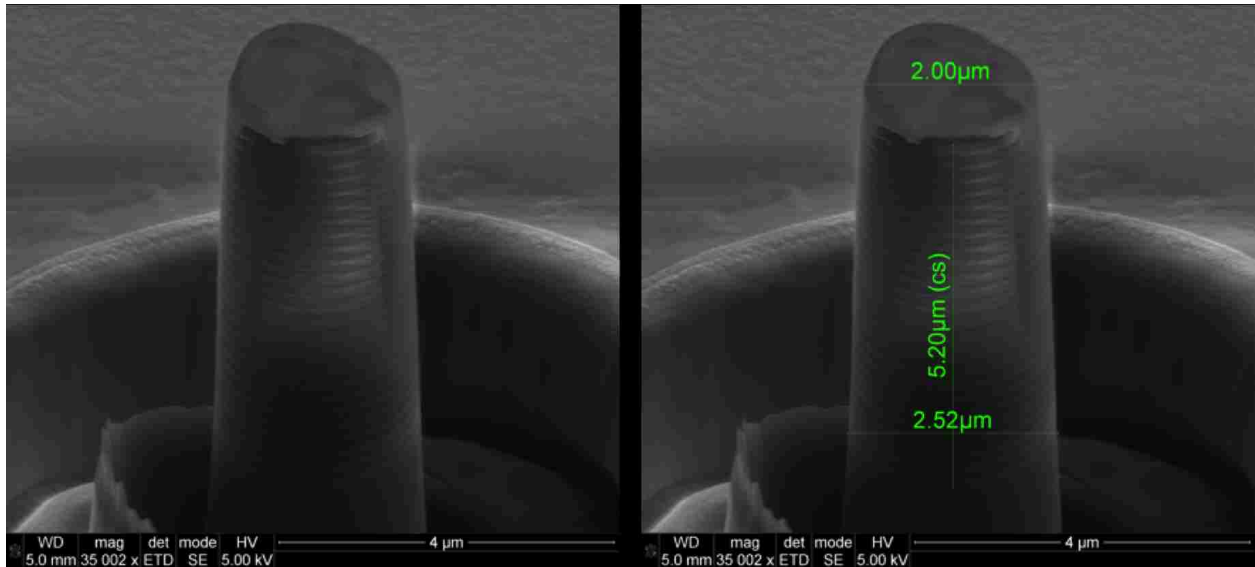


Figure 2.13 Micropillar of 51 alternating ~80nm layers Al/SiO₂ nanolaminate

Taper of the pillar in Figure 2.13 is noted by the measurements of pillar width at base and at tip. It is important to note that the specimen is charging significantly leading to difficulty imaging. This difficulty in imaging would make digital image correlation highly susceptible to error and therefore it was determined that the limited time available with the FIB machine at CINT would be more effective if used in TEM sample creation rather than micropillar fabrication.

Chapter 3. Nanoindentation

3.1. Theory of Nanoindentation

The goal of the majority of nanoindentation tests is to determine material properties of a specimen from the load displacement data. Primarily, as in the tests performed for this thesis, the focus is on extracting the elastic modulus and hardness. Many forms of conventional indentation hardness tests exist relying on the size measurement of a residual plastic impression as a function of indenter load. Thus giving the area of contact for a given indenter load.[86] Nanoindentation is a form of nanomechanical characterization for materials, similar to the larger scale indentation tests, however, the size of residual impression is only up to a few microns therefore making it difficult to accurately measure the size of residual indentation impression via optical methods. Thus rather than measure the residual impression post indentation, the depth of indenter penetration relative to the specimen surface is calculated from the maximum plastic depth. Typically experimental data is recorded for displacement and time while load is applied from zero to a predetermined max and back to zero. Using certain indenters with tips of known geometries then allows the size of contact area to be determined. This procedure allows for the modulus of the specimen to be determined from a measurement of the rate of change of load and depth of the contact, referred to as the contact stiffness.[86]

All indentations performed throughout this thesis were conducted using the NanoTest 600 system which will be described more thoroughly in section 3.4. The NanoTest software used for the analysis here utilizes a method developed by Oliver and Pharr.[35, 87] This method uses the load vs. displacement curves to determine the hardness and elastic modulus of a given material. All the indentations were conducted using a Berkovich indenter.

Berkovich indentation behavior and response has been well established in literature[4, 14, 34, 35, 48, 49, 73, 78, 80, 83, 88-90] and can also translate well to modeling [2, 48-50, 52-56, 91-94], but spherical indenters provide a smoother transition between elastic and elastic-plastic contact as well as providing a more diffuse stress field under the indenter tip.[86] Therefore the Berkovich tip was used in this study as a reference to verify results

with previous information. Spherical tip will be used in future studies to bring light to the system in a new manner. As mentioned previously, the critical aspect of nanoindentation is the known geometry for indenters and the subsequent ability to determine penetration depth. As such the Berkovich tip is a three sided pyramid which is geometrically self similar. It has a flat profile with a total included angle of 142.3 degrees and a half angle of 65.35 degrees.[86] The Berkovich indenter can be seen in Figure 3.1. A typical indentation curve is shown in Figure 3.2.[95] This figure also shows the values needed to do the analysis described by the Oliver and Pharr [87] method.

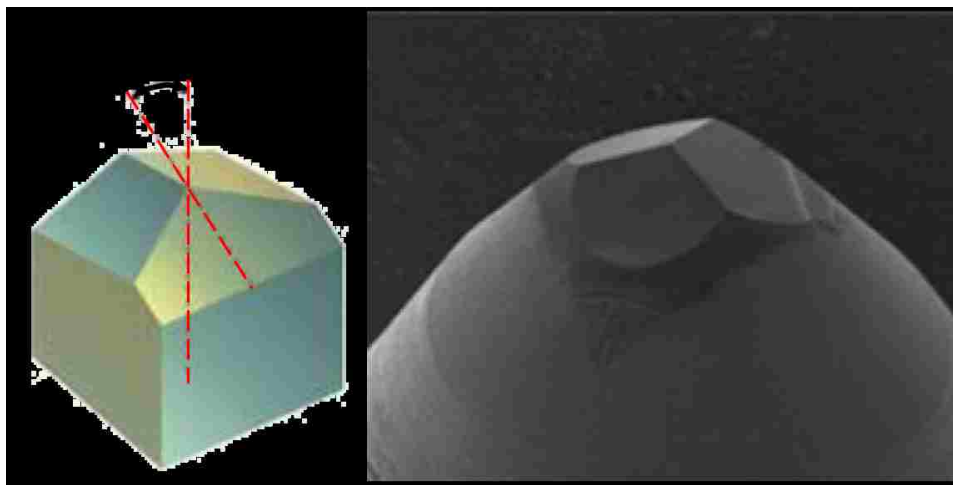


Figure 3.1 Berkovich indenter (left) and geometry and SEM image of a Berkovich indenter tip (right).[96, 97]

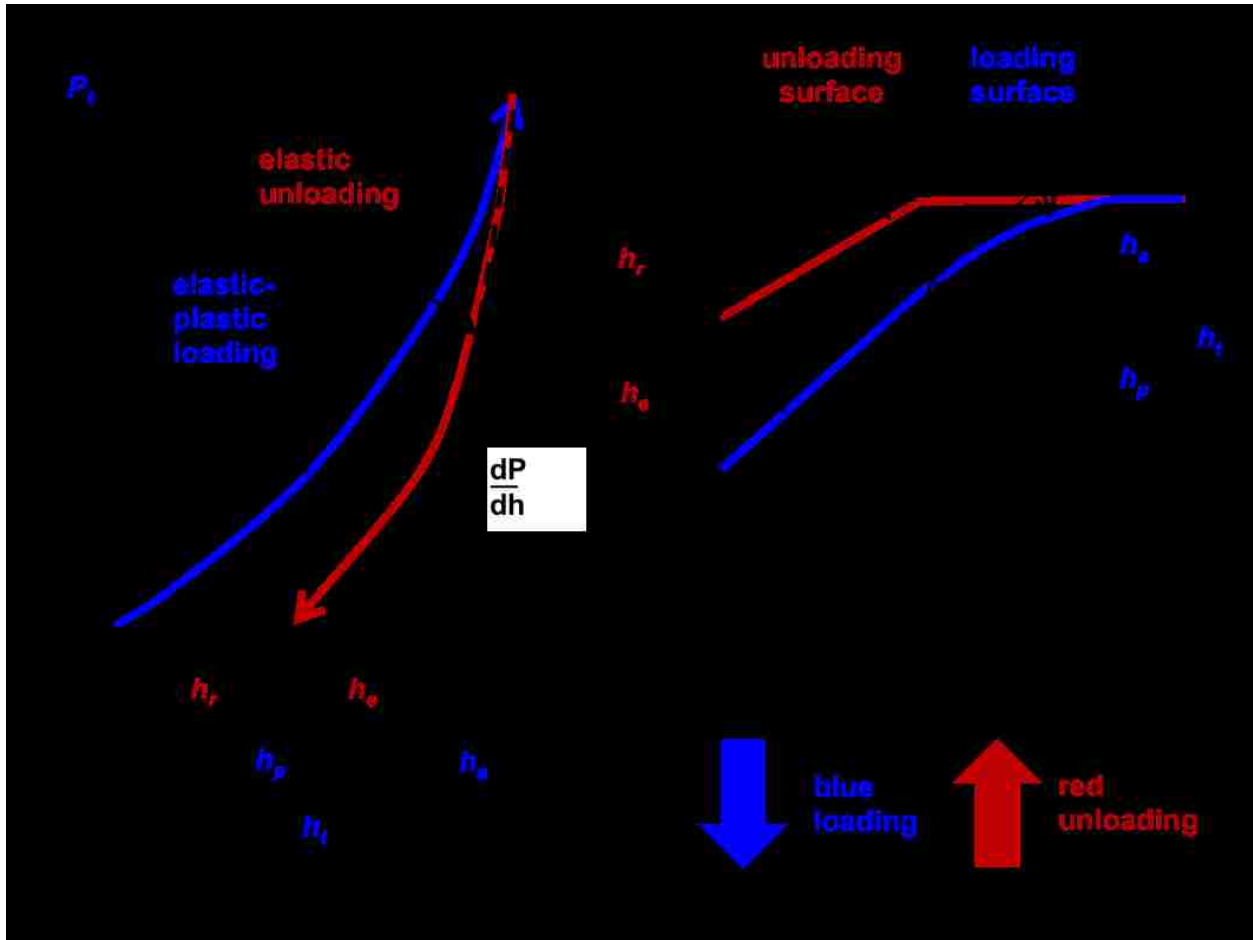


Figure 3.2 (a) Typical load vs. displacement curve for an elastic-plastic specimen loaded using a conical indenter. (b) Cross-sectional geometry of a conical indenter trace in the sample. Shows sample surface under full load and no load.

The values shown in Figure 3.2 are defined as follows:

- P_t , maximum load reached during indentation
- h_t , total depth at the maximum load of P_t
- h_e , elastic displacement recovered during unloading
- h_r , residual impression depth
- h_a , the distance from edge of contact to specimen surface at full load
- h_p , depth at full load where indenter is in contact with specimen
- a , the radius of area under indentation when unloaded

From these definitions one can conclude that

$$h_t = h_p + h_a \quad (3.1)$$

Also, for a Berkovich indenter the projected area of indenter, A , relative to the depth from indenter tip to edge of contact with specimen, h_p , is:

$$A = 3\sqrt{3}h_p^2 \tan^2\theta = 24.5h_p^2 \quad (3.2)$$

In this equation θ refers to the face angle of the Berkovich indenter of 65.3° . This geometry relates to a conical indenter with a half angle of $\alpha=70.3^\circ$ which is depicted in Figure 3.2. The 70.3° of a conical indenter simplifies images and simulations while allowing for the same area of contact, A , that would result from a Berkovich indenter. This fact will be exploited in Chapter 4 where a conical indenter will be used to simulate the Berkovich indentation.

As mentioned earlier, nanoindentation differs from normal indentation because it is based on the area under compression. This area is approximated at full load based on the depth of the indenter tip as described in Figure 3.2 and Equation 3.3, which is why nanoindentation is sometimes referred to as depth sensing indentation. Once this area under indentation, A , is determined from h_p , the hardness, H , can be computed as follows.

$$H = \frac{P_t}{A} \quad (3.3)$$

This is derived from the knowledge that mean contact pressure of the contact is equal to the indenter load divided by the projected area of contact, and then extrapolating into the fully developed plastic zone where it can be taken as the hardness, H . [86] Therefore when the projected contact area solved for in Equation 3.4 is substituted the hardness for a Berkovich indentation becomes:

$$H = \frac{P_t}{24.5h_p^2} \quad (3.4)$$

A similar situation can be described for the spherical indenter tip as can be seen in Figure 3.3. The analysis of indentation reviewed here will again be that of Oliver and Pharr, an alternative method was developed by Field and Swain [98-100] but is not pursued here. Either method is valid and usable for both types of indenters.

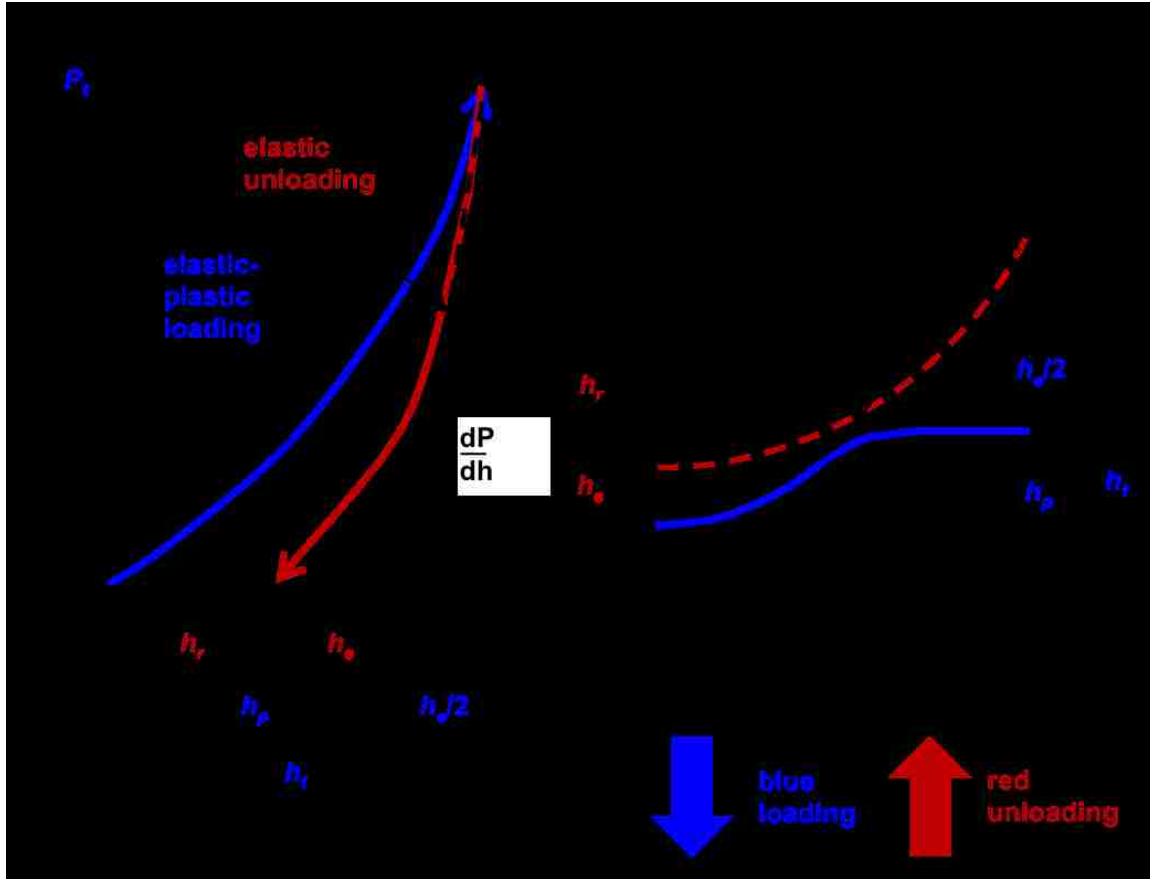


Figure 3.3 (a) Typical load vs. displacement curve for an elastic-plastic specimen loaded using a spherical indenter. (b) Cross sectional geometry for loading using spherical indenter of radius R_i , shows residual impression radius, R_r .

The values in Figure 3.3 are the same as in Figure 3.2 with the addition of R_i , the radius of spherical indenter used, and R_r , the radius of the residual impression left in the specimen surface upon unloading. The result of this type of indentation is again Equation 3.4, however, the area is circular and results in the hardness equation:

$$H = \frac{P_t}{\pi a^2} \quad (3.5)$$

Where a is the radius of the contact circle at full load as can be found in Figure 3.3 and can be approximated as in Equation 3.6 assuming $h_p \ll a$.

$$a = \sqrt{2R_i h_p - h_p^2} \approx \sqrt{2R_i h_p} \quad (3.6)$$

Full derivation on the Oliver and Pharr[35, 80, 87] analyses for these indenters is not rewritten here, however, the resultant equations for elastic modulus via Berkovich and spherical indenters can be found in Equations 3.7a and b, respectively.[86]

$$E^* = \frac{dP}{dh} \frac{1}{2h_p} \frac{1}{\beta} \sqrt{\frac{\pi}{24.5}} \quad (3.7a)$$

$$E^* = \frac{dP}{dh} \frac{1}{2a} \quad (3.7b)$$

It should be noted that these equations are actually equivalent and that the correction factor β applied for the Berkovich indenter is 1.034. These equations represent the theoretical calculation and when nanoindentation is applied there are several corrections that account for instrumental errors.

3.2. Calculations for Instrumented Indentation

In practice, the software of the NanoTest performs an analysis of the load-displacement data incorporating information from several calibrations to improve accuracy. This software begins analysis by fitting the unloading curve, 100% to 40% of the maximum load in this study, to the polynomial in Equation 3.8.[95, 101]

$$P = \alpha(h - h_r)^m \quad (3.8)$$

$$S = \frac{dP}{dh} \alpha m (h_t - h_r)^{m-1} \quad (3.9)$$

$$h_p = h_t - \varepsilon \frac{P_t}{S} \quad (3.10)$$

In these equations α and m are constants determined by the least squares fit and h_r is the displacement when $P=0$ upon return as in Figure 3.2. The polynomial is then differentiated to give Equation 3.9 for the contact stiffness, S , which in turn can be used to calculate the contact depth, h_p . Within Equation 3.10 is included ε , an experimentally determined correction factor for the indenter tip ($\varepsilon=0.75$ for the Berkovich and $\varepsilon=1$ for the spherical).

$$A(h_p) = 24.5h_p^2 + f(h_p) \quad (3.11)$$

As before the value of h_p is used to determine the area, A , however, due to tip blunting and manufacturing difficulties to achieve a perfect Berkovich indenter shape, the software uses the function in Equation 3.11 where $f(h_p)$ is a function determined from

calibration(fifth order polynomial was used for all analyses here). The coefficients of the function determined using a curve called the diamond area function or DAF for short.[95] This is a graph obtained from indentations done on a sample of known mechanical properties, in this case fused silica. These indentations are carried out over a load range 0.5-200 mN resulting in a full depth range from ~10-1200 nm(see Figure 3.4).

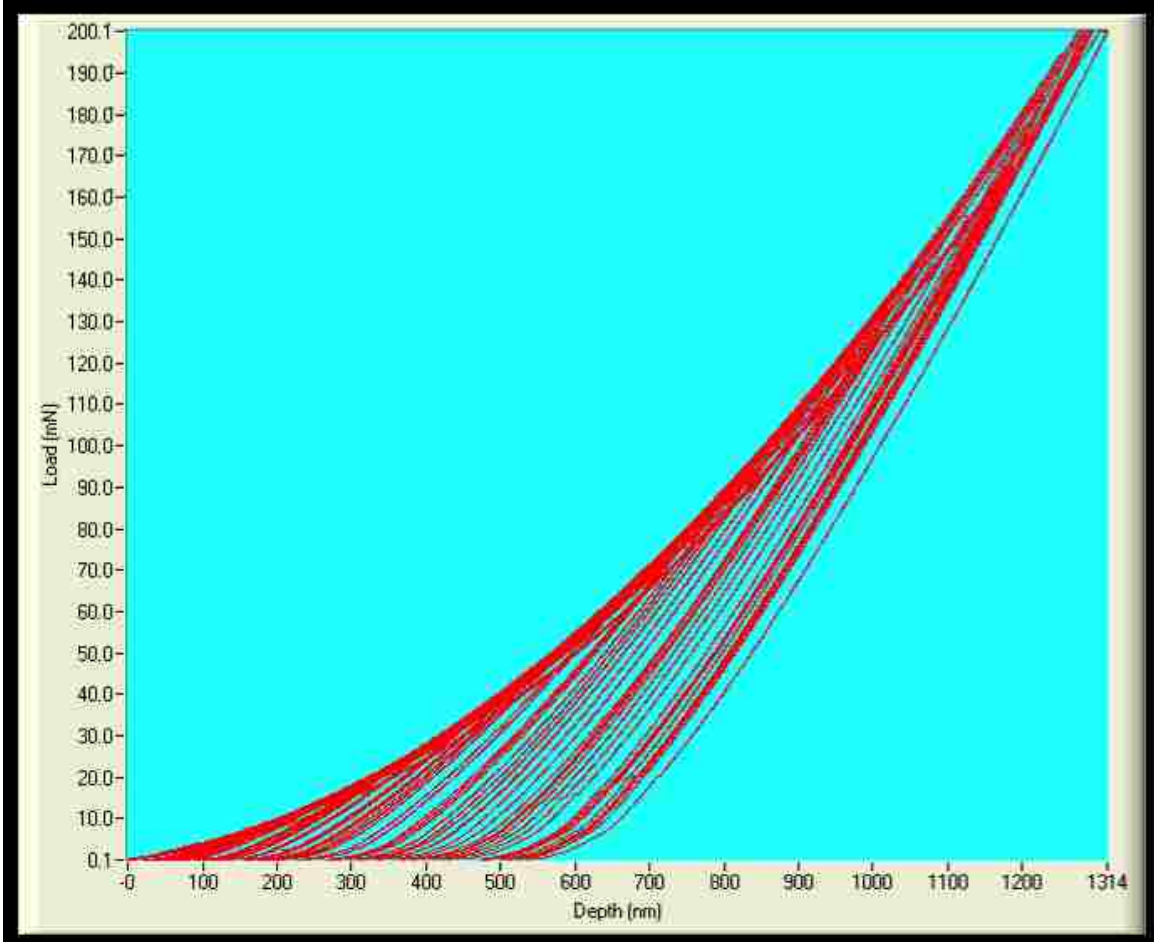


Figure 3.4 Load vs. Displacement curves for the indentations of fused silica which were used to develop the DAF file applied for analyses of all Berkovich indentations.

After completion of the indentations on the known reference sample, the loading data determines the DAF coefficients to fit the curve as can be found in Figure 3.5. Inserting the coefficients into Equation 3.11 gives our equation for area as a function of the plastic depth that can be found in Equation 3.12 below.

$$A(h_p) = 6.90 \times 10^{-5} h_p^4 - 0.0564 h_p^3 + 60.7 h_p^2 + 5050 h_p + 1.26 \times 10^5 \quad (3.12)$$

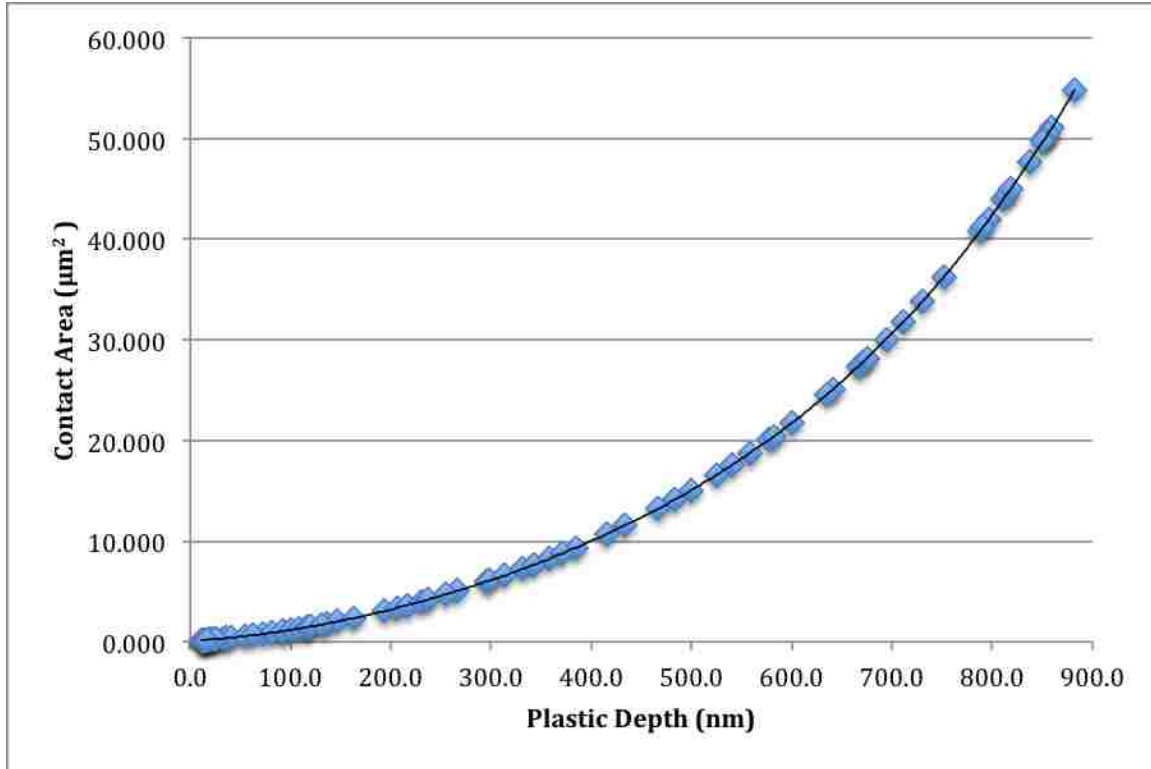


Figure 3.5 Diamond Area Function coefficients determined using fifth order polynomial. Resulting polynomial is used within Equation 4.11 for all subsequent analyses to determine contact area which is critical for calculations of hardness and elastic modulus.

For indentations of large depth (greater than one micron), we assume an ideal Berkovich shape which is in good agreement with the tests done on fused silica. This allows for calculation of the frame compliance of the system. Frame compliance was found to be $C_f = 0.061296 \text{ nm/mN}$.

Having determined the diamond area function and frame compliance allows for calculation of effective modulus which is completed by the software according to Equation 3.13, similar version of Equations 3.7 to account for calibrations.

$$E_{eff} = \frac{\sqrt{\pi}}{2} \frac{1}{\sqrt{A(h_p)}} \frac{1}{\frac{1}{S} - C_f} \quad (3.13)$$

Other calibrations and adjustments are made within the software such as the depth calibration and thermal drift correction and as such will be discussed in subsequent sections.

3.3. Indentation of Thin Films

Thin films of many materials have been studied by researchers using nanoindentation technique for a variety of reasons including the commonly small surface coverage of these films and the ability to measure spatial distribution of properties.[2, 4, 14, 18, 28, 30, 31] Unfortunately, additional complications arise when performing nanoindentation on a film that are not a concern when testing single material samples. Some of these concerns include the measurement of mechanical properties without influence from the substrate, delamination of deposited films from each other and the substrate, and finally plasticity within the unloading response during indentation. [2, 4, 14, 18, 28, 30, 31] One primary concern is the difficulty to avoid unintentional measurement of the substrate properties. In an effort to minimize the substrate effect it is common to measure up to a maximum depth of 10% the film thickness or less although this has been suggested to have no physical basis.[102] In our investigation the 10% depth was used as a guide for load determination and indentations we conducted both above and below this depth for a more robust determination of properties as a function of indentation depth. Furthermore there will always be some amount of elastic deformation within the substrate when doing indentation of thin films and as such the common 10% rule does not apply to measurement of the elastic modulus. There are computational methods to determine the elastic modulus of a thin film when substrate effect is unavoidable,[72, 103-106] however, these do not need to be used here. Rather the substrate effect can be eliminated through plotting the measured modulus against the scaling parameter, finding the trend of this relationship, and then measuring the intercept value for modulus. The scaling factor a/t is the radius of contact circle over thickness of film and therefore the film modulus can be taken as the modulus that would be measured with zero area under compression.[86] This is illustrated in Figure 3.6 which shows the values the a and t upon a conical indentation cross section, as well as a representative plot showing the projected film modulus.

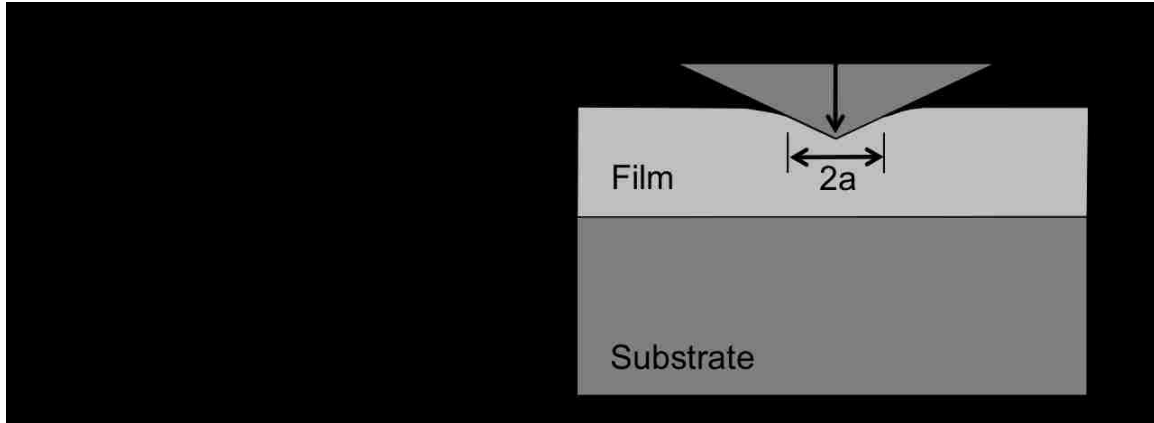


Figure 3.6 Scaling parameter a/t used to remove substrate effect when finding the Young's modulus for a thin film.

Similarly there are several methods for establishing an effective hardness due to the complex behavior of the plastic zone under and around the indenter. These methods range from empirically deriving correction factors to modifying the rule of mixtures, with different considerations for soft layers on hard substrates and soft layers on hard substrates.[107-110] Despite all these methods there is no method that successfully covers a wide range of material behaviors and therefore in the absence of a truly rigorous relationship the most common way to deal with hardness measurements is the previously mentioned 10% rule. For the multilayers investigated within this thesis the thickness is sufficiently large that the plastic zone is not directly interacting with the substrate and therefore no explicit relationship was applied for determining film hardness.

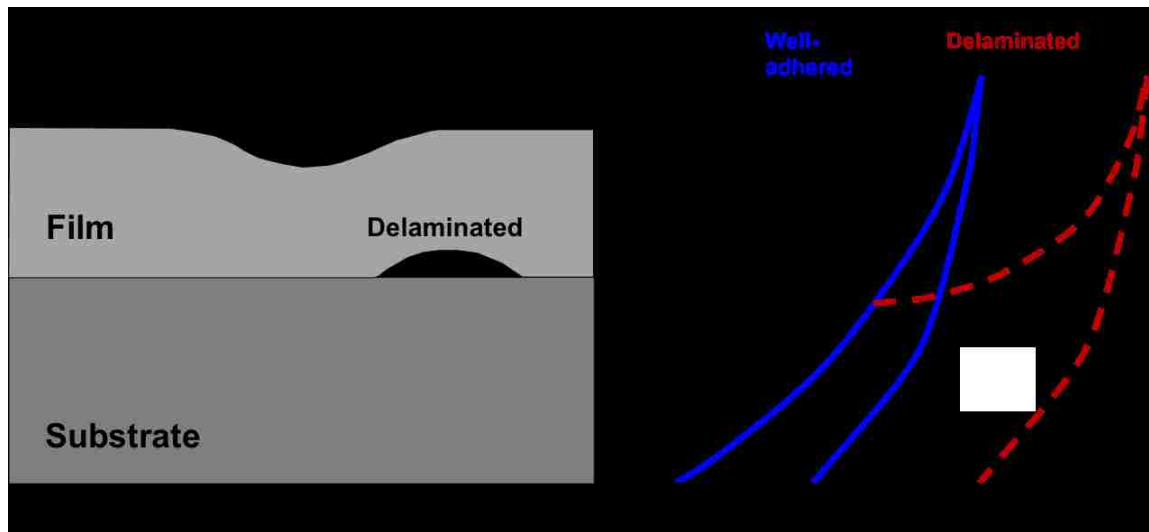


Figure 3.7 (left) Schematic of film delamination and separation from substrate under spherical indentation. (right) Characteristic shape and features of load-displacement curve typical to samples that are well-adhered and delaminated.

Another significant concern when working with thin films is delamination or debonding of the film from the substrate or another film. Delamination is difficult to anticipate as fabrication is often a complex task but more concerning may be that it is difficult to recognize and confirm without large amounts of post indentation processing and imaging. Film adhesion is often tested using a bent wafer technique and the Stoney equation[111] but can also be tested using indentation by applying load in a controlled manner until film failure.[86] Indentation stresses are not always enough to cause delamination of films and when indenting to shallow depths relative to the film thickness it is unlikely to encounter delamination. However, concern of delamination should always be considered when indenting thin films due to the high stress nature of indentation. If there is a distinct rightward shift in the loading section of the load-displacement curve then potentially a delamination, fracture, or dislocationburst has occurred.[86, 112] Figure 3.7 shows the common geometry of delaminated areas at left and the characteristic change in loading rate at right. Figure 3.8 shows a cross section of an Al/SiC nanolaminate similar to the ones investigated in this thesis where delamination has occurred.

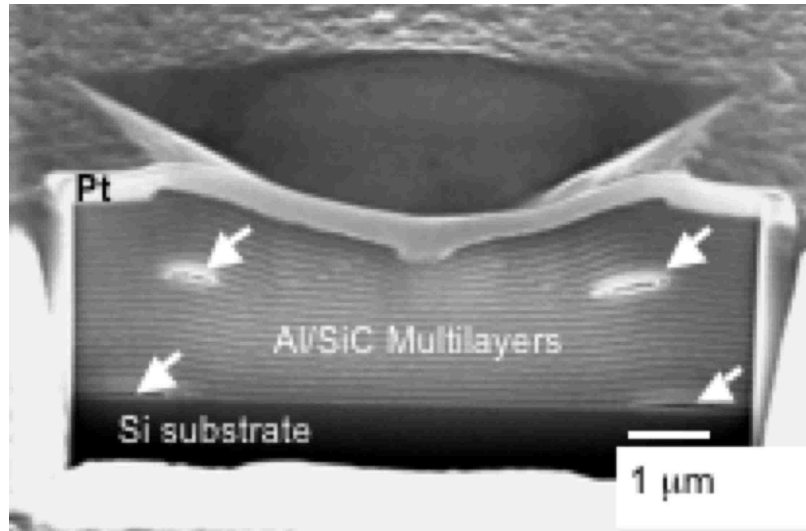


Figure 3.8 Cross sectional view showing delamination in 41 layer Al/SiC nanolaminate with approximately 50nm layers. Delamination shown by white arrows on either side of indentation between layers and at layer and substrate interface.[55]

While all of these complications pose challenges to research of thin films, our focus will be upon an issue specific to multilayers. While the basic theory of nanoindentation relies upon the assumption that the unloading response is purely elastic there is numerical evidence of plasticity during nanoindentation unloading of nanolaminates.[48-52, 54-57] Shown in Figure 3.9 are contour plots of the equivalent plastic strain for a simulated Berkovich indentation of a 41-layer nanolaminate with Al and SiC layers of 50nm. These show the presence of plastic deformation upon unloading of the specimen which can be seen most clearly in the increase of red shown just to the right of the indentation center. It is also easy to see in the growth of the light blue near the layer/substrate interface. The equivalent plastic strain is a value that measures the accumulated plastic strain within an element rather than the classic plastic strain value which is constrained by the sign (and therefore direction) of deformation.

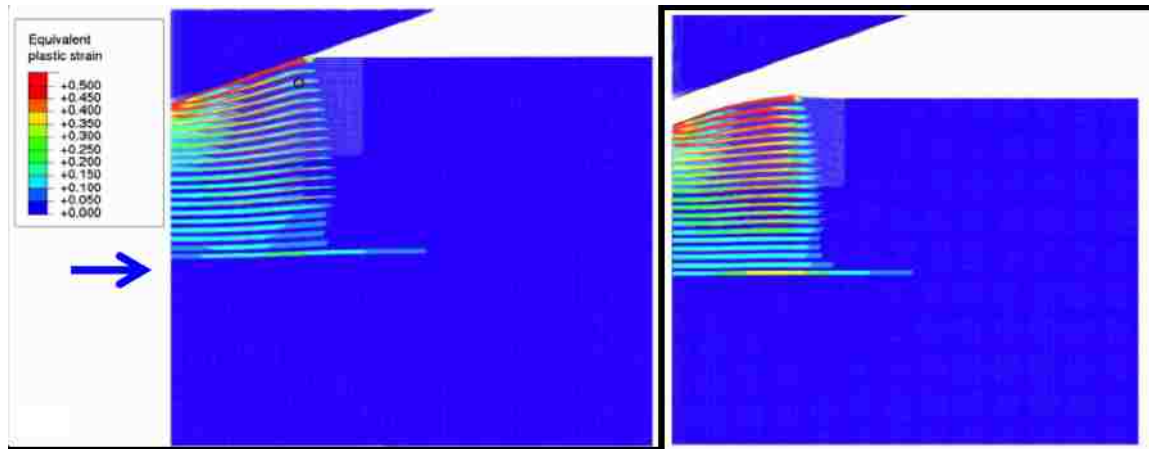


Figure 3.9 Simulated load-displacement curve during indentation unloading. Contour plots of the equivalent plastic strain as indenter retracts from full load for an indentation of 0.5 μm . Images adapted from Tang[54] and show only the material close to the indentation site. The scale is the same for both images and the blue arrow at left shows the interface between silicon substrate and the first layer of the Al/SiC nanolaminate.

The presence of the inelastic portion of unloading within multilayer nanolaminates is a significant concern and therefore the current treatment for nanoindentation calculations[87, 98] seems to be insufficient based on improper assumption that the unloading of the material is a purely elastic process.

As a brief note there are several measures that can be taken to minimize errors and are common practice including utilization of a properly fitted DAF file, precautions to minimize vibration and thermal environmental disruptions, and hold periods at max and near min load to minimize the effect of creep and correction of thermal drift. Although all these calibrations and corrections were carefully implemented, not all of the concerns are listed in this thesis and all calibrations will not be discussed as a full review of theory and implementation would be far too extensive and unnecessary.

3.4. The NanoTest System

The Nano Test 600 is a pendulum based nanoindentation machine developed by Micro Materials Ltd. United Kingdom consisting of 3 separate operating modules: indentation, scanning (scratch), and impact. All three modules can be used in conjunction with the low load head which is 0.1-500 mN. The system provides a following wide range of testing

options: spherical indentation, pin-on-disc wear testing, continuous contact compliance (CCC) measurement, high temperature testing, wet-stage testing, AFM scanning, nano-positioning, nanoscratch, friction and impact/impulse testing. Transverse sample movements during loading enable scanning measurements (scratch testing, fatigue and wear testing) while sample oscillation at constant load is used for impact testing, contact fatigue testing, nano-positioning, and dynamic testing. The system is placed inside a thermally insulated cabinet upon a vibration-damping inertial mount. The cabinet serves to provide a thermally controlled environment with reduced air turbulence and increased soundproofing to reduce acoustic disturbances.

Layout of the NanoTest system can be found in Figure 3.10. At its heart sits a pendulum mounted to a frictionless pivot. A coil is mounted at the top of the pendulum; when a current is applied, this coil is attracted towards a permanent magnet, producing motion of the diamond tip towards the sample and into the sample surface. The displacement of the diamond tip indenter is measured by means of a parallel plate capacitor with one plate attached to the diamond holder. Therefore when the tip moves, the capacitance changes, which is measured by means of a capacitance bridge unit located so as to minimize stray capacitance effects.

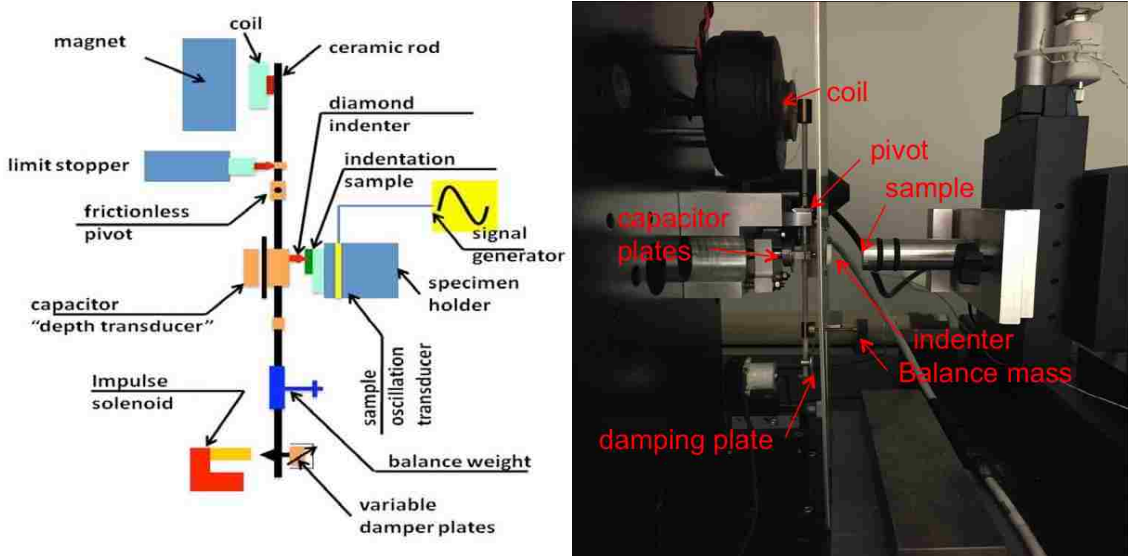


Figure 3.10 Schematic and Picture of NanoTest 600 components

Sample positioning displacement is achieved by means of three DC motors driving micrometer stages in an XYZ configuration. The motor control electronics consists of a motherboard containing three power modules, an IEEE interface module and a backlash control board. The motor power supply is driven by the controllers through visual interface of the system software in the computer, with motor positioning obtained by means of magnetic encoders. The motor control board communicates with the system computer via the IEEE bus. The limit stop defines the maximum outward movement of the diamond, and also the operating orientation of the pendulum, when a load is applied. Its position is manually adjusted with a micrometer. The equilibrium position of the pendulum is adjusted automatically.[95, 101, 113]

The theoretical resolutions of the UNM system are a load resolution of 1 nN and a depth resolution of 0.004 nm as given by Micro Materials Ltd. at the time of purchase.[95]

Due to the location's environmental factors (vibration from other labs, student movement, vehicles driving by, slamming of doors, elevator movement, etc.) the machine cannot actually reach this level of accuracy. In an effort to minimize error a variety of calibrations can be performed, some more often than others. Some of these are:

Load calibration – Establishes the forces that can be applied at the diamond tip during a measurement.

Depth calibration – Relates the change in capacitance to a known distance moved by a sample in contact with the pendulum.

Frame Compliance – Corrects for “flexibility” in the structure of the machine.

Microscope Sample Stage – First of two microscope calibrations in which the distance from the indenter tip to the focal plane of the microscope is determined.

Microscope Cross Hair – Second of the microscope calibrations necessary to position the sample for precisely placed indentations. This entails determining the Cartesian offset between the indenter tip and the microscope center within the focal plane.

There are two different methods for accurately determining the machine/frame compliance of the NanoTest system. First method is an indirect method using a reference sample of known modulus; fused silica. The second method is the direct compliance measurement method. One needs to know the exact area of impression of the indenter at

any depth to be able to do the analysis using this method, while the indirect method assumes an ideal Berkovich shape for high loads/depths.

Knowing the properties of the reference sample, fused silica in our study, some maximum load indentations, 200 mN for example, are carried out on the reference sample from which the frame compliance is calculated. The direct method uses a rigid pin to solder the stage to the indenter. A simple load ramp-up is done and the only compliance due to the machine flexibility is measured. For our machine compliance was measured on a reference sample of fused silica. From the measured data the contact compliance can be determined and then the sample compliance is obtained from: *Total (measured) compliance (C_t) = contact compliance (C) + Machine/frame compliance (C_f)* When the sample compliance is small (high modulus sample) the machine compliance makes up an appreciable fraction of the total measured deformation and so small errors in the machine compliance can affect the accuracy of the sample modulus determination.

3.5. Sample Specimen Mounting

Particularly important for the accuracy of results is proper calibration and test execution. Much of the calibration information has been outlined in section 3.4. Outlined here is the importance of properly mounting a sample using glue as we discovered throughout the experimental process. Many nanoindenters use SEM pucks for mounting samples and as such it is common to mount specimens using some form of adhesive tape for ease of sample removal. While this may be sufficient in some situations we have found that for stiffer samples this can cause a significant change in indenter derived mechanical properties. The effect of the tape was first noticed during preliminary testing while samples were still being fabricated. The first large test was the spherical indentation of a 4000nm thick specimen of SiC deposited onto a Si wafer. The Load vs. Depth information resulted in the rightmost 25 curves found Figure 3.11. When these results were reviewed it was clear something abnormal was occurring. First, it should be noted that there is an exceptionally large amount of creep both during the top dwell as well as during what is intended to be bottom dwell to measure thermal drift during the test. Second, as the load increases each series of five indents is clearly separate and within the later groupings the maximum depth decreases as load increases. While the first observation is important it could be explained

in a variety of ways and is not addressed extensively here. Clearly there is a massive amount of compression occurring within the tape at all times, however, it could be assumed that the stiffer specimen material will elastically recover first before the tape. This second observation is the more significant of the two as this behavior is antithetical to the mechanics of the specimen but can be understood in context of the mount and in turn explains the grouping.

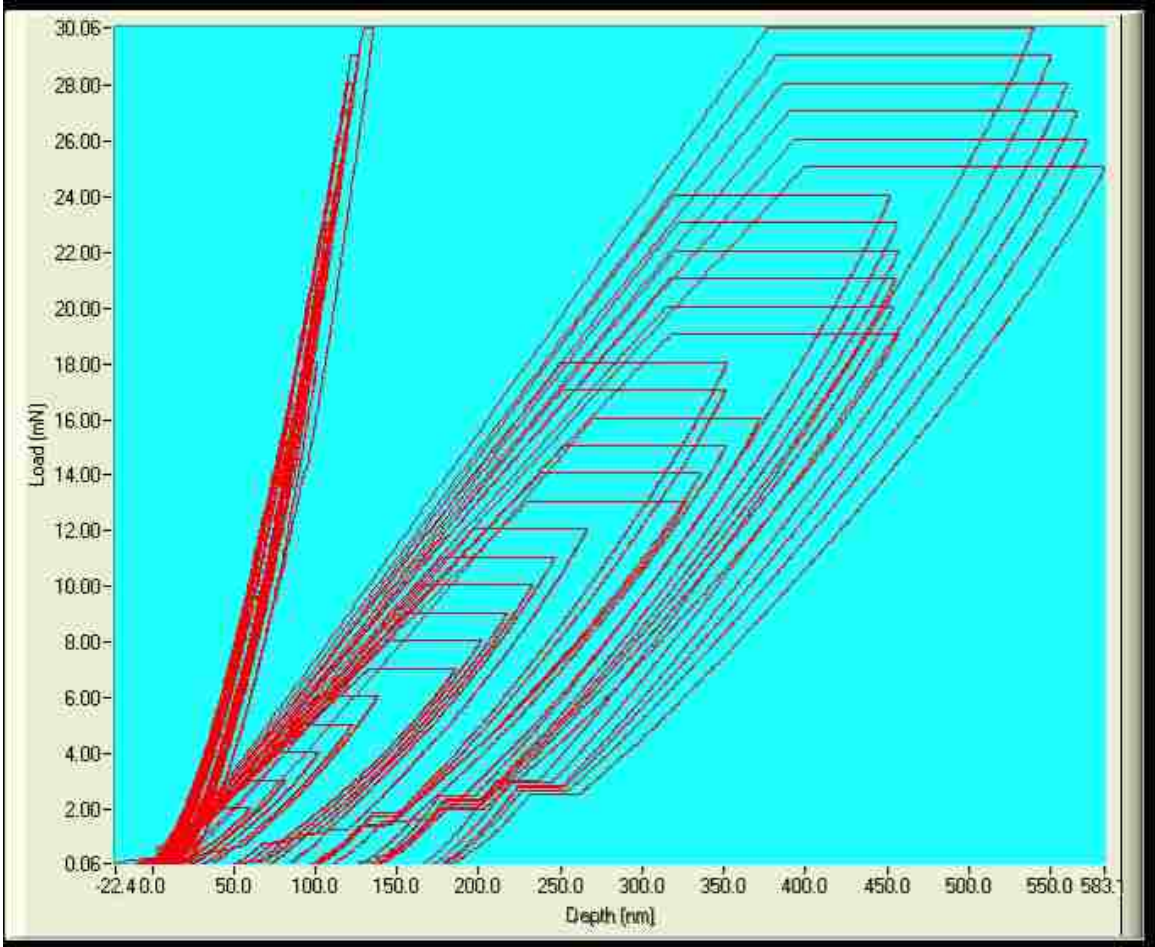


Figure 3.11 Indentation response of glued (left series) and taped (right series) SiC specimen under extreme loading with a spherical indenter

In order to understand we must first have knowledge of the system and how the indentation schedule was conducted. These 25 indentations were run in a 5x5 matrix where the indenter moves laterally for a row of indents then rasters back over and moves to another line in a fashion similar to a typewriter. What Figure 3.11 shows is that at low loads the tape is being compressed along with the sample and then elastically recovering

between indentations. However, as the loads increase the tape does not have enough time to recover back to its original position or has undergone plastic deformation therefore the indentation is occurring with the sample sitting at a deeper position. Therefore, the effect of the tape looks less pronounced because the point at which the indenter comes into contact with the sample (and reads zero depth) already includes the plastic deformation or depth of the viscoelastically compressed tape. The result is that the indenter sees a “stiffer” sample as load increases although the measured depth actually decreases. This is particularly interesting when seen in the plot of Depth vs. Modulus seen in Figure 3.12. It is natural for Americans to read a graph from left to right as if reading words, however, in this circumstance there is a section in which the assumption of left to right is actually incorrect. Looking at the rightmost data it would be logical that because we know depth increases as load increases the modulus must decrease with increased load. However the indents were actually completed in order from right to left as load increased but depth decreased.

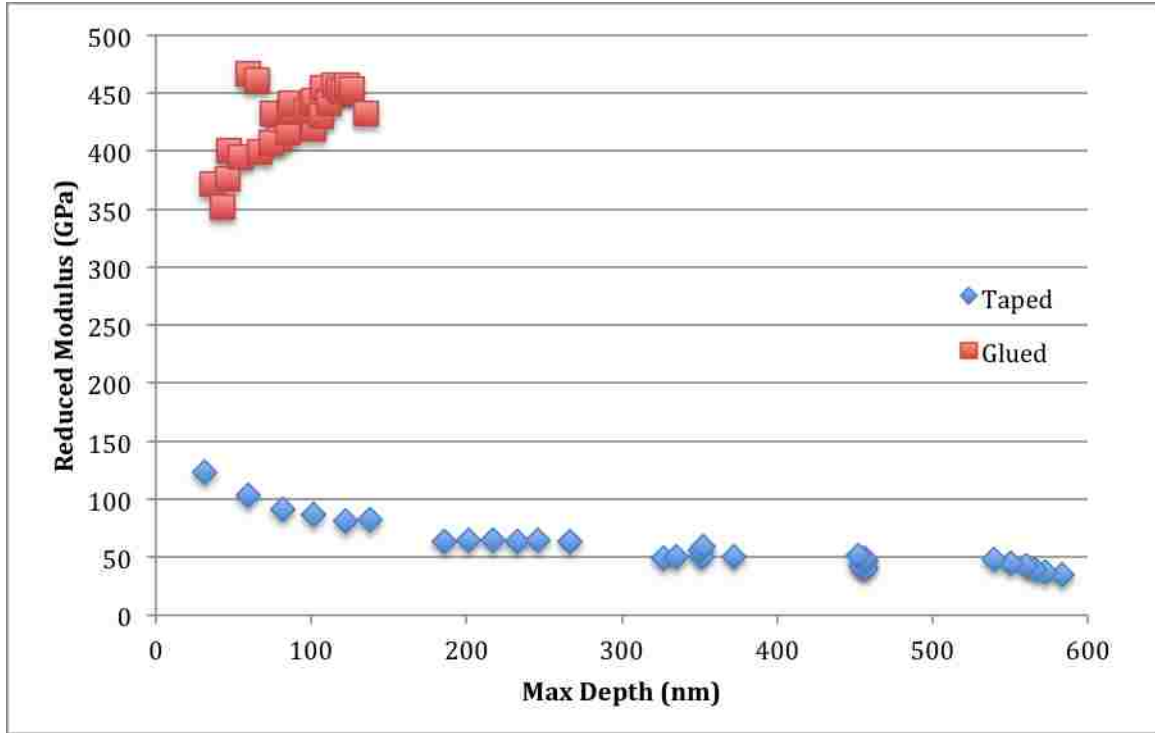


Figure 3.12 Modulus vs. Depth of Taped and Glued SiC Specimen

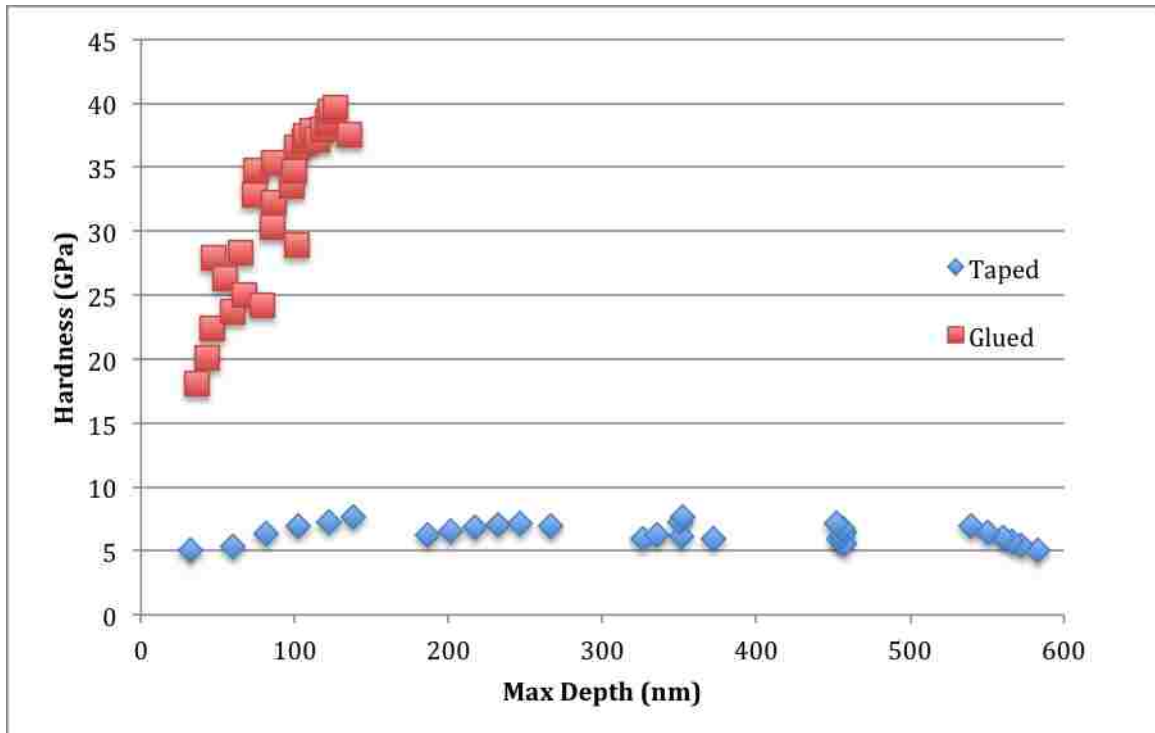


Figure 3.13 Hardness vs. Depth of Taped and Glued SiC Specimen

Although this explains the visual behavior seen in Figure 3.11 the question remained whether mounting samples on tape was a viable option. Stiffer mounting solutions exist such as thermal glues and quick setting super glues, however, tape is highly desirable to gluing sample as it allows for rapid mounting and easy, non-destructive removal of specimen from mounts. Thermal glues can often be reheated for non-destructive removal of samples however the elevated temperatures at which they become liquid would cause thermal expansion in the multilayered samples studied here thus potentially causing damage at interfaces. Therefore, the option left for mounting specimens was permanent super glue (not desirable as removing samples is very challenging).

A test of the same loads and same specimen was conducted to determine if the glue was a better solution for sample mounting. The resultant data is shown at left in Figure 3.11 and the modulus values can be seen at top left in Figure 3.12. Furthermore, the hardness found in these two indentation schedules can be found in Figure 3.13, which clearly illustrated the significant difference between the two mounting methods. The material properties found in this preliminary study were significantly closer to literature values[114] for the glued specimen and so it was determined that glue should be used rather than tape. It should be noted for both the modulus and hardness values displayed for this specimen, the spherical tip had not yet been calibrated for DAF and thus the analysis was done assuming a perfect sphere of 5 μ m radius. Therefore trends shown are likely significant, however, the values may be slightly off.

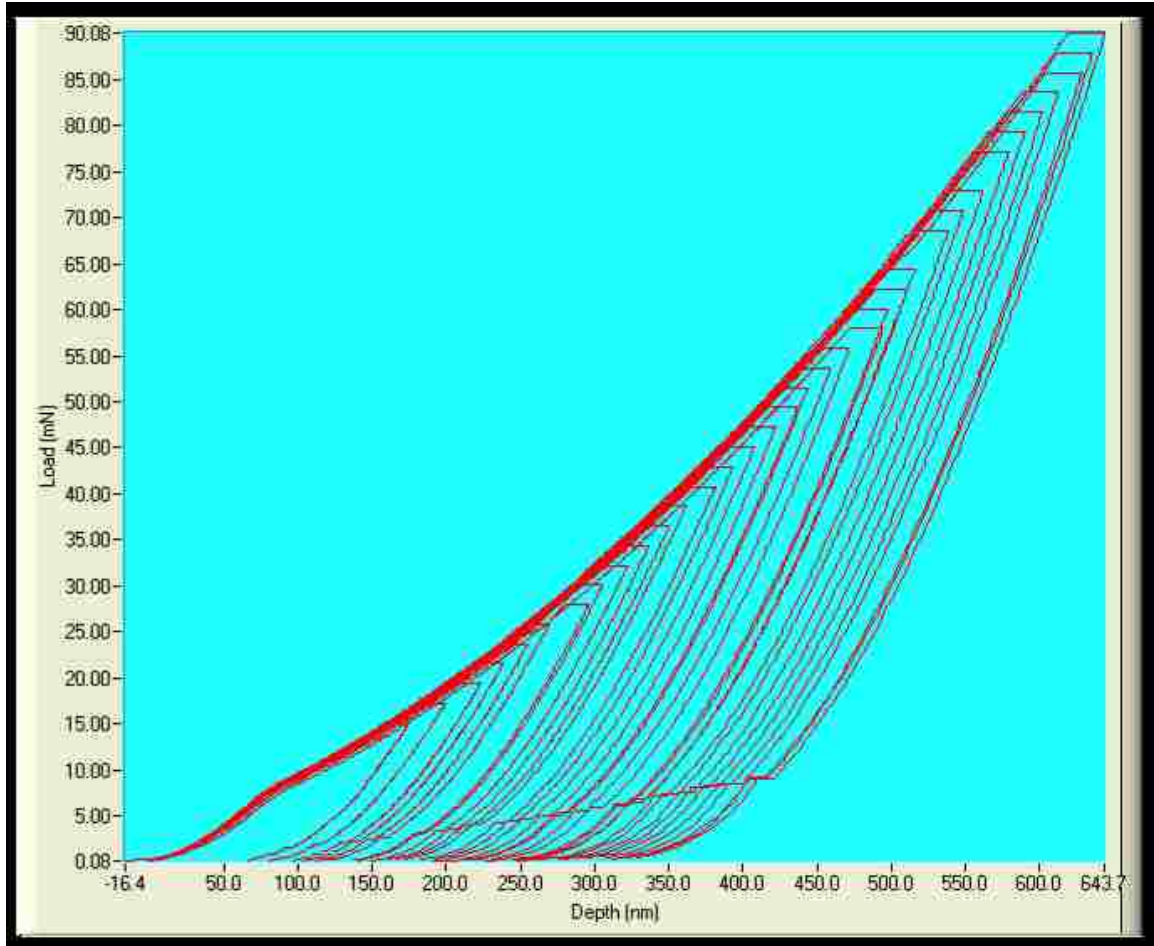


Figure 3.14 Berkovich indentation response of alternating 80nm Al/80nm SiC multilayer on Si wafer glued to sample stub

As the permanence of the glue is a significant difficulty for our specific imaging needs one more test was conducted to verify that tape was not a viable option for testing. Here multilayer samples consisting of alternating 80nm Al and 80 nm SiC deposited upon a Si wafer and mounted to the sample stub with both tape and glue were indented using a Berkovich indenter. The response of the glued specimen can be found in Figure 3.14 and it is important to note the consistency of the loading curves. Each indentation follows almost the exact same curve as loading occurs and creep depth is consistent with what would be expected as load increases. This same data (with only a simplified set of indents) is displayed in Figure 3.15 on the same plot as the response of the same specimen when taped to the sample stub.

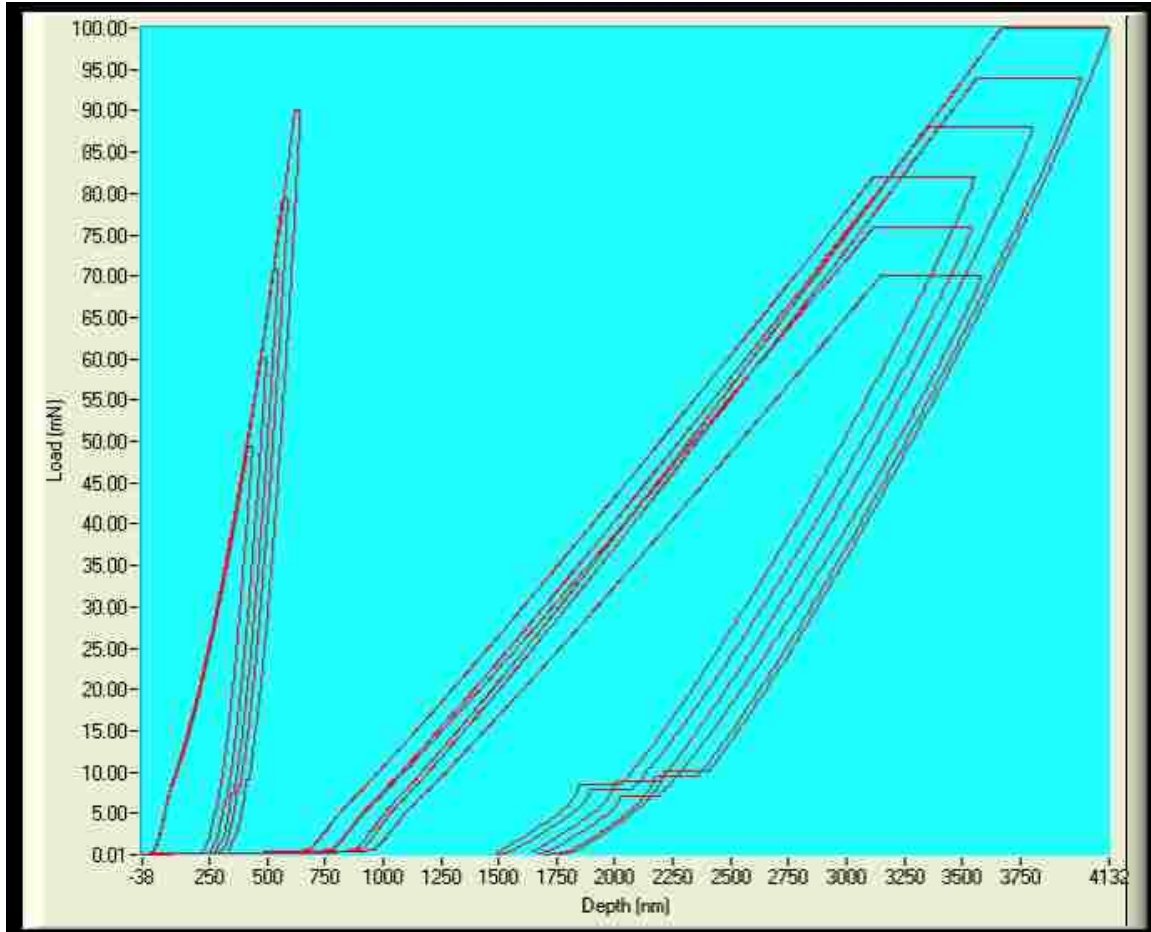


Figure 3.15 Berkovich indentation response of alternating 80nm Al/80nm SiC multilayer on Si wafer glued to sample stub (left) and taped to sample stub (right)

Note first the initial glide of the sample as it settles back from initial contact until pushing back upon the indenter, which causes a large miscalculation in hardness. Then the loading and unloading slope are significantly less extreme, resulting in a significantly less stiff outcome and therefore massively affecting the modulus. Finally note the large creep sections as mentioned before. All signs of inconsistent and inaccurate indentation and therefore solidifying the truth that hard setting glue must be used for all indentations in this thesis.

3.6. Indentation Results

For ease of viewing all figures for the indentation results sections will be presented together at the end of each section rather than within the text. Pictures for section 3.7 can

be found on pages 53-55, for section 3.8 on pages 60-65, and for section 3.9 on pages 71-82.

It should be noted that based on the results of indentations on reference samples and the surface roughness of the samples, we have exclude results from shallow indentations, i.e. <100 nm. These indentations although generally showing the same results as presented, had a high degree of uncertainty and deviation and therefore were considered to be unreliable. It should also be noted that the results displayed in the graphs of this chapter show reduced, or effective, modulus and not the elastic modulus. These are similar values, however. As mentioned previously the reduced modulus is a composite modulus of coating and indenter and as such must be converted into Young’s modulus using Equation 3.14 which relates the true, reduced, and indenter values.

$$\frac{1}{E_{eff}} = \frac{1 - \nu^2}{E} + \frac{1 - \nu_i^2}{E_i} \tag{3.14}$$

In Table 3-1 can be found a summary of the results as described in the following sections. For this table the modulus and hardness values have been extracted from the indentation response recorded from experimentation while the Poisson’s ratio is reported as values from literature sources. We will largely be comparing the Bulk Young’s modulus from literature to the reduced modulus with the understanding that these are not identical measures due to the nature of these materials and the differences in crystal or grain structure.[114]

Table 3-1 Properties from single material thin film and bare substrate indentations

Material	Young’s Modulus (GPa)	Hardness (GPa)	Poisson’s Ratio (ν)
Silicon Wafer	114	7.3	0.28
Quartz Substrate	65	4-7	0.16
Aluminum	133	1.5	0.33
Silicon Carbide	207	16.3	0.17
Silicon Dioxide	59	4-6	0.16

3.7. Substrates and Reference

The first series of indentations completed focus on the calibration of the instrument and indenter tip. These include primary indentations of the reference material (fused silica) and the two substrates. As discussed before the indentations on fused silica are used to develop a diamond area function (DAF) that is used in analysis of the indentation data. The DAF used for this thesis is explained greater in section 3.2 and graphs that can be found in Figure 3.16. The modulus of the fused silica comes out almost perfect as the analysis was calibrated through these indentations with only slight error persistent from the indentation process itself.

Following the creation of a DAF file, we tested the silicon wafer and quartz substrates to determine the mechanical properties of each, which is necessary to understand how the substrate is contributing to the measured modulus of the thin films. The silicon wafer was used as the substrate for most of the indentations as is common to most thin film tests. The silicon wafer data shows good agreement with the values for substrate modulus and hardness near the 112 GPa and 7 GPa reported in literature, respectively.[114] There is a significant drop at low load that is consistent with the drop shown in the DAF file (not pictured). This is due to poor indentations at low loads, an unfortunate problem that persisted despite attempts to correct. Low load indentations are much more susceptible to vibration and other sources of error. The hardness increases as would be expected by relative to the increasing indentation depth due to the relative hardness of fused silica. The indentations on the bare quartz substrate showed highly variable mechanical properties due to the polycrystalline nature of our quartz substrate. Therefore, the location of indentations impacted the measured properties significantly according to the orientation of the crystal grain under indenter tip at each location. Despite this the overall response of quartz substrate falls about what would be expected and all samples that use the quartz substrate are films with thickness greater than 4 μ m thick so properties were assumed to be that of bulk quartz with modulus \sim 70 GPa and hardness of 7 GPa.[114]

As an example of the differentiation between the reduced and Young's moduli, the graph of reduced modulus for the DAF file shows a trend line at about 69.6 GPa. This would be the indentation derived reduced modulus (E_{eff}) expected when using a diamond

indenter that results from applying Equation 3.14 to the corresponding 71.7 GPa Young's modulus that is the commonly accepted value for fused silica.

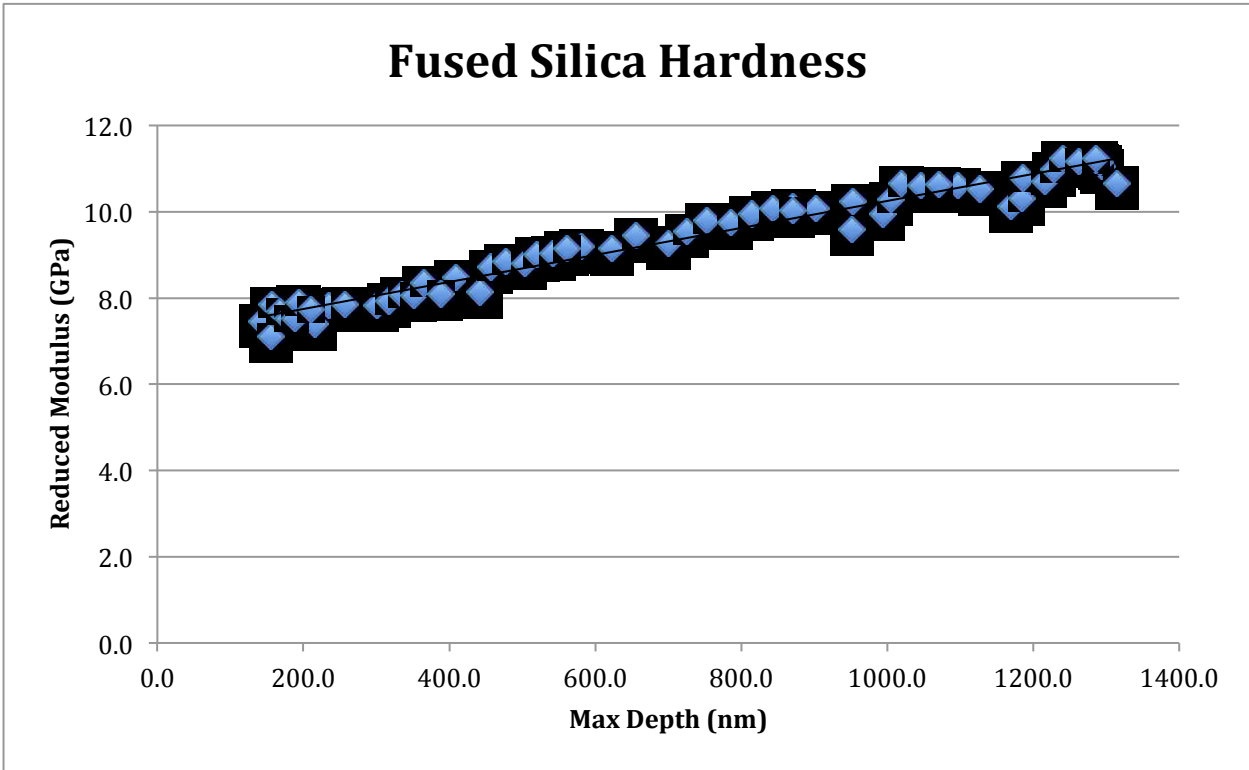
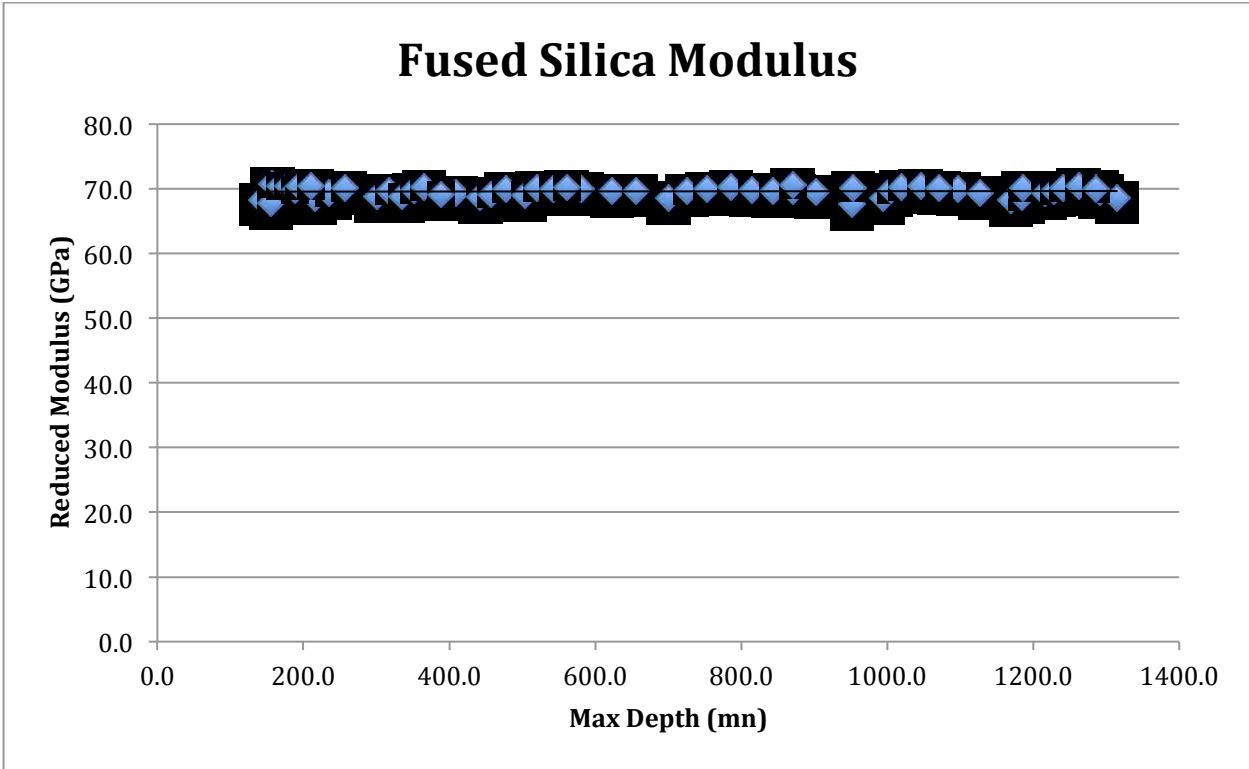


Figure 3.16 Reduced modulus and hardness against maximum indentation depth for reference sample, fused silica. The modulus indentations were used in creation of the DAF

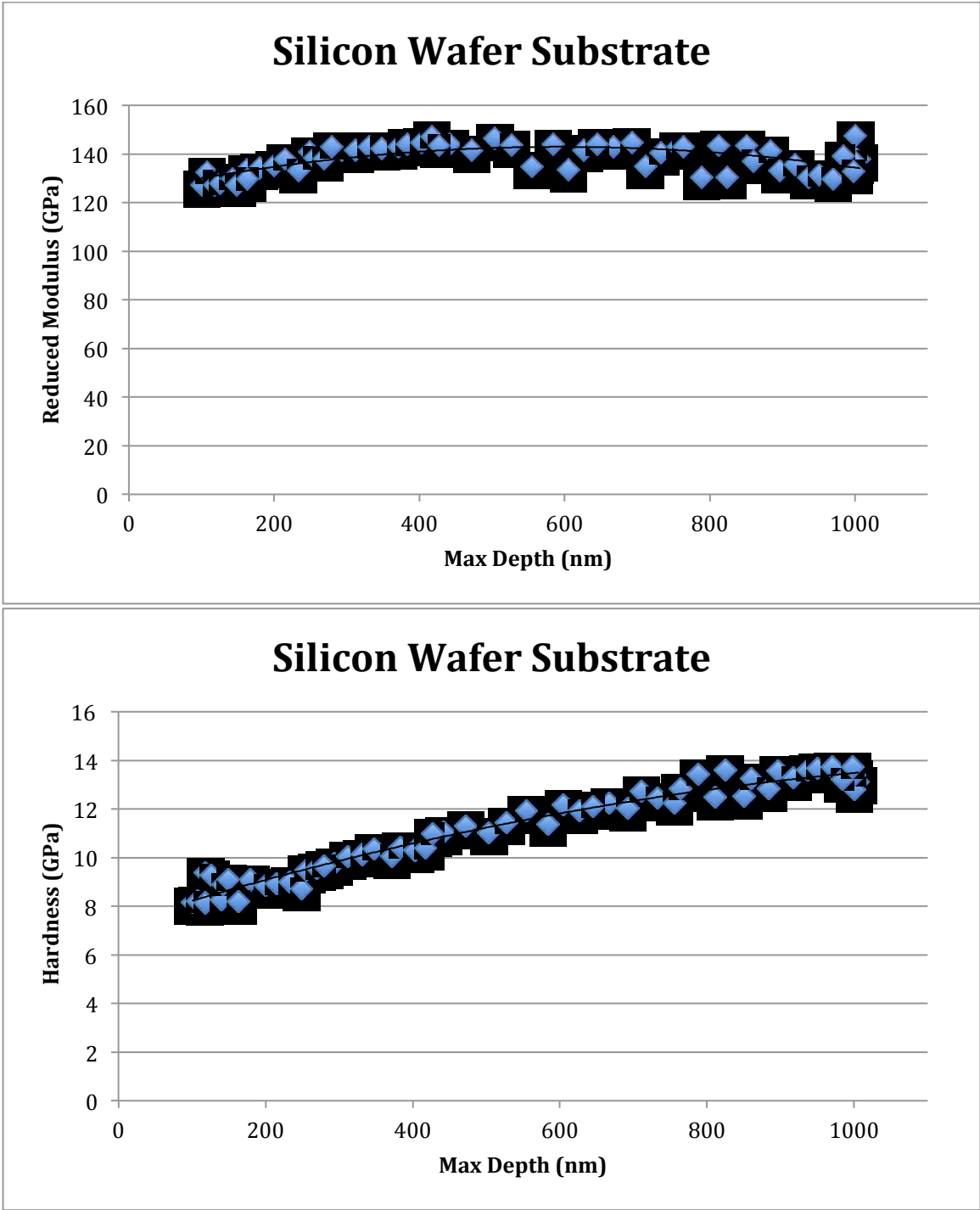


Figure 3.17 Reduced modulus and hardness vs. indentation depth for the silicon substrate. Resulting modulus of 124 GPa and hardness of 7.3 after substrate effect removed.

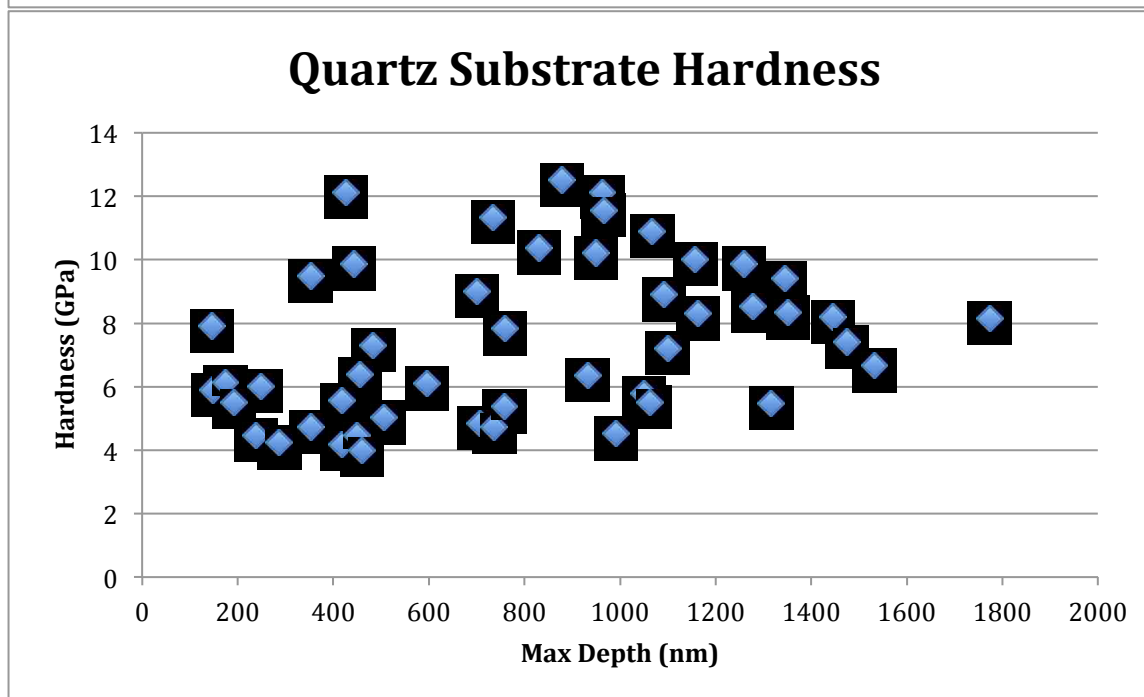
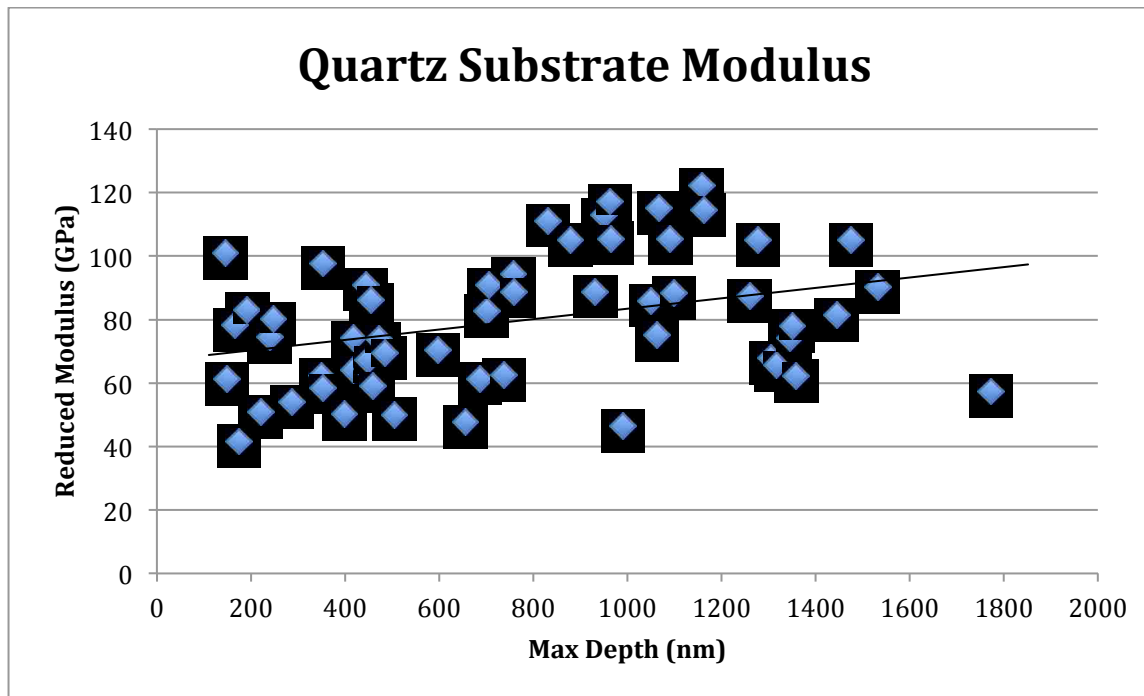


Figure 3.18 Reduced modulus and hardness vs. indentation depth for the quartz substrate. Resulting modulus of 67 GPa after substrate effect removed.

3.8. Single Layer Thin Films

After completion of substrate testing, thin film indentation was conducted starting with coatings of a single material. These were tested in order to determine and characterize the indentation derived modulus response based on film thickness and indentation depth. Films of the three materials (Al, SiC, and SiO₂) deposited on silicon wafer were tested both under individual load cycles and cyclic load cycles.

Results of the indentations were analyzed for the conversion from reduced modulus and to remove the substrate effect. These values are our best approximation of the indentation derived Young's modulus for the experiments upon our fabricated thin films and can be found in Table 3-1.

Determination of the indentation derived Young's modulus can often be a difficult task and the true value is deceptively elusive. In the case of the aluminum presented here the results of the indentations are confusing but lead to interesting conclusions. The bulk modulus for aluminum is 69 GPa.[114] Therefore it would be expected for Al coatings onto Si wafer that, given a soft film upon a hard substrate, indentation would yield an increasing modulus due to the substrate effect as indentation depth increases. However, we see the opposite in this case, because the nanoindentation derived modulus values for Al are slightly higher than that of the Si wafer. This trend is exhibited by the different film samples and thicknesses and so is unlikely to be a pure effect of film thickness and the documented increase in modulus from thin films. We can attribute some of the strength, especially at low indentation depths, to growth of the oxide layer, Alumina, upon the surface. Alumina, or Al₂O₃, has a elastic modulus of 370 GPa[114] and so this could contribute to increasing the exhibited results for shallow indentations, specifically because the derived modulus at zero depth approaches this value. If this was true, the modulus should have dropped to values between that of the bulk Al (~70 GPa) and the silicon substrate (~114 GPa). Measured moduli with increasing indentation depth, however, plateaus to ~130GPa. Moreover, based on other works the increase in modulus observed here far exceeds what would be expected from the thin oxide layer.[5, 33, 34, 115-117] Another possible explanation maybe that the face centered cubic (FCC) cubic structure of aluminum in the deposited layers consist of columnar grains with their closed pack directions through the thickness of the sample. As such, Al grains would have grown in the

[1 1 0] direction. Even assuming this possibility, modulus would be only slightly higher than the bulk values and not to the measured levels, i.e., ~130 GPa. The last considered possibility is that the Al has somehow been oxidized throughout the thickness; this is very unlikely due to the highly controlled environment inside the deposition chamber and at room temperature aluminum forms about a 3nm thick passivation layer of alumina, Al_2O_3 . [112] The measured hardness values are however too low alumina and this possibility is also unlikely. In the end, we are incapable of extracting the exact value of the deposited aluminum's elastic modulus nor can we quantify the specific amount of influence the oxide layer has upon the single layer film results without additional investigation. Furthermore this oxidation would only occur upon the top layer of a nanolaminate so it should have less of an effect upon a nanolaminate than a single film. Despite our efforts we are left with the question of what the true value for modulus of this Al film is and what the value for each layer within our multilayer structure would be. For further analyses we used the reduced modulus of 150 GPa for Aluminum understanding that this is as close as we can get given the current information. Consideration was given to the possibility of pushback from the sample being the leading cause of high modulus values. As such the load-displacement curves were examined by plotting the data before and after application of the thermal drift correction as can be seen in Figure 3.25. There does appear to be significant drift before the correction is applied in some cases. However considering the amount of creep at max load and the length of the thermal drift hold time relative to the indentation load cycle time this is not unexpected and does not provide insight into the mechanisms contributing to the high modulus values returned from the indentations. Finally, without micro-characterization of the exposed edge of aluminum and further TEM and X-ray analysis (such as energy dispersive X-ray; EDX) it is impossible to say how much impact the oxide layer would have and what contributes to the unexpectedly high values of elastic modulus. This was not a focus of this thesis and we therefore didn't perform further characterization of these samples.

Although the SiC results are simpler and show high precision, the range of results was surprising. Common values for SiC modulus are around 420 GPa [114, 117] which is double the results we returned. Even knowing that the 420 GPa is for crystalline SiC and more common 270-300 GPa values for amorphous SiC, [14, 48, 51, 56, 83] our results still fall low.

We didn't TEM in order to determine the structure of this deposited SiC, however, we expect this low modulus value to be a result of amorphous structure of sputtered SiC and measurement errors including the effect of glue compliance. The error for SiC should be small as harder films are much less prone to error however we can still see that beyond about 300 nm of indentation depth the results begin to mirror the substrate properties. This is in line with the loose rule of thumb for indenting to a maximum of 10% the film thickness. Beyond this point it seems that the substrate and the stub/glue affect the result significantly and the indentations results begin to taper. This phenomenon is exhibited in the aluminum as well, however, is not present with the SiO₂ possibly due to the close properties to the reference fused silica sample. The SiO₂ is difficult to characterize on its own without comparison, because each sample shows such a different response. This may be due to the substrate being significantly more rigid than the film and therefore a thinner film exhibit a much higher modulus than a thicker film at the same indentation depth because the substrate effect is proportionally much higher. The results above 100 nm may come into conflict with the 10% indentation depth here as the 4000nm film exhibits properties a little below the 70-78 GPa modulus and 5.5-7 GPa hardness of bulk SiO₂. [114] Meanwhile, the 1000nm film shows properties closest to literature values, at about 10% indentation depth, and the 500 nm results are higher than literature values possibly due to the increased substrate effect. Knowing this we can see the possible opposite effect within the results of the SiC where the 1000nm film has a small but distinctly lower reduced modulus than that of the 4000nm film and yet the trend of the two result in nearly identical Young's modulus calculations. Another possible explanation for the elevation of properties between SiO₂ samples may be that the film forms based on initial contact with the substrate and therefore there is a crystalline portion of growth and the size of this crystalline portion relative to the total film thickness may affect the indentation derived properties. We cannot rule this out without imagery of the structure near the substrate. We have TEM images within the nanolaminate that exhibit amorphous SiO₂ layers, however, even the first of these was deposited upon aluminum that exhibited columnar grain growth potentially breaking up SiO₂ crystal growth initiation. The surface of the Si wafers is commercially manufactured to a high finish and has a small oxide layer, this is a very different surface for deposition than the deposited aluminum layers. It is therefore speculated that the structure

of SiO₂ (and maybe that of SiC and Al) and its mechanical properties may alter with the type of substrate layer is deposited on.

Indentations displayed in the first three sets of graphs relate to individual indentations where at each indentation location only one load cycle was applied. Following these are results of cyclic indentations on ~4 microns thick samples in which ten load cycles were completed to the same load. Each location is depicted with the same marker but the results evolve with each cycle. The first graph of each set shows the modulus against the indentation depth, however, the second shows each cycle's modulus result against the cycle number. These results tend to have the same trend of decreasing modulus while indentation cycle and depth increase. This is believed to be due to the decaying effects of creep. Single material films will be discussed more in Chapter 4 along with the results of simulations.

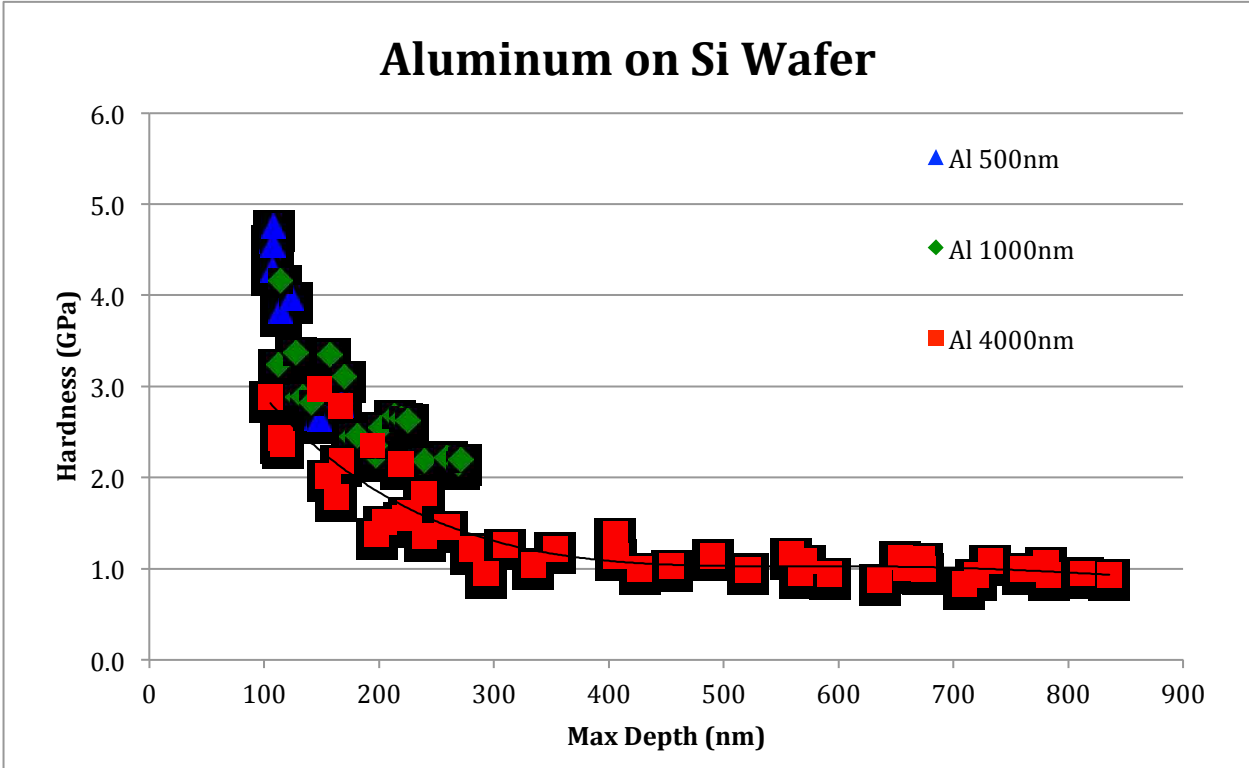
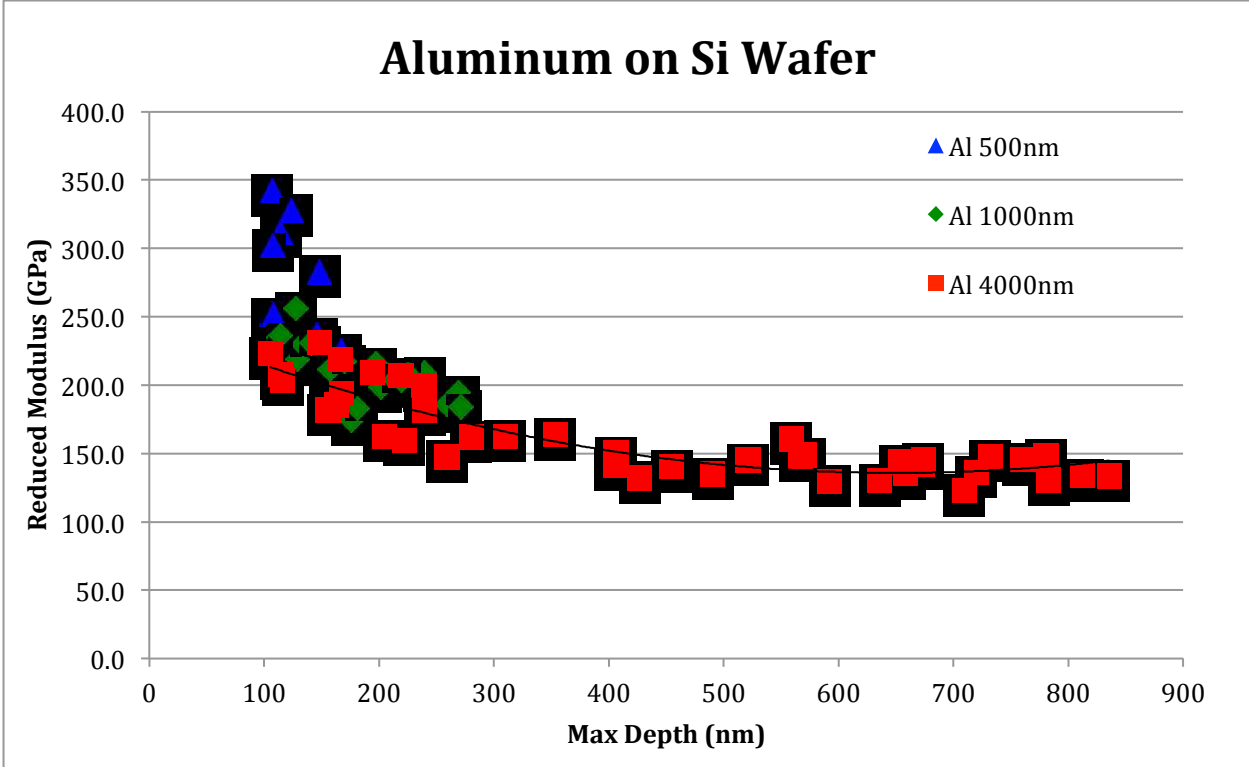


Figure 3.19 Reduced modulus and hardness against the indentation depth for aluminum samples. Resulting modulus of 150 GPa after substrate effect removed likely due to the effect of oxide growth.

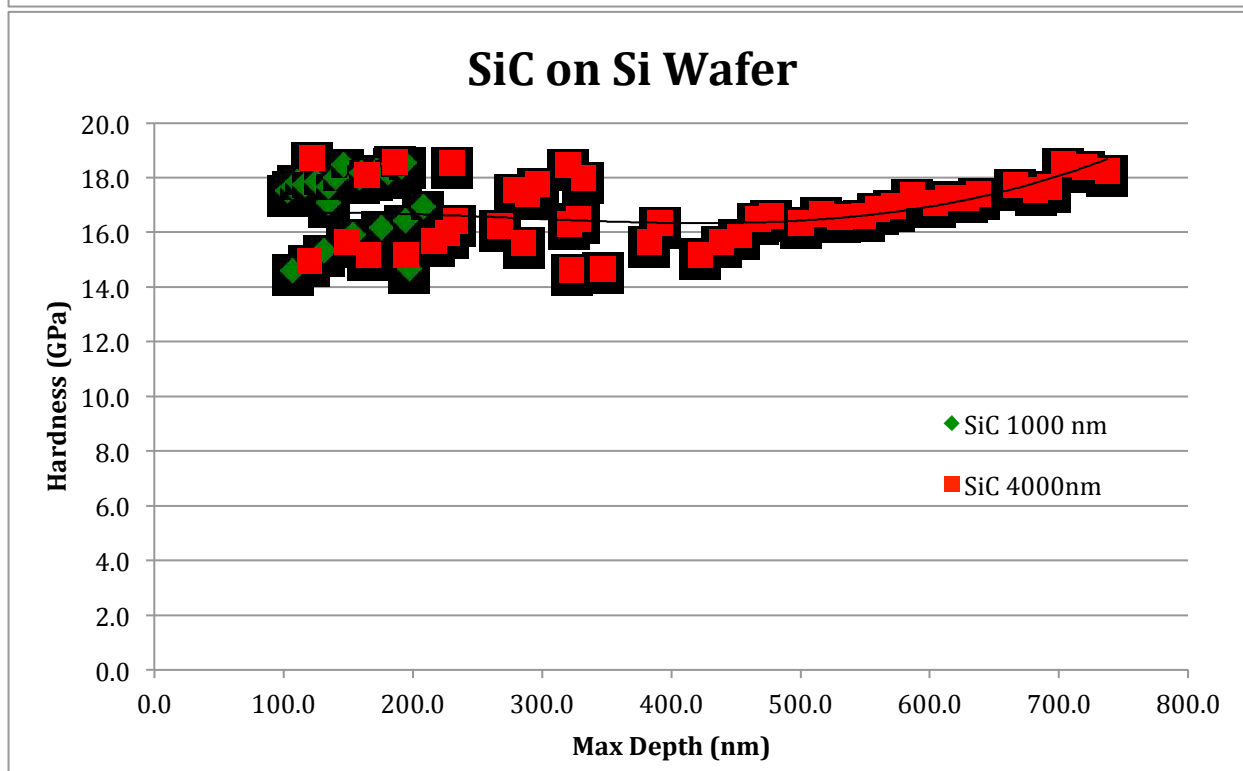
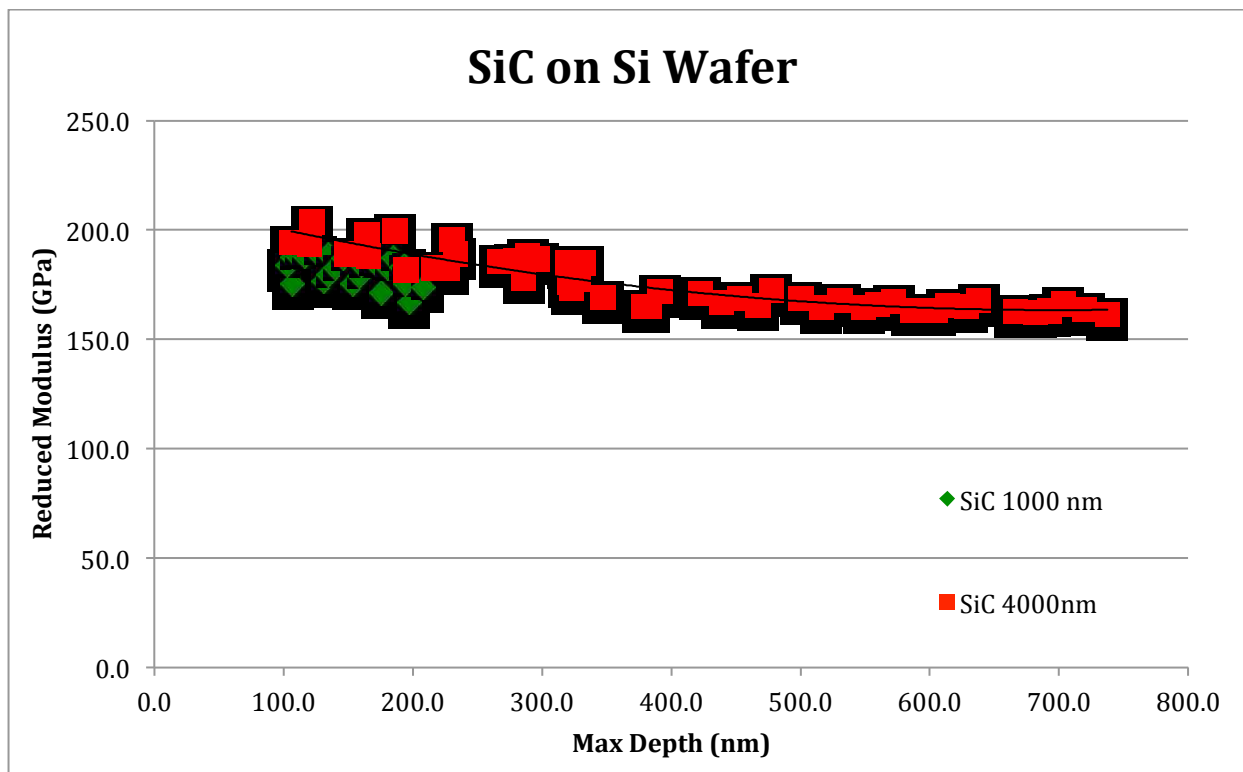


Figure 3.20 Reduced modulus and hardness against the indentation depth for silicon carbide samples. Resulting modulus of 213 GPa and hardness of 16.3 after substrate effect removed.

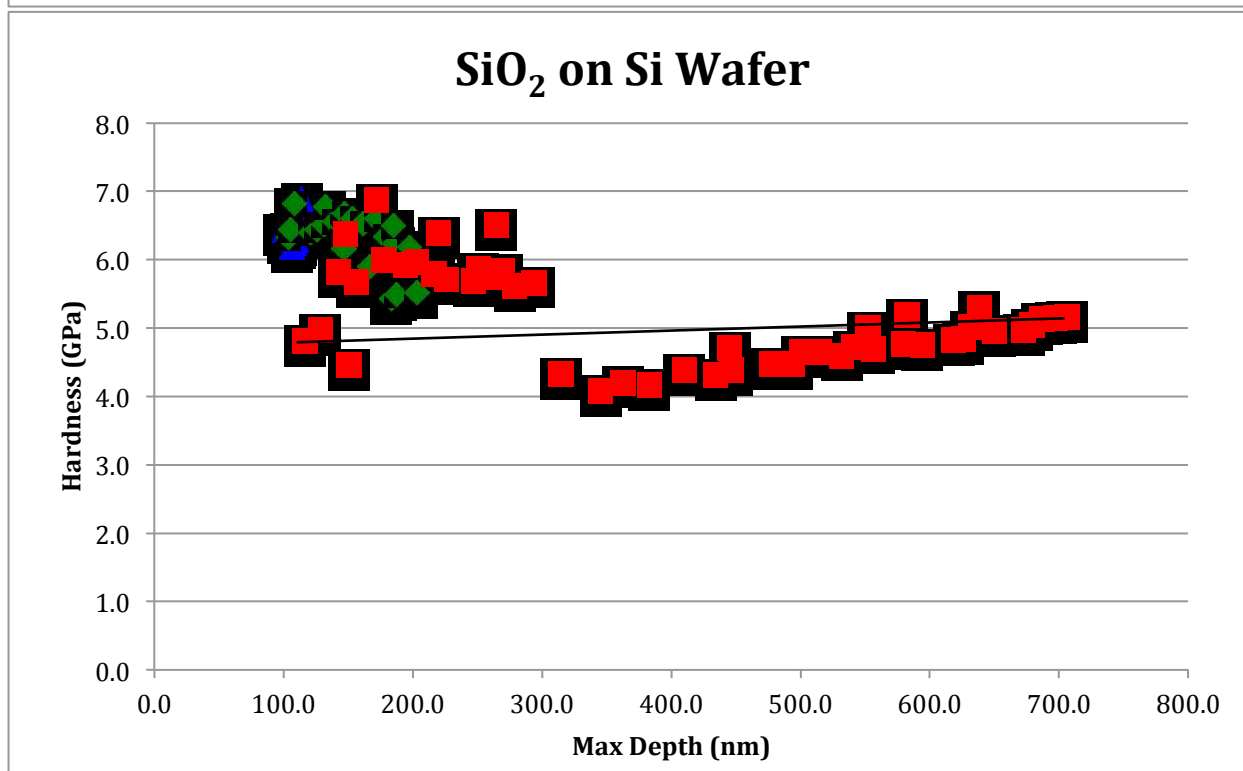
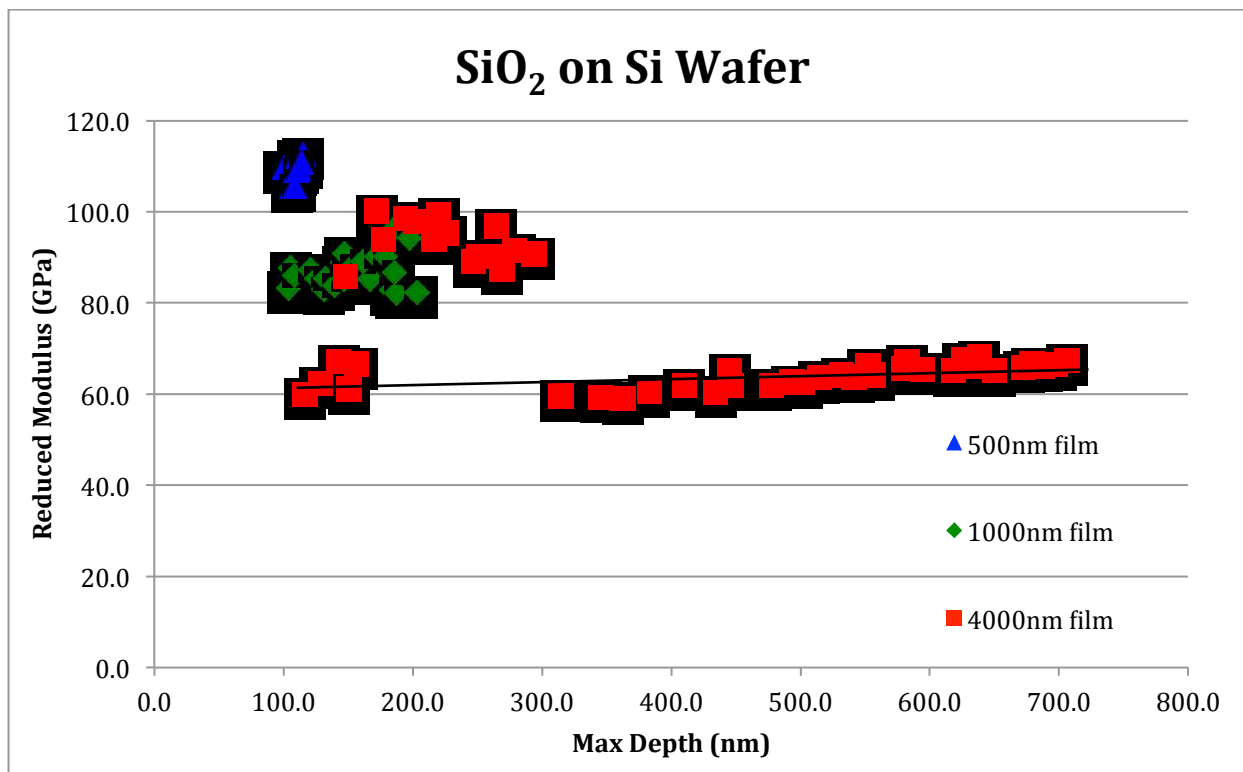


Figure 3.21 Reduced modulus and hardness against the indentation depth for silicon dioxide samples. Resulting modulus of 60 GPa after substrate effect removed.

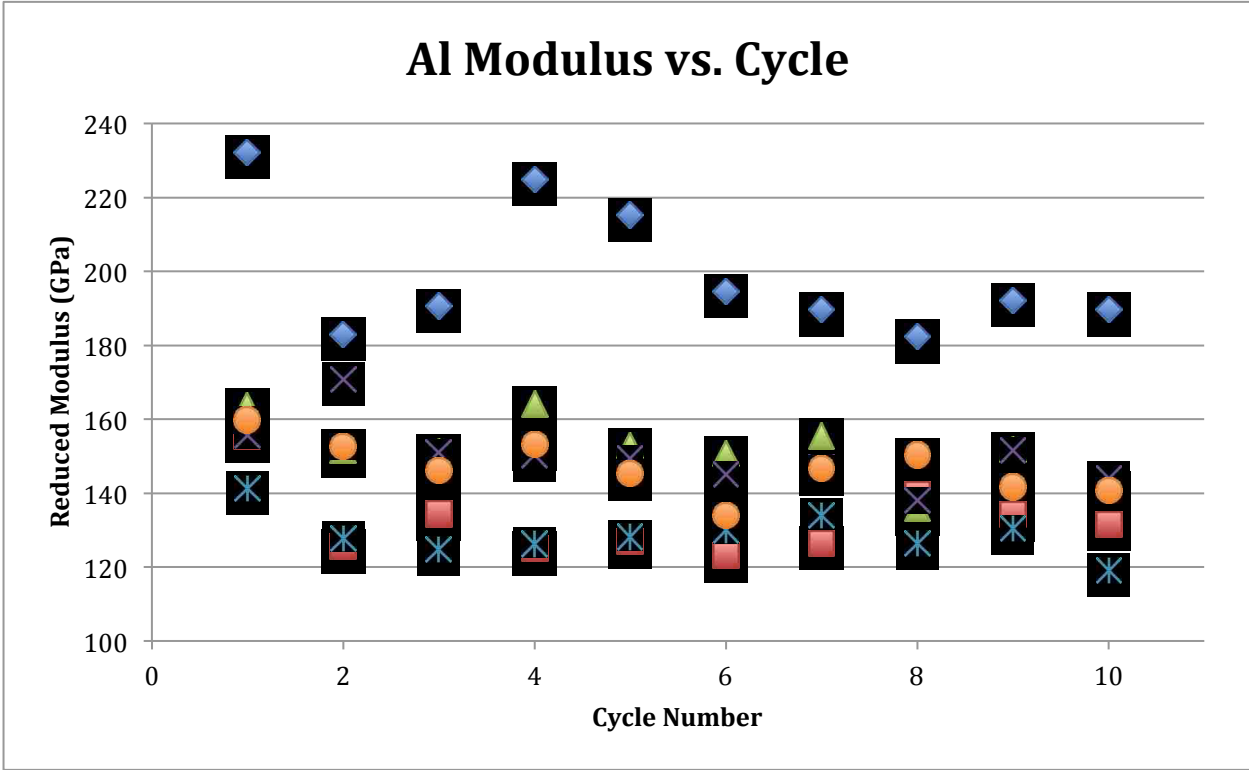
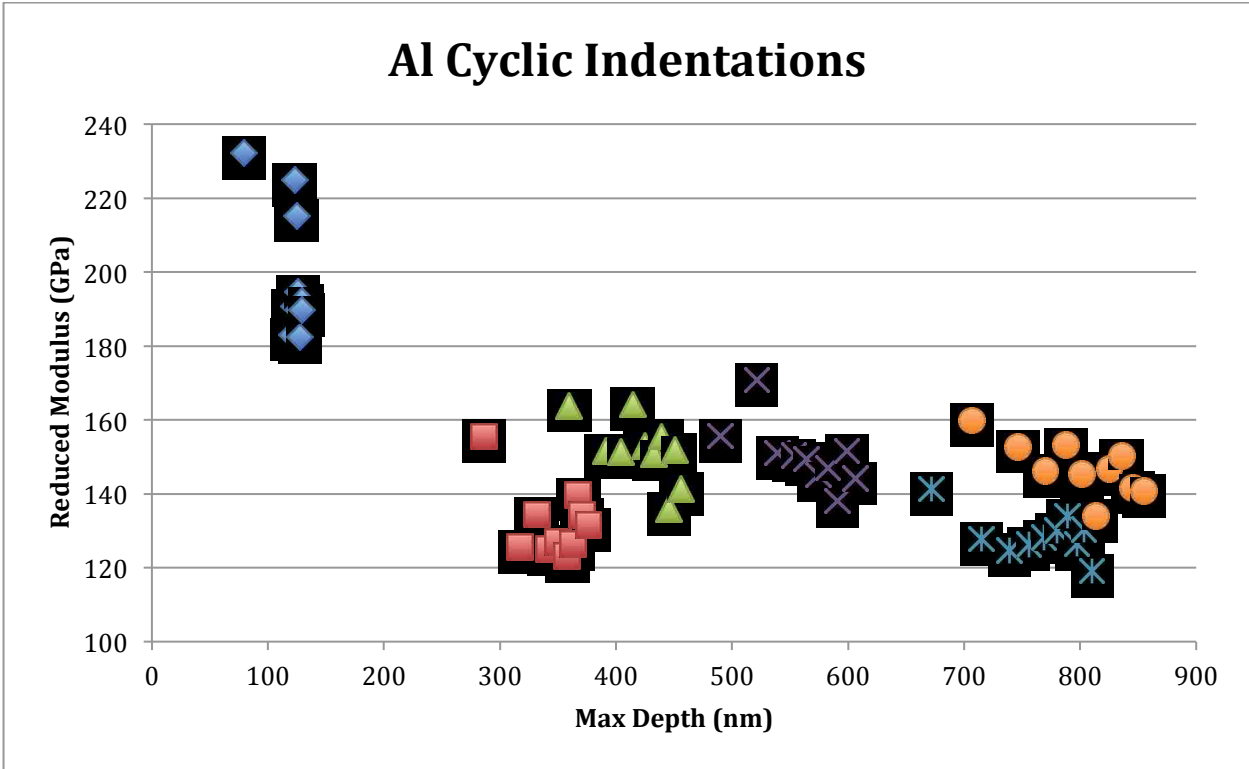


Figure 3.22 Cyclic indentation reduced modulus for Al on Si wafer samples against depth and cycle.

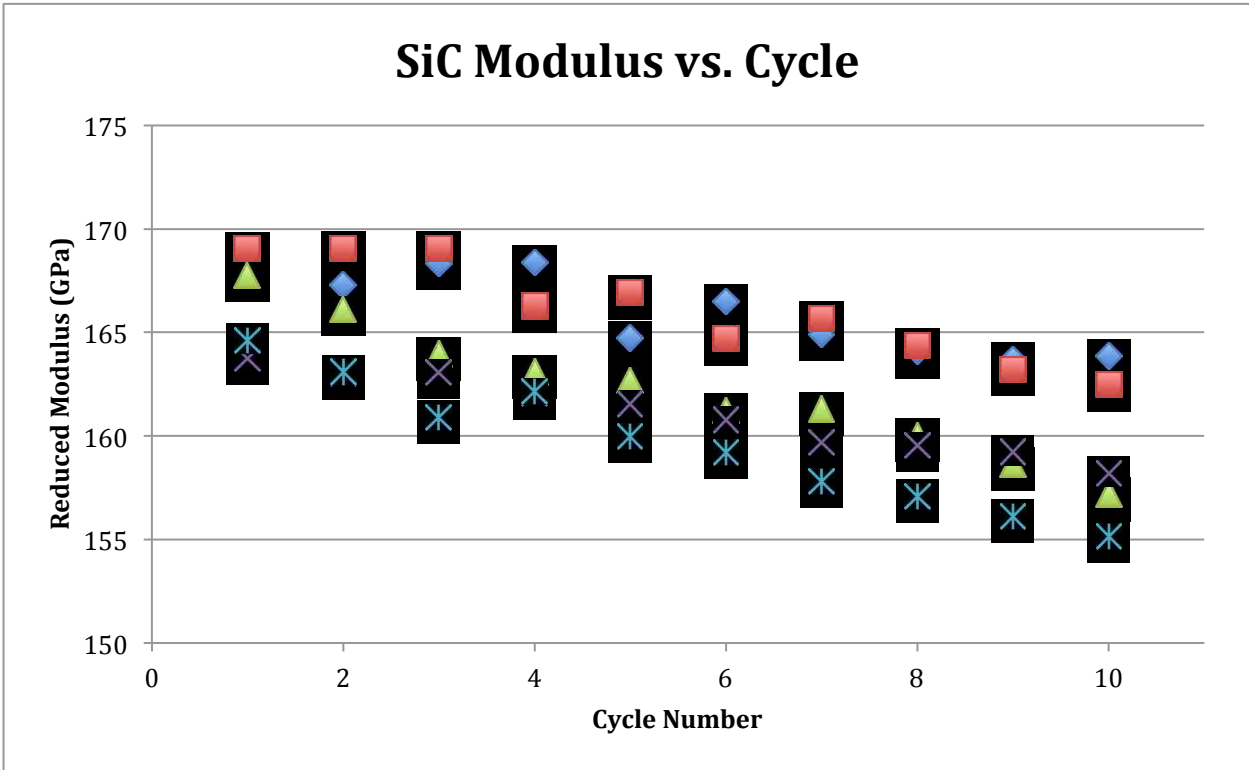
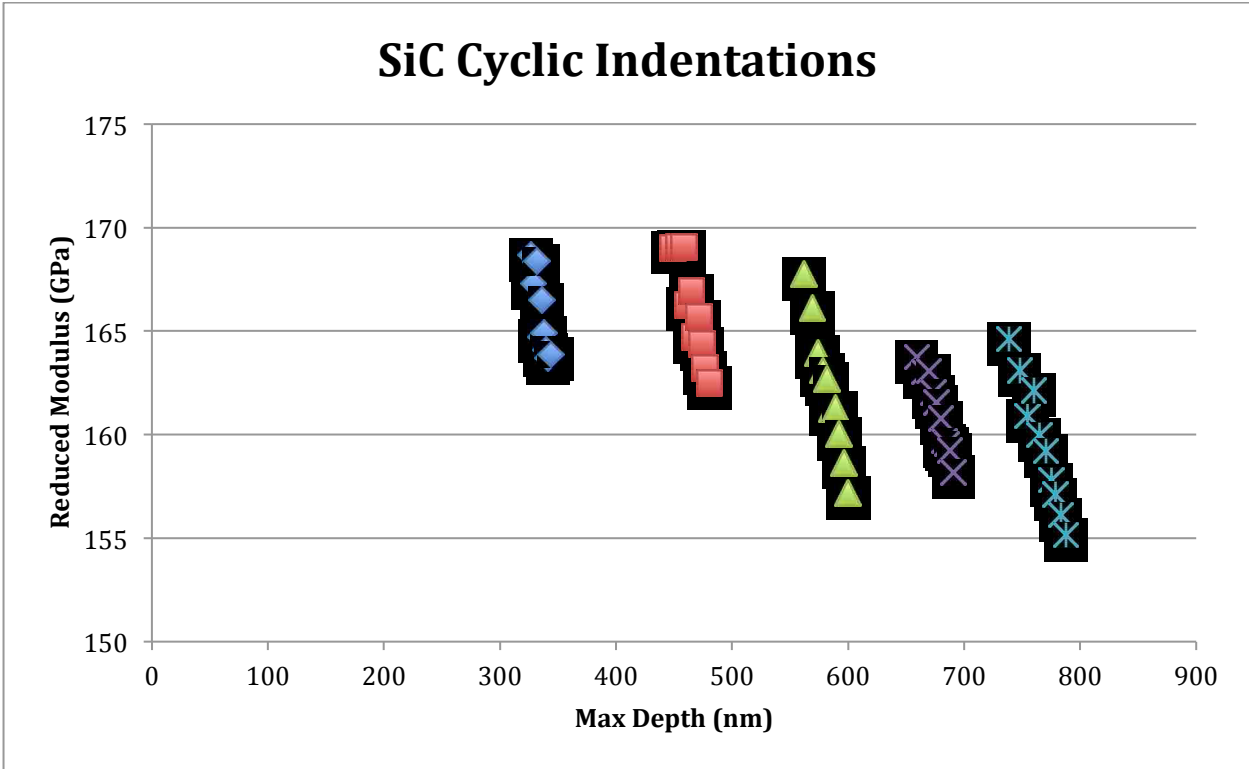


Figure 3.23 Cyclic indentation reduced modulus for SiC on Si wafer samples against depth and cycle.

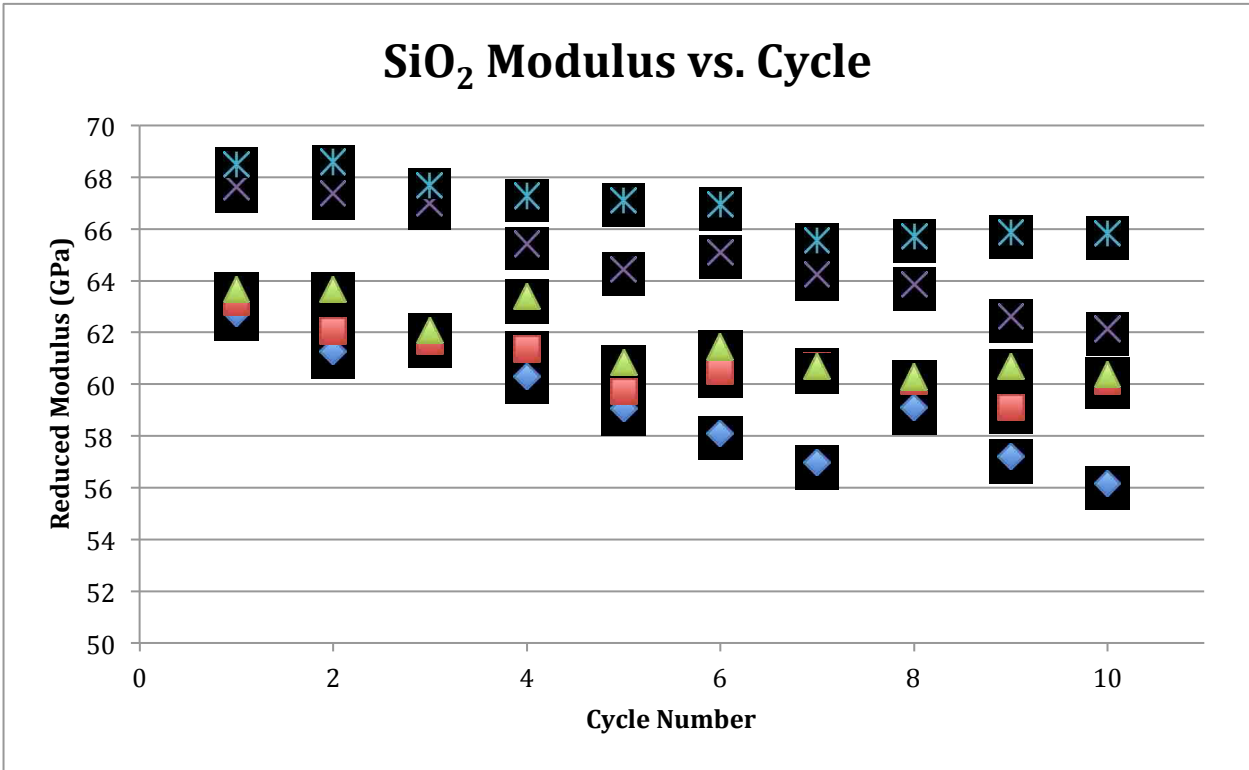
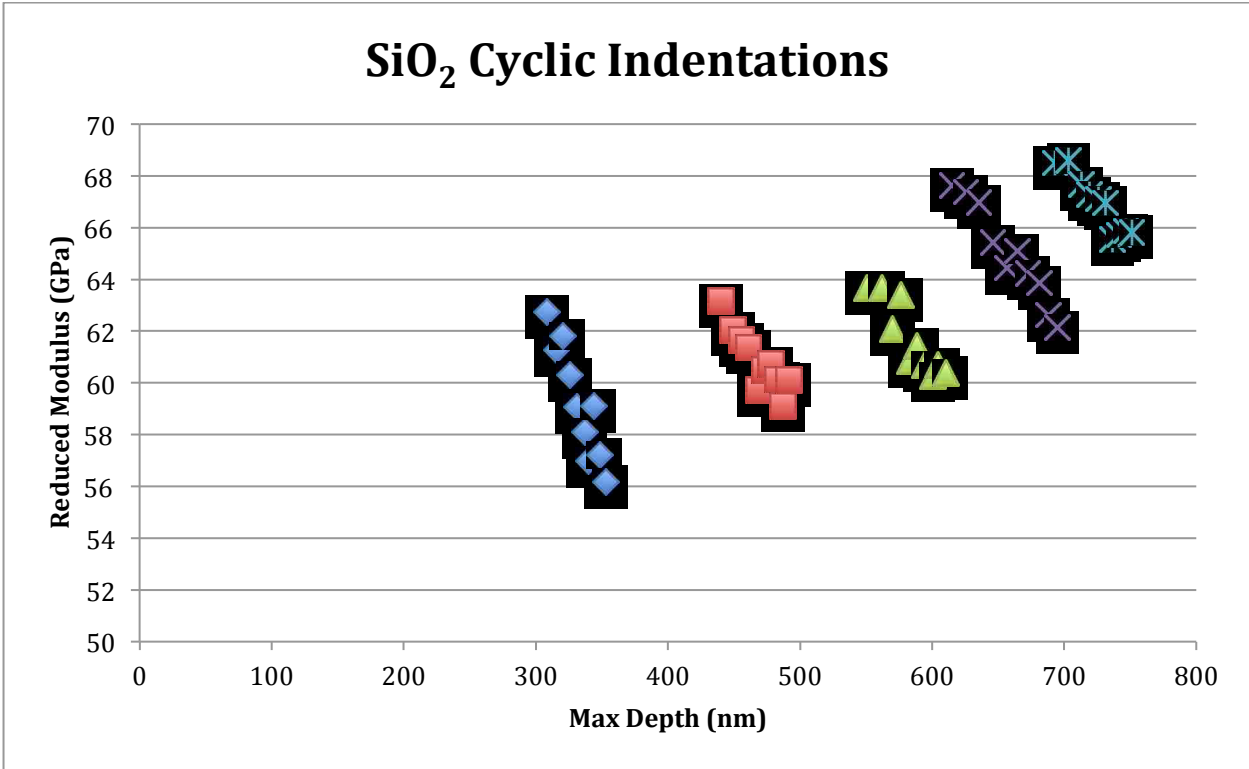


Figure 3.24 Cyclic indentation reduced modulus for SiO₂ on Si wafer samples against depth and cycle.

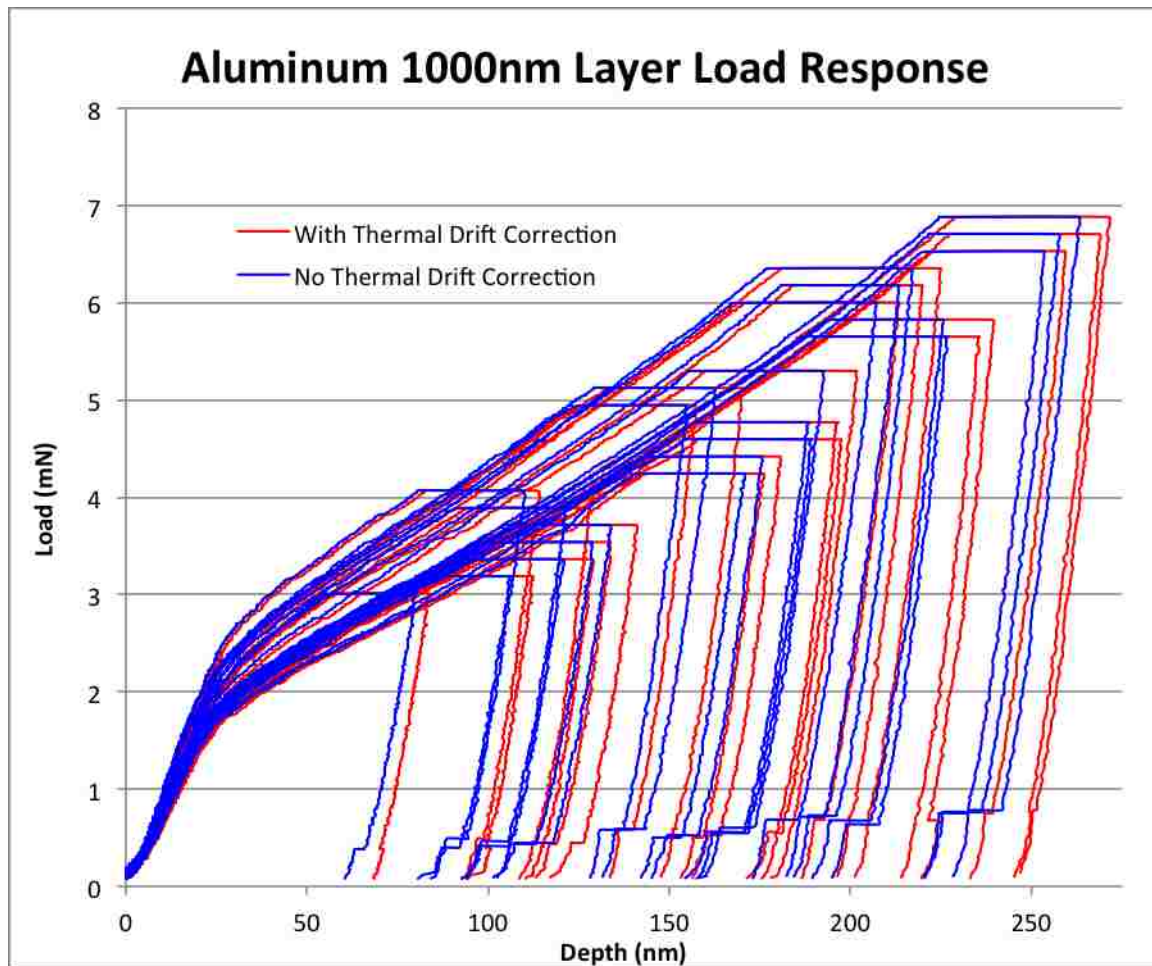


Figure 3.25 Loading information for selected single cycle indentations upon a 1000nm thick aluminum film upon silicon wafer substrate. Used as part of the investigation into the extreme stiffness found for the aluminum thin films. Shows the load vs. displacement curves both before and after the thermal drift correction was applied.

3.9. Multilayered Thin Films

After the indentations of references, substrates, and individual material thin films had been completed, experimentation began on the multilayered films. The results of these indentation schedules can be found in Table 3-2 below. The hardness is directly from the indentation response with consideration to remove the substrate effect. The Poisson's ratios reported in this table are either values for the bulk material (*italic*) [2, 48, 51, 54, 114] or the results of simulations (underlined) intended to discern an accurate value for Poisson's ratios of multilayer structures as the rule of mixtures cannot be applied to Poisson's ratio. Finally the Young's modulus is the converted reduced modulus from the indentation results using Equation 3.14 as discussed previously.

Table 3-2 Indentation derived modulus and hardness with reference Poisson's ratio

Material/Nanolaminate	Young's Modulus (GPa)	Hardness (GPa)	Poisson's Ratio (ν)
Silicon Wafer	114	7.3	<i>0.28</i>
Quartz Substrate	65	4-7	<i>0.16</i>
Aluminum	133	1.5	<i>0.33</i>
Silicon Carbide	207	16.3	<i>0.17</i>
Silicon Dioxide	59	4-6	<i>0.16</i>
Al 40nm/SiC 120nm	184	10.9	<u>0.182</u>
Al 80nm/SiC 80nm	167	11.6	<u>0.208</u>
Al 120nm/SiC 40nm	146	9.7	<u>0.252</u>
Al 40nm/SiO ₂ 120nm	75	5.7	<u>0.177</u>
Al 80nm/SiO ₂ 80nm	91	5.0	<u>0.206</u>
Al 120nm/SiO ₂ 40nm	107	3.0	<u>0.252</u>

Presented in Table 3-3 are a comparison of results from the indentation derived reduced modulus, the converted Young's Modulus, and an estimated elastic modulus in which the rule of mixtures (RoM) was applied to each nanolaminate. This RoM estimate, shown in Equation 3.15, uses the Young's modulus results of the individual layer tests and the intended ratio of materials as the volume fraction.

$$E_{RoM} = fE_1 + (1 - f)E_2 \text{ where the volume fraction, } f = \frac{V_1}{V_1+V_2} \quad (3.15)$$

As can be seen the RoM estimate accurately predicted the Young's modulus of the nanolaminate with a 1-6% overshoot. Overall it was concluded that the RoM estimate based on individual indentation results was an accurate method of prediction as the errors in the deposition and indentation processes would be larger than the error in the estimate. Moreover, it can be concluded that the modulus values measured for thicker single layer films is similar to those of the nanolaminates in the multilayered coatings. This is a significant finding as it verifies that the rule of mixtures will deliver at least a reasonable estimate for expected modulus of hard soft multilayers when the indentation derived properties of the constituent materials have been derived from single material thin films. Similarly this finding allows for the custom design of multilayer films targeted to a specific property range without an expensive fabrication and testing cycle.

Indentation derived hardness values (relative measure of materials yield or tensile strength) for the multilayers are very interesting. For the Al/SiC nanolaminates, hardness values for different Al fractions from 0.25 to 0.75 are very high and similar in magnitude. This is due to the confined Al layers between the hard SiC layers and the nanometers size of Al grains. Both these factors contribute to the strengthening of Al layers by hindering dislocation motion. It is speculated that while the modulus follows the rule of mixture, hardness can be high as long as thin SiC layers exist between the Al nanolayers. This is not particularly true for the Al/SiO₂ system, where the hardness of SiO₂ is much lower compared to SiC, hence is not effective in impeding the dislocations.

Table 3-3 Measured and calculated moduli for comparison

Nanolaminate	Reduced Modulus	Young's Modulus	Rule of Mixtures Modulus
Al 40nm/SiC 120nm	190	184	189
Al 80nm/SiC 80nm	175	167	170
Al 120nm/SiC 40nm	156	146	152
Al 40nm/SiO ₂ 120nm	77	75	77
Al 80nm/SiO ₂ 80nm	95	91	96
Al 120nm/SiO ₂ 40nm	115	107	114

As with the previous two sections, indentation results for individual indentations and cyclic indentations can be found at the end of the section. The first six figures show the individual indentation results (reduced modulus and hardness) for a given nanolaminate both on Si wafer and Quartz substrates. These nanolaminates should be identical as they are deposited at the same time side by side. Therefore the differences between films can be attributed to the substrates themselves or the variability in growth of the individual nanolaminates. Overall, the results are very close after consideration of the substrate effect. In each of these cases the nanolaminate on the Si wafer is presented in blue while the laminate on quartz is shown in red. It should be noted that all the laminates were constructed with an aluminum top layer under the assumption that the aluminum would be a softer layer and therefore decrease the indenter tip wear thereby yielding more consistent results over time. The unfortunate and unforeseen result was the formation of a highly elastic yet relatively soft layer on the top. As such it is possible to see a dramatic increase in the modulus of the nanolaminates as the max indentation depth decreases.

This phenomenon is particularly evident in the second series of graphics which show the combined indentation results based on the two materials within the multilayered structure. Within these graphics each color represents a different series of indentations, specifically to highlight the relative ranges over which the results of each thickness ratio fall. In these figures the triangular markers indicate a deposition upon the Si wafer while the X's denote depositions upon the quartz substrate. From these it is fairly clear to see the effect increasing volume fractions of a stiffer material have upon the resulting nanolaminate properties. Similarly it can be found in these that the overall shape of the response is largely consistent with the effects from the substrate.

Finally, the cyclic indentation is presented in a similar manner to the individual layer tests above. The reduced modulus result for each cycle is plotted against both the indentation depth and the cycle number. For these, there are only three colors of marker plotted which relate to the thickness ratio of the layer structure. Red is always the least aluminum (25% volume fraction Al and 40nm layers intended), then green at 50% aluminum, and blue at 75% aluminum (80 and 120 nm Al layer respectively). Each series of cyclic indentations are given a different shaped marker so as to show the trend from cycle

number within each series. The cyclic indentations on a specific nanolaminate are all a series of ten indentations to a consistent load resulting in similar depth range for each series of ten cycles. However, the laminates have different thicknesses and hardness and therefore the resulting depth range is not identical between laminate samples. The load and depth range is an important point to understand as the depth range of the indentations changes the relative contribution to the modulus of the substrate. This is clear when looking at the results against indentation depth, however, can cause confusion when reviewing the modulus against cycle number, which is intended to highlight the trend and change of the modulus rather than the values themselves. We were excited to see the result of the cyclic indentations against cycle number as it was expected to give insight into the effects of the unloading plasticity. As such, it was expected that the unloading induced plasticity affect the modulus values for the first cycles and the effect to go away in subsequent cycles. The cyclic results of the multilayers were, however, largely similar to those of the individual layers exhibiting a mostly linear decrease in modulus of about 10% over the ten cycles. In summary, modulus values drop with depth mainly due to the substrate effect and that the results are inconclusive in terms of experimentally measuring the effect of unloading induced plasticity on modulus values.

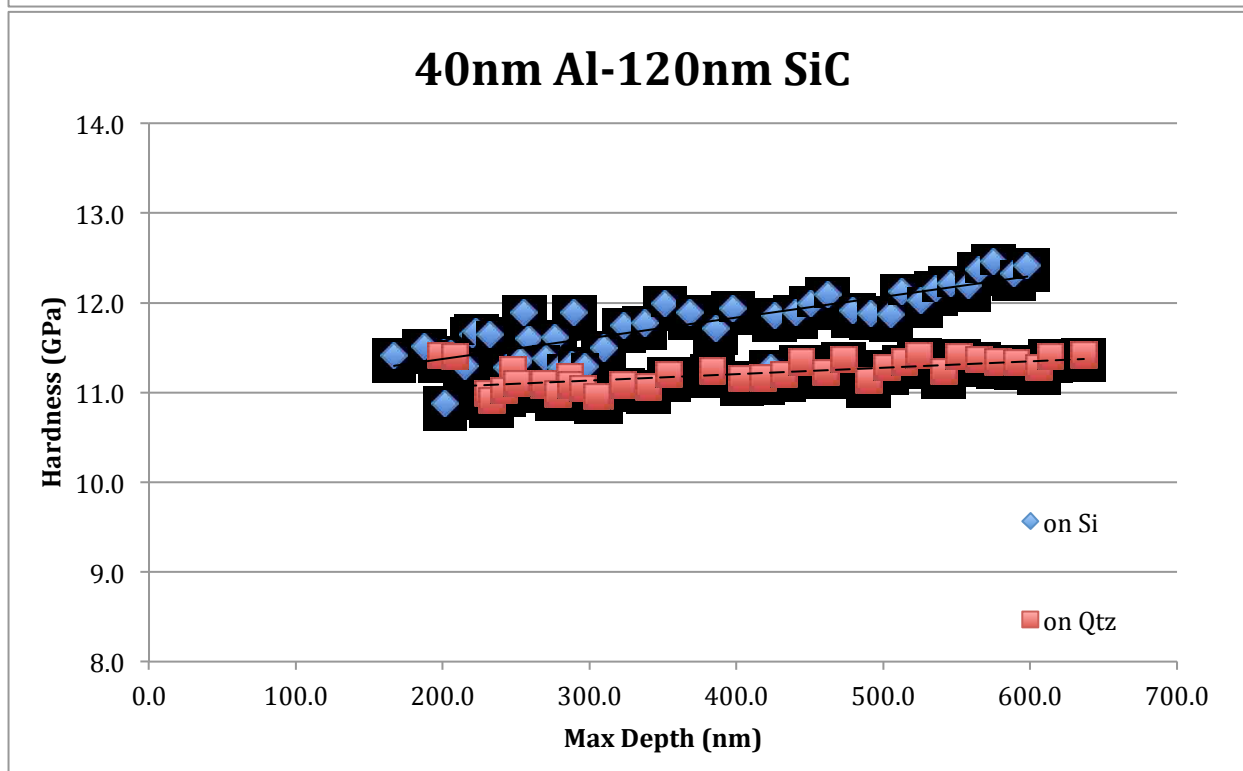
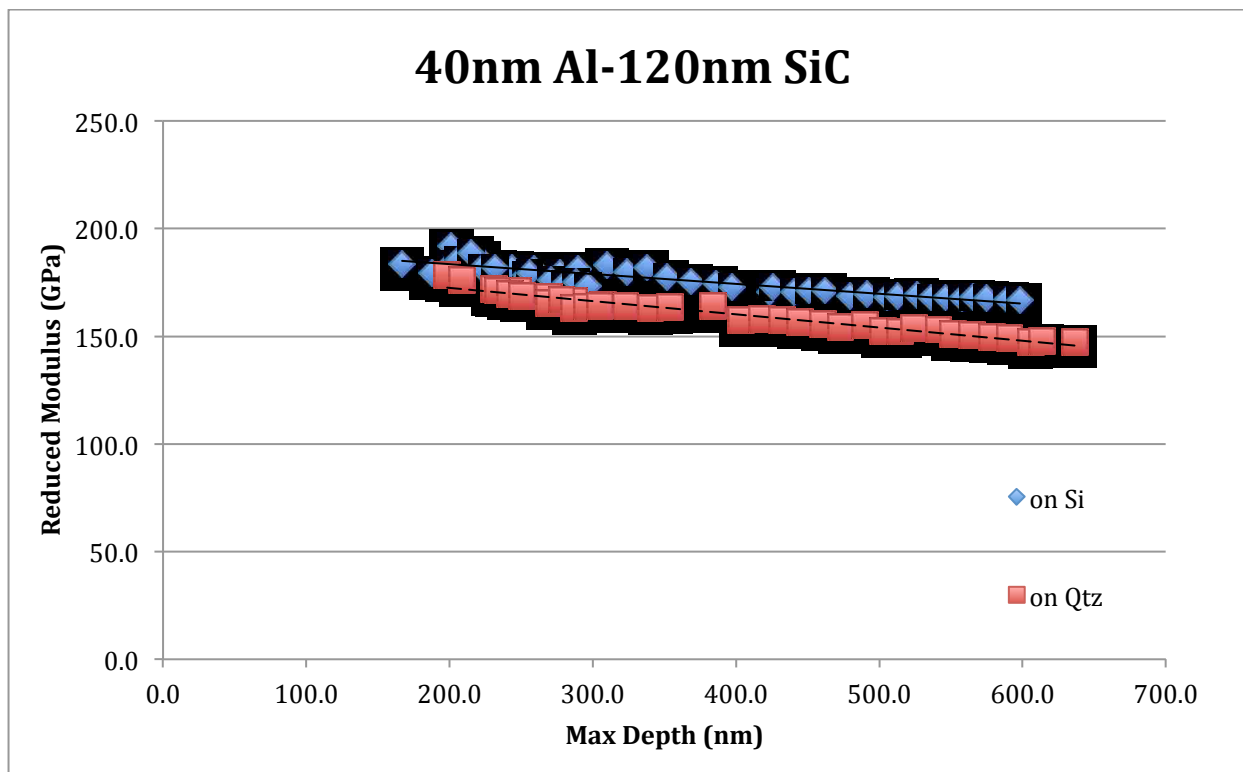


Figure 3.26 Reduced modulus and hardness for 40/120 Al-SiC nanolaminate. Resulting modulus of 190 GPa and hardness of 10.9 after substrate effect removed.

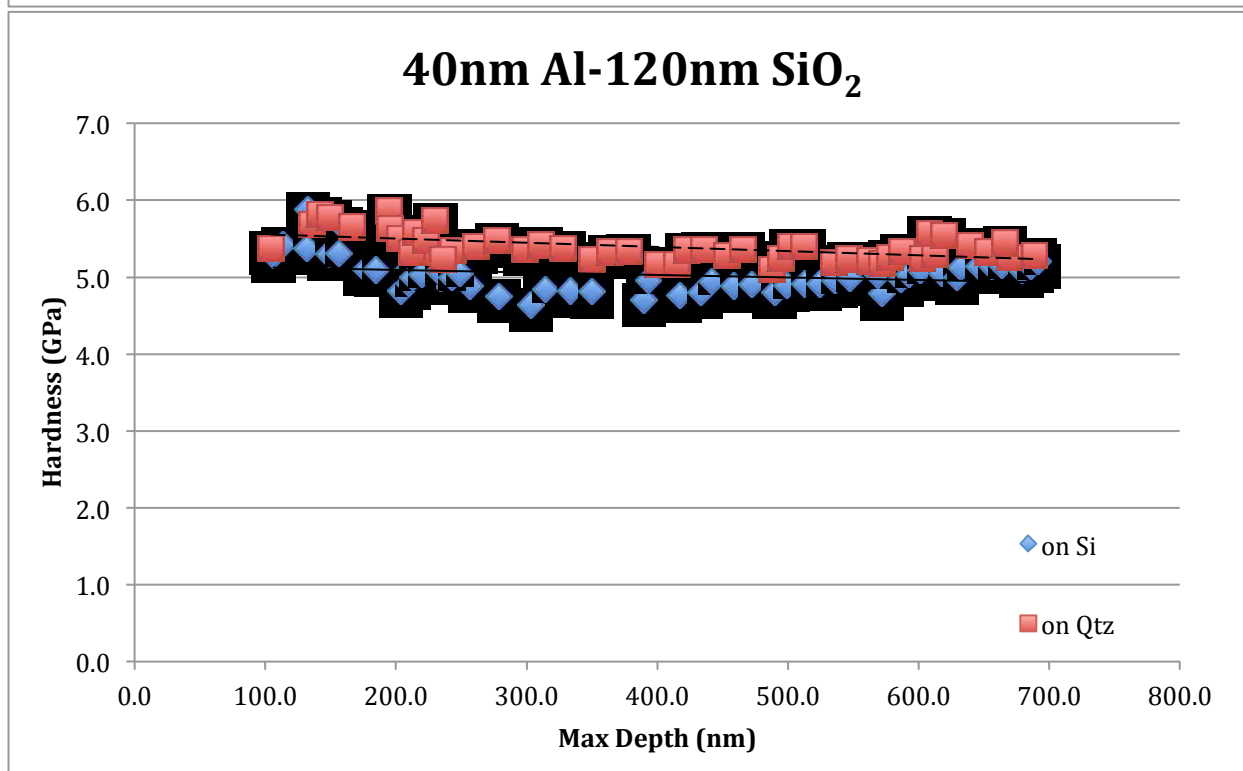
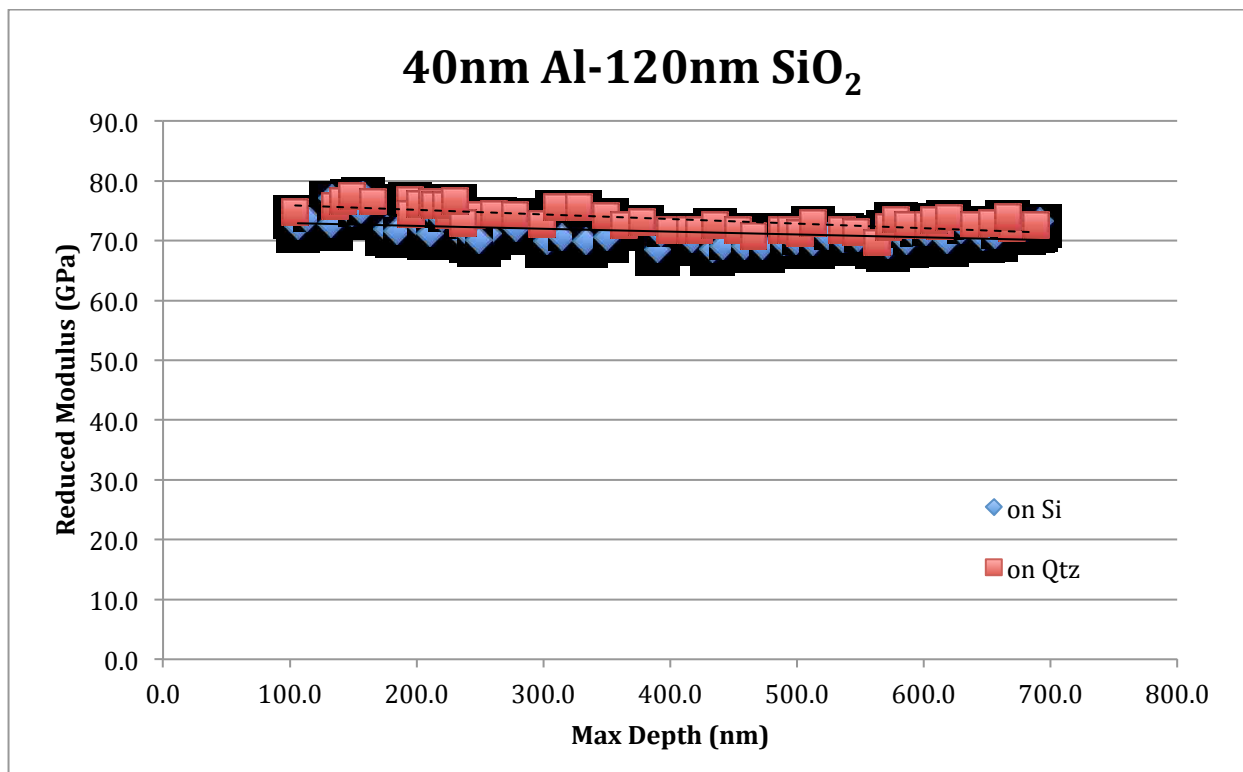


Figure 3.27 Reduced modulus and hardness for 40/120 Al-SiO₂ nanolaminate. Resulting modulus of 77 GPa and hardness of 5.7 GPa after substrate effect removed.

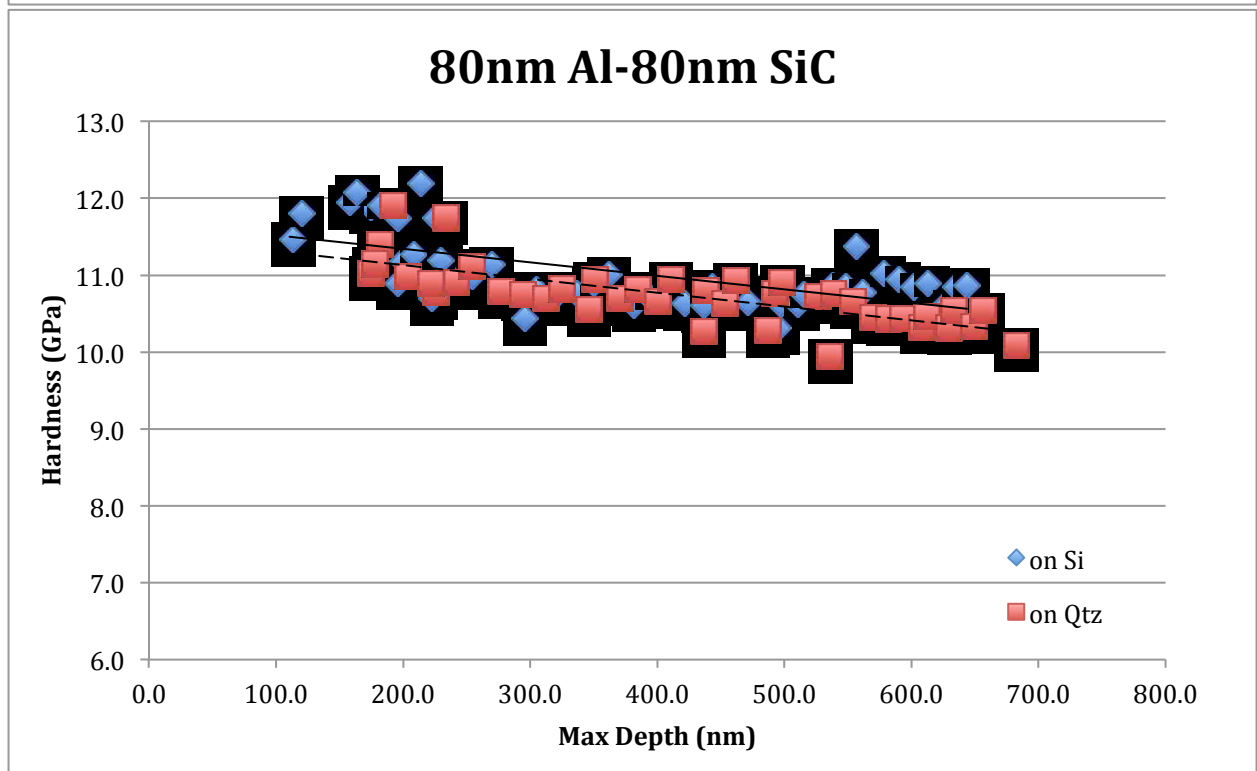
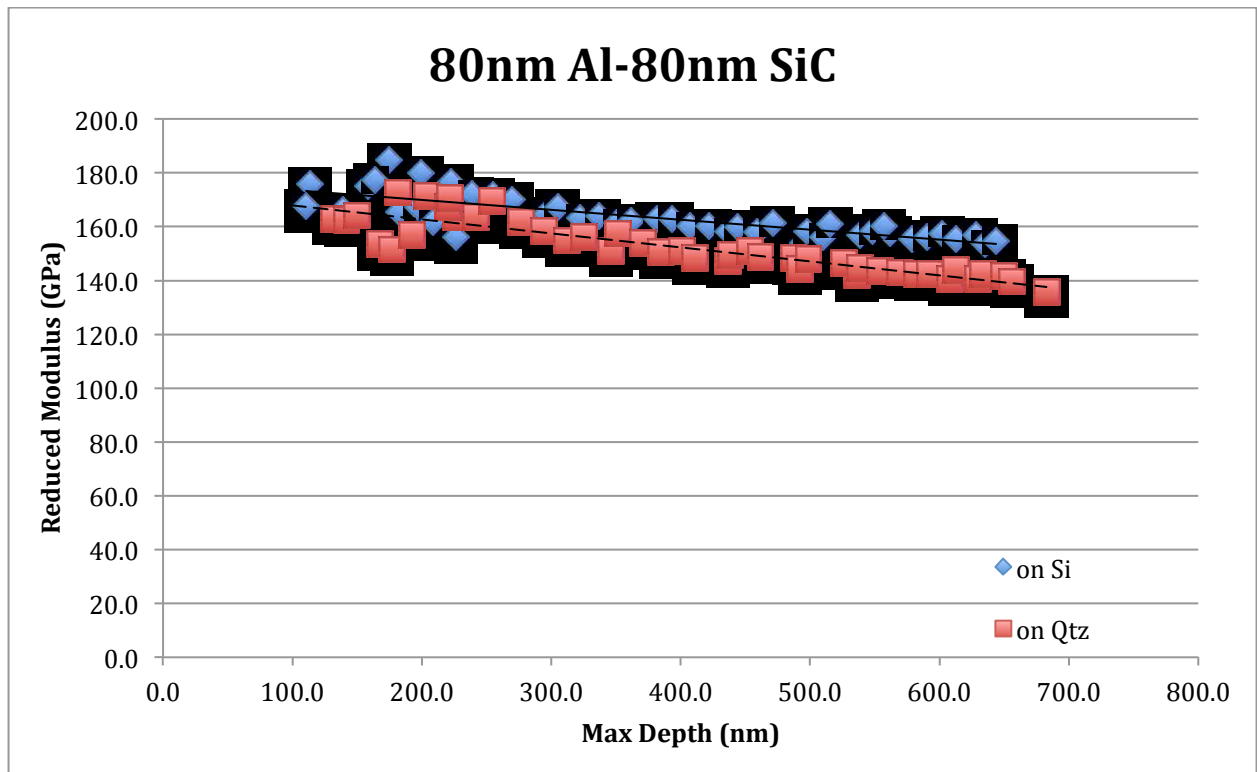


Figure 3.28 Reduced modulus and hardness for 80/80 Al-SiC nanolaminate Resulting modulus of 175 GPa and hardness of 11.6 GPa after substrate effect removed.

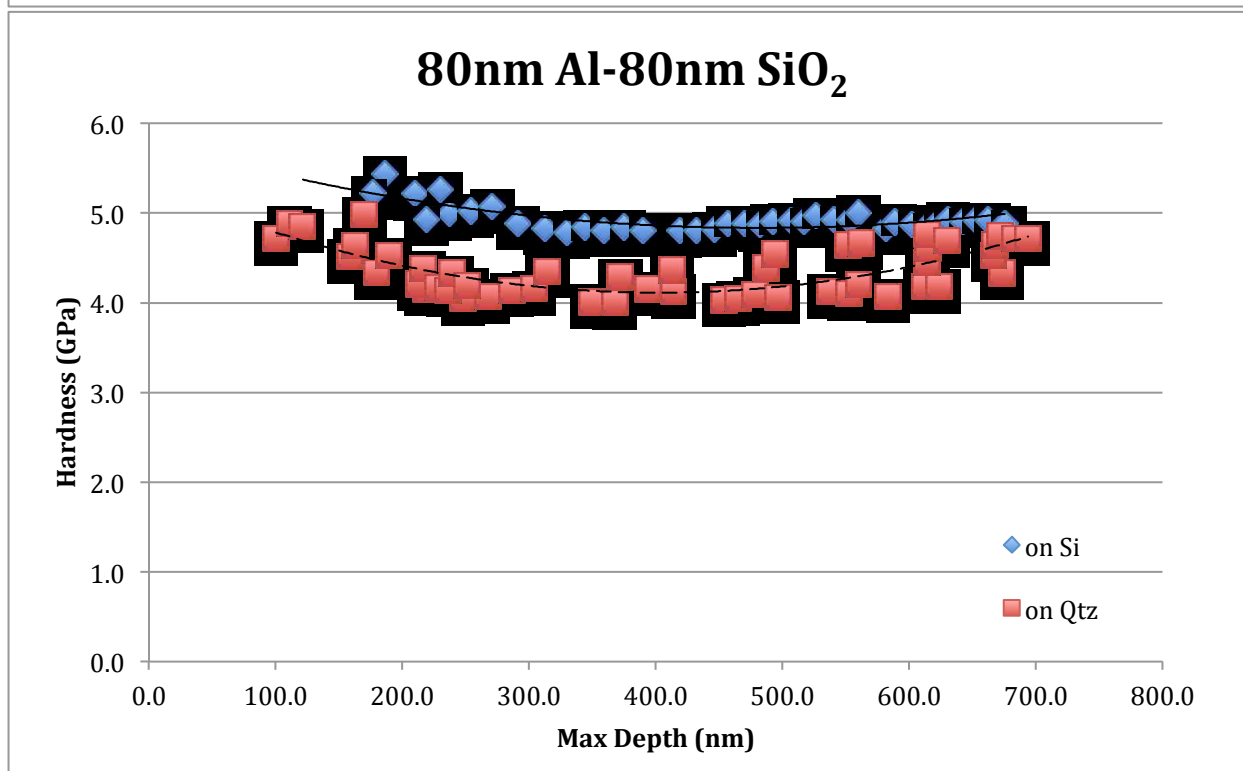
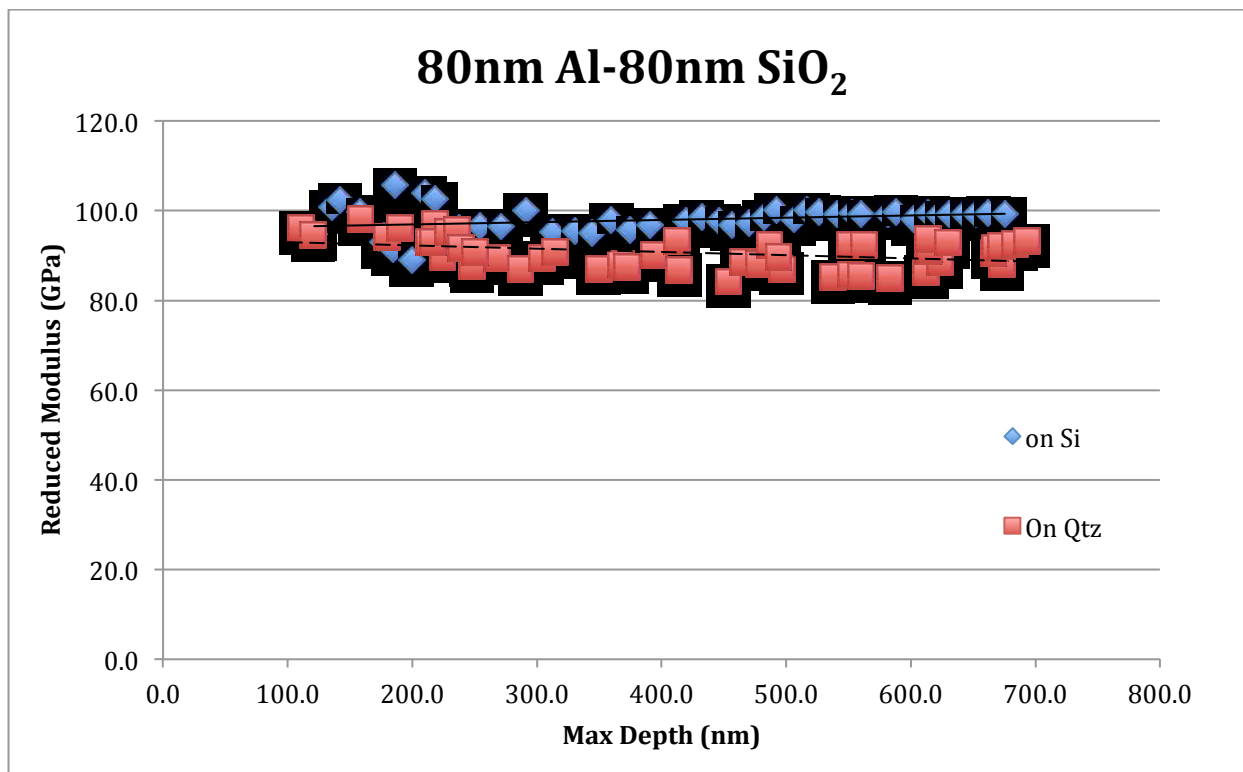


Figure 3.29 Reduced modulus and hardness for 80/80 Al-SiO₂ nanolaminate. Resulting modulus of 95 GPa and hardness of 5.0 GPa after substrate effect removed.

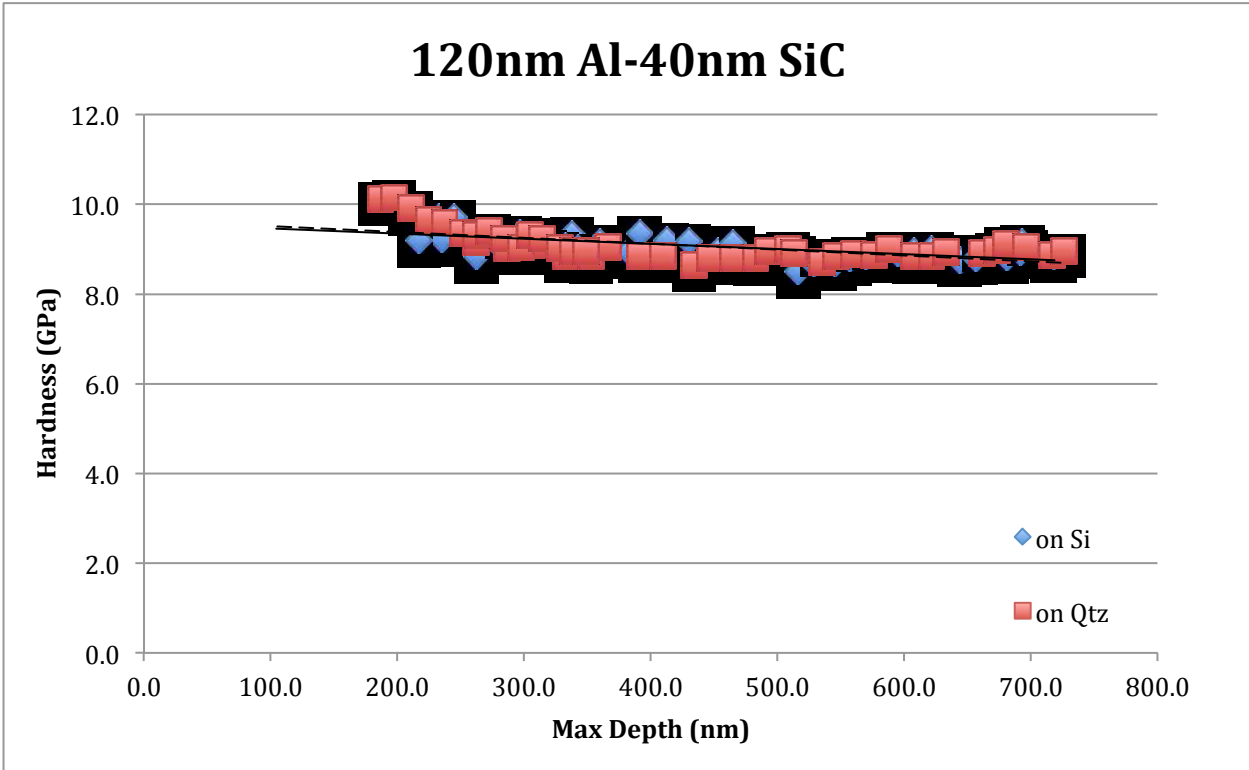
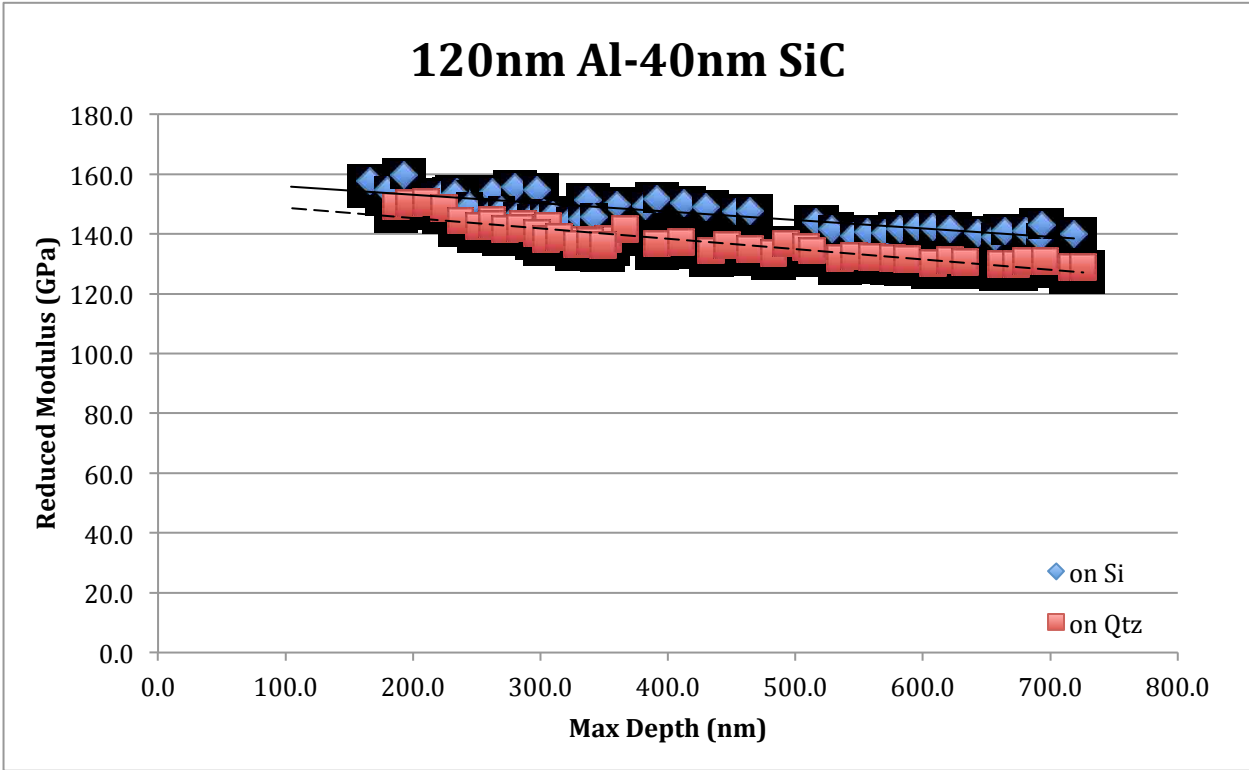


Figure 3.30 Reduced modulus and hardness for 120/40 Al-SiC nanolaminate. Resulting modulus of 156 GPa and hardness of 9.7 GPa after substrate effect removed.

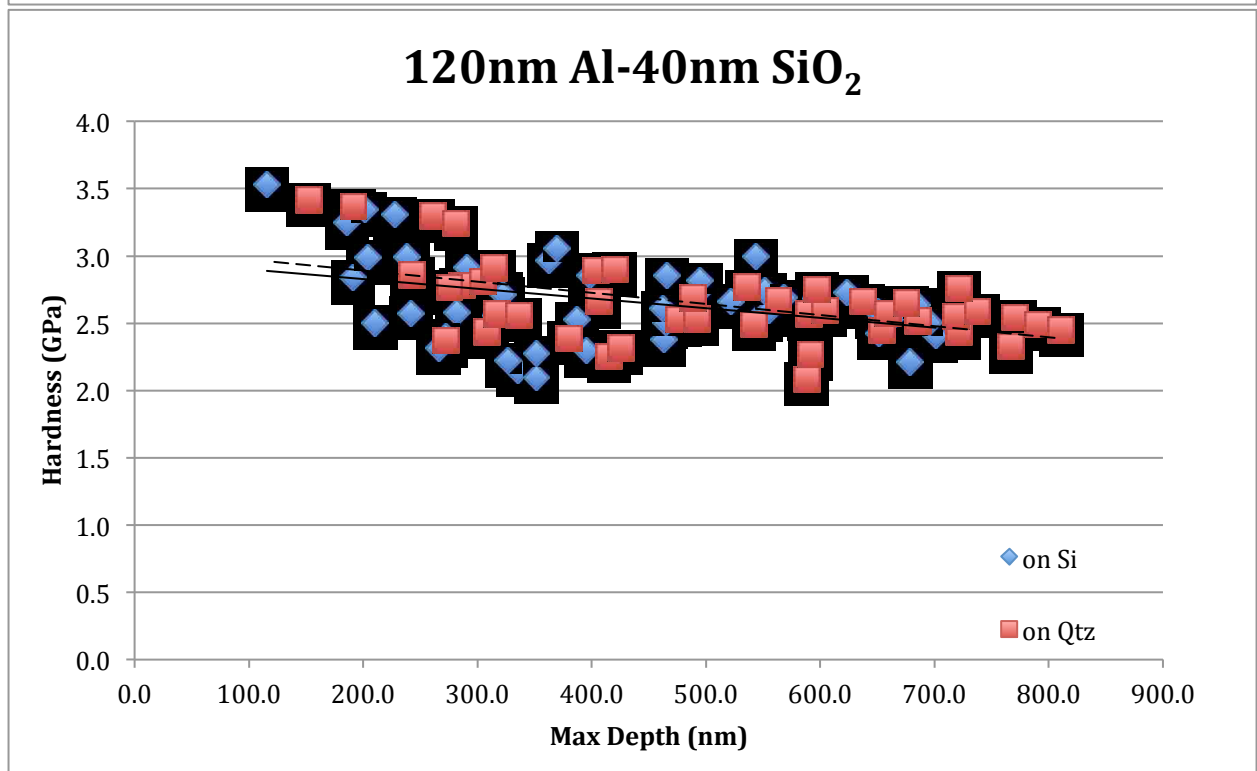
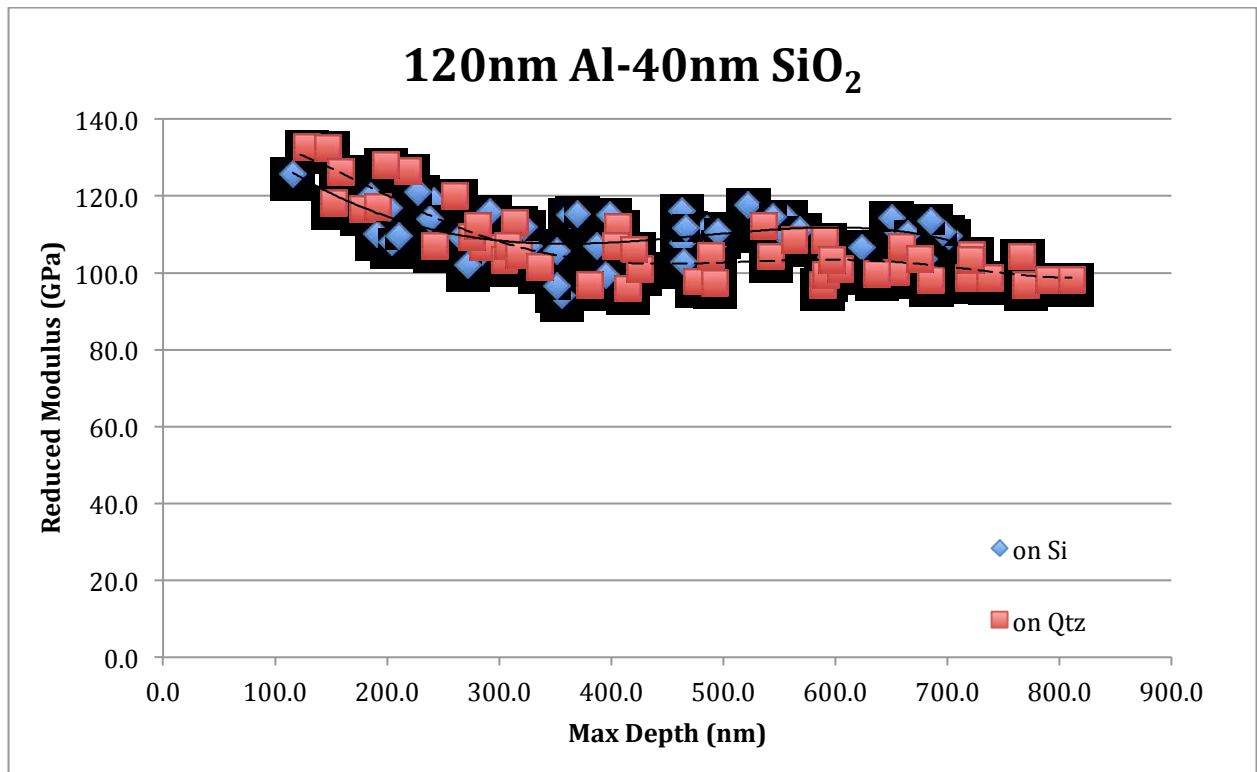


Figure 3.31 Reduced modulus and hardness for 120/40 Al-SiO₂ nanolaminate. Resulting modulus of 115 GPa and hardness of 3.0 GPa after substrate effect removed and consideration for alumina.

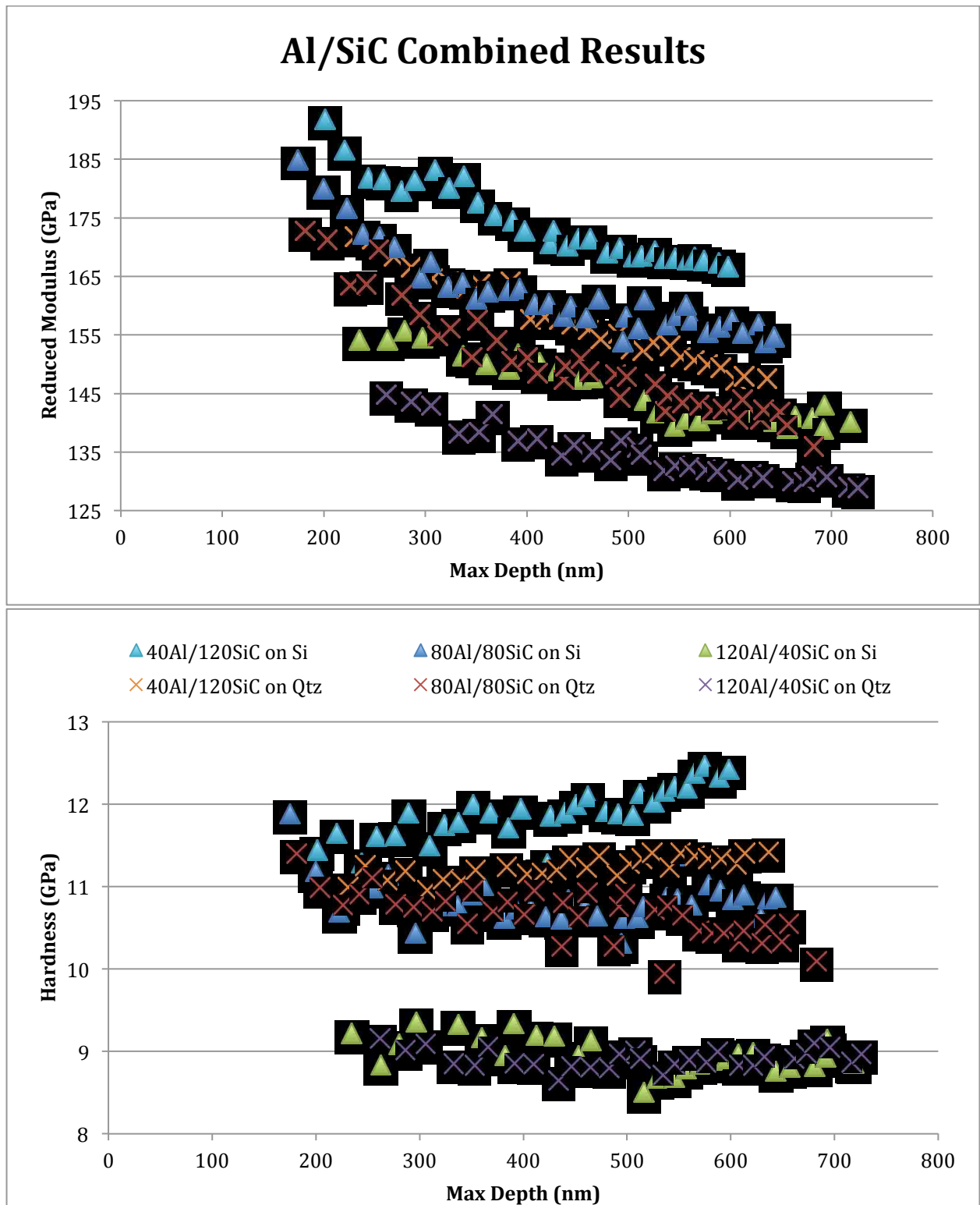


Figure 3.32 Reduced modulus and hardness against max depth for Al-SiC nanolaminate individual cycle indentations, for reference on the effect of modulation ratio on properties.

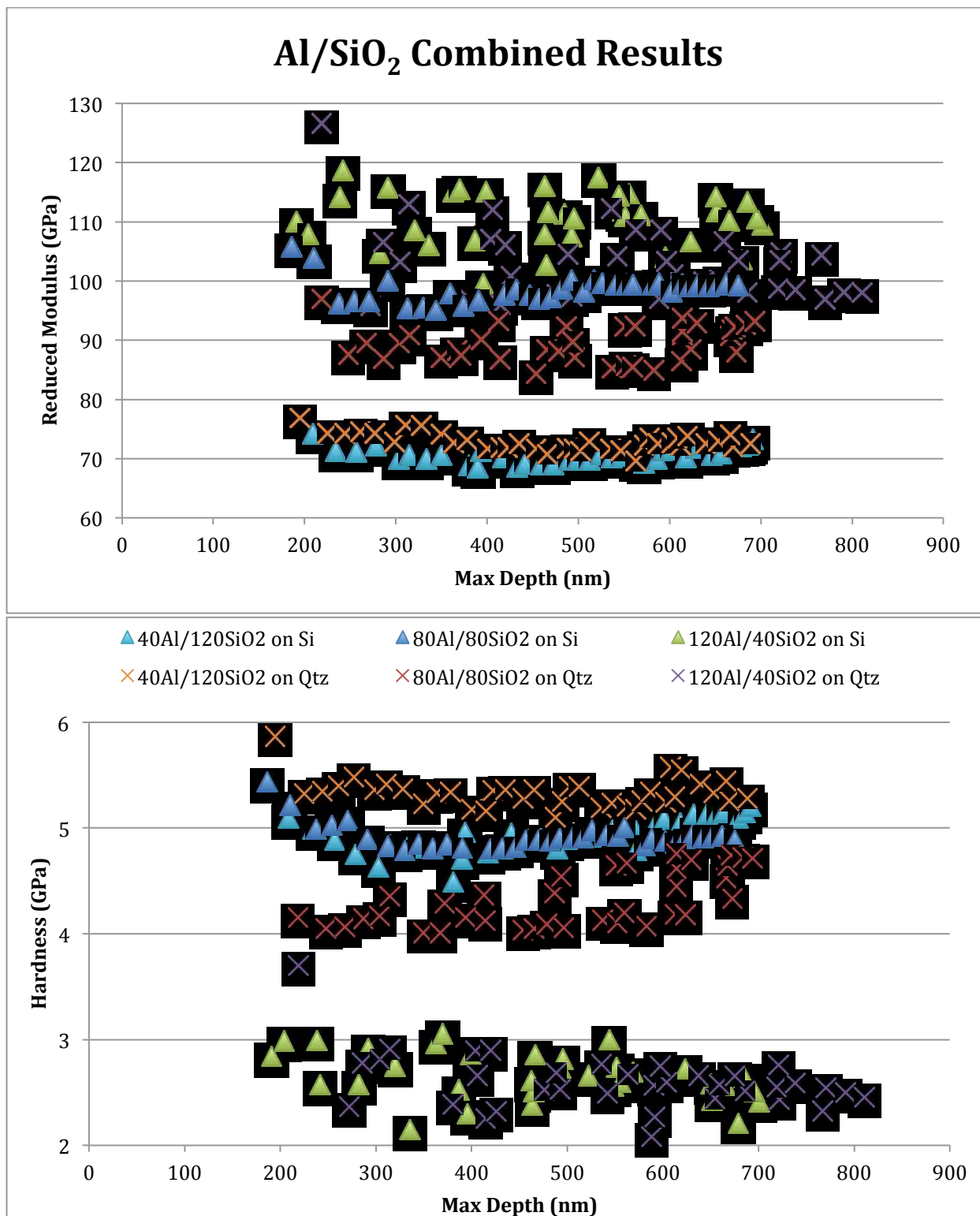


Figure 3.33 Reduced modulus and hardness against max depth for Al-SiO₂ nanolaminates

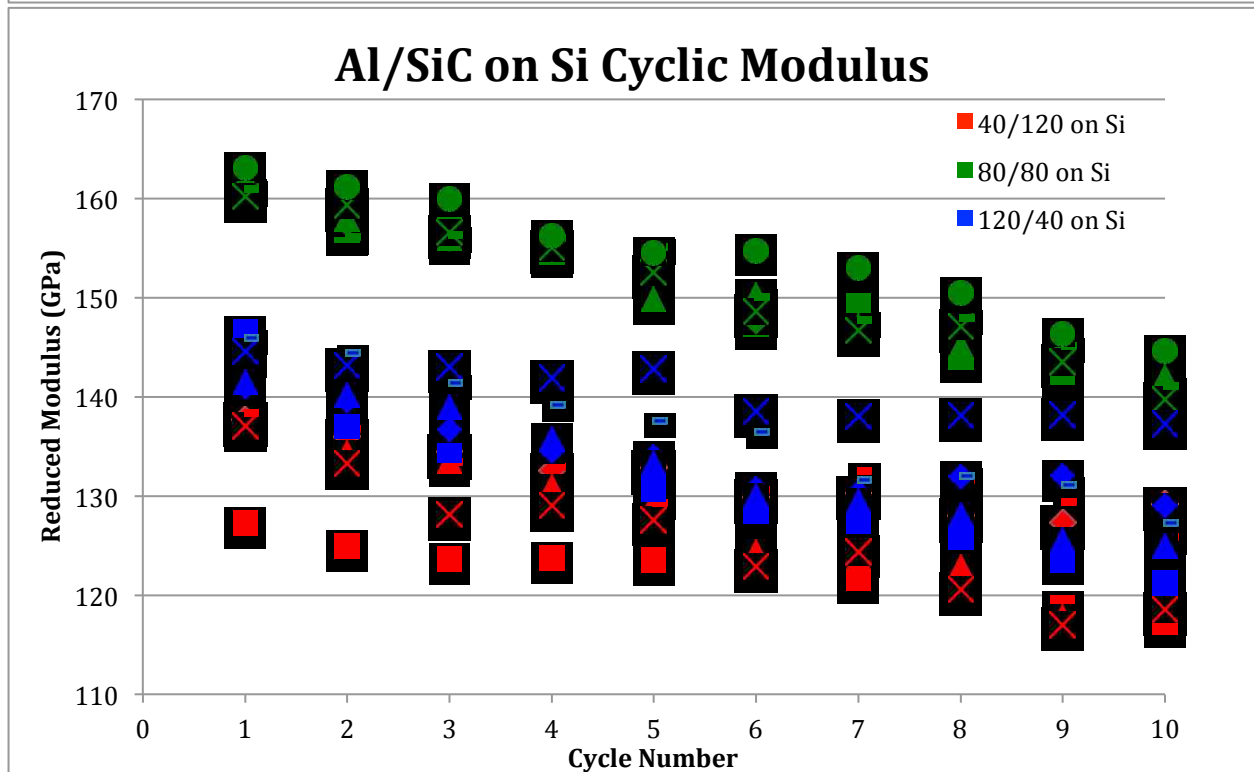
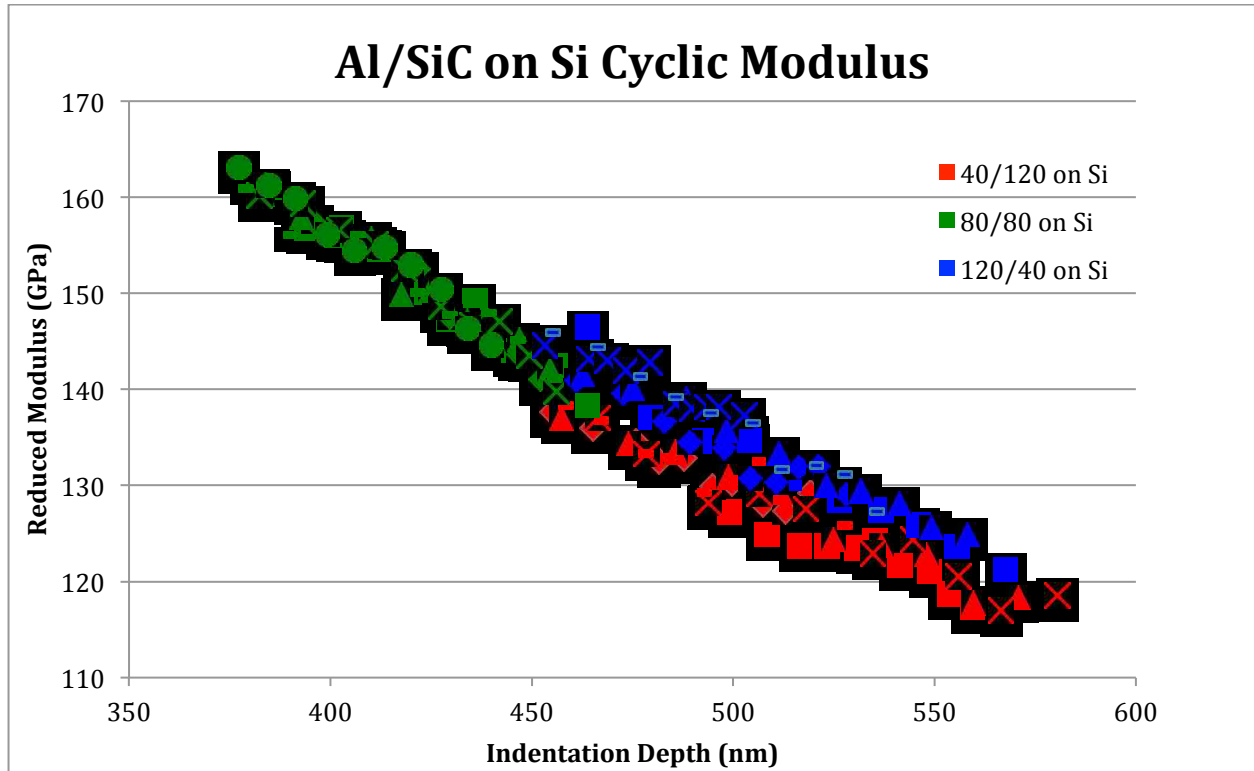


Figure 3.34 Cyclic indentation results for Al-SiC nanolaminates on Si wafer vs. depth and cycle number

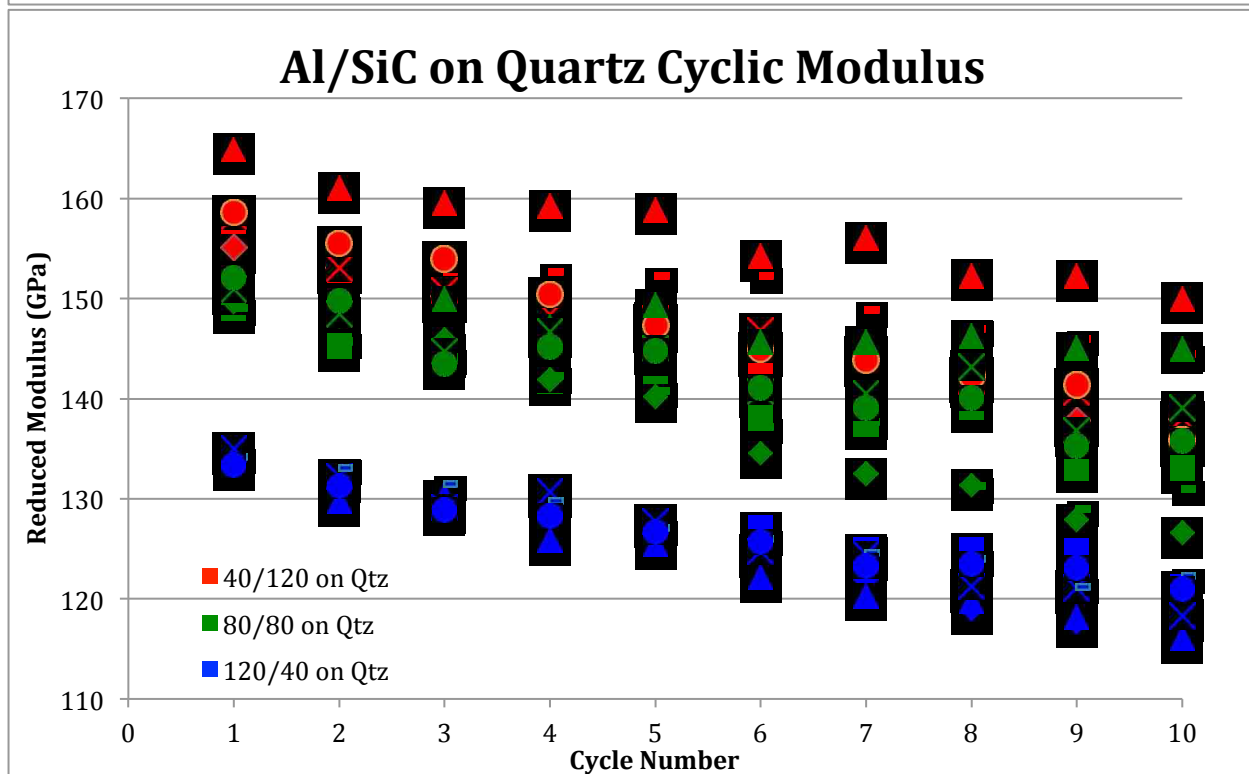
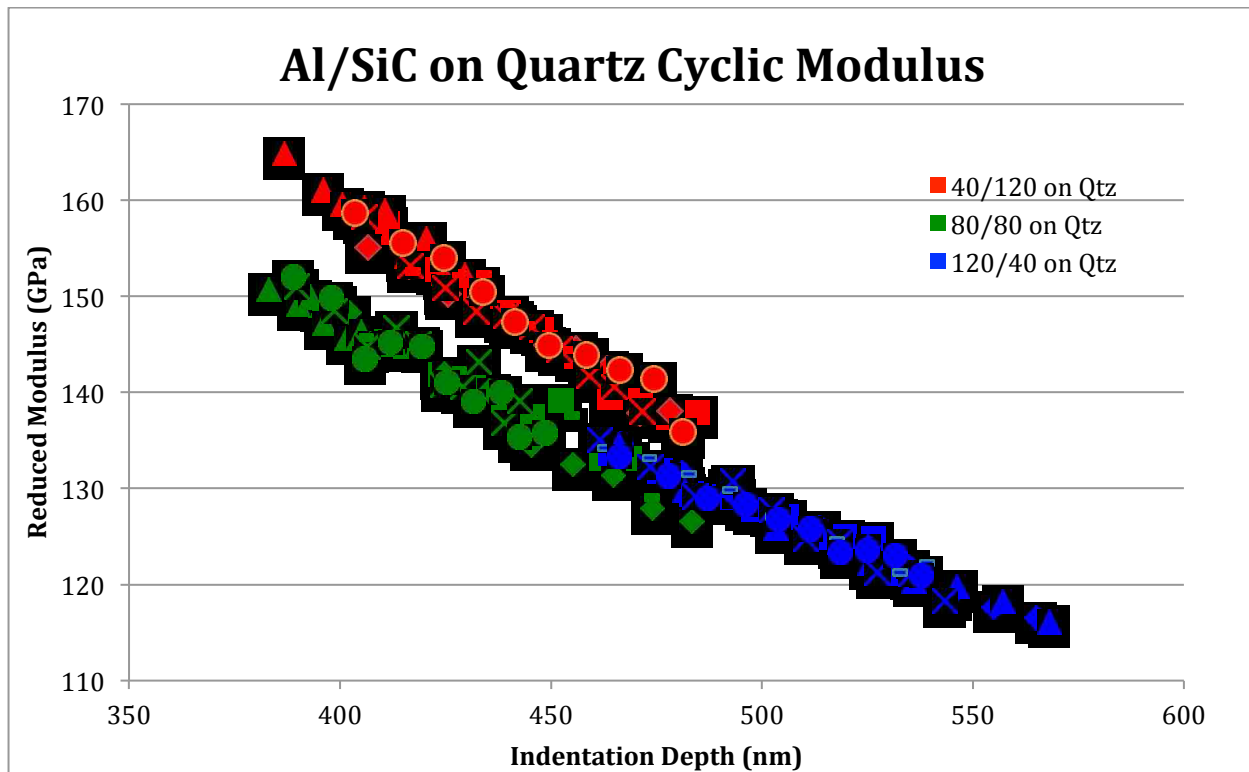


Figure 3.35 Cyclic indentation results for Al-SiC nanolaminates on quartz substrate vs. depth and cycle number

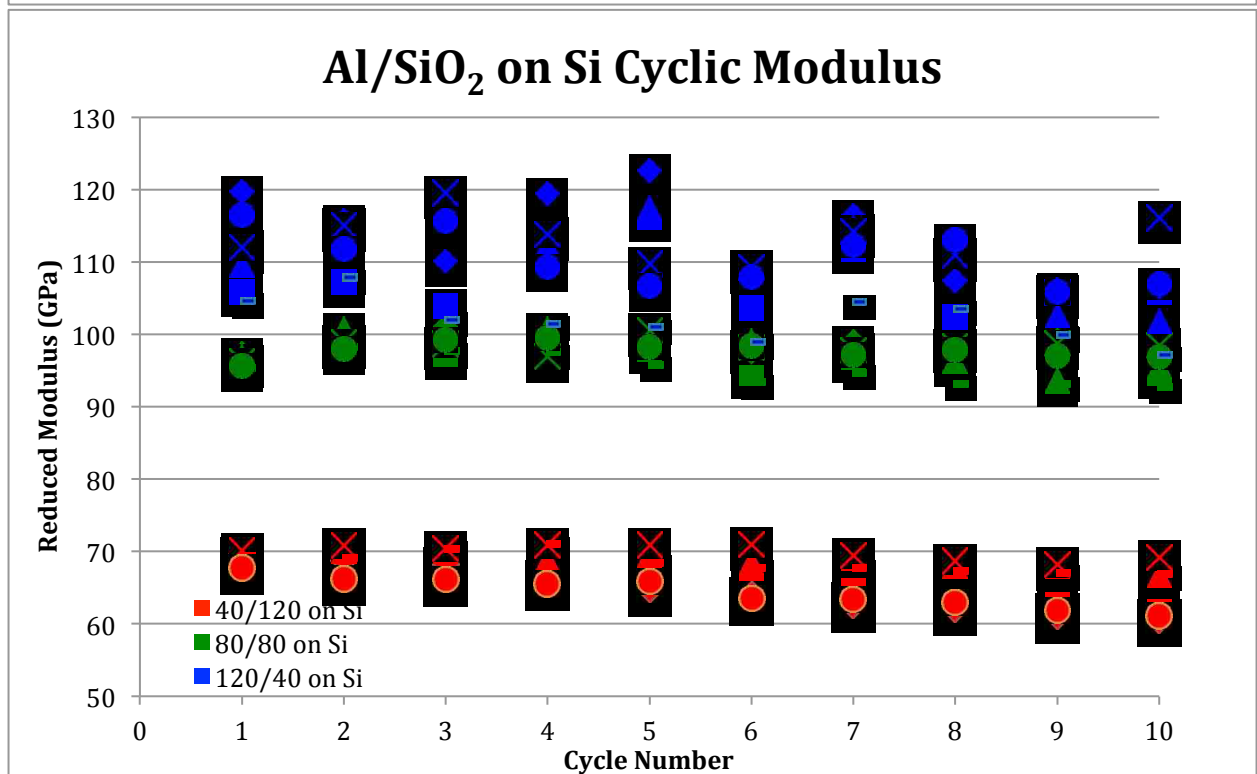
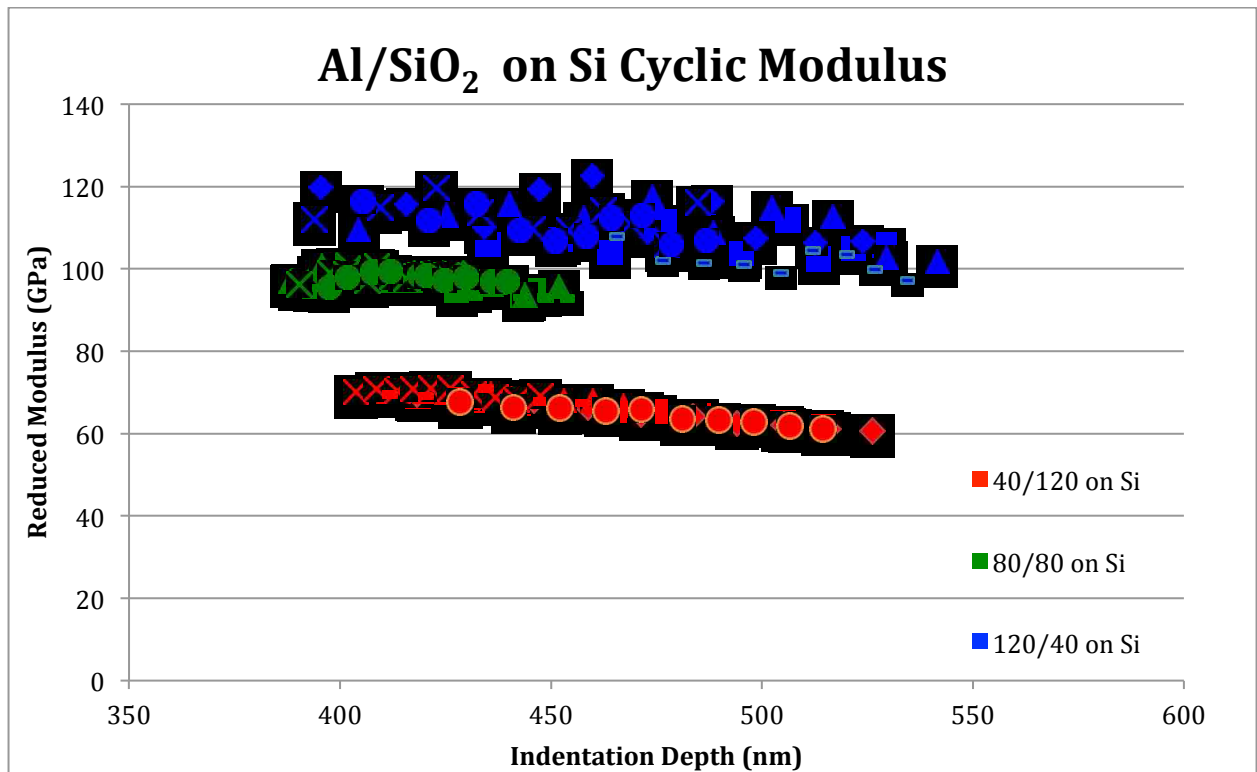


Figure 3.36 Cyclic indentation results for Al-SiO₂ nanolaminates on Si wafer vs. depth and cycle number

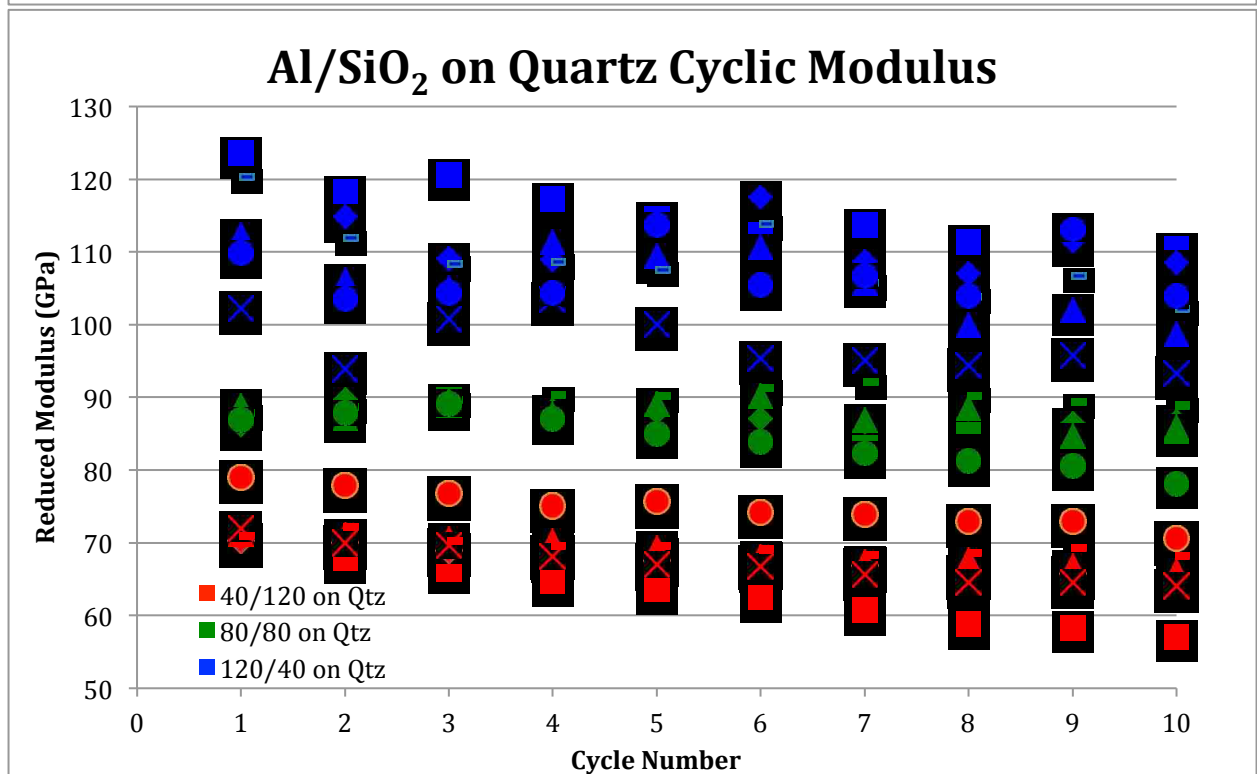
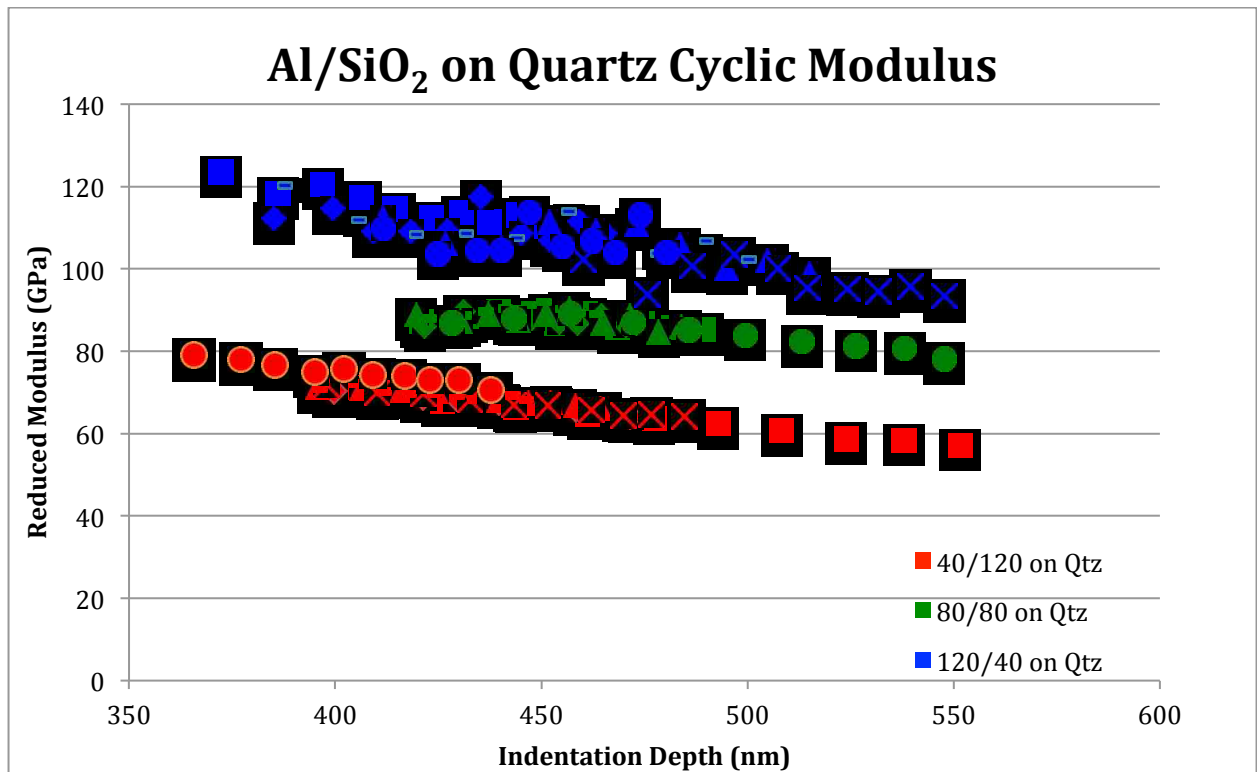


Figure 3.37 Cyclic indentation results for Al-SiO₂ nanolaminates on quartz substrate

Chapter 4. FEM: Modeling and Simulation

4.1. Introduction

Within the research conducted for this thesis, the primary intention for simulations was to lend insight into the microscopic deformation behavior of the nanolaminates. In particular the simulations gives an improved understanding of potential delamination concerns, changes within the nanolaminates when subjected to cyclic loading, and the effect of unloading plasticity. Due to the nano-scale operations and accumulation of damage internally, the system studied here is difficult to image or characterize using physical methods. No imaging can be completed while the system is under load and any internal imaging of the nanolaminate either pre or post indentation requires some form of cutting through the multilayered coating and substrate, which is laborious, requires expensive equipment, and inherently damaging or warping the sample through inducing or releasing internal stresses.

Therefore the initial intent of simulations was to verify that we could reproduce the plastic deformation upon unloading of a multilayer composite under nanoindentation and subsequently to further explore this phenomenon. It is widely understood that any elastoplastic material under a load will undergo first elastic deformation and then plastic deformation but only elastic deformation (or recovery) upon removal of said load. However, under specific circumstances involving a multilayered composite of alternating rigid and ductile layers with thicknesses on the nanoscale, the presence of plastic deformation during unloading of a specimen can be shown, thus defying the basics of the mechanics of materials.[49, 50, 52-56] This demonstration is performed within the wider basis of research intending to characterize the mechanical properties, specifically the elastic (Young's) modulus, of multilayered nanosystems.

As an exploratory effort into the practicality of future research some preliminary simulations were conducted based off previous work presented by G. Tang and Y.L. Shen that demonstrated the possibility of this phenomenon in a 41 layer metal-ceramic composite.[54] Using an adapted version of the ABAQUS code implemented by Tang we can find a theoretical modulus and show the previously mentioned plastic deformation within

the unloading period. The simulations conducted area all axisymmetric models which utilize a conical indenter with a prescribed semi-angle such that the area of indentation is equivalent to that of a Berkovich indenter. A schematic of the setup is shown in Figure 4.1.

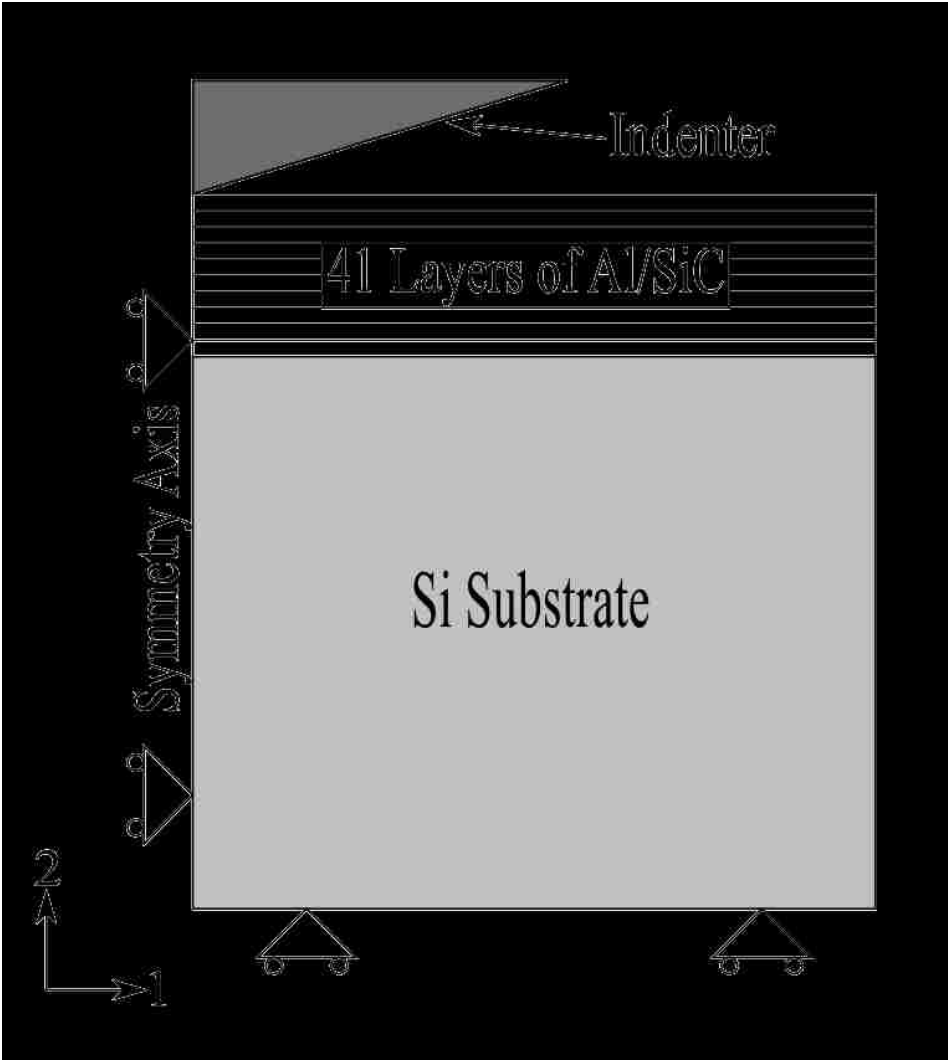


Figure 4.1 Schematic of geometric setup for preliminary simulations[48]

To check the feasibility of future work, three simulations of like geometry but utilizing different materials were run and compared. The materials of said simulations were Aluminum-Silicon Carbide layers on Silicon substrate, Aluminum-Silicon Dioxide layers on Silicon substrate, and Aluminum-Silicon Dioxide layers on Silicon Dioxide substrate. The load-displacement data for these three situations is shown in Figure 4.2. It should be noted that the material properties used in these simulations are bulk properties or those derived from previous experimentation[52, 54] rather than the nanoindentation derived ones from

the previous chapter. During this preliminary stage the material were defined as elastic-plastic with elastic moduli of: $E_{Al}=59$ GPa, $E_{SiC}=277$ GPa, $E_{SiO_2}=187$ GPa, and $E_{Si}=187$ GPa. Specific values can be found in the sample code in APPENDIX A: Sample Code - Berkovich Indentation of 80nm Al/80nm SiC.

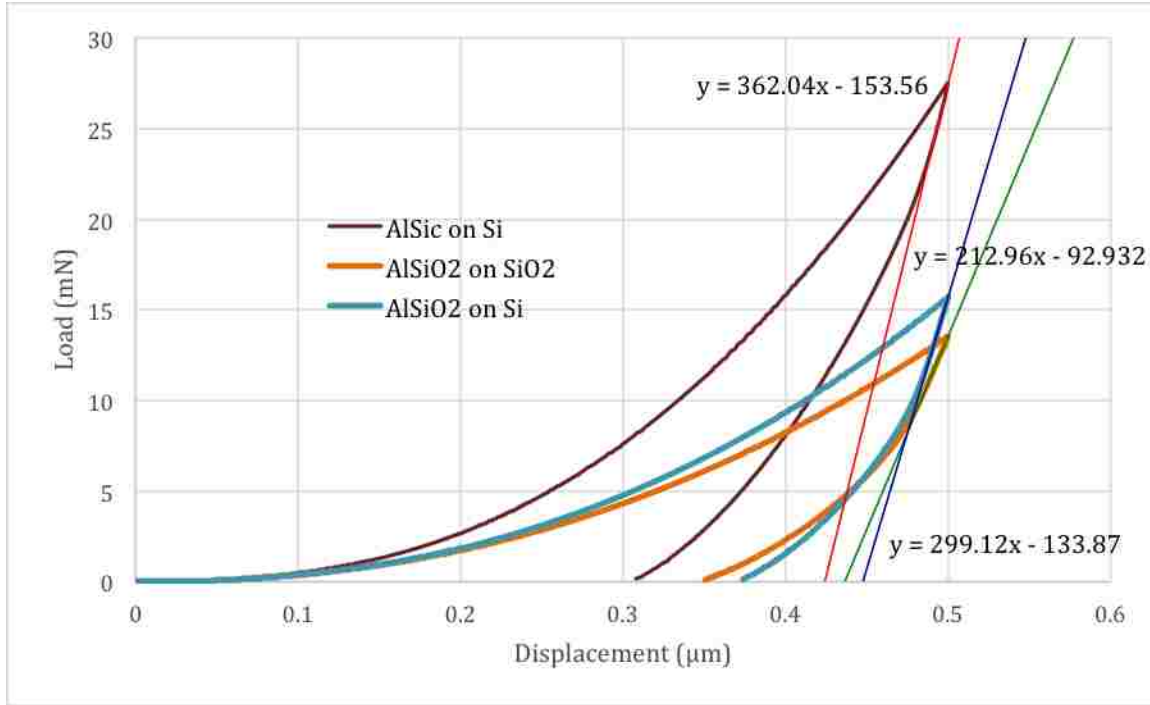


Figure 4.2 Load Displacement Data for 41 Layer Tests

The slope of the unloading information from the first 2% of indentation depth has been extracted in order to calculate the composite Young's modulus and hardness according to the following equations:

$$H = \frac{P}{A} \quad (4.1)$$

$$\text{and } \frac{1}{E_{eff}} = \frac{1-\nu^2}{E} + \frac{1-\nu_i^2}{E_i} \quad (4.2)$$

$$\text{where } E_{eff} = \frac{S\sqrt{\pi}}{2\beta\sqrt{A}} \quad (4.3)$$

This relies upon diamond indenter values of $\nu_i = 0.07$ and $E_i = 1141$ MPa, $\beta = 1.06$, and a composite Poisson's ratio that was approximated to be 0.25 using the Rule of Mixtures thus giving the results shown in Table 4-1. For the preliminary simulations, the value β was taken to be the same as in previous work on unloading induced plasticity [52,

54] however simulations presented later use a value $\beta = 1.034$ as per more recent work on viscoplastic effects.[91]

Table 4-1 Results of 41 Layer Verification Test

Sample	Substrate	Hardness (GPa)	Modulus (GPa)
Al/SiC	Si	4.56	129.34
Al/SiO ₂	Si	2.55	103.46
Al/SiO ₂	SiO ₂	2.42	75.54

As can be seen from this, the introduction of SiO₂ in place of SiC has the understandable effect of slightly lowering the hardness and significantly decreasing the modulus as would be expected by substituting a significantly softer material for a more rigid one. What is interesting to note is that although both the Aluminum and Silicone Dioxide have a bulk modulus around 70 GPa when they are incorporated into a nanolaminate the resultant structure shows a modulus over 100 GPa. This increase in strength is a well documented phenomenon and as such is not novel but is important to note as it affirmed basic understandings that were critical to proceeding with the simulations.[2-4, 7, 9, 14, 16, 20, 28, 48-56] Another point of note in this is to reiterate the use of the SiO₂ as a substrate is intended to illustrate and quantify the substrate effect on the calculated properties. Comparing the two nanolaminates, of Al/SiO₂ highlights that the substrate effect on the 41 layer system explored previously is significant, almost causing a 30 GPa change in modulus. This is an issue that must be kept in mind as simulations continue as it is a confounding variable that may lead to incorrect conclusions. That being said it is still significant that there is a noticeably higher modulus for the Al/SiO₂ nanolaminate on SiO₂ substrate than would be found from either pure Al or pure SiO₂.

Finally, for verification of the unloading induced plasticity we can see pictures showing the equivalent plastic strain (PEEQ) during unloading for the multilayered systems are included below and demonstrate clear evidence of plastic deformation within specific layers during the unloading process. PEEQ is an accumulated measure of the plastic strain within a body, however, unlike the plastic strain magnitude PEEQ will continue to increase in the event of a loading reversal. This makes PEEQ a significantly less common value for study but is the most significant measure of plastic strain for our study as we are

specifically interested in the plasticity during the unloading portion of the indentation. Thus the portion of the plastic strain that is often ignored is the critical value in our study. Shown in Figure 4.3 are progressions of increased plastic deformation within the aluminum layers of the three samples simulated for this verification. As the indenter is removed from the multilayer the PEEQ increases. This increase is particularly apparent just below and to the right of the indenter where there is clear growth of the red area expands.

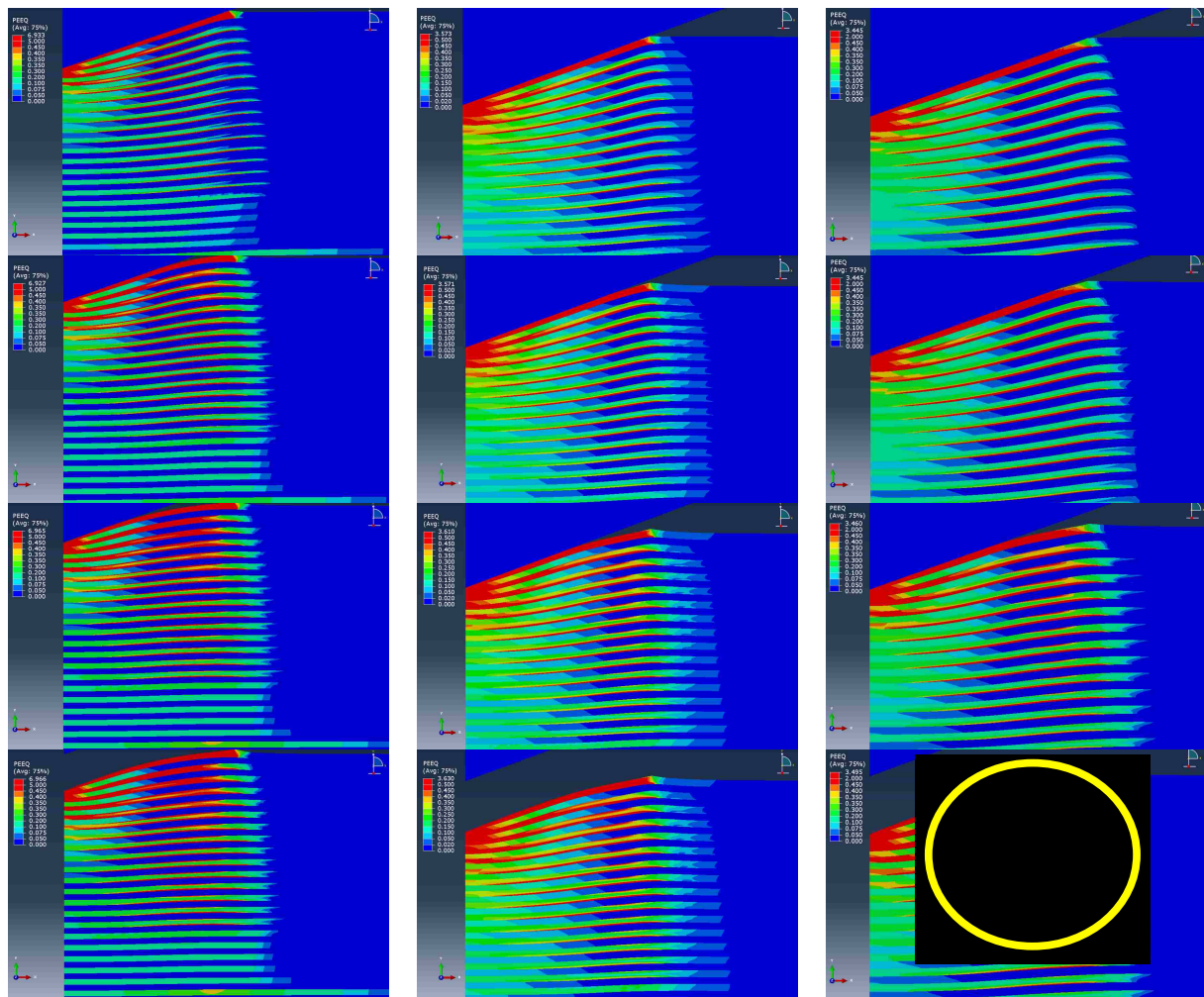


Figure 4.3 Snapshots of simulations showing unloading plasticity. From left to right samples are Al/SiO₂ on SiO₂, Al/SiO₂ on Si, and Al/SiC on Si. As indenter is retracted from full load (top to bottom) plastic deformation within the aluminum layers developing to the right side of the indenter, highlighted in the area of the yellow circle.

4.2. Simulation Set Up

These results were encouraging but were just a basis from which to start and a verification of the expected phenomenon. For the study, we simulated 51 layer nanolaminates, identical to those of the experiments, of varied thicknesses ratio (layers of dimensions 40nm/120nm, 80nm/80nm, and 120nm/40nm), under indentation from both Berkovich and spherical indenters, and with substrates both of silicon wafer and quartz. The first step in creating accurate models was to retrieve an accurate value for the Poisson's ratio, ν , corresponding to each multilayer coating of varied material and thickness ratio. The importance of this lies in the realization that a nanolaminate does not act in the same fashion as bulk materials and that the Rule of Mixtures (RoM) is a limited approximation tool when dealing with Poisson's Ratio in this situation and has no mechanical validity.

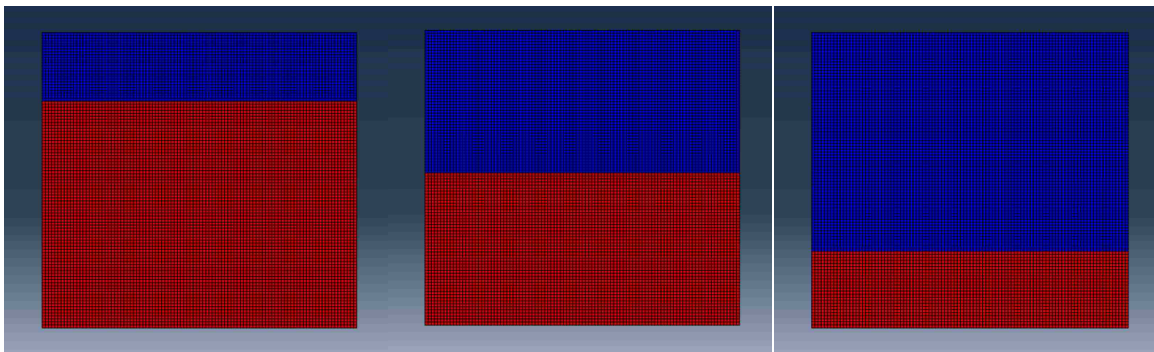


Figure 4.4 Post Compression Samples of 25%, 50%, and 75% Aluminum used in determination of the Poisson's Ratio, ν , for multilayer structure

To find an accurate value of Poisson's ratios simulations were conducted using a subsection of the multilayer to represent the whole. The area chosen was a square with the midline being the interface between the two materials which represents a slice with height corresponding to half a layer of Al and half a layer of ceramic, which when extrapolated to multiple layers will have the same Poisson's ratio as if all layers were simulated. The width of the representative area does not actually matter in the simulation due to the nature of the ratio so long as the boundary conditions are properly determined. Top and bottom edges are held such that elements are constrained to a horizontal line with the bottom edge fixed in the vertical direction and the top having an applied load to induce strain. The sides are constrained to remain linear thus accounting for the material that would be present in

a wider sample. In reality of the indentations the width to height ratio of the material being compressed is extremely large and the edges are significantly far from the indentation site so as to be almost infinite. Therefore, the boundary condition accounts for the inability of the material in the nanoindentation tests to extrude out the sides or deform in a buckling manner.

As a verification of the simulation, Poisson’s ratio for each Al, SiC, and SiO₂ were found using the split geometry but defining both materials as the same. For the single material samples the initial value of Poisson’s ratio was equivalent to that of the bulk material. As for the composite systems they all had ν below the Rule of Mixtures prediction and the values can be found in Table 4-2. Full material definition for these can be found in the Appendix and the Poisson’s ratios used for each material were 0.33 for Al, 0.17 for SiC, and 0.16 for SiO₂.

Table 4-2 Poisson's Ratio (Simulation Results)

Composite	ν (simulation)	ν (Rule of Mixtures)
25% Al, 75% SiC	0.182	0.210
50% Al, 50% SiC	0.208	0.250
75% Al, 25% SiC	0.252	0.290
25% Al, 75% SiO ₂	0.177	0.2025
50% Al, 50% SiO ₂	0.206	0.245
75% Al, 25% SiO ₂	0.252	0.2875

The next step was to create indenter geometries that could be implemented for use in simulation without negatively impacting the results. The indenters needed to have sufficient elements at the tip and any other points that may come in contact with the surface of the multilayer structure so as to accurately replicate true indenter deformation under compression. Two indenter types were created, a conical indenter in place of the classic Berkovich indenter, and a spherical indenter intended to give a lower stress field. The conical indenter is designed with a 70.3° semi-angle such that during simulated indentation the area under compression at any given depth is the same as would be present in a physical indentation using a Berkovich indenter. This is necessary as the Berkovich indenter’s four-sided pyramidal geometry cannot be constructed within an axisymmetric model relying on rotation around a central axis. This method is commonly practiced[12, 35, 48, 49, 53, 55, 56, 72, 80, 83, 93, 94, 118-120] and yields the same indentation-derived

modulus as simulations of a true Berkovich indenter. A basic spherical indenter geometry can be seen in Figure 4.5 which highlights the structure of how the spherical surface was created and thus resolved into a single square element in the center. It should be noted, however, that as physical spherical indenters are created by rounding the tip of a cone that there is a maximum depth of indentation beyond which the physical indenter profile transitions from a sphere to a cone. This is an important consideration for those modeling a spherical indentation, however, this is not a concern for as long as the maximum depth of indentations does not approach the depth at which this geometry transition occurs.

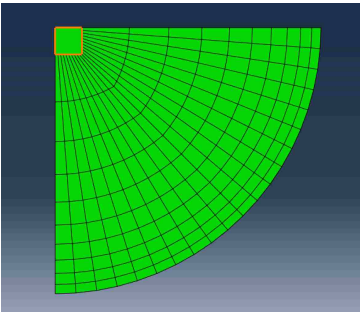


Figure 4.5 Basic Spherical Indenter Design

It should be noted that the model is axisymmetric and therefore the image is effectively a cross-sectional view that would be rotated around a central axis located along the left edge of the indenter thus creating a hemisphere. Two more images can be found in Figure 4.6 which shows the more complex spherical indenter used and a conical indenter. As discussed these are axisymmetric models that represent a three dimensional simulation within the ABAQUS program.

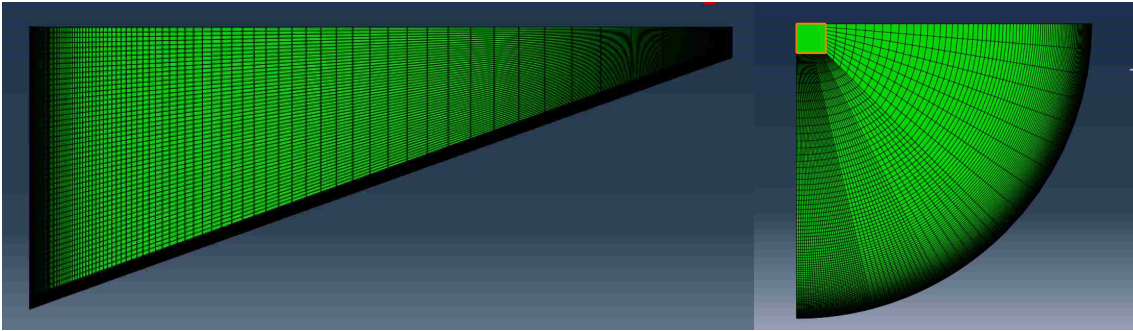


Figure 4.6 Spherical and Conical Indenter Geometries

Finally the multilayer geometries were defined. The general layout and constraints of the simulation are similar to those in the preliminary simulations and a schematic can be found in Figure 4.7.

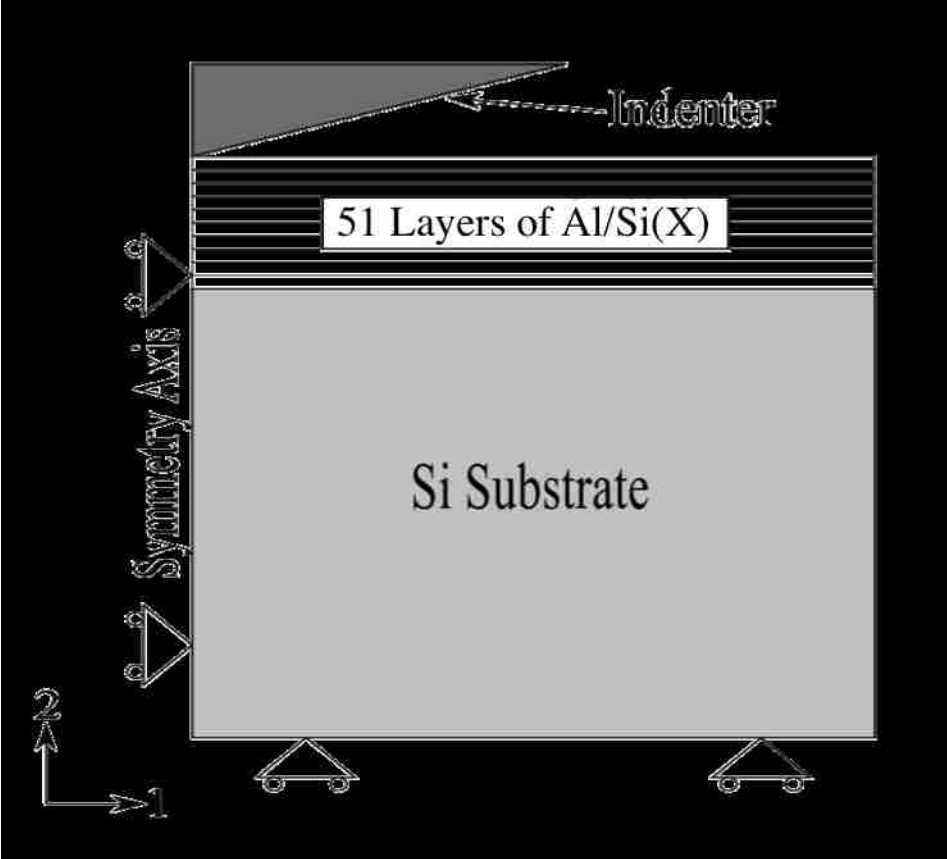


Figure 4.7 Schematic of simulation general geometry

An example model geometry definition can be found in the appendix and basically includes three sections: the main substrate, the main multilayer structure, and an extension portion of lower resolution far from the indentation site. These three areas can be seen in



Figure 4.8 Model Geometry Sections and Seize Reference

The substrate is defined with high resolution, small elements, in the regions near the central axis and multilayer coating interface where stress and strain fields exist and require attention. The elements grow and resolution decreases as the model transitions to regions far from the indentation site as no stress fields exist in these areas. In this manner we manage the necessary computational resources and decrease simulation run time. This can be seen in Figure 4.9 .

Similarly the 51 layers of thin film coating are defined with extremely high resolutions near the central axis decreasing in resolution with respect to their radial position. This requires a large amount of computational power but guarantees accurate results in the area close to the indentation site, a necessity for effective extraction of indentation derived hardness and modulus. There were actually three versions of the geometry corresponding to the three different variations of layer thickness ratios of 25, 50, and 75% Aluminum (40nm Al/120nm ceramic, 80nm Al/80nm ceramic, 120nm Al/40nm ceramic respectively). These three definitions all have the 51 layers of material and in each circumstance the 25 bilayers require $4\mu\text{m}$ of material with the final layer determining the overall height above the substrate surface (4.04 , 4.08 , and $4.012\ \mu\text{m}$ respectively).

The third area is a section of additional low resolution material in which stresses are exceptionally small to nonexistent but the area is simulated to guarantee no bulk effects present in physical indentation are removed in the simulation. This section requires only one element for each layer of the thin film coating and ten elements for the extra substrate.

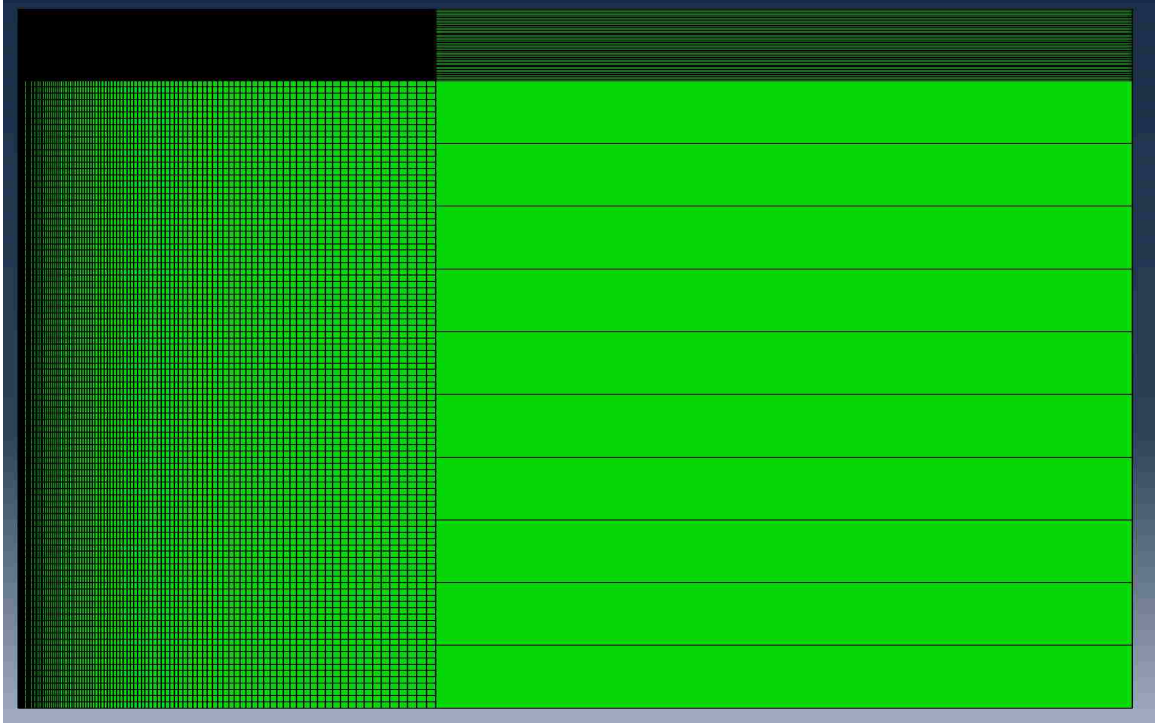


Figure 4.9 Element Structure of Multilayer Structure upon Substrate

As can be seen in the code found in APPENDIX A: Sample Code - Berkovich Indentation of 80nm Al/80nm SiC, the substrate and each layer, including those portions defined in the additional material section, are defined as a certain material which in turn defines elastic, plastic, and viscoelastic properties for each section. The values for these properties are extracted from physical experiments previously conducted.[50, 52, 55, 76, 91, 94] Model geometry definition can be found in the appendix and begins with definition of the substrate of either Si or Quartz. On the substrate a multilayer structure was created starting with an aluminum layer and alternating material definitions until there are cumulatively 51 layers. These layers are meant to simulate the multilayers to be fabricated with thicknesses that are 40nm/120nm, 80nm/80nm, 120nm/40nm of metal and ceramic, respectively. Therefore, three different models for the multilayered structure were

constructed with cumulative multilayer thickness of 4.04, 4.08, and 4.12 above the substrate surface.

After geometry definition a second geometry was defined with extra mass in the substrate and the “additional material” section. This model was used to verify indentations and guarantee that the defined model had adequate volume to prevent any effects from being lost. The results of the regular model and the extra mass model were consistent and therefore we proceeded with simulations using the model geometry described above.

4.3. Individual Indentations

Individual load cycle indentations were completed using both Berkovich and spherical indenters as can be found in the appendices. The indentations were completed over a variety of depth ranges from 200-800nm, which represent a depth range of 5-20% of the film thickness. Three multilayer geometries, representing the different thickness ratios, were defined upon a silicon substrate. Simulations were not conducted upon the Quartz substrate although this can easily be accomplished if needed for future work. These simulations were a verification that the unloading plasticity described in Figure 4.3 was present in all these circumstances and as an examination of the stress fields within the layers. These simulations also provided insight into the level of shear stress at the substrate/film interface for insight into potential delamination. For individual load cycles viscous effects were not incorporated into the model and we believe that further investigation with viscous effects would yield greater insight into the layer interactions, however, further microstructural characterization of the constituent materials is required to provide accurate properties for the simulation. Additional exploration of simulated single cycle indentation is unlikely to yield meaningful results without representative material definitions. For example of the indentation results see Figure 4.10 which shows the elastic modulus and hardness derived from a series of indentations on an aluminum and silicon carbide laminate with 51 alternating layers with thickness of 80nm for both materials. For this case the rule of mixtures predicted a modulus of 168 GPa.

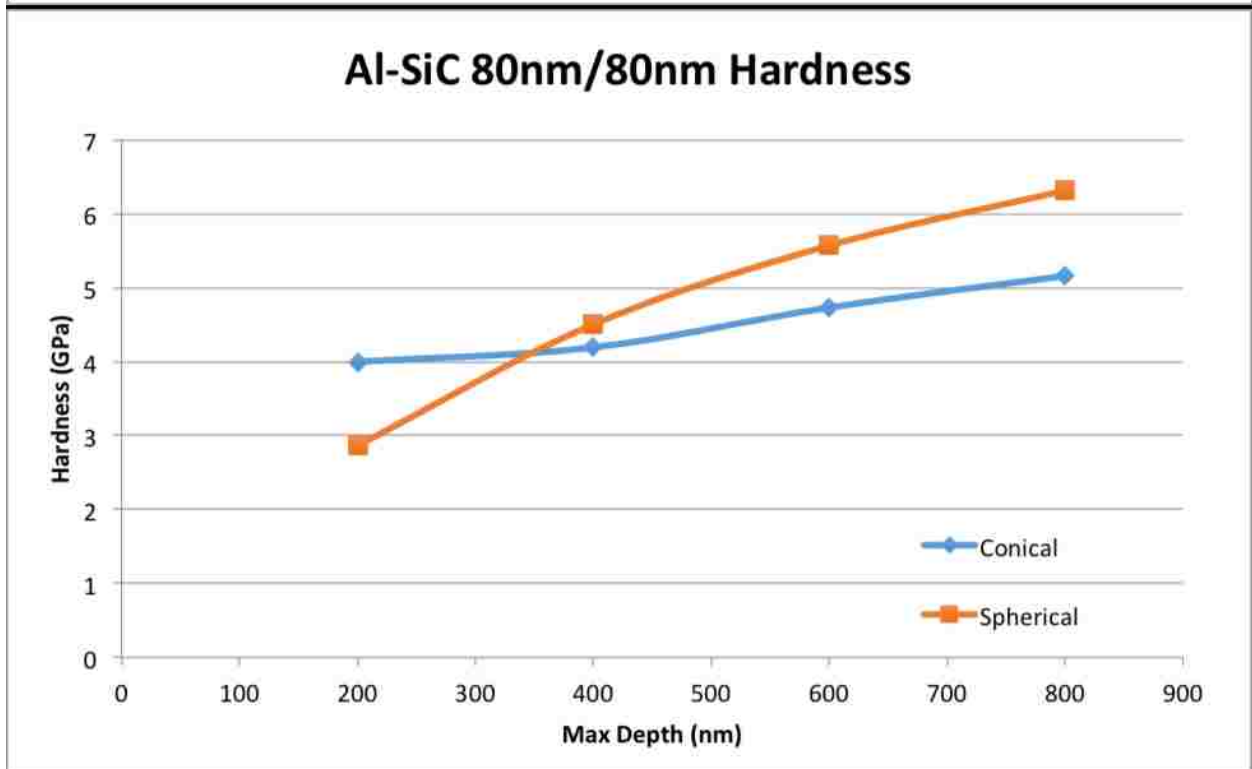
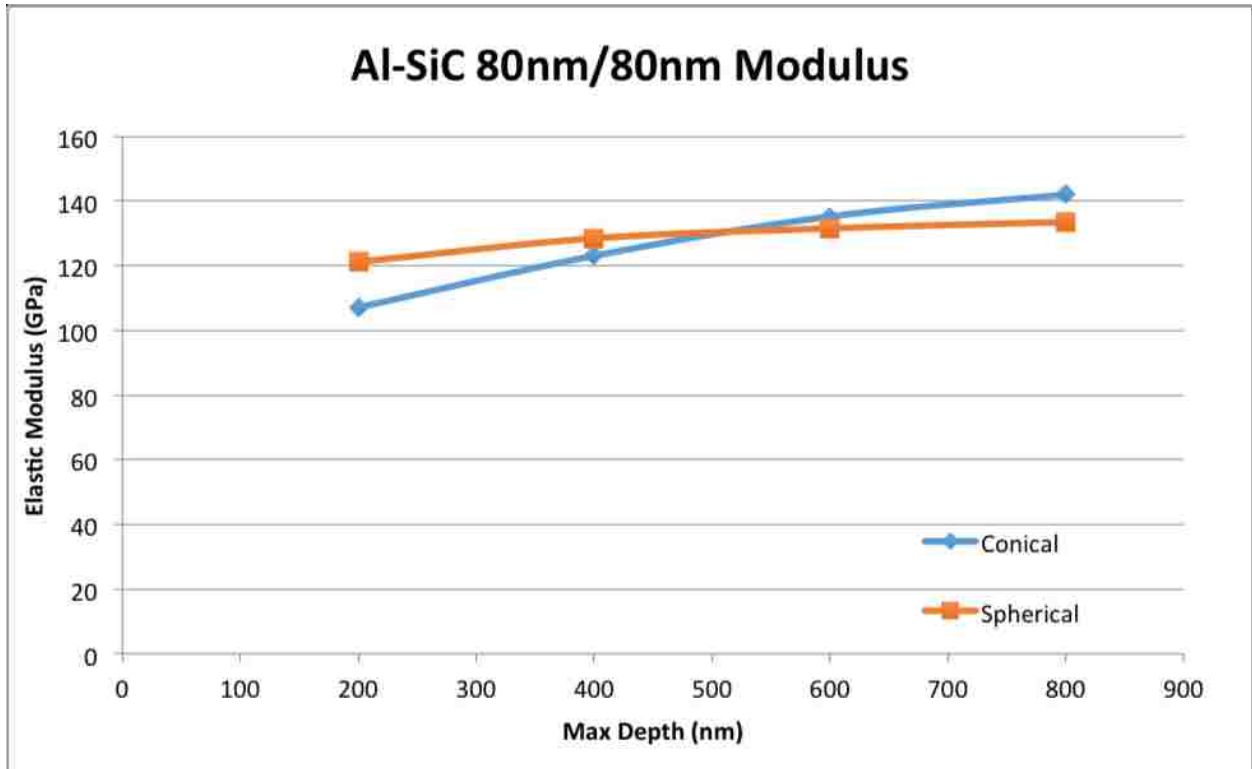


Figure 4.10 Simulated single indentations of an aluminum and silicon carbide nanolaminate. Results in hardness of 3.5 GPa and Young's modulus of 97 GPa.

4.4. Cyclic Indentations

After confirming that unloading plasticity was present in all individual indentations, cyclic indentations were investigated to test the hypothesis of this thesis: cyclic indentation can remove the unloading plasticity effect on extracted modulus. Of interest was also the investigation of the effect of this phenomenon on the indentation derived modulus and hardness. Cyclic indentations had been conducted upon multilayers as discussed in the Nanoindentation chapter but had not shown a significant variation from cyclic indentations on single material layers.

To match the indentation setup, cyclic simulations were initially attempted with load-controlled definition. Unfortunately the load-controlled simulations were computationally slow and had trouble converging and so it was decided that depth controlled simulations would be conducted instead. This posed the problem that each load and unload step required a significant number of iterations to hone the depth to a correct load value. Although unfortunate and time consuming, this process was capable of converging while delivering time and load consistent curves. To better understand the effect of the multilayered structure we began by testing a single layer of aluminum (consisting of 51 identical Al layers) with and without viscous effects based on properties from literature.[91] The load versus displacement curves for these tests can be found in Figure 4.11 and Figure 4.12, respectively. All Figures for this section are displayed at the end of the section on pages 100-107. For clarity many of these results show both the full load vs. displacement curves and a zoomed in view of the hysteresis loop. The first simulation of an aluminum thin film with no viscous effects does not have a zoomed view as the second indentation is understandably the exact load curve as the unloading of cycle 1. With a purely elastic-plastic laminate there is minimal change in the loading behavior due to creep and with a single material we do not see the unloading plasticity under investigation. The modulus and hardness for this and the other cyclic simulations can be seen with respect to indentation cycle number in Figure 4.15. The results of the non-viscous aluminum are insignificant and intended as just a verification of the purely elastic-plastic material behaving as expected. Viscous aluminum shows a decrease in hardness due to the

increasing area under the indenter and the modulus gradually decreases as expected in a similar fashion to what was seen in the physical indentations.

The Al/SiC cyclic results were more significant and unexpected. For the non-viscous case we see the expected decrease in hardness, again due to constant peak load but increasing area under the indenter, and an increase in modulus that rapidly plateaus to a constant value. This plateau represents the decay of creep effects within the constituent materials, specifically aluminum, and the plasticity during unloading has begun to decay. This decay is illustrated in Figure 4.16 through Figure 4.18 that show a zoomed in view around the indenter to a depth of about 30 layers. Displayed is a color map of the PEEQ in the area of the laminate on a blue to red scale where red has been set as a maximum value above which white will be used. This scale is consistent between the three figures and is intended to highlight the regions in which the PEEQ is increasing for each cycle on the Al/SiC laminate. It can be seen that in the first and second cycle the PEEQ increases dramatically not only around the indentation site itself but deeper into the laminate structure. For cycle 1 this can be seen near the central axis for the 13th and 15th layer, within the body of the aluminum layers up to layer 15, and the top interface of the aluminum down to the 27th layer as shown with the yellow arrows. Similarly the growth in cycle 2 unload is apparent near the central axis for layers 9-25 and within the body for layers 9-25. However by the 8th cycle this effect has begun to saturate the laminate and therefore the change is only really prominent within the top 5 layers directly beneath the yellow arrow as can be seen by the white highlight bridging layer three. Visually the PEEQ increase is less dramatic deeper in the laminate, only exhibiting large increases of plastic strain near the indentation site itself where the small depth indentation still has a large effect on the material. It was unexpected for there still to be unloading plasticity in cycle 8 when the modulus had plateaued (Figure 4.15) however this did partially validate the concept showing that the unloading plasticity will decay with cyclic loading.

Another unexpected result was that of the viscous Al/SiC simulation. Upon introduction of viscous effects to the aluminum we expected that we would see similar results to that of the physical indentations however we saw an almost identical response to the non-viscous case. We are unsure why exactly this may be, but believe that it is one of two potential situations; a question which can be resolved with future investigation. The

first possibility is that the nanolaminate in the physical simulations was either not experiencing the unloading induced plasticity, or experiencing a small enough amount so as to show no discernable decaying response. This can be investigated through cyclic indentations at a lower load and microstructural characterization of the physical system. A second possibility is that there are viscous effects related to the SiC layers that were not anticipated and therefore not captured within the simulation. We consider this to be the more likely scenario as our SiC properties were defined based on crystalline SiC but we have seen amorphous SiC result from similar deposition situations previously.[25, 76] Amorphous SiC would have significantly different material properties and without further microstructural investigation we cannot say what effect this may propagate through the current simulation. We are encouraged, however, by the similarity of the simulated and physical indentation hysteresis loops. The loading response of physical cyclic indentation upon the 80nm Al/80nm SiC specimen is presented in Figure 4.19. In this experiment the indenter is held at the max load for a period to allow for creep to occur resulting in the horizontal portion at max load. This cannot be accomplished within the simulation as it is depth controlled rather than load controlled as discussed previously. Despite our limitation to depth-controlled simulation, however, the physical indentation shows a very similar trend within the hysteresis and is encouraging for future work.

As a side note, it is interesting to see a brief drop in the modulus results of both the viscous and elastic-plastic Al/SiC simulations (Figure 4.15). This happens to occur at an indentation depth of almost exactly 10% the multilayer thickness. We have not determined why this may be or why it occurs however there are occasional anomalies associated with the specific location of these indentations too. The process to find the max depth for each cycle, required many simulations be run to a range of max depths starting from the previous unload step. During this process graphing the resultant load for each max depth attempt was helpful to more efficiently narrowing down the correct depth for each step. Thereby, a curve of resultant max load vs. input max depth was formed for each cycle depth determination. However for some steps this curve was not monotonically increasing as would be expected. Rather, as can be seen in Figure 4.20, the curve occasionally exhibited inconsistent behavior with drastically irregular increases only to drop before increasing again making determination of a max depth highly difficult.

At this point we have abstained from conducting cyclic simulations upon a laminate with SiO₂ as a constituent material due to the fact that we have TEM characterization of the deposited SiO₂ clearly showing an amorphous structure. Apart from our indentation upon single material thin films we have little information about the potential mechanical properties and therefore we understand that we would encounter similar issues to those encountered modeling SiC. Being unable to certify the viscous properties of the SiO₂ we predict this analysis would thus yield little new information.

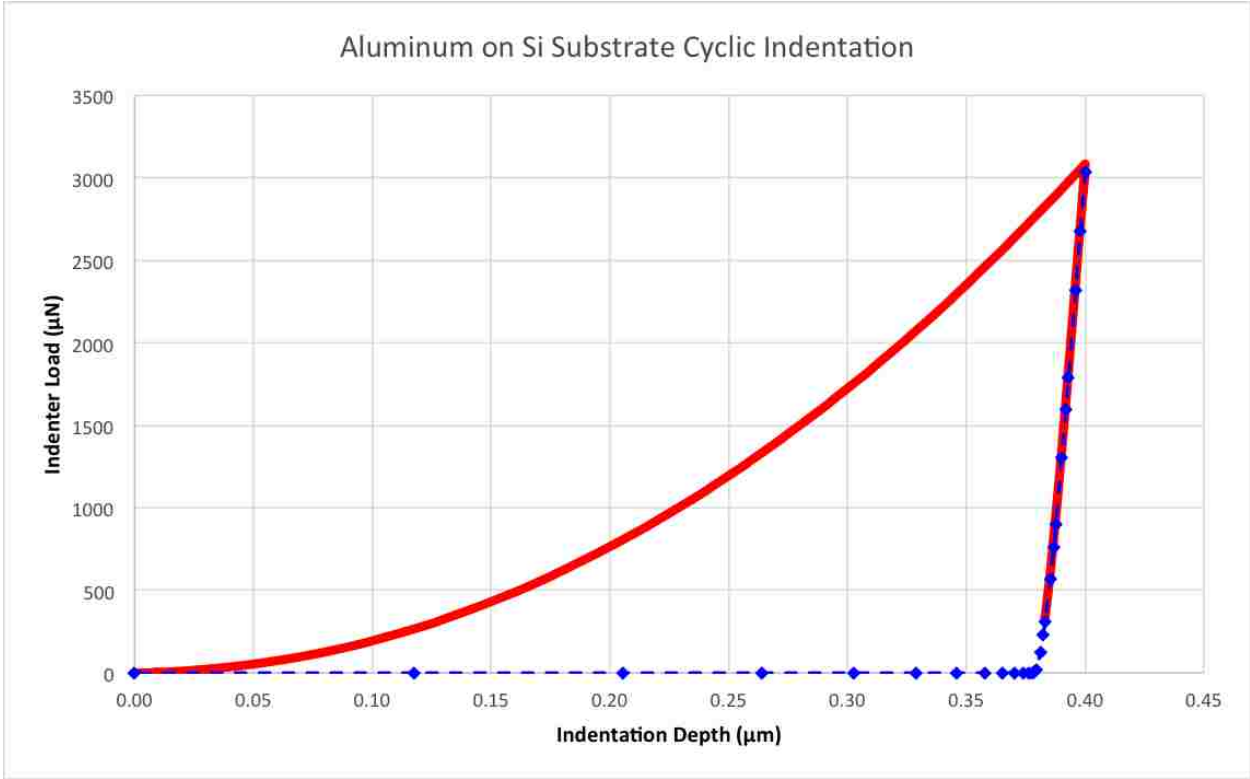


Figure 4.11 Load vs. displacement results from a cyclic indentation of 4.08µm thick Al layer upon a Si substrate. Modeled from 51 layer geometry but with all layers defined as Al with no viscous effects. First indentation cycle (unloading to 10% of full load) is shown in solid red while the second indentation cycle is shown in dashed blue. Second cycle follows first cycle unload perfectly.

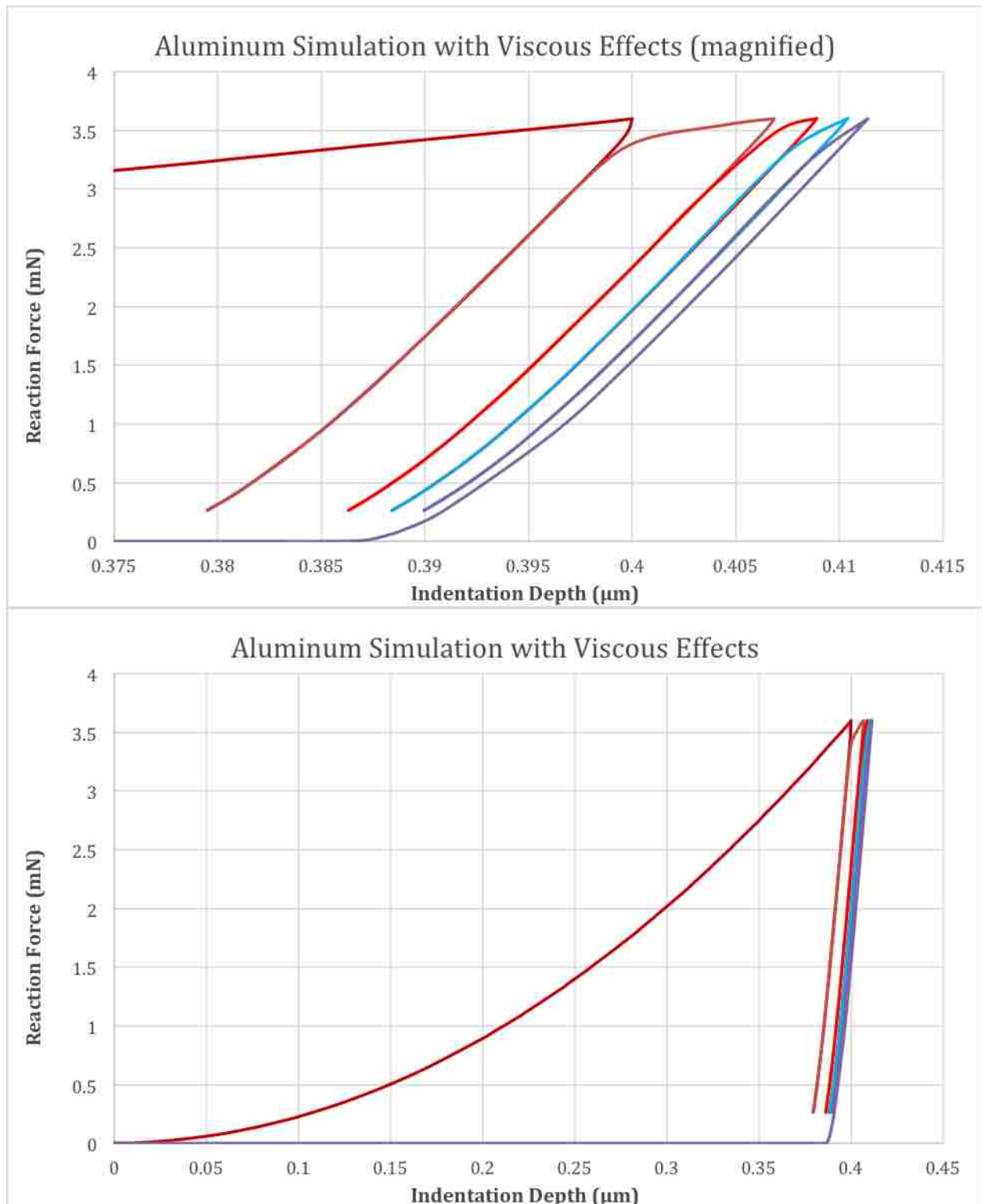


Figure 4.12 Cyclic load vs. displacement for a 4.08μm Al film including viscous properties upon Si substrate.

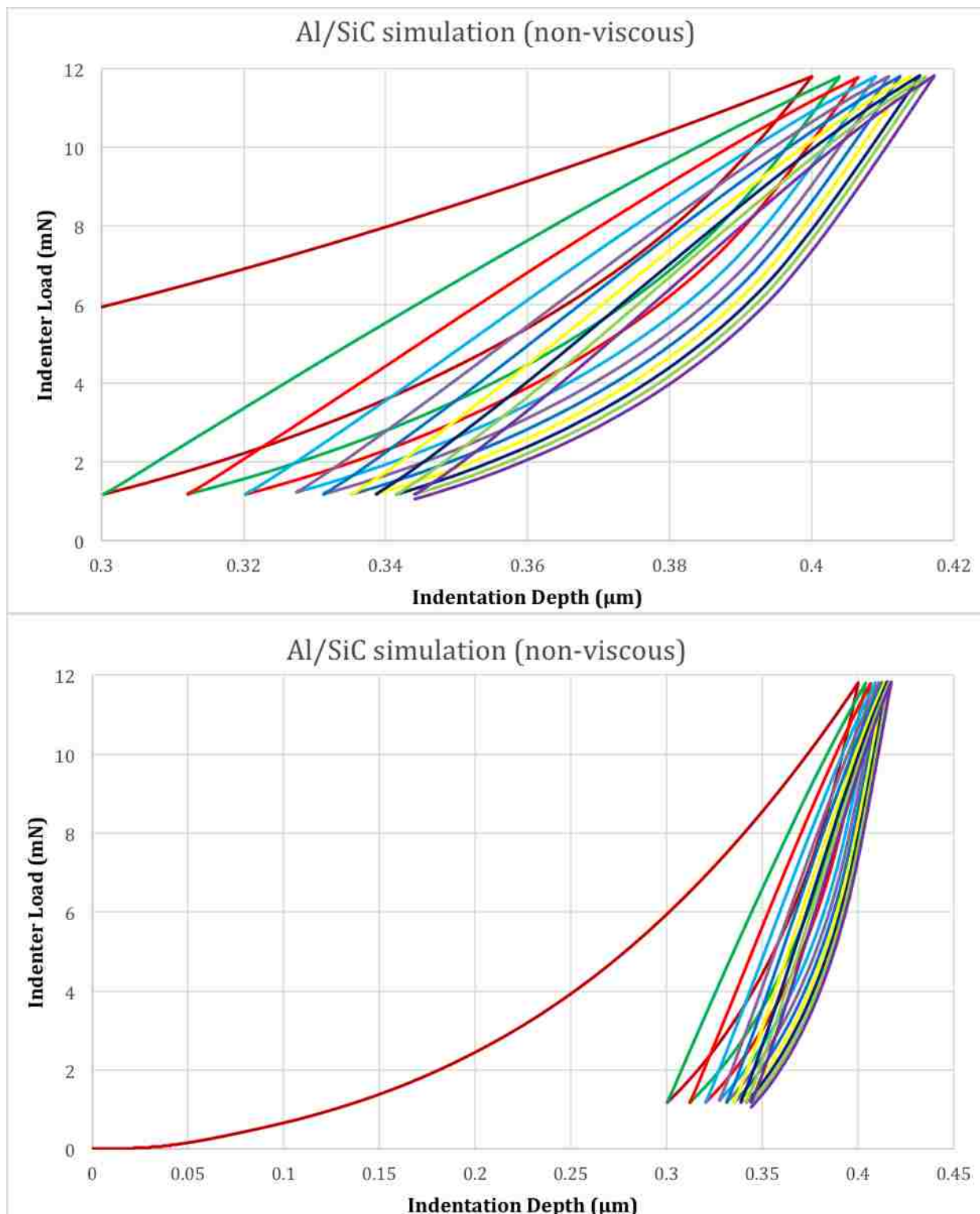


Figure 4.13 Cyclic load vs. displacement for a 51 layer nanolaminate with 26x purely elastic-plastic 80nm thick Al layers and 25x80nm thick SiC layers film upon Si substrate. Final unloading is not pictured, each cycle is depicted with a different color so as to better follow the hysteresis loops.

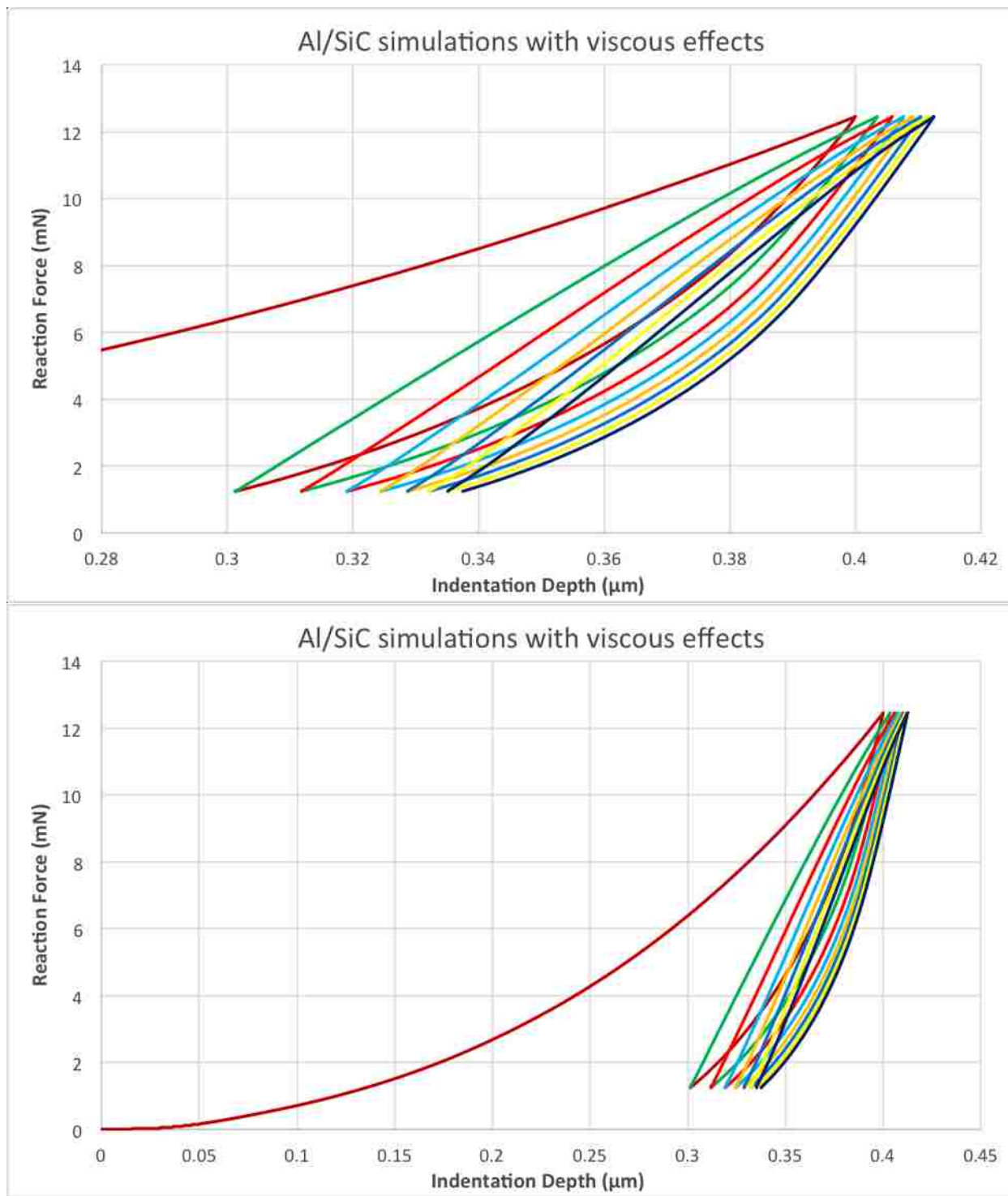


Figure 4.14 Cyclic load vs. displacement for a 51 layer nanolaminate with 26x80nm thick Al layers including viscous properties and 25x80nm thick SiC layers film upon Si substrate. Final unloading is not pictured, each cycle is depicted with a different color so as to better follow the hysteresis loops.

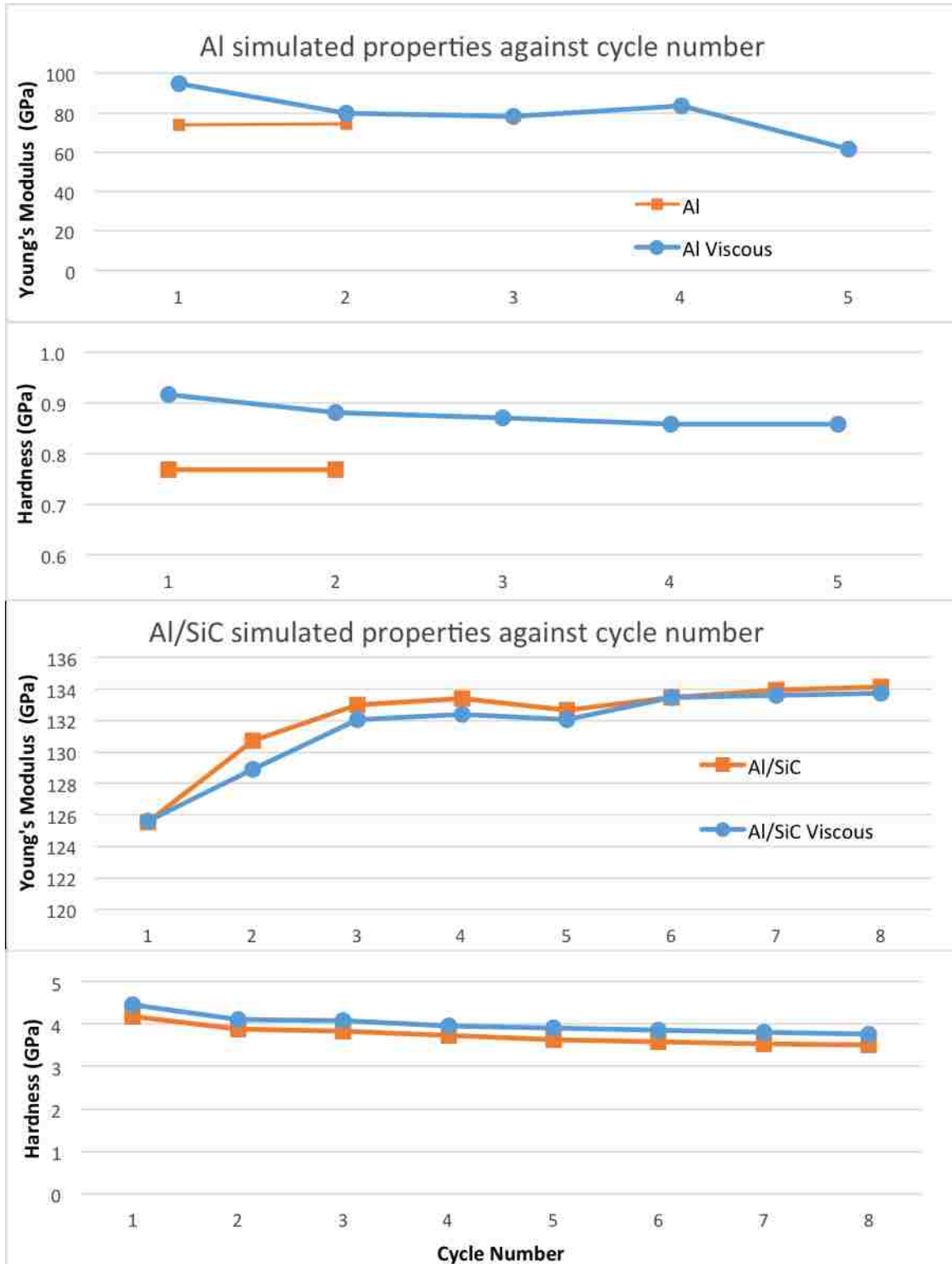


Figure 4.15 Modulus and hardness results against cycle number for the Al and Al/SiC cyclic simulations. Note the similarity in shape of trends and the final modulus value.

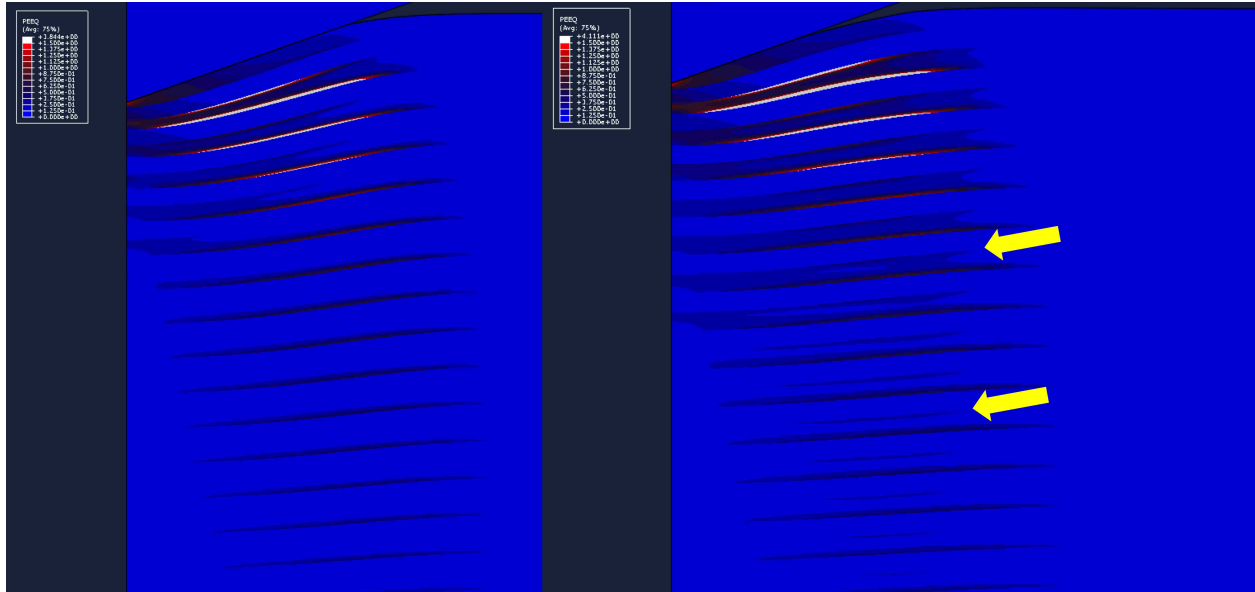


Figure 4.16 Unloading to 10% of full load for cycle 1 of simulated Berkovich indentation of 51 layer Al-SiC 80nm/80nm nanolaminate. Note increased PEEQ throughout the laminate as a whole, especially the aluminum layers 9-25 layer deep.

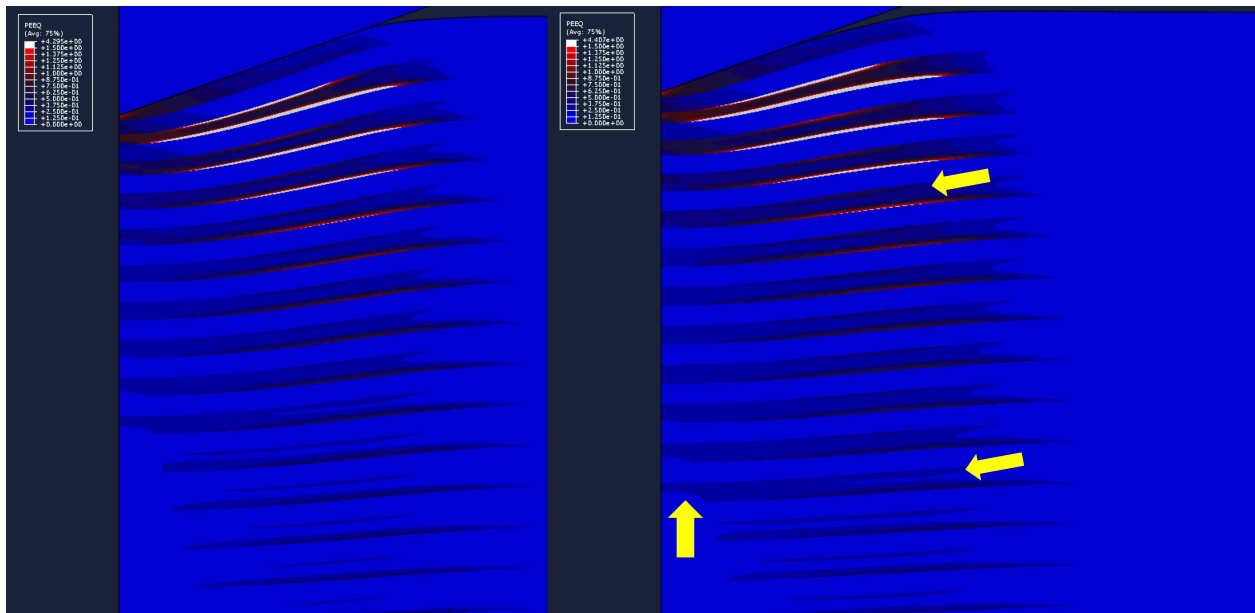


Figure 4.17 Unloading to 10% of full load for cycle 2 of simulated Berkovich indentation of 51 layer Al-SiC 80nm/80nm nanolaminate. Note increased PEEQ throughout the laminate as a whole, especially the aluminum layers 9-25 layer deep.

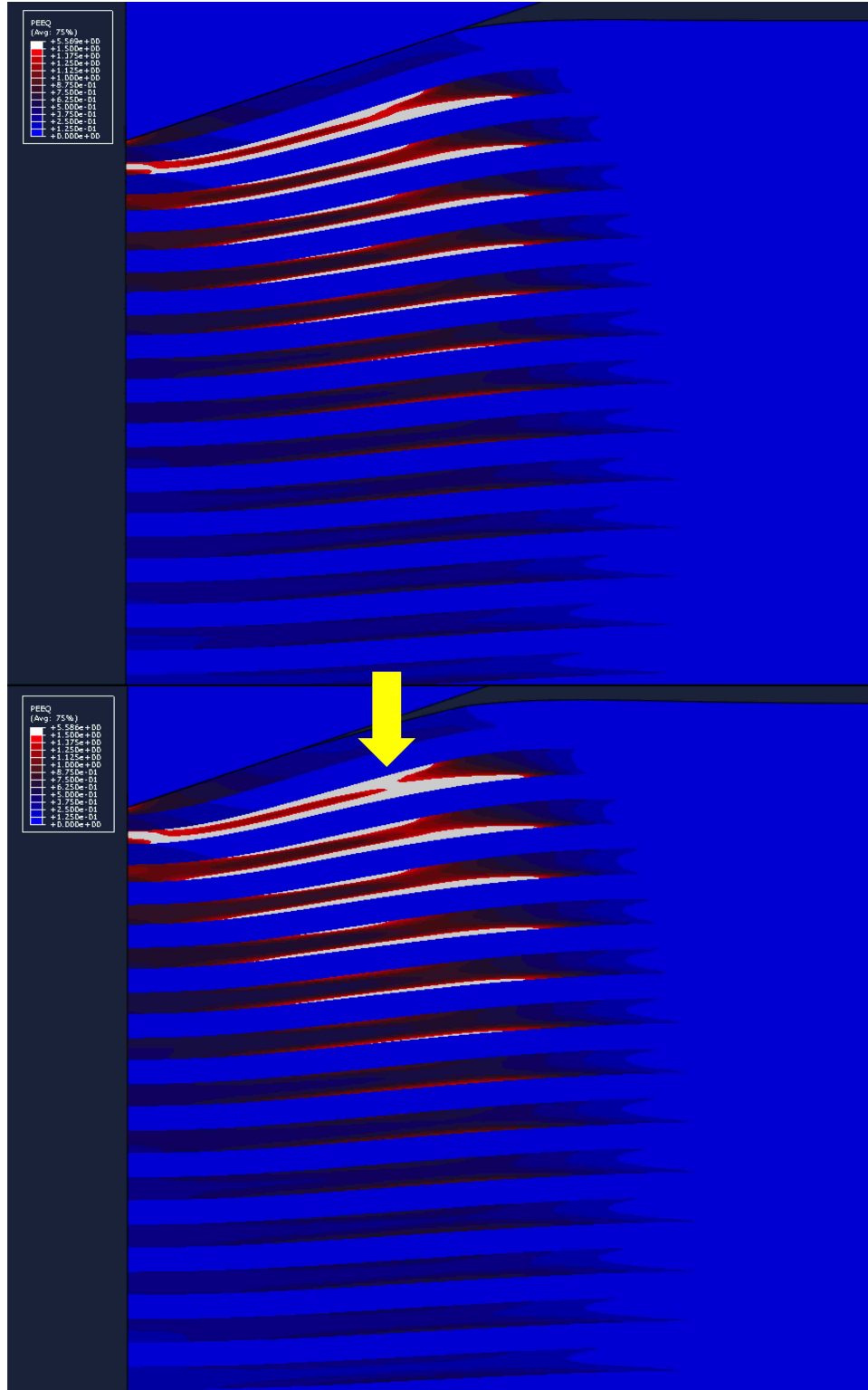


Figure 4.18 Unloading to 10% of full load for cycle 8 of simulated Berkovich indentation of 51 layer Al-SiC 80nm/80nm nanolaminate. Note that increased plasticity is largely localized close to the indenter rather than throughout the laminate structure.

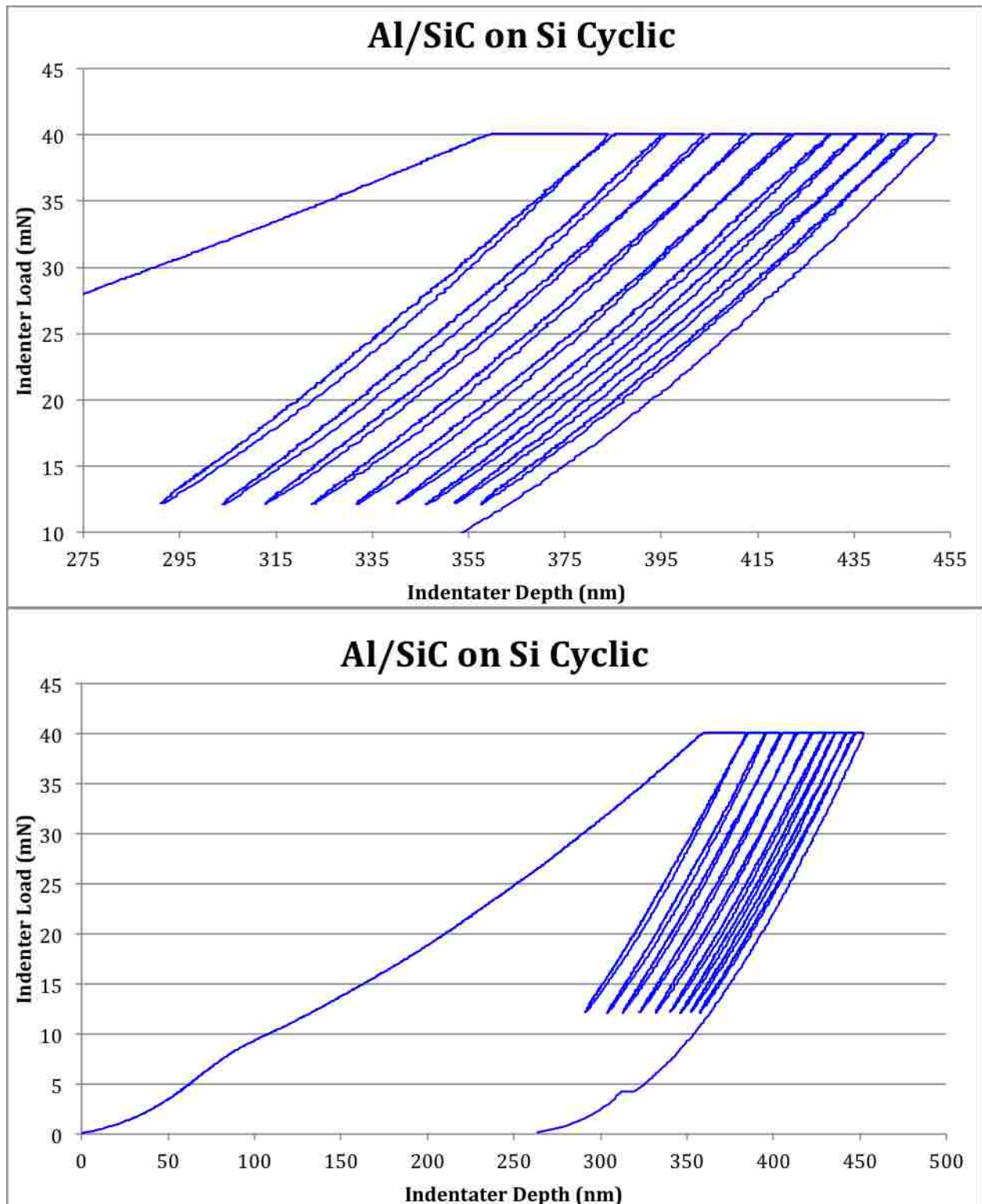


Figure 4.19 Cyclic indentation of 51 layer 80nm Al/80nm SiC nanolaminate with a Berkovich tip. Although difficult to see the hysteresis loop is similar to that seen in the simulations with less overlap and less curve due to the hold at max hold to take up the creep effects.

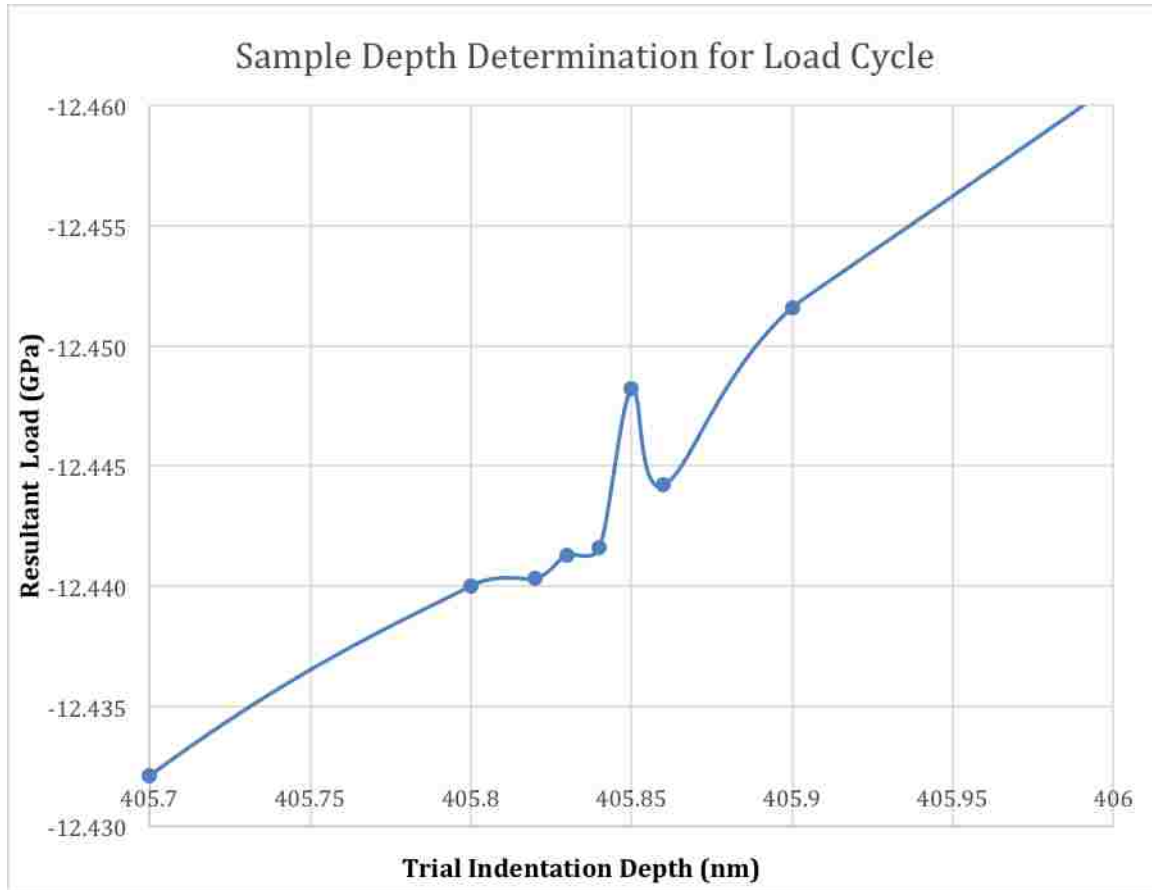


Figure 4.20 Sample curve of determination for the depth corresponding to a specific max load for a cycle within the Al/SiC multilayer simulation with viscous properties. Note the curve shows little consistency in slope and is not even monotonic as would be expected.

Chapter 5. Conclusions and Future Work

5.1. Conclusions

The majority of the conclusions we have drawn from our research are mentioned in the previous chapters, however, included here is a review of some more important findings. In particular we present the questions encountered that require future work to explain and observations of importance. After this section are several areas of future work that would be enlightening to pursue. Some of this can be completed more easily requiring only knowledge of the simulation and time while others are extensive such as the micropillar compression, which requires not only extensive time and equipment.

It should be noted that the deposition process and fabrication of multilayers appears to have gone well. Our samples are close to the intended thicknesses and appear to be of consistent structure. Furthermore the multilayer structures appeared to have a relatively small amount of undulation within the layers, a known problem resulting from the columnar growth of the Al where the waviness increases with each layer deposited and can result in serious variation of properties.[48, 50] This research would benefit significantly from microstructural characterization of these materials, however, the macrostructure appears to be consistent not only between single material thin films but also within the multilayered structures. This is important as it enables us to have confidence in the indentations and extract properties with low deviation.

The indentation results delivered were reliable only within a certain depth range. In order to improve this we suggest using a spherical indenter and performing all indentations within a short period of time beginning with calibration of the machine and verifying that the DAF with regular indentations upon the reference sample. Similarly choosing a smaller set of indentations to perform will preserve the tip of the indenter and minimize other errors related to time between initial calibration and final indentations. Our indentations were conducted over a period of a year and the amount of recalibration and therefore wear in the indenter was probably significant. This was also a potential source of error due to other users changing the indenter tip and potential damaging or altering the setup.

As a whole the results were what were expected. The quartz substrate was a poor sample for indentation but performed well as a substrate. The high stiffness of the Al sample surfaces was probably the single most difficult to manage as it persisted to a depth greater than anticipated and influenced all the multilayer results. Further microstructural and elemental analyses are required to get to the bottom of this. Another important conclusion about the material structure was that both the SiC and the SiO₂ are amorphous and therefore do not exhibit bulk crystalline properties, nor can bulk properties be assumed for simulations. This unknown structure and material properties make certification of our simulation results impossible however they appear to have a high consistency with the results of the multilayered indentations.

The multilayer indentations showed that there was good predictability for the properties of a nanolaminate by using the rule of mixtures and the indentation derived properties from single material films. This is a significant conclusion as it opens the possibility of fabricating single layer films, testing these films, and designing an applicable nanolaminate based on these results. This is important as fabrication is not only expensive and time intensive, but also fabrication of a multilayer requires a deposition chamber that can handle at least two material targets. The results of multilayered cyclic indentation did not show significant difference from the single material films and we cannot fully explain this behavior using the simulations without further characterization of the constituents. If there is in fact no plastic deformation during the unloading phase within the indentations this would be a significant finding as the simulations have a large amount of this effect even at low loads and the diffuse stress field of a spherical indenter. Again, additional characterization and imaging will need to be performed in order to support this.

The simulations appeared reliable with respect to previous findings and the trends of the cyclic indentation for single material were consistent with the physical results. However the cyclic simulations were not consistent with the indentation for the multilayer which we believe is most likely a result of the SiC being amorphous and having local viscous effects, a condition not present within the simulations. While more characterization of the ceramics would be useful for improving the simulations a less robust but faster method could be to estimate viscous properties and combined with the results of single material indentations run simulations to try and match the physical results.

One major process that was intended to bring light to the effects of unloading plasticity and the multilayer structure was micropillar compression. Although several pillars were fabricated we were unfortunately unable to conduct the compression tests intended due to imaging problems and time constraints on machinery. Micropillar compression is discussed in the next two sections as a potential investigation for the future.

5.2. Introduction to Micropillar Compression

Many methods of nanomechanical characterization have been the center of increasing focus as the pursuit of nanomaterials has advanced. These methods are necessary for testing materials with a small volume and therefore critical to characterizing a wide variety of materials with novel applications. Often these methods are minimally invasive and as such can also be used to test specimen within the intended lifespan of the specimen therefore allowing for continued use while verifying reliability. Similarly these methods characterize site specific mechanical properties on a micro or nanoscale. This is particularly useful for determining properties of constituent materials for modeling a larger composite within simulations as will be discussed in Chapter 4.

Instrumented indentation, as discussed in Chapter 3 is the most common of nanomechanical characterization methods as it requires relatively little sample preparation. Other methods include micropillar compression involving a pillar of material compressed by a flat punch. This is inherently a compressive test only however and it is often important to study the tensile behavior of materials especially in when studying brittle materials as compressive stresses are known to decrease crack propagation. Popular techniques for applying tensile stresses are single cantilever bending,[9, 16, 29, 121-123] clamped beam bending,[9, 124, 125] double cantilever compression,[9, 126] and pillar splitting.[9, 73] It should be noted these all rely upon geometrically derived tensile stresses by a compressive load. Novel tests such as the one in Figure 5.1(right) utilize a bone shaped cantilever pulled by a C shaped indenter tip have been used to demonstrate a purely tensile test on a micro scale.[127]

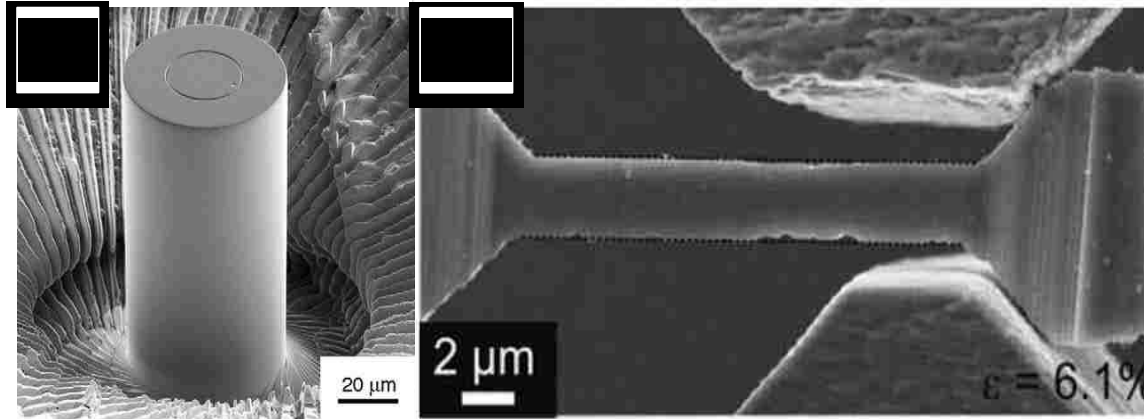


Figure 5.1 Micropillar and Dogbone Cantilever (from [127, 128])

Of these characterization techniques the most feasible for use in this thesis is that of micropillar compression. The size constraint on many techniques excludes them from being used in our study where the max height of multilayer structures was expected to be approximately 4 μm. Micropillar compression can be conducted on a much smaller sample than cantilever bending or pulling however as such was investigated. There are many techniques for pillar fabrication including focused ion beam (FIB) milling, lathe milling, lithography, and selective etching. The scale of our materials made chemical methods such as lithography and selective etching largely unreasonable. Lathe milling is a fairly popular method allowing pillars to be made with very little taper, which is ideal.[51, 128, 129] This involves a sample milled at low incident angle and rotated in small increments, however, there are drawbacks affiliated with lathe milling such as increased FIB damage, redeposition, and fabrication time, which can be more detrimental than the small amount of taper retained using the annular milling from FIB.[57] The most popular method and the one intended for use in this thesis is that of the focused ion beam milling. This entails FIB removal of material in an annular pattern thus resulting in a free standing pillar.[51, 75, 76, 84, 89, 130] In the case of thin films, the FIB is used to mill through film material until the substrate is reached. Therefore when the pillar is compressed the resultant analysis can take only the thin film into account and substrate effect can be ignored.

5.3. Micropillars and FIB with Ga Ions

Based on the advantage of micropillar compression to provide analysis free of substrate effect it was selected for application in the study of this thesis. For the reasons outlined above FIB milling was chosen as the fabrication technique. One concern with FIB milling is the damage incurred by ion beam upon the pillar therefore lowering accuracy of the compression test. Ion beam irradiation has been shown to introduce microstructural changes to the milled surface which in turn can affect the mechanical properties of said material.[81, 82, 130] Damage is accumulated based on the bombardment of the ions and the chemistry of ions used. When the beam of ions impact the pillar sidewall the high kinetic energy of ions leads to a higher concentration of defects such as dislocation loops, implanted ions, self-interstitials, and vacancies,[115] as well as a thin amorphized layer. [57, 127]

Gallium, Helium, and Xenon are the most widely used ion sources for FIB milling, each with specific benefits and drawbacks. The most common of these by far and the source used at the Center for Integrated NanoTechnologies is Gallium (Ga). Unfortunately Ga is reactive and therefore implanted ions form alloys locally with wall materials, especially metals.[76] In our circumstance this is of particular concern as it means the aluminum will be susceptible to Ga liquid metal embrittlement.[131-133]

During initial investigation and planning of the project proposal Ga liquid metal embrittlement was considered to be an acceptable concern. It was decided micropillar compression testing offered a unique opportunity to identify the true multilayer coating modulus. Micropillars of the layered coatings were to be milled using FIB and then used compression testing (using a flat head indenter) inside an SEM chamber. Digital image correlation (DIC) technique was to be used to capture the full strain field over the pillar surface enabling extraction of Young's modulus of the multilayer where the substrate effects will be eliminated by direct measurement of strain field. Thus based on the clear advantages of using micropillar compression and digital image correlation to determine mechanical properties in a manner inherently free from the substrate effect, a series of micropillar compressions was planned. Upon further investigation it was found that studies characterizing the Ga concentration at embrittled boundaries show concentrations of approximately 10-25 wt.% Ga depending on the pillar diameter.[134]

However other sources have suggested that the penetration depth of Ga may be <60nm for a beam at 30 kV[81, 135] which would be a small volume for a micropillar of diameter 1-2 μ m. Another group conducted micropillar compression tests on Al/SiC nanolaminates of 40 alternating \sim 60nm layers of Al and SiC[14] and argued that for very small diameters in monolithic materials approaching the 50–60 nm damage depth, ion beam-induced surface damage might have an influence on the micropillar compression behavior[116]. In nanolaminates, the micropillar diameter does not influence the flow stress significantly,[51] since the characteristic length scale that controls the mechanical response, the layer thickness, is much smaller than the micropillar diameter.[75] They concluded that micropillar compression tests are a critical tool for characterizing the mechanical performance of nanoscale multilayers with limited interface strength. However there main suggestion was that they found interfacial slip in micropillars that was not possible in nanoindentation when the layers were constrained by the surrounding undeformed material.[75]

We believe that micropillar compression is an adequate process by which to capture the strain field within the nanolaminate in order to more accurately remove the substrate effect from the modulus calculation. Furthermore this style of characterization will allow us to see what occurs within the nanolaminate during compression. We will be able to look directly at the interfaces between material as well as at the structure of each layer during loading. Finally the micropillar test should demonstrate whether the unloading plasticity is an artifact of indentation only or if it is present in the layers on a broader scale when a less violent stress situation is present. As it stands our understanding of the unloading plasticity is that it is localized around the indentation site however we have no manner of determining if that is solely due to the intensity of the stress when the indenter is removed or if this would be a mechanism present on a larger scale when more uniform loading occurs.

5.4. Microstructural Characterization

Potentially the single most important work yet to be conducted is the microstructural characterization of the deposited materials. Without proper understanding of the material structures we cannot estimate the properties of these materials or anticipate how they

interact with each other in the large nanolaminate structure. The first step would be to investigate the growth the aluminum oxide upon the exposed aluminum surfaces. Determining the rate of growth along with the maximum and nominal thickness of the alumina will allow us to better understand the aluminum thin films. This is critical on multiple levels, first it will enable a better estimate of the aluminum properties that would exist within the embedded layers of the nanolaminate. Currently we know that the aluminum grows in a columnar grain structure but do not know the variation in the modulus or hardness of these grains. Second, this would allow better understanding of the contribution of the alumina to the properties derived from indenting the nanolaminate structures. This second point is of critical importance as if the indenter is behaving in a manner other than that expected in nanoindentation theory our results will contain major errors.

The other materials that need to be investigated are the SiC and SiO₂. Currently our only insight into the structure of the SiC is from previous work conducted by others and as such imaging our current batch depositions will enable a better estimate of the modulus and also lead to prediction of the viscous properties. The viscous properties are of particular note as they will help the evolution of our finite element model as we strive to find a computational method for predicting the composite properties of hard soft multilayers. Microstructural characterization of the SiO₂ would have the same effect, enabling us to broaden or simulation's scope to include other materials. Currently the rule of mixtures estimate from single thin film indentation is a good estimate for the modulus for this system however the larger picture is still obfuscated and the mechanisms at work within the multilayer structure are unknown.

5.5. Adapted Simulations and Comparison to Indentation

The current simulations include material properties that were used in previous work or derived from bulk material. Future work should include the application of the indentation-derived properties of the single material thin films and substrates. With these updated material properties it would be possible to verify if the simulations return the results seen from indentation and may lead to improving the basic simulation or understanding a mechanism of the indentation we have not anticipated. One particular area of interest that

either the previously mentioned microstructural characterization or improved modeling could explain is the increasing modulus of SiO₂ at low loads as seen in Figure 3.21.

Furthermore, the work we have completed so far is more to verify the modeling and attempt to duplicate physical indentations so as to study the indentation mechanics more robustly. Application of the indentation derived properties may lead to novel simulation findings or the ability to predict the behavior and properties of the laminate as a whole allowing for improved designability of hard/soft multilayers whereby the application of said layers may become more feasible without extensive testing required.

5.6. Spherical indentations

We would like to conduct more spherical indentations in order to compare the results with the Berkovich indentations. As discussed before the Berkovich indenter has a significantly sharper stress field. Indentations using a spherical indenter, particularly cyclic indentations may be helpful in determining the role of unloading induced plasticity in the determination of mechanical properties and give insight into the process of this plasticity in general. Unfortunately the aluminum oxide growth will likely effect the spherical indenter even more than the Berkovich when testing the multilayers as the indenter may test a shallower depth than the Berkovich indenter.

5.7. SiC and SiO₂ viscosity and Al/SiO₂ cyclic simulations

As mentioned previously one major improvement to the modeling attempt would be that of determining the viscous properties of the two ceramic materials. By characterizing the physical properties of the SiC and SiO₂ the mechanical properties of these and the aluminum could be programmed into the simulation to determine if the simulation results match the physical results. If not the simulation likely needs to be adapted to include other considerations. If the simulation does match the results of the physical indentations then the simulation can be used to understand the mechanisms at work within the multilayer as indentation occurs. This would be highly enlightening and open the door to many potential insights that can then be tested and potentially verified using post-indentation imaging. Similarly if the viscous effects of the SiO₂ can be understood the model can be expanded to

a larger variety of materials, potentially leading to commercial development and implementation for design of high performance coatings.

5.8. Delamination concerns/void growth

Serious consideration was given to the possibility of delamination or void nucleation and propagation occurring either between layers or between the film and substrate. During indentation of the multilayers we became aware of an odd artifact in the load versus displacement curves as shown in Figure 5.2. It can be seen that there is a change in the loading rate at about 75nm of indentation depth on all samples. This behavior is commonly an indication of delamination[86] and so the initial concern was that delamination may be occurring. However for this to be the case delamination would likely be occurring during indentation somewhere between the second and sixth layers. We could see no presence of delamination in the multilayer that was imaged using TEM and this artifact was almost perfectly consistent in the loading curve instead of appearing at different loads and depths depending upon the indentation. Furthermore this effect appeared upon some indentations of single material films as can be seen in Figure 5.3 at right. This evidence led us to the conclusion that it could not be the result of delamination, although there was no investigation directly into this phenomenon, and so we searched for another explanation. Figure 5.3 at left was the same sample of SiC as in the image at right and did not exhibit this loading rate change which led to the idea that this was an effect that started after a certain date and persisted from then on. Logically this would imply damage to the indenter tip which could be sustained through blunting or side impact. If the indenter tip was seriously deformed this would be a significant problem as the deformed indenter would need to be used to create a second DAF file or the tests would need to be redone. However it was determined that the indenter shape was not compromised by running indentations on the fused silica and comparing those to the indentations used in creating the DAF. As can be seen in Figure 5.4 there was no difference in the shape of the loading curves for the DAF and the verification indentations. This artifact is as of yet unexplained but merits investigation to determine why this may be occurring especially because it is not a consistent occurrence.

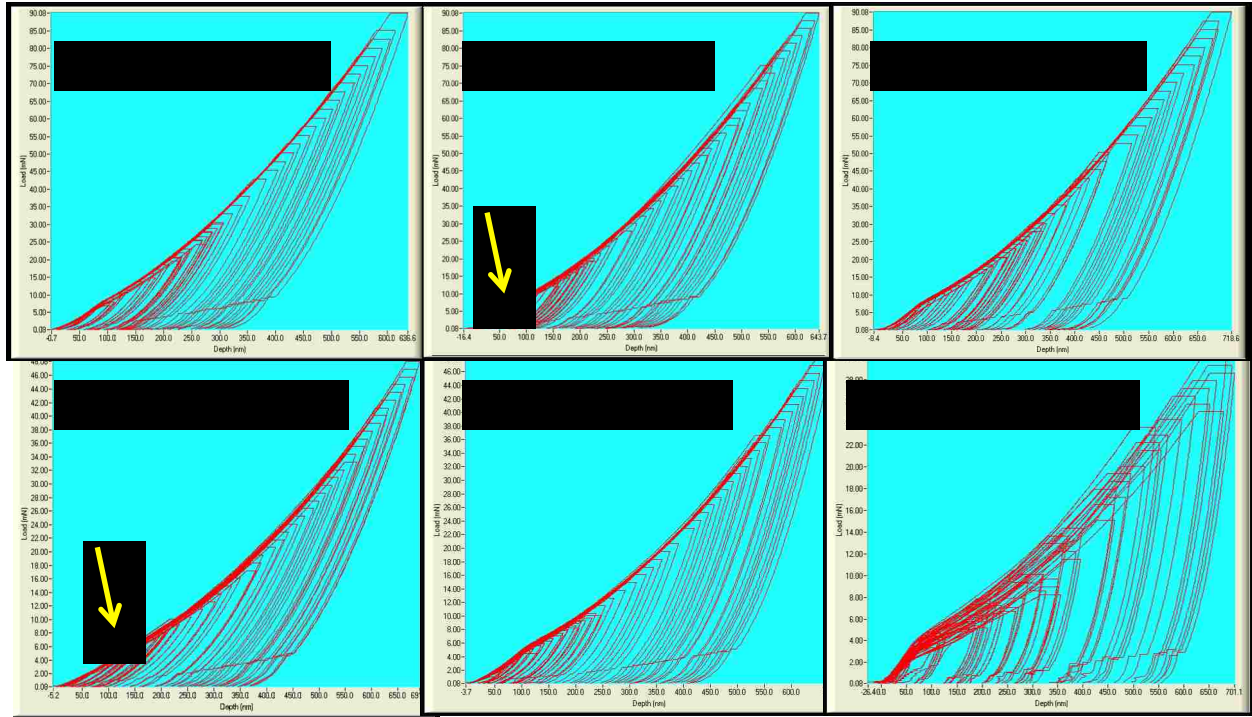


Figure 5.2 Load vs. displacement curves for many indents on the nanolaminate structures all of which show a significant and abrupt change in the loading rate at about 75nm of indentation depth.

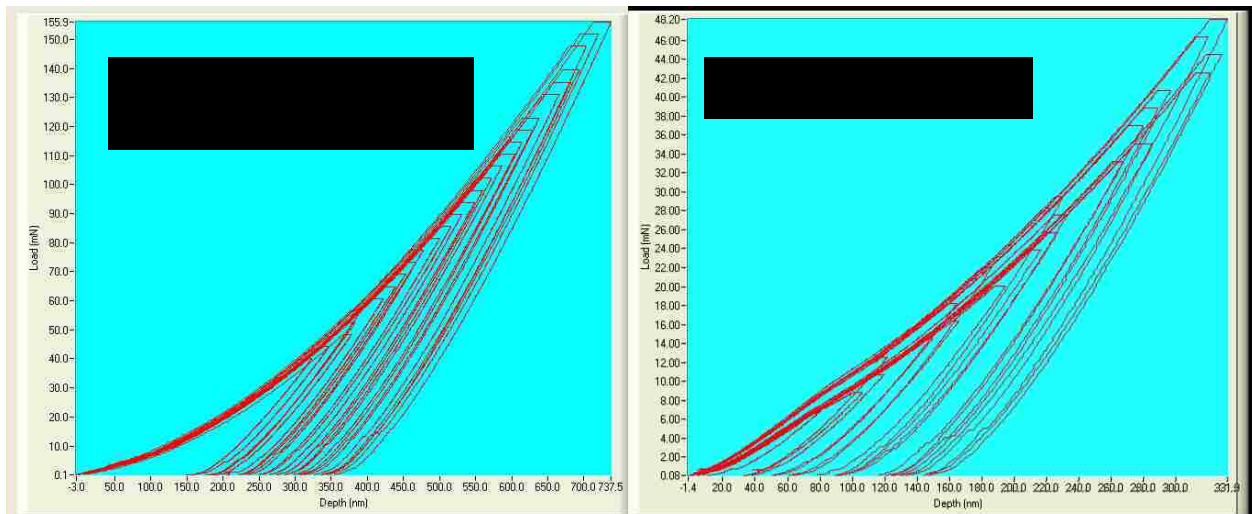


Figure 5.3 Load vs. displacement curves for a specific SiC sample that did not show the loading rate change during one set of indentations (left) but did in another (right).

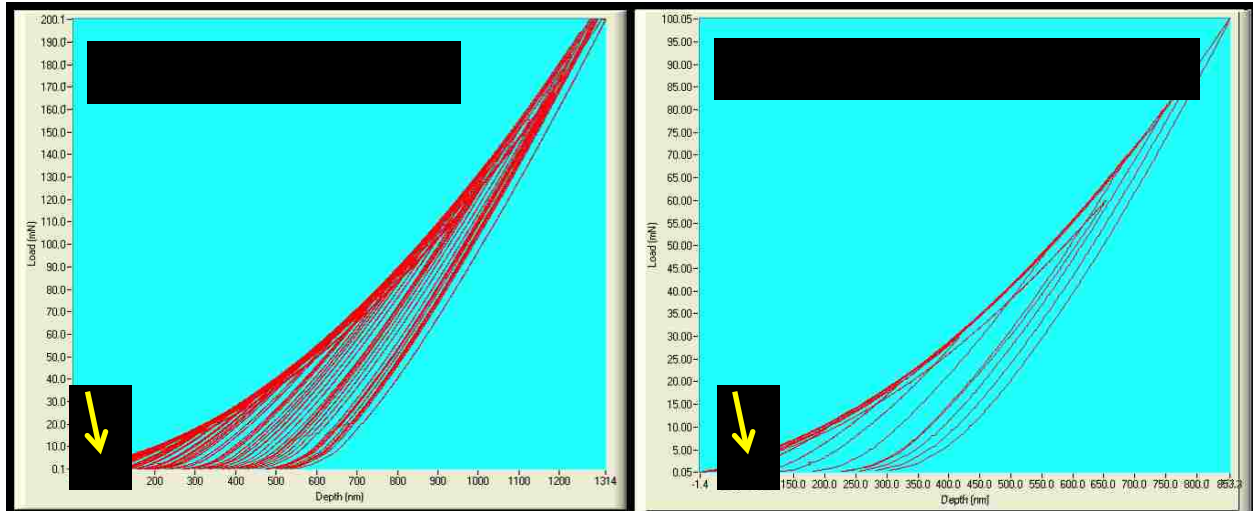


Figure 5.4 Load vs. displacement curves for fused silica. At left are the original indentations used to create the DAF file, at right are tests completed after all other indentation were completed that show the exact same loading curve shape. Neither of these sets of indentations exhibited the loading rate change discussed.

APPENDIX A: Sample Code - Berkovich Indentation of 80nm Al/80nm SiC

Within this appendix can be found a sample indentation code for a single depth controlled load cycle Berkovich indentation of an 80nm Al/80nm SiC nanolaminate upon an Si Wafer. Editing this code and/or exchanging portions for code found in the following appendices allows for spherical all variables included in this thesis to be accomplished.

```
*HEADING
80/80 Al/SiC Conical Indentation Cyclic with viscous effect
*preprint, echo=no, model=no, history=no
*****
**NODE DEFINITIONS
*****
** MULTILAYER CORNERS
*node
1000001, 0, 0
1001001, 15, 0
2001001, 40, 0
1510511, 0, 4.08
1511511, 15, 4.08
2511511, 40, 4.08
899901, 0, -36
900901, 15, -36
1900901, 40, -36
**
** FILL SIDES
*NGEN, nset=left1
899901, 1000001, 1001
*NGEN, nset=left2
1000001, 1510511, 1001
*NGEN, nset=right1
900901, 1001001, 1001
*NGEN, nset=right2
1001001, 1511511, 1001
*NGEN, nset=farright1
1900901, 2001001, 1001
*NGEN, nset=farright2
2001001, 2511511, 1001
*NSET, NSET=LEFT, GENERATE
899901, 1510511, 1001
*NSET, NSET=RIGHT, GENERATE
900901, 1511511, 1001
*NSET, NSET=FARRIGHT, GENERATE
1900901, 2511511, 1001
** FILL LAYER CENTER
*nfill, bias=0.998, nset=alln
left,right,1000,1
**
*NSET, nset=bottom, generate
899901, 900901, 10
```

```

*NSET, nset=surf-top, generate
1510511, 1511511, 1
**
**
** INDENTER CORNERS
*node
** LEFT side indenter
** LEFT side indenter
3000001, 0.000, 4.081
3004901, 0.000, 4.131
3009901, 0.000, 5.200
** RIGHT side indenter
3000100, 2.792, 5.081
3005000, 2.792, 5.131
3010000, 2.792, 5.200
**
** FILL INDENTER SIDES
*NGEN, nset=ind-left-low
3000001, 3004901, 100
*NGEN, nset=ind-left-top
3004901, 3009901, 100
*NGEN, nset=ind-right-low
3000100, 3005000, 100
*NGEN, nset=ind-right-top
3005000, 3010000, 100
**
** FILL INDENTER CENTER
*NSET, nset=indleft, generate
3000001, 3009901, 100
*NSET, nset=indright, generate
3000100, 3010000, 100
*nfill, bias=0.95
indleft, indright, 99, 1
**
** INDENTER NODE SETS
*nset, nset=indall, generate
3000001, 3010000, 1
*nset, nset=indtop, generate
3009901, 3010000, 1
*nset, nset=indbot, generate
3000001, 3000100, 1
*nset, nset=indtip
3010000
*nset, nset=indtop-1, generate
3009901, 3009999, 1
**
**Interface Constraint Node Sets
*NGEN, nset=bot1
1000002, 1000010, 1
*NGEN, nset=bot2
1000012, 1000020, 1
*NGEN, nset=bot3
1000022, 1000030, 1
*NGEN, nset=bot4
1000032, 1000040, 1

```


*NGEN, nset=bot5
1000042, 1000050, 1
*NGEN, nset=bot6
1000052, 1000060, 1
*NGEN, nset=bot7
1000062, 1000070, 1
*NGEN, nset=bot8
1000072, 1000080, 1
*NGEN, nset=bot9
1000082, 1000090, 1
*NGEN, nset=bot10
1000092, 1000100, 1
*NGEN, nset=bot11
1000102, 1000110, 1
*NGEN, nset=bot12
1000112, 1000120, 1
*NGEN, nset=bot13
1000122, 1000130, 1
*NGEN, nset=bot14
1000132, 1000140, 1
*NGEN, nset=bot15
1000142, 1000150, 1
*NGEN, nset=bot16
1000152, 1000160, 1
*NGEN, nset=bot17
1000162, 1000170, 1
*NGEN, nset=bot18
1000172, 1000180, 1
*NGEN, nset=bot19
1000182, 1000190, 1
*NGEN, nset=bot20
1000192, 1000200, 1
*NGEN, nset=bot21
1000202, 1000210, 1
*NGEN, nset=bot22
1000212, 1000220, 1
*NGEN, nset=bot23
1000222, 1000230, 1
*NGEN, nset=bot24
1000232, 1000240, 1
*NGEN, nset=bot25
1000242, 1000250, 1
*NGEN, nset=bot26
1000252, 1000260, 1
*NGEN, nset=bot27
1000262, 1000270, 1
*NGEN, nset=bot28
1000272, 1000280, 1
*NGEN, nset=bot29
1000282, 1000290, 1
*NGEN, nset=bot30
1000292, 1000300, 1
*NGEN, nset=bot31
1000302, 1000310, 1
*NGEN, nset=bot32

1000312, 1000320, 1
*NGEN, nset=bot33
1000322, 1000330, 1
*NGEN, nset=bot34
1000332, 1000340, 1
*NGEN, nset=bot35
1000342, 1000350, 1
*NGEN, nset=bot36
1000352, 1000360, 1
*NGEN, nset=bot37
1000362, 1000370, 1
*NGEN, nset=bot38
1000372, 1000380, 1
*NGEN, nset=bot39
1000382, 1000390, 1
*NGEN, nset=bot40
1000392, 1000400, 1
*NGEN, nset=bot41
1000402, 1000410, 1
*NGEN, nset=bot42
1000412, 1000420, 1
*NGEN, nset=bot43
1000422, 1000430, 1
*NGEN, nset=bot44
1000432, 1000440, 1
*NGEN, nset=bot45
1000442, 1000450, 1
*NGEN, nset=bot46
1000452, 1000460, 1
*NGEN, nset=bot47
1000462, 1000470, 1
*NGEN, nset=bot48
1000472, 1000480, 1
*NGEN, nset=bot49
1000482, 1000490, 1
*NGEN, nset=bot50
1000492, 1000500, 1
*NGEN, nset=bot51
1000502, 1000510, 1
*NGEN, nset=bot52
1000512, 1000520, 1
*NGEN, nset=bot53
1000522, 1000530, 1
*NGEN, nset=bot54
1000532, 1000540, 1
*NGEN, nset=bot55
1000542, 1000550, 1
*NGEN, nset=bot56
1000552, 1000560, 1
*NGEN, nset=bot57
1000562, 1000570, 1
*NGEN, nset=bot58
1000572, 1000580, 1
*NGEN, nset=bot59
1000582, 1000590, 1

*NGEN, nset=bot60
1000592, 1000600, 1
*NGEN, nset=bot61
1000602, 1000610, 1
*NGEN, nset=bot62
1000612, 1000620, 1
*NGEN, nset=bot63
1000622, 1000630, 1
*NGEN, nset=bot64
1000632, 1000640, 1
*NGEN, nset=bot65
1000642, 1000650, 1
*NGEN, nset=bot66
1000652, 1000660, 1
*NGEN, nset=bot67
1000662, 1000670, 1
*NGEN, nset=bot68
1000672, 1000680, 1
*NGEN, nset=bot69
1000682, 1000690, 1
*NGEN, nset=bot70
1000692, 1000700, 1
*NGEN, nset=bot71
1000702, 1000710, 1
*NGEN, nset=bot72
1000712, 1000720, 1
*NGEN, nset=bot73
1000722, 1000730, 1
*NGEN, nset=bot74
1000732, 1000740, 1
*NGEN, nset=bot75
1000742, 1000750, 1
*NGEN, nset=bot76
1000752, 1000760, 1
*NGEN, nset=bot77
1000762, 1000770, 1
*NGEN, nset=bot78
1000772, 1000780, 1
*NGEN, nset=bot79
1000782, 1000790, 1
*NGEN, nset=bot80
1000792, 1000800, 1
*NGEN, nset=bot81
1000802, 1000810, 1
*NGEN, nset=bot82
1000812, 1000820, 1
*NGEN, nset=bot83
1000822, 1000830, 1
*NGEN, nset=bot84
1000832, 1000840, 1
*NGEN, nset=bot85
1000842, 1000850, 1
*NGEN, nset=bot86
1000852, 1000860, 1
*NGEN, nset=bot87

```

1000862, 1000870, 1
*NGEN, nset=bot88
1000872, 1000880, 1
*NGEN, nset=bot89
1000882, 1000890, 1
*NGEN, nset=bot90
1000892, 1000900, 1
*NGEN, nset=bot91
1000902, 1000910, 1
*NGEN, nset=bot92
1000912, 1000920, 1
*NGEN, nset=bot93
1000922, 1000930, 1
*NGEN, nset=bot94
1000932, 1000940, 1
*NGEN, nset=bot95
1000942, 1000950, 1
*NGEN, nset=bot96
1000952, 1000960, 1
*NGEN, nset=bot97
1000962, 1000970, 1
*NGEN, nset=bot98
1000972, 1000980, 1
*NGEN, nset=bot99
1000982, 1000990, 1
*NGEN, nset=bot100
1000992, 1001000, 1
**sets from 1000001 to 1001001
*NGEN, nset=right_bond
1001001, 1511511, 1001
**for the time being we will not deal with the linear constraint
**of the right/center edge as it is far enough from indentation
**
*****
**ELEMENT INFORMATION
*****
**
**INDENTER ELEMENTS
*element, type=cax4
3000001, 3000001, 3000002, 3000102, 3000101
*elgen, elset=indenter_el
3000001, 99, 1, 1, 99, 100, 99
**
*****
*** some tip-tip elements, make them rigid *****
*****
*elset, elset=indtip_el
3000001
3000002
3000003
3000004
3000005
3000006
3000007
3000008

```

```

3000009
3000010
3000011
3000012
3000100
3000101
3000102
3000199
3000200
3000298
*****
*****
**
**
**
** MULTILAYER ELEMENTS
*element, type=cax4
900000, 899901, 899911, 900912, 900902
*elgen, elset=small_substrate_el
900000, 100, 10, 10, 100, 1001, 1000
*element, type=cax4
1000000, 1000001, 1000002, 1001003, 1001002
*elgen, elset=small_layers_el
**1000000, 1000, 1, 1, 505, 1001, 1000 (for 4.04)
1000000, 1000, 1, 1, 510, 1001, 1000
**1000000, 1000, 1, 1, 515, 1001, 1000 (for 4.12um)
*element, type=cax4
1900000, 900901, 1900901, 1910911, 910911
*elgen, elset=farright_sub_el
1900000, 1, 1, 1, 10, 10010, 1
*element, type=cax4
**1900101, 1001001, 2001001, 2006006, 1006006 (for 4.04)
1900101, 1001001, 2001001, 2011011, 1011011
** 1900101, 1001001, 2001001, 2016016, 1016016 (for 4.12um)
*elgen, elset=farright_al_el
1900101, 1, 1, 1, 26, 20020, 2
*element, type=cax4
**1900102, 1006006, 2006006, 2021021, 1021021 (for 4.04)
1900102, 1011011, 2011011, 2021021, 1021021
**1900102, 1016016, 2016016, 2021021, 1021021 (for 4.12um)
*elgen, elset=farright_cer_el
1900102, 1, 1, 1, 25, 20020, 2
**startnode, #ofelem horiz, node inc, el inc, #ofelem vert, nodeinc, elinc
** Define Element Sets
**
**
**
**GENERATE ELEMENT SETS FOR EACH LAYER: (SWAP THESE OUT FOR 412/408/404)
*elset, elset=layer01_el, generate
1000000, 1009999, 1
*elset, elset=layer02_el, generate
1010000, 1019999, 1
*elset, elset=layer03_el, generate
1020000, 1029999, 1
*elset, elset=layer04_el, generate

```

```
1030000, 1039999, 1
*elset, elset=layer05_el, generate
1040000, 1049999, 1
*elset, elset=layer06_el, generate
1050000, 1059999, 1
*elset, elset=layer07_el, generate
1060000, 1069999, 1
*elset, elset=layer08_el, generate
1070000, 1079999, 1
*elset, elset=layer09_el, generate
1080000, 1089999, 1
*elset, elset=layer10_el, generate
1090000, 1099999, 1
*elset, elset=layer11_el, generate
1100000, 1109999, 1
*elset, elset=layer12_el, generate
1110000, 1119999, 1
*elset, elset=layer13_el, generate
1120000, 1129999, 1
*elset, elset=layer14_el, generate
1130000, 1139999, 1
*elset, elset=layer15_el, generate
1140000, 1149999, 1
*elset, elset=layer16_el, generate
1150000, 1159999, 1
*elset, elset=layer17_el, generate
1160000, 1169999, 1
*elset, elset=layer18_el, generate
1170000, 1179999, 1
*elset, elset=layer19_el, generate
1180000, 1189999, 1
*elset, elset=layer20_el, generate
1190000, 1199999, 1
*elset, elset=layer21_el, generate
1200000, 1209999, 1
*elset, elset=layer22_el, generate
1210000, 1219999, 1
*elset, elset=layer23_el, generate
1220000, 1229999, 1
*elset, elset=layer24_el, generate
1230000, 1239999, 1
*elset, elset=layer25_el, generate
1240000, 1249999, 1
*elset, elset=layer26_el, generate
1250000, 1259999, 1
*elset, elset=layer27_el, generate
1260000, 1269999, 1
*elset, elset=layer28_el, generate
1270000, 1279999, 1
*elset, elset=layer29_el, generate
1280000, 1289999, 1
*elset, elset=layer30_el, generate
1290000, 1299999, 1
*elset, elset=layer31_el, generate
1300000, 1309999, 1
```

```

*elset, elset=layer32_el, generate
1310000, 1319999, 1
*elset, elset=layer33_el, generate
1320000, 1329999, 1
*elset, elset=layer34_el, generate
1330000, 1339999, 1
*elset, elset=layer35_el, generate
1340000, 1349999, 1
*elset, elset=layer36_el, generate
1350000, 1359999, 1
*elset, elset=layer37_el, generate
1360000, 1369999, 1
*elset, elset=layer38_el, generate
1370000, 1379999, 1
*elset, elset=layer39_el, generate
1380000, 1389999, 1
*elset, elset=layer40_el, generate
1390000, 1399999, 1
*elset, elset=layer41_el, generate
1400000, 1409999, 1
*elset, elset=layer42_el, generate
1410000, 1419999, 1
*elset, elset=layer43_el, generate
1420000, 1429999, 1
*elset, elset=layer44_el, generate
1430000, 1439999, 1
*elset, elset=layer45_el, generate
1440000, 1449999, 1
*elset, elset=layer46_el, generate
1450000, 1459999, 1
*elset, elset=layer47_el, generate
1460000, 1469999, 1
*elset, elset=layer48_el, generate
1470000, 1479999, 1
*elset, elset=layer49_el, generate
1480000, 1489999, 1
*elset, elset=layer50_el, generate
1490000, 1499999, 1
*elset, elset=layer51_el, generate
1500000, 1509999, 1
**
**
**
**
** ELEMENT SET FOR ALL SUBSTRATE
*elset, elset=substrate_el
farright_sub_el
small_substrate_el
**
** ELEMENT SET FOR ALL ALUMINUM
*elset, elset=al_el
farright_al_el
layer01_el
layer03_el
layer05_el

```

```
layer07_el
layer09_el
layer11_el
layer13_el
layer15_el
layer17_el
layer19_el
layer21_el
layer23_el
layer25_el
layer27_el
layer29_el
layer31_el
layer33_el
layer35_el
layer37_el
layer39_el
layer41_el
layer43_el
layer45_el
layer47_el
layer49_el
**layer51_el
**
** ELEMENT SET FOR ALL CERAMIC LAYERS
*elset, elset=cer_el
farright_cer_el
layer02_el
layer04_el
layer06_el
layer08_el
layer10_el
layer12_el
layer14_el
layer16_el
layer18_el
layer20_el
layer22_el
layer24_el
layer26_el
layer28_el
layer30_el
layer32_el
layer34_el
layer36_el
layer38_el
layer40_el
layer42_el
layer44_el
layer46_el
layer48_el
layer50_el
**
**
*****
```


** constrain layer/substrate interface to lines

*mpc

linear, bot1, 1000001, 1000011
linear, bot2, 1000011, 1000021
linear, bot3, 1000021, 1000031
linear, bot4, 1000031, 1000041
linear, bot5, 1000041, 1000051
linear, bot6, 1000051, 1000061
linear, bot7, 1000061, 1000071
linear, bot8, 1000071, 1000081
linear, bot9, 1000081, 1000091
linear, bot10, 1000091, 1000101
linear, bot11, 1000101, 1000111
linear, bot12, 1000111, 1000121
linear, bot13, 1000121, 1000131
linear, bot14, 1000131, 1000141
linear, bot15, 1000141, 1000151
linear, bot16, 1000151, 1000161
linear, bot17, 1000161, 1000171
linear, bot18, 1000171, 1000181
linear, bot19, 1000181, 1000191
linear, bot20, 1000191, 1000201
linear, bot21, 1000201, 1000211
linear, bot22, 1000211, 1000221
linear, bot23, 1000221, 1000231
linear, bot24, 1000231, 1000241
linear, bot25, 1000241, 1000251
linear, bot26, 1000251, 1000261
linear, bot27, 1000261, 1000271
linear, bot28, 1000271, 1000281
linear, bot29, 1000281, 1000291
linear, bot30, 1000291, 1000301
linear, bot31, 1000301, 1000311
linear, bot32, 1000311, 1000321
linear, bot33, 1000321, 1000331
linear, bot34, 1000331, 1000341
linear, bot35, 1000341, 1000351
linear, bot36, 1000351, 1000361
linear, bot37, 1000361, 1000371
linear, bot38, 1000371, 1000381
linear, bot39, 1000381, 1000391
linear, bot40, 1000391, 1000401
linear, bot41, 1000401, 1000411
linear, bot42, 1000411, 1000421
linear, bot43, 1000421, 1000431
linear, bot44, 1000431, 1000441
linear, bot45, 1000441, 1000451
linear, bot46, 1000451, 1000461
linear, bot47, 1000461, 1000471
linear, bot48, 1000471, 1000481
linear, bot49, 1000481, 1000491
linear, bot50, 1000491, 1000401
linear, bot51, 1000501, 1000511
linear, bot52, 1000511, 1000521
linear, bot53, 1000521, 1000531

```

linear, bot54, 1000531, 1000541
linear, bot55, 1000541, 1000551
linear, bot56, 1000551, 1000561
linear, bot57, 1000561, 1000571
linear, bot58, 1000571, 1000581
linear, bot59, 1000581, 1000591
linear, bot60, 1000591, 1000601
linear, bot61, 1000601, 1000611
linear, bot62, 1000611, 1000621
linear, bot63, 1000621, 1000631
linear, bot64, 1000631, 1000641
linear, bot65, 1000641, 1000651
linear, bot66, 1000651, 1000661
linear, bot67, 1000661, 1000671
linear, bot68, 1000671, 1000681
linear, bot69, 1000681, 1000691
linear, bot70, 1000691, 1000701
linear, bot71, 1000701, 1000711
linear, bot72, 1000711, 1000721
linear, bot73, 1000721, 1000731
linear, bot74, 1000731, 1000741
linear, bot75, 1000741, 1000751
linear, bot76, 1000751, 1000761
linear, bot77, 1000761, 1000771
linear, bot78, 1000771, 1000781
linear, bot79, 1000781, 1000791
linear, bot80, 1000791, 1000801
linear, bot81, 1000801, 1000811
linear, bot82, 1000811, 1000821
linear, bot83, 1000821, 1000831
linear, bot84, 1000831, 1000841
linear, bot85, 1000841, 1000851
linear, bot86, 1000851, 1000861
linear, bot87, 1000861, 1000871
linear, bot88, 1000871, 1000881
linear, bot89, 1000881, 1000891
linear, bot90, 1000891, 1000901
linear, bot91, 1000901, 1000911
linear, bot92, 1000911, 1000921
linear, bot93, 1000921, 1000931
linear, bot94, 1000931, 1000941
linear, bot95, 1000941, 1000951
linear, bot96, 1000951, 1000961
linear, bot97, 1000961, 1000971
linear, bot98, 1000971, 1000981
linear, bot99, 1000981, 1000991
linear, bot100, 1000991, 1001001
**sets from 1000001 to 1001001
**
*****
** SETS FOR INDENTATIONS STEPS (CONTACT)
** Define the indenter surface (edge of indenter nearest multilayer)
*elset, elset=indsurf_el, generate
3000001, 3000099, 1
** Define the multilayer surface (top of multilayer)

```

```

*elset, elset=topsurf_el, generate
**1504000, 1504999, 1 (uncomment for 4.04)
1509000, 1509999, 1
**1514000, 1514999, 1 (uncomment for 4.12um)
*SURFACE, NAME=INDSURF
indsurf_el, s1
*SURFACE, type=ELEMENT, NAME=TOPSURF
topsurf_el, s3
**
*CONTACT PAIR, INTERACTION=INTERACTION1
TOPSURF, INDSURF
*SURFACE INTERACTION, NAME=INTERACTION1
*FRICTION
0.1
**
*****
** DEFINE SECTIONS AND THEIR MATERIALS
*Solid Section, elset=substrate_el, material=Si
*Solid Section, elset=al_el, material=Al-viscous
*Solid Section, elset=cer_el, material=SiC-viscous
*Solid Section, elset=indenter_el, material=diamond
*Solid section, elset=indtip_el, material=tip
*Solid section, elset=layer51_el, material=Al_top
**
*****
** MATERIAL PROPERTY DEFINITIONS:
*****
*Material, name=AL
*Elastic
59000.0, 0.33
*Plastic
200.0, 0.0
300.0, 0.5
400.0, 3.0
**~~~~~
*Material, name=Al_top
*Elastic
59000.0, 0.33
*Plastic
200.0, 0.0
8770.0, 2.0
**~~~~~
*Material, name=SiC
*Elastic
277000., 0.17
*Plastic
8770.0, 0.0
**~~~~~
*Material, name=Si
*elastic
187000.0, 0.28
**~~~~~
*material, name=diamond
*elastic
1141000.0, 0.07

```

```

**-----
*material, name=tip
*elastic
9999000.0, 0.0
**-----
*Material, name=AL-viscous
*Elastic
59000.0, 0.33
*Plastic
200.0, 0.0
300.0, 0.5
400.0, 3.0
*Rate Dependent, type=YIELD RATIO
    1.,    0.
    1., 1e-06
    1.0305, 5e-06
    1.0436, 1e-05
    1.074, 5e-05
    1.0871, 0.0001
    1.1176, 0.0005
    1.1307, 0.001
    1.1612, 0.005
    1.1743, 0.01
    1.2047, 0.05
    1.2178, 0.1
    1.2483, 0.5
**-----
*Material, name=SiC-viscous
*Elastic
277000.0, 0.17
**Plastic
** fictitious
**200.0, 0.0
**300.0, 0.5
**400.0, 3.0
** Use Deng et al SiC modulus, yield=hardness/2.93
*Plastic
8770.0,    0.
****
*****
** BOUNDARY CONDITIONS:
**EQUATION
2
indtop-1, 2, 1.0, 3010000, 2, -1.0
*BOUNDARY
indleft, 1
left, 1
bottom, 2
**
**RESTART,WRITE,OVERLAY
*****
** LOADING DEFINITONS
*****
**
** STEP: Load

```

```

**
*STEP, INC=1000, NLGEOM=YES
load
*Static
5e-03, 1., 1e-25, 1.
*BOUNDARY, OP=MOD
indtip, 2, 2, -0.400
*OUTPUT, FIELD, variables=preselect, frequency=5000
*NODE OUTPUT
  U, RF
*NODE OUTPUT, NSET=surf-top
  COORD
*ELEMENT OUTPUT
  S, E, PEEQ, EE
*OUTPUT, HISTORY, frequency=1
*NODE OUTPUT, NSET=indtip
  U2, RF2
*End Step

** -----
**
** STEP: Unload
**
*STEP, INC=1000, NLGEOM=YES
load
*Static
5e-03, 1., 1e-25, 1.
*BOUNDARY, OP=MOD
indtip, 2, 2, -0.00
*OUTPUT, FIELD, variables=preselect, frequency=5000
*NODE OUTPUT
  U, RF
*NODE OUTPUT, NSET=surf-top
  COORD
*ELEMENT OUTPUT
  S, E, PEEQ, EE
*OUTPUT, HISTORY, frequency=1
*NODE OUTPUT, NSET=indtip
  U2, RF2
*End Step

```

APPENDIX B: Sample Code - Spherical Indenter Geometry

Within this appendix are portions of code that need to be exchanged for definition and utilization of a spherical indenter of radius=5 μm . It should be noted that three spherical indenters were used all identical apart from the initial position which can be seen in the node definitions and is a result of having three different thicknesses for nanolaminate geometry.

```
*****
**NODE DEFINITIONS
*****
**SPHERICAL INDENTER 404
*NODE
9999, 0.0, 9.04
1, 0.00, 8.54
53, 0.5, 8.54
62, 0.5, 9.04
**INDENTER OUTSIDE EDGE
10001, 0, 4.0401
10002, 0.0436326775, 4.0401903847
10003, 0.0872620322, 4.0407615242
10004, 0.1308847415, 4.0417133751
10005, 0.1744974835, 4.0430458649
10006, 0.2180969368, 4.0447588921
10007, 0.2616797812, 4.0468523262
10008, 0.3052426977, 4.0493260079
10009, 0.3487823687, 4.0521797487
10010, 0.3922954786, 4.0554133313
10011, 0.4357787137, 4.0590265095
10012, 0.4792287626, 4.0630190082
10013, 0.5226423163, 4.0673905232
10014, 0.5660160688, 4.0721407216
10015, 0.609346717, 4.0772692418
10016, 0.6526309611, 4.0827756931
10017, 0.6958655048, 4.0886596563
10018, 0.7390470556, 4.0949206832
10019, 0.7821723252, 4.101558297
10020, 0.8252380293, 4.1085719923
10021, 0.8682408883, 4.1159612349
10022, 0.9111776275, 4.1237254622
10023, 0.9540449769, 4.1318640828
10024, 0.9968396721, 4.1403764769
10025, 1.0395584541, 4.1492619963
10026, 1.0821980697, 4.1585199644
10027, 1.1247552717, 4.1681496761
10028, 1.1672268193, 4.178150398
10029, 1.209609478, 4.1885213686
10030, 1.2519000203, 4.1992617981
10031, 1.2940952255, 4.2103708686
10032, 1.3781867791, 4.2336915203
10033, 1.4618585236, 4.2584762202
```

10034,	1.5450849719,	4.2847174185
10035,	1.6278407723,	4.312407122
10036,	1.7101007166,	4.3415368961
10037,	1.7918397477,	4.3720978675
10038,	1.8730329671,	4.4040807272
10039,	1.9536556424,	4.4374757327
10040,	2.0336832154,	4.4722727118
10041,	2.1130913087,	4.5084610648
10042,	2.1918557339,	4.5460297685
10043,	2.2699524987,	4.5849673791
10044,	2.3473578139,	4.6252620357
10045,	2.4240481012,	4.6669014643
10046,	2.5751903746,	4.7541634965
10047,	2.7231951751,	4.8466471603
10048,	2.8678821818,	4.9442397786
10049,	3.0090751158,	5.0468224498
10050,	3.1466019552,	5.1542701927
10051,	3.280295145,	5.2664520989
10052,	3.4099918003,	5.3832314919
10053,	3.5355339059,	5.5044660941
10054,	3.8302222156,	5.8260619516
10055,	4.0957602214,	6.1721178182
10056,	4.3301270189,	6.54
10057,	4.5315389352,	6.9269086913
10058,	4.6984631039,	7.3298992834
10059,	4.8296291314,	7.7459047745
10060,	4.9240387651,	8.1717591117
10061,	4.9809734905,	8.6042212863
10062,	5, 9.04	

```

**
** FILL INDENTER EDGES
*NGEN, nset=inside_low
1, 53, 1
*NGEN, nset=inside_right
53,62,1
** FILL INDENTER CENTER
*NSET, nset=outside_low, generate
10001, 10053, 1
*NSET, nset=outside_right, generate
10053, 10062, 1
*nfill, bias=1.04, nset=indfill_low
inside_low, outside_low, 100, 100
*nfill, bias=1.04, nset=indfill_right
inside_right, outside_right, 100, 100
**
**
**
**SETS FOR BOUNDARY CONDITIONS:
*NSET, nset=indtopn-corner, generate
62, 9962, 100
*NSET, nset=indtip
9999
*NSET, nset=indtop
9999
indtopn-corner

```

```

*NSET, nset=indleftnocorner, generate
1, 10001, 100
*NSET, nset=indleft
9999
indleftnocorner
*NSET, nset=bottom, generate
899901, 900901, 10
**
*****
**ELEMENT INFORMATION
*****
**
**INDENTER
*element, type=cax4
1,9999,1,53,62
11, 1,101,102,2
*elgen, elset=indenter_spher
11, 61, 1, 1, 100, 100, 100
*elset, elset=indenter_el
indenter_spher, 1
**

```


APPENDIX C: Sample Code - 120nm/40nm Nanolaminate Geometry

Within this appendix are portions of code that need to be exchanged for definition and utilization of a 4.12 μ m thick nanolaminate with Al layers 120nm thick and ceramic layers 40nm thick.

```
*****
**NODE DEFINITIONS
*****
** MULTILAYER CORNERS
*node
1000001, 0, 0
1001001, 15, 0
2001001, 40, 0
1515516, 0, 4.12
1516516, 15, 4.12
2516516, 40, 4.12
899901, 0, -36
900901, 15, -36
1900901, 40, -36
**
** FILL SIDES
*NGEN, nset=left1
899901, 1000001, 1001
*NGEN, nset=left2
1000001, 1515516, 1001
*NGEN, nset=right1
900901, 1001001, 1001
*NGEN, nset=right2
1001001, 1516516, 1001
*NGEN, nset=farright1
1900901, 2001001, 1001
*NGEN, nset=farright2
2001001, 2516516,1001
*NSET, NSET=LEFT, GENERATE
899901, 1515516, 1001
*NSET, NSET=RIGHT, GENERATE
900901, 1516516, 1001
*NSET, NSET=FARRIGHT, GENERATE
1900901, 2516516, 1001
** FILL LAYER CENTER
*nfill, bias=0.998, nset=alln
left,right,1000,1
**
*NSET, nset=bottom, generate
899901, 900901, 10
**
**
**
*NGEN, nset=bot1
1000002, 1000010, 1
*NGEN, nset=bot2
```

100012, 100020, 1
*NGEN, nset=bot3
100022, 100030, 1
*NGEN, nset=bot4
100032, 100040, 1
*NGEN, nset=bot5
100042, 100050, 1
*NGEN, nset=bot6
100052, 100060, 1
*NGEN, nset=bot7
100062, 100070, 1
*NGEN, nset=bot8
100072, 100080, 1
*NGEN, nset=bot9
100082, 100090, 1
*NGEN, nset=bot10
100092, 100100, 1
*NGEN, nset=bot11
100102, 100110, 1
*NGEN, nset=bot12
100112, 100120, 1
*NGEN, nset=bot13
100122, 100130, 1
*NGEN, nset=bot14
100132, 100140, 1
*NGEN, nset=bot15
100142, 100150, 1
*NGEN, nset=bot16
100152, 100160, 1
*NGEN, nset=bot17
100162, 100170, 1
*NGEN, nset=bot18
100172, 100180, 1
*NGEN, nset=bot19
100182, 100190, 1
*NGEN, nset=bot20
100192, 100200, 1
*NGEN, nset=bot21
100202, 100210, 1
*NGEN, nset=bot22
100212, 100220, 1
*NGEN, nset=bot23
100222, 100230, 1
*NGEN, nset=bot24
100232, 100240, 1
*NGEN, nset=bot25
100242, 100250, 1
*NGEN, nset=bot26
100252, 100260, 1
*NGEN, nset=bot27
100262, 100270, 1
*NGEN, nset=bot28
100272, 100280, 1
*NGEN, nset=bot29
100282, 100290, 1

*NGEN, nset=bot30
1000292, 1000300, 1
*NGEN, nset=bot31
1000302, 1000310, 1
*NGEN, nset=bot32
1000312, 1000320, 1
*NGEN, nset=bot33
1000322, 1000330, 1
*NGEN, nset=bot34
1000332, 1000340, 1
*NGEN, nset=bot35
1000342, 1000350, 1
*NGEN, nset=bot36
1000352, 1000360, 1
*NGEN, nset=bot37
1000362, 1000370, 1
*NGEN, nset=bot38
1000372, 1000380, 1
*NGEN, nset=bot39
1000382, 1000390, 1
*NGEN, nset=bot40
1000392, 1000400, 1
*NGEN, nset=bot41
1000402, 1000410, 1
*NGEN, nset=bot42
1000412, 1000420, 1
*NGEN, nset=bot43
1000422, 1000430, 1
*NGEN, nset=bot44
1000432, 1000440, 1
*NGEN, nset=bot45
1000442, 1000450, 1
*NGEN, nset=bot46
1000452, 1000460, 1
*NGEN, nset=bot47
1000462, 1000470, 1
*NGEN, nset=bot48
1000472, 1000480, 1
*NGEN, nset=bot49
1000482, 1000490, 1
*NGEN, nset=bot50
1000492, 1000500, 1
*NGEN, nset=bot51
1000502, 1000510, 1
*NGEN, nset=bot52
1000512, 1000520, 1
*NGEN, nset=bot53
1000522, 1000530, 1
*NGEN, nset=bot54
1000532, 1000540, 1
*NGEN, nset=bot55
1000542, 1000550, 1
*NGEN, nset=bot56
1000552, 1000560, 1
*NGEN, nset=bot57

1000562, 1000570, 1
*NGEN, nset=bot58
1000572, 1000580, 1
*NGEN, nset=bot59
1000582, 1000590, 1
*NGEN, nset=bot60
1000592, 1000600, 1
*NGEN, nset=bot61
1000602, 1000610, 1
*NGEN, nset=bot62
1000612, 1000620, 1
*NGEN, nset=bot63
1000622, 1000630, 1
*NGEN, nset=bot64
1000632, 1000640, 1
*NGEN, nset=bot65
1000642, 1000650, 1
*NGEN, nset=bot66
1000652, 1000660, 1
*NGEN, nset=bot67
1000662, 1000670, 1
*NGEN, nset=bot68
1000672, 1000680, 1
*NGEN, nset=bot69
1000682, 1000690, 1
*NGEN, nset=bot70
1000692, 1000700, 1
*NGEN, nset=bot71
1000702, 1000710, 1
*NGEN, nset=bot72
1000712, 1000720, 1
*NGEN, nset=bot73
1000722, 1000730, 1
*NGEN, nset=bot74
1000732, 1000740, 1
*NGEN, nset=bot75
1000742, 1000750, 1
*NGEN, nset=bot76
1000752, 1000760, 1
*NGEN, nset=bot77
1000762, 1000770, 1
*NGEN, nset=bot78
1000772, 1000780, 1
*NGEN, nset=bot79
1000782, 1000790, 1
*NGEN, nset=bot80
1000792, 1000800, 1
*NGEN, nset=bot81
1000802, 1000810, 1
*NGEN, nset=bot82
1000812, 1000820, 1
*NGEN, nset=bot83
1000822, 1000830, 1
*NGEN, nset=bot84
1000832, 1000840, 1

```

*NGEN, nset=bot85
1000842, 1000850, 1
*NGEN, nset=bot86
1000852, 1000860, 1
*NGEN, nset=bot87
1000862, 1000870, 1
*NGEN, nset=bot88
1000872, 1000880, 1
*NGEN, nset=bot89
1000882, 1000890, 1
*NGEN, nset=bot90
1000892, 1000900, 1
*NGEN, nset=bot91
1000902, 1000910, 1
*NGEN, nset=bot92
1000912, 1000920, 1
*NGEN, nset=bot93
1000922, 1000930, 1
*NGEN, nset=bot94
1000932, 1000940, 1
*NGEN, nset=bot95
1000942, 1000950, 1
*NGEN, nset=bot96
1000952, 1000960, 1
*NGEN, nset=bot97
1000962, 1000970, 1
*NGEN, nset=bot98
1000972, 1000980, 1
*NGEN, nset=bot99
1000982, 1000990, 1
*NGEN, nset=bot100
1000992, 1001000, 1
**sets from 1000001 to 1001001
*NGEN, nset=right_bond
1001001, 1516516, 1001
**for the time being we will not deal with the linear constraint
**of the right/center edge as it is far enough from indentation
**
*****
**ELEMENT INFORMATION
*****
**
**
** MULTILAYER ELEMENTS
*element, type=cax4
900000, 899901, 899911, 900912, 900902
*elgen, elset=small_substrate_el
900000, 100, 10, 10, 100, 1001, 1000
*element, type=cax4
1000000, 1000001, 1000002, 1001003, 1001002
*elgen, elset=small_layers_el
**1000000, 1000, 1, 1, 505, 1001, 1000 (for 4.04)
**1000000, 1000, 1, 1, 510, 1001, 1000 (for 4.08um)
1000000, 1000, 1, 1, 515, 1001, 1000
*element, type=cax4

```

```

1900000, 900901, 1900901, 1910911, 910911
*elgen, elset=farright_sub_el
**1900101, 1001001, 2001001, 2006006, 1006006 (for 4.04)
**1900101, 1001001, 2001001, 2011011, 1011011 (for 4.08um)
1900000, 1, 1, 1, 10, 10010, 1
*element, type=cax4
1900101, 1001001, 2001001, 2016016, 1016016
*elgen, elset=farright_al_el
1900101, 1, 1, 1, 26, 20020, 2
*element, type=cax4
**1900102, 1006006, 2006006, 2021021, 1021021 (for 4.04)
**1900102, 1011011, 2011011, 2021021, 1021021 (for 4.08um)
1900102, 1016016, 2016016, 2021021, 1021021
*elgen, elset=farright_cer_el
1900102, 1, 1, 1, 25, 20020, 2
**startnode, #ofelem horiz, node inc, el inc, #ofelem vert, nodeinc, elinc
** Define Element Sets
**
**
**
**GENERATE ELEMENT SETS FOR EACH LAYER:
*elset, elset=layer01_el, generate
1000000, 1014999, 1
*elset, elset=layer02_el, generate
1015000, 1019999, 1
*elset, elset=layer03_el, generate
1020000, 1034999, 1
*elset, elset=layer04_el, generate
1035000, 1039999, 1
*elset, elset=layer05_el, generate
1040000, 1054999, 1
*elset, elset=layer06_el, generate
1055000, 1059999, 1
*elset, elset=layer07_el, generate
1060000, 1074999, 1
*elset, elset=layer08_el, generate
1075000, 1079999, 1
*elset, elset=layer09_el, generate
1080000, 1094999, 1
*elset, elset=layer10_el, generate
1095000, 1099999, 1
*elset, elset=layer11_el, generate
1100000, 1114999, 1
*elset, elset=layer12_el, generate
1115000, 1119999, 1
*elset, elset=layer13_el, generate
1120000, 1134999, 1
*elset, elset=layer14_el, generate
1135000, 1139999, 1
*elset, elset=layer15_el, generate
1140000, 1154999, 1
*elset, elset=layer16_el, generate
1155000, 1159999, 1
*elset, elset=layer17_el, generate
1160000, 1174999, 1

```

```
*elset, elset=layer18_el, generate
1175000, 1179999, 1
*elset, elset=layer19_el, generate
1180000, 1194999, 1
*elset, elset=layer20_el, generate
1195000, 1199999, 1
*elset, elset=layer21_el, generate
1200000, 1214999, 1
*elset, elset=layer22_el, generate
1215000, 1219999, 1
*elset, elset=layer23_el, generate
1220000, 1234999, 1
*elset, elset=layer24_el, generate
1235000, 1239999, 1
*elset, elset=layer25_el, generate
1240000, 1254999, 1
*elset, elset=layer26_el, generate
1255000, 1259999, 1
*elset, elset=layer27_el, generate
1260000, 1274999, 1
*elset, elset=layer28_el, generate
1275000, 1279999, 1
*elset, elset=layer29_el, generate
1280000, 1294999, 1
*elset, elset=layer30_el, generate
1295000, 1299999, 1
*elset, elset=layer31_el, generate
1300000, 1314999, 1
*elset, elset=layer32_el, generate
1315000, 1319999, 1
*elset, elset=layer33_el, generate
1320000, 1334999, 1
*elset, elset=layer34_el, generate
1335000, 1339999, 1
*elset, elset=layer35_el, generate
1340000, 1354999, 1
*elset, elset=layer36_el, generate
1355000, 1359999, 1
*elset, elset=layer37_el, generate
1360000, 1374999, 1
*elset, elset=layer38_el, generate
1375000, 1379999, 1
*elset, elset=layer39_el, generate
1380000, 1394999, 1
*elset, elset=layer40_el, generate
1395000, 1399999, 1
*elset, elset=layer41_el, generate
1400000, 1414999, 1
*elset, elset=layer42_el, generate
1415000, 1419999, 1
*elset, elset=layer43_el, generate
1420000, 1434999, 1
*elset, elset=layer44_el, generate
1435000, 1439999, 1
*elset, elset=layer45_el, generate
```

```
1440000, 1454999, 1
*elset, elset=layer46_el, generate
1455000, 1459999, 1
*elset, elset=layer47_el, generate
1460000, 1474999, 1
*elset, elset=layer48_el, generate
1475000, 1479999, 1
*elset, elset=layer49_el, generate
1480000, 1494999, 1
*elset, elset=layer50_el, generate
1495000, 1499999, 1
*elset, elset=layer51_el, generate
1500000, 1514999, 1
**
```


APPENDIX D: Sample Code - 40nm/120nm Nanolaminate Geometry

Within this appendix are portions of code that need to be exchanged for definition and utilization of a 4.04 μ m thick nanolaminate with Al layers 40nm thick and ceramic layers 120nm thick.

```
*****
**NODE DEFINITIONS
*****
** MULTILAYER CORNERS
*node
1000001, 0, 0
1001001, 15, 0
2001001, 40, 0
**1515516, 0, 4.12
**1516516, 15, 4.12
**2516516, 40, 4.12
**1510511, 0, 4.08
**1511511, 15, 4.08
**2511511, 40, 4.08
1505506, 0, 4.04
1506506, 15, 4.04
2506506, 40, 4.04
899901, 0, -36
900901, 15, -36
1900901, 40, -36
**
** FILL SIDES
*NGEN, nset=left1
899901, 1000001, 1001
*NGEN, nset=left2
1000001, 1505506, 1001
*NGEN, nset=right1
900901, 1001001, 1001
*NGEN, nset=right2
1001001, 1506506, 1001
*NGEN, nset=farright1
1900901, 2001001, 1001
*NGEN, nset=farright2
2001001, 2506506, 1001
*NSET, NSET=LEFT, GENERATE
899901, 1505506, 1001
*NSET, NSET=RIGHT, GENERATE
900901, 1506506, 1001
*NSET, NSET=FARRIGHT, GENERATE
1900901, 2506506, 1001
** FILL LAYER CENTER
*nfill, bias=0.998, nset=alln
left,right,1000,1
**
*NSET, nset=bottom, generate
899901, 900901, 10
```

```
**
*****
**Interface Constraint Node Sets
*NGEN, nset=bot1
100002, 100010, 1
*NGEN, nset=bot2
100012, 100020, 1
*NGEN, nset=bot3
100022, 100030, 1
*NGEN, nset=bot4
100032, 100040, 1
*NGEN, nset=bot5
100042, 100050, 1
*NGEN, nset=bot6
100052, 100060, 1
*NGEN, nset=bot7
100062, 100070, 1
*NGEN, nset=bot8
100072, 100080, 1
*NGEN, nset=bot9
100082, 100090, 1
*NGEN, nset=bot10
100092, 100100, 1
*NGEN, nset=bot11
100102, 100110, 1
*NGEN, nset=bot12
100112, 100120, 1
*NGEN, nset=bot13
100122, 100130, 1
*NGEN, nset=bot14
100132, 100140, 1
*NGEN, nset=bot15
100142, 100150, 1
*NGEN, nset=bot16
100152, 100160, 1
*NGEN, nset=bot17
100162, 100170, 1
*NGEN, nset=bot18
100172, 100180, 1
*NGEN, nset=bot19
100182, 100190, 1
*NGEN, nset=bot20
100192, 100200, 1
*NGEN, nset=bot21
100202, 100210, 1
*NGEN, nset=bot22
100212, 100220, 1
*NGEN, nset=bot23
100222, 100230, 1
*NGEN, nset=bot24
100232, 100240, 1
*NGEN, nset=bot25
100242, 100250, 1
*NGEN, nset=bot26
100252, 100260, 1
```

*NGEN, nset=bot27
1000262, 1000270, 1
*NGEN, nset=bot28
1000272, 1000280, 1
*NGEN, nset=bot29
1000282, 1000290, 1
*NGEN, nset=bot30
1000292, 1000300, 1
*NGEN, nset=bot31
1000302, 1000310, 1
*NGEN, nset=bot32
1000312, 1000320, 1
*NGEN, nset=bot33
1000322, 1000330, 1
*NGEN, nset=bot34
1000332, 1000340, 1
*NGEN, nset=bot35
1000342, 1000350, 1
*NGEN, nset=bot36
1000352, 1000360, 1
*NGEN, nset=bot37
1000362, 1000370, 1
*NGEN, nset=bot38
1000372, 1000380, 1
*NGEN, nset=bot39
1000382, 1000390, 1
*NGEN, nset=bot40
1000392, 1000400, 1
*NGEN, nset=bot41
1000402, 1000410, 1
*NGEN, nset=bot42
1000412, 1000420, 1
*NGEN, nset=bot43
1000422, 1000430, 1
*NGEN, nset=bot44
1000432, 1000440, 1
*NGEN, nset=bot45
1000442, 1000450, 1
*NGEN, nset=bot46
1000452, 1000460, 1
*NGEN, nset=bot47
1000462, 1000470, 1
*NGEN, nset=bot48
1000472, 1000480, 1
*NGEN, nset=bot49
1000482, 1000490, 1
*NGEN, nset=bot50
1000492, 1000500, 1
*NGEN, nset=bot51
1000502, 1000510, 1
*NGEN, nset=bot52
1000512, 1000520, 1
*NGEN, nset=bot53
1000522, 1000530, 1
*NGEN, nset=bot54

1000532, 1000540, 1
*NGEN, nset=bot55
1000542, 1000550, 1
*NGEN, nset=bot56
1000552, 1000560, 1
*NGEN, nset=bot57
1000562, 1000570, 1
*NGEN, nset=bot58
1000572, 1000580, 1
*NGEN, nset=bot59
1000582, 1000590, 1
*NGEN, nset=bot60
1000592, 1000600, 1
*NGEN, nset=bot61
1000602, 1000610, 1
*NGEN, nset=bot62
1000612, 1000620, 1
*NGEN, nset=bot63
1000622, 1000630, 1
*NGEN, nset=bot64
1000632, 1000640, 1
*NGEN, nset=bot65
1000642, 1000650, 1
*NGEN, nset=bot66
1000652, 1000660, 1
*NGEN, nset=bot67
1000662, 1000670, 1
*NGEN, nset=bot68
1000672, 1000680, 1
*NGEN, nset=bot69
1000682, 1000690, 1
*NGEN, nset=bot70
1000692, 1000700, 1
*NGEN, nset=bot71
1000702, 1000710, 1
*NGEN, nset=bot72
1000712, 1000720, 1
*NGEN, nset=bot73
1000722, 1000730, 1
*NGEN, nset=bot74
1000732, 1000740, 1
*NGEN, nset=bot75
1000742, 1000750, 1
*NGEN, nset=bot76
1000752, 1000760, 1
*NGEN, nset=bot77
1000762, 1000770, 1
*NGEN, nset=bot78
1000772, 1000780, 1
*NGEN, nset=bot79
1000782, 1000790, 1
*NGEN, nset=bot80
1000792, 1000800, 1
*NGEN, nset=bot81
1000802, 1000810, 1

```

*NGEN, nset=bot82
1000812, 1000820, 1
*NGEN, nset=bot83
1000822, 1000830, 1
*NGEN, nset=bot84
1000832, 1000840, 1
*NGEN, nset=bot85
1000842, 1000850, 1
*NGEN, nset=bot86
1000852, 1000860, 1
*NGEN, nset=bot87
1000862, 1000870, 1
*NGEN, nset=bot88
1000872, 1000880, 1
*NGEN, nset=bot89
1000882, 1000890, 1
*NGEN, nset=bot90
1000892, 1000900, 1
*NGEN, nset=bot91
1000902, 1000910, 1
*NGEN, nset=bot92
1000912, 1000920, 1
*NGEN, nset=bot93
1000922, 1000930, 1
*NGEN, nset=bot94
1000932, 1000940, 1
*NGEN, nset=bot95
1000942, 1000950, 1
*NGEN, nset=bot96
1000952, 1000960, 1
*NGEN, nset=bot97
1000962, 1000970, 1
*NGEN, nset=bot98
1000972, 1000980, 1
*NGEN, nset=bot99
1000982, 1000990, 1
*NGEN, nset=bot100
1000992, 1001000, 1
**sets from 1000001 to 1001001
*NGEN, nset=right_bond
1001001, 1506506, 1001
**for the time being we will not deal with the linear constraint
**of the right/center edge as it is far enough from indentation
**
*****
**ELEMENT INFORMATION
*****
**
** MULTILAYER ELEMENTS
*element, type=cax4
900000, 899901, 899911, 900912, 900902
*elgen, elset=small_substrate_el
900000, 100, 10, 10, 100, 1001, 1000
*element, type=cax4
1000000, 1000001, 1000002, 1001003, 1001002

```

```

*elgen, elset=small_layers_el
1000000, 1000, 1, 1, 505, 1001, 1000
**1000000, 1000, 1, 1, 510, 1001, 1000 (for 4.08um)
**1000000, 1000, 1, 1, 515, 1001, 1000 (for 4.12um)
*element, type=cax4
1900000, 900901, 1900901, 1910911, 910911
*elgen, elset=farright_sub_el
1900000, 1, 1, 1, 10, 10010, 1
*element, type=cax4
1900101, 1001001, 2001001, 2006006, 1006006
**1900101, 1001001, 2001001, 2011011, 1011011 (for 4.08um)
**1900101, 1001001, 2001001, 2016016, 1016016 (for 4.12um)
*elgen, elset=farright_al_el
1900101, 1, 1, 1, 26, 20020, 2
*element, type=cax4
1900102, 1006006, 2006006, 2021021, 1021021
**1900102, 1011011, 2011011, 2021021, 1021021 (for 4.08um)
**1900102, 1016016, 2016016, 2021021, 1021021 (for 4.12um)
*elgen, elset=farright_cer_el
1900102, 1, 1, 1, 25, 20020, 2
**startnode, #ofelem horiz, node inc, el inc, #ofelem vert, nodeinc, elinc
** Define Element Sets
**
**GENERATE ELEMENT SETS FOR EACH LAYER: (SWAP THESE OUT FOR 412/408/404)
*elset, elset=layer01_el, generate
1000000, 1004999, 1
*elset, elset=layer02_el, generate
1005000, 1019999, 1
*elset, elset=layer03_el, generate
1020000, 1024999, 1
*elset, elset=layer04_el, generate
1025000, 1039999, 1
*elset, elset=layer05_el, generate
1040000, 1044999, 1
*elset, elset=layer06_el, generate
1045000, 1059999, 1
*elset, elset=layer07_el, generate
1060000, 1064999, 1
*elset, elset=layer08_el, generate
1065000, 1079999, 1
*elset, elset=layer09_el, generate
1080000, 1084999, 1
*elset, elset=layer10_el, generate
1085000, 1099999, 1
*elset, elset=layer11_el, generate
1100000, 1104999, 1
*elset, elset=layer12_el, generate
1105000, 1119999, 1
*elset, elset=layer13_el, generate
1120000, 1124999, 1
*elset, elset=layer14_el, generate
1125000, 1139999, 1
*elset, elset=layer15_el, generate
1140000, 1144999, 1
*elset, elset=layer16_el, generate

```

1145000, 1159999, 1
*elset, elset=layer17_el, generate
1160000, 1164999, 1
*elset, elset=layer18_el, generate
1165000, 1179999, 1
*elset, elset=layer19_el, generate
1180000, 1184999, 1
*elset, elset=layer20_el, generate
1185000, 1199999, 1
*elset, elset=layer21_el, generate
1200000, 1204999, 1
*elset, elset=layer22_el, generate
1205000, 1219999, 1
*elset, elset=layer23_el, generate
1220000, 1224999, 1
*elset, elset=layer24_el, generate
1225000, 1239999, 1
*elset, elset=layer25_el, generate
1240000, 1244999, 1
*elset, elset=layer26_el, generate
1245000, 1259999, 1
*elset, elset=layer27_el, generate
1260000, 1264999, 1
*elset, elset=layer28_el, generate
1265000, 1279999, 1
*elset, elset=layer29_el, generate
1280000, 1284999, 1
*elset, elset=layer30_el, generate
1285000, 1299999, 1
*elset, elset=layer31_el, generate
1300000, 1304999, 1
*elset, elset=layer32_el, generate
1305000, 1319999, 1
*elset, elset=layer33_el, generate
1320000, 1324999, 1
*elset, elset=layer34_el, generate
1325000, 1339999, 1
*elset, elset=layer35_el, generate
1340000, 1344999, 1
*elset, elset=layer36_el, generate
1345000, 1359999, 1
*elset, elset=layer37_el, generate
1360000, 1364999, 1
*elset, elset=layer38_el, generate
1365000, 1379999, 1
*elset, elset=layer39_el, generate
1380000, 1384999, 1
*elset, elset=layer40_el, generate
1385000, 1399999, 1
*elset, elset=layer41_el, generate
1400000, 1404999, 1
*elset, elset=layer42_el, generate
1405000, 1419999, 1
*elset, elset=layer43_el, generate
1420000, 1424999, 1

```
*elset, elset=layer44_el, generate
1425000, 1439999, 1
*elset, elset=layer45_el, generate
1440000, 1444999, 1
*elset, elset=layer46_el, generate
1445000, 1459999, 1
*elset, elset=layer47_el, generate
1460000, 1464999, 1
*elset, elset=layer48_el, generate
1465000, 1479999, 1
*elset, elset=layer49_el, generate
1480000, 1484999, 1
*elset, elset=layer50_el, generate
1485000, 1499999, 1
*elset, elset=layer51_el, generate
1500000, 1504999, 1
**
**
```


LIST OF REFERENCES

1. Alpas, A.T., et al., *The Mechanical-Properties of Laminated Microscale Composites of Al/Al₂O₃*. Journal of Materials Science, 1990. **25**(3): p. 1603-1609.
2. Chawla, N., et al., *Indentation mechanics and fracture behavior of metal/ceramic nanolaminate composites*. Journal of Materials Science, 2008. **43**(13): p. 4383-4390.
3. Chou, T.C., et al., *Mechanical-Properties and Microstructures of Metal Ceramic Microlaminates .2. A Mo/Al₂O₃ System*. Journal of Materials Research, 1992. **7**(10): p. 2774-2784.
4. Chou, T.C., et al., *Mechanical-Properties and Microstructures of Metal Ceramic Microlaminates .1. Nb/Mosi₂ Systems*. Journal of Materials Research, 1992. **7**(10): p. 2765-2773.
5. Ding, Y., D.O. Northwood, and A.T. Alpas, *The Microstructure and Mechanical-Properties of Nanocrystalline Laminated Al/Al₂O₃ Composites Fabricated by Magnetron Sputtering*. Interfaces Ii, 1995. **189**:-: p. 309-314.
6. Ghalandari, L., et al., *Production of Al/Sn multilayer composite by accumulative roll bonding (ARB): A study of microstructure and mechanical properties*. Materials Science and Engineering a-Structural Materials Properties Microstructure and Processing, 2016. **661**: p. 179-186.
7. Ghalandari, L., M.M. Mandavian, and M. Reihanian, *Microstructure evolution and mechanical properties of Cu/Zn multilayer processed by accumulative roll bonding (ARB)*. Materials Science and Engineering a-Structural Materials Properties Microstructure and Processing, 2014. **593**: p. 145-152.
8. Ghalandari, L. and M.M. Moshksar, *High-strength and high-conductive Cu/Ag multilayer produced by ARB*. Journal of Alloys and Compounds, 2010. **506**(1): p. 172-178.
9. Jaya, B.N., C. Kirchlechner, and G. Dehm, *Can microscale fracture tests provide reliable fracture toughness values? A case study in silicon*. Journal of Materials Research, 2015. **30**(5): p. 686-698.
10. Ko, S.W., et al., *Chemical solution deposition of copper thin films and integration into a multilayer capacitor structure*. Journal of Electroceramics, 2010. **24**(3): p. 161-169.
11. Laraia, V.J. and A.H. Heuer, *Novel Composite Microstructure and Mechanical-Behavior of Mollusk Shell*. Journal of the American Ceramic Society, 1989. **72**(11): p. 2177-2179.

12. Llorca, J., A. Needleman, and S. Suresh, *An Analysis of the Effects of Matrix Void Growth on Deformation and Ductility in Metal Ceramic Composites*. Acta Metallurgica Et Materialia, 1991. **39**(10): p. 2317-2335.
13. Lopez, S., M.S. Wong, and W.D. Sproul, *Thermal-Behavior of Carbon Nitride and Tin/Nbn Superlattice Films*. Journal of Vacuum Science & Technology a-Vacuum Surfaces and Films, 1995. **13**(3): p. 1644-1648.
14. Lotfian, S., et al., *Effect of layer thickness on the high temperature mechanical properties of Al/SiC nanolaminates*. Thin Solid Films, 2014. **571**: p. 260-267.
15. Manoharan, M.P., A.V. Desai, and M.A. Haque, *Fracture toughness characterization of advanced coatings*. Journal of Micromechanics and Microengineering, 2009. **19**(11).
16. Matoy, K., et al., *A comparative micro-cantilever study of the mechanical behavior of silicon based passivation films*. Thin Solid Films, 2009. **518**(1): p. 247-256.
17. Meyers, M.A. and A.M. Hodge, *Advances in biological materials and biomaterials science*. Jom, 2008. **60**(3): p. 18-18.
18. Misra, A., J.P. Hirth, and R.G. Hoagland, *Length-scale-dependent deformation mechanisms in incoherent metallic multilayered composites*. Acta Materialia, 2005. **53**(18): p. 4817-4824.
19. Pelizzo, M.G., et al., *Innovative methods for optimization and characterization of multilayer coatings*. Euv and X-Ray Optics: Synergy between Laboratory and Space, 2009. **7360**.
20. Qi, W., et al., *Layer-by-layer assembled graphene oxide composite films for enhanced mechanical properties and fibroblast cell affinity*. Journal of Materials Chemistry B, 2014. **2**(3): p. 325-331.
21. Tan, X.H. and Y.L. Shen, *Modeling analysis of the indentation-derived yield properties of metallic multilayered composites*. Composites Science and Technology, 2005. **65**(11-12): p. 1639-1646.
22. Waskiewicz, W.K., et al., *Achieving Uniform Multilayer Coatings on Figured Optics*. Osa Proceedings on Soft-X-Ray Projection Lithography, 1991. **12**: p. 97-100.
23. Wei, C.H., et al., *Tribological characteristics of titanium nitride and titanium carbonitride multilayer films Part II. The effect of coating sequence on tribological properties*. Thin Solid Films, 2001. **381**(1): p. 104-118.
24. Wiklund, U., P. Hedenqvist, and S. Hogmark, *Multilayer cracking resistance in bending*. Surface & Coatings Technology, 1997. **97**(1-3): p. 773-778.

25. Windt, D.L. and J.A. Bellotti, *Performance, structure, and stability of SiC/Al multilayer films for extreme ultraviolet applications*. Applied Optics, 2009. **48**(26): p. 4932-4941.
26. Windt, D.L., et al., *X-ray multilayer coatings for use at energies above 100 keV*. X-Ray Optics, Instruments, and Missions Iii, 2000. **4012**: p. 442-447.
27. Windt, D.L. and W.K. Waskiewicz, *Multilayer Facilities Required for Extreme-Ultraviolet Lithography*. Journal of Vacuum Science & Technology B, 1994. **12**(6): p. 3826-3832.
28. Wu, F.B., S.K. Tien, and J.G. Duh, *Manufacture, microstructure and mechanical properties of CrWN and CrN/WN nanolayered coatings*. Surface & Coatings Technology, 2005. **200**(5-6): p. 1514-1518.
29. Wurster, S., C. Motz, and R. Pippan, *Characterization of the fracture toughness of micro-sized tungsten single crystal notched specimens*. Philosophical Magazine, 2012. **92**(14): p. 1803-1825.
30. Xu, Z.Y., et al., *Effect of modulation periods on the microstructure and mechanical properties of DLC/TiC multilayer films deposited by filtered cathodic vacuum arc method*. Applied Surface Science, 2015. **328**: p. 319-324.
31. Ziebert, C. and S. Ulrich, *Hard multilayer coatings containing TiN and/or ZrN: A review and recent progress in their nanoscale characterization*. Journal of Vacuum Science & Technology A, 2006. **24**(3): p. 554-583.
32. Zuppella, P., et al., *Innovative multilayer coatings for space solar physics: performances and stability over time*. Euv and X-Ray Optics: Synergy between Laboratory and Space Ii, 2011. **8076**.
33. Deng, X., et al., *Nanoindentation behavior of nanolayered metal-ceramic composites*. Journal of Materials Engineering and Performance, 2005. **14**(4): p. 417-423.
34. Herbert, E.G., et al., *Measuring the elastic modulus and residual stress of freestanding thin films using nanoindentation techniques*. Journal of Materials Research, 2009. **24**(9): p. 2974-2985.
35. Oliver, W.C. and G.M. Pharr, *An Improved Technique for Determining Hardness and Elastic-Modulus Using Load and Displacement Sensing Indentation Experiments*. Journal of Materials Research, 1992. **7**(6): p. 1564-1583.
36. Oliver, W.C. and G.M. Pharr, *Measurement of hardness and elastic modulus by instrumented indentation: Advances in understanding and refinements to methodology*. Journal of Materials Research, 2004. **19**(1): p. 3-20.

37. Pharr, G.M., *Recent advances in small-scale mechanical property measurement by nanoindentation*. Current Opinion in Solid State & Materials Science, 2015. **19**(6): p. 315-316.
38. Kirsten Parratt, J.M.Y., Gerald R. Poirier, Nan Yao, *Plasma-Etching of the Organic Layer in Nacre*. Soft Nanoscience Letters, 2014. **4**(3): p. 6.
39. Barthelat, F., *Biomimetics for next generation materials*. Philosophical Transactions of the Royal Society of London A: Mathematical, Physical and Engineering Sciences, 2007.
40. Sarikaya M, A.I., *Nacre of abalone shell: a natural multifunctional nanolaminated ceramic-polymer composite material*. Results and Problems in Cell Differentiation 1992. **19**: p. 1-26.
41. Wang, R.Z. and H.S. Gupta, *Deformation and Fracture Mechanisms of Bone and Nacre*. Annual Review of Materials Research, Vol 41, 2011. **41**: p. 41-73.
42. Schmidt, D.F., *Nanolaminates - Bioinspired and beyond*. Materials Letters, 2013. **108**: p. 328-335.
43. Chen, Y., M. Sullivan, and B.C. Prorok, *The Growth and Mechanical Properties of Abalone Nacre Mesolayer*. Mechanics of Biological Systems and Materials, Vol 6, 2016: p. 127-131.
44. Humburg, H., et al., *Combination of biological mechanisms for a concept study of a fracture-tolerant bio-inspired ceramic composite material*. Journal of Materials Science, 2014. **49**(23): p. 8040-8050.
45. Lackner, J.M., et al., *Plastic deformation in nano-scale multilayer materials - A biomimetic approach based on nacre*. Thin Solid Films, 2013. **534**: p. 417-425.
46. Lenau, T. and T. Hesselberg, *Biomimetic Self-Organization and Self-Healing*. Engineered Biomimicry, 2013: p. 333-358.
47. Merrill, M.H. and C.T. Sun, *Fast, simple and efficient assembly of nanolayered materials and devices*. Nanotechnology, 2009. **20**(7).
48. Jamison, R.D. and Y.L. Shen, *Indentation behavior of multilayered thin films: Effects of layer undulation*. Thin Solid Films, 2014. **570**: p. 235-242.
49. Jamison, R.D. and Y.L. Shen, *Indentation-derived elastic modulus of multilayer thin films: Effect of unloading-induced plasticity*. Journal of Materials Research, 2015. **30**(15): p. 2279-2290.

50. Jamison, R.D. and Y.L. Shen, *Indentation and overall compression behavior of multilayered thin-film composites: Effect of undulating layer geometry*. Journal of Composite Materials, 2016. **50**(4): p. 507-521.
51. Singh, D.R.P., et al., *Micropillar compression of Al/SiC nanolaminates*. Acta Materialia, 2010. **58**(20): p. 6628-6636.
52. Singh, D.R.P., et al., *Anomalous viscoplasticity during nanoindentation of Al/SiC nanolaminated composites*. Materials Science and Engineering a-Structural Materials Properties Microstructure and Processing, 2011. **528**(13-14): p. 4608-4614.
53. Tang, G. and Y.L. Shen, *Indentation Mechanics for Micro- and Nano-Layered Composites*. MicroNano2008-2nd International Conference on Integration and Commercialization of Micro and Nanosystems, Proceedings, 2008: p. 287-292.
54. Tang, G., Y.L. Shen, and N. Chawla, *Plastic deformation during indentation unloading in multilayered materials*. Journal of Applied Physics, 2008. **104**(11).
55. Tang, G., et al., *Indentation behavior of metal-ceramic multilayers at the nanoscale: Numerical analysis and experimental verification*. Acta Materialia, 2010. **58**(6): p. 2033-2044.
56. Tang, G., et al., *Elastic properties of metal-ceramic nanolaminates measured by nanoindentation*. Materials Science and Engineering a-Structural Materials Properties Microstructure and Processing, 2009. **502**(1-2): p. 79-84.
57. Mayer, C.R., *Mechanical Behavior of Al-SiC Nanolaminate Composites Using Micro-Scale Testing Methods*. 2016, Arizona State University.
58. Chen, D.X., et al., *Ag films with enhanced adhesion fabricated by solution process for solar reflector applications*. Solar Energy Materials and Solar Cells, 2016. **151**: p. 154-161.
59. Song, S.H., et al., *Characterization of Al₂O₃ and ZnO multilayer thin films deposited by low temperature thermal atomic layer deposition on transparent polyimide*. Journal of Vacuum Science & Technology A, 2017. **35**(1).
60. Zhao, R.P., et al., *MOCVD-derived multilayer Gd_{0.5}Y_{0.5}Ba₂Cu₃O_{7-δ} films based on a novel heating method*. Superconductor Science & Technology, 2017. **30**(2).
61. Singh, M., et al., *Plasma assisted synthesis and growth mechanism of rare V₂O₅ nanostructured thin films*. Journal of Alloys and Compounds, 2017. **690**: p. 532-541.
62. Yan, B., et al., *A review of atomic layer deposition providing high performance lithium sulfur batteries*. Journal of Power Sources, 2017. **338**: p. 34-48.

63. Jacob, A.A., et al., *Structural, optical and photodetection characteristics of Cd alloyed ZnO thin film by spin coating*. Journal of Alloys and Compounds, 2017. **695**: p. 3753-3759.
64. Choi, K.H., J. Ali, and K.H. Na, *Fabrication of graphene-nanoflakeipoly(4-vinylphenol) polymer nanocomposite thin film by electrohydrodynamic atomization and its application as flexible resistive switching device*. Physica B-Condensed Matter, 2015. **475**: p. 148-155.
65. Tyunkov, A., et al., *Electron Beam Deposition of Ceramic Coatings at Fore-Vacuum Pressure*. Prospects of Fundamental Sciences Development (Pfsd-2016), 2016. **1772**.
66. Walker, E.S., et al., *Large-Area Dry Transfer of Single-Crystalline Epitaxial Bismuth Thin Films*. Nano Letters, 2016. **16**(11): p. 6931-6938.
67. Kramer, A., et al., *ZnO thin films on single carbon fibres fabricated by Pulsed Laser Deposition (PLD)*. Applied Surface Science, 2017. **399**: p. 282-287.
68. Salih, A.T., et al., *Single-material multilayer ZnS as anti-reflective coating for solar cell applications*. Optics Communications, 2017. **388**: p. 84-89.
69. Wang, Z.Y., et al., *Dense and high-stability Ti₂AlN MAX phase coatings prepared by the combined cathodic arc/sputter technique*. Applied Surface Science, 2017. **396**: p. 1435-1442.
70. Miyata, H., *Epitaxial growth of a surfactant-silica mesostructure on oriented polyimide films*. Microporous and Mesoporous Materials, 2007. **101**(1-2): p. 296-302.
71. Madou, M.J., *Fundamentals of Microfabrication: The Science of Miniturization*. 2 ed. 2002, Boca Raton, Florida: CRC Press LLC.
72. Ogilvy, J.A., *A Parametric Elastic Model for Indentation Testing of Thin-Films*. Journal of Physics D-Applied Physics, 1993. **26**(12): p. 2123-2131.
73. Sebastiani, M., et al., *A novel pillar indentation splitting test for measuring fracture toughness of thin ceramic coatings*. Philosophical Magazine, 2015. **95**(16-18): p. 1928-1944.
74. Wei, C.H., et al., *Tribological characteristics of titanium nitride and titanium carbonitride multilayer films Part I. The effect of coating sequence on material and mechanical properties*. Thin Solid Films, 2001. **381**(1): p. 94-103.
75. Lotfian, S., et al., *High temperature micropillar compression of Al/SiC nanolaminates*. Acta Materialia, 2013. **61**(12): p. 4439-4451.
76. Mayer, C.R., et al., *Anisotropy, size, and aspect ratio effects on micropillar compression of Al-SiC nanolaminate composites*. Acta Materialia, 2016. **114**: p. 25-32.

77. Oliver, W.C. and G.M. Pharr, *Nanoindentation in materials research: Past, present, and future*. Mrs Bulletin, 2010. **35**(11): p. 897-907.
78. Pharr, G.M. and A. Bolshakov, *Understanding nanoindentation unloading curves*. Journal of Materials Research, 2002. **17**(10): p. 2660-2671.
79. Pharr, G.M., et al., *Effects of Residual-Stress on the Measurement of Hardness and Elastic-Modulus Using Nanoindentation*. Materials Reliability in Microelectronics Iv, 1994. **338**: p. 127-134.
80. Pharr, G.M., W.C. Oliver, and F.R. Brotzen, *On the Generality of the Relationship among Contact Stiffness, Contact Area, and Elastic-Modulus during Indentation*. Journal of Materials Research, 1992. **7**(3): p. 613-617.
81. Bei, H. and S. Shim, *Effects of focused ion beam milling on the nanomechanical behavior of a molybdenum-alloy single crystal*. Applied Physics Letters, 2007. **91**(11).
82. El-Awady, J.A., et al., *Effects of focused ion beam induced damage on the plasticity of micropillars*. Physical Review B, 2009. **80**(10).
83. Mayer, C., et al., *Orientation dependence of indentation behavior in Al-SiC nanolaminate composites*. Materials Letters, 2016. **168**: p. 129-133.
84. Moser, B., et al., *Strength and fracture of Si micropillars: A new scanning electron microscopy-based micro-compression test*. Journal of Materials Research, 2007. **22**(4): p. 1004-1011.
85. Baldwin, J.K., *Compiled Discussions and Presentations*. 2015-2016: Los Alamos, NM.
86. Fischer-Cripps, A.C., *Nanoindentation*, ed. F.F. Ling. 2002, New York, NY: Springer-Verlag New York, Inc.
87. Pharr, G.M. and W.C. Oliver, *Measurement of Thin-Film Mechanical-Properties Using Nanoindentation*. Mrs Bulletin, 1992. **17**(7): p. 28-33.
88. Jian, S.R., G.J. Chen, and T.C. Lin, *Berkovich Nanoindentation on AlN Thin Films*. Nanoscale Research Letters, 2010. **5**(6): p. 935-940.
89. Singh, D.R.P., N. Chawla, and Y.L. Shen, *Focused Ion Beam (FIB) tomography of nanoindentation damage in nanoscale metal/ceramic multilayers*. Materials Characterization, 2010. **61**(4): p. 481-488.
90. Tsui, T.Y., W.C. Oliver, and G.M. Pharr, *Indenter geometry effects on the measurement of mechanical properties by nanoindentation with sharp indenters*. Thin Films: Stresses and Mechanical Properties Vi, 1997. **436**: p. 147-152.
91. Blada, C.B. and Y.L. Shen, *Viscoplastic analysis of cyclic indentation behavior of thin metallic films*. Journal of Applied Physics, 2013. **113**(6).

92. Luo, X., et al., *Molecular-dynamics simulation of Al/SiC interface structures*. Physical Review B, 1999. **59**(15): p. 10125-10131.
93. Sulsky, D. and H.L. Schreyer, *Axisymmetric form of the material point method with applications to upsetting and Taylor impact problems*. Computer Methods in Applied Mechanics and Engineering, 1996. **139**(1-4): p. 409-429.
94. Wen, F.L. and Y.L. Shen, *Plastic deformation in multilayered thin films during indentation unloading: a modeling analysis incorporating viscoplastic response*. Mechanics of Time-Dependent Materials, 2011. **15**(3): p. 277-291.
95. Tehrani, M., *Effect of Moderate Magnetic Annealing on the Microstructure and Mechanical Behavior of a Structural Epoxy*, in *Mechanical Engineering*. 2009, The University of New Mexico: Albuquerque, NM.
96. DIA, T. *Diamond Indenters*. Feb. 4, 2017].
97. Goryachev, I.S., Alexey. *Encyclopedic Dictionary of Nanotechnology: Indenter*. [] 2017 Feb. 4, 2017].
98. Field, J.S. and M.V. Swain, *A Simple Predictive Model for Spherical Indentation*. Journal of Materials Research, 1993. **8**(2): p. 297-306.
99. Bell, T.J., J.S. Field, and M.V. Swain, *Stress-Strain Behavior of Thin-Films Using a Spherical Tipped Indenter*. Thin Films : Stress and Mechanical Properties Iii, 1992. **239**: p. 331-336.
100. Bell, T.J., J.S. Field, and M.V. Swain, *Elastic Plastic Characterization of Thin-Films with Spherical Indentation*. Thin Solid Films, 1992. **220**(1-2): p. 289-294.
101. Beake, B., S. Goodes, S. Jones, R. Parkinson, N. Pickford and J. Smith, *NanoTest Manual Version 3.0*. 2006.
102. Hay, J.L., M.E. O'Hern, and W.C. Oliver, *The importance of contact radius for substrate-independent property measurement of thin films*. Fundamentals of Nanoindentation and Nanotribology, 1998. **522**: p. 27-32.
103. Doerner, M.F. and W.D. Nix, *A method for interpreting the data from depth-sensing indentation instruments*. Journal of Materials Research, 1986. **1**(4): p. 601-609.
104. Elsherbiney, M.G.D. and J. Halling, *Hertzian Contact of Surfaces Covered with Metallic-Films*. Wear, 1976. **40**(3): p. 325-337.
105. Gao, H.J., C.H. Chiu, and J. Lee, *Elastic Contact Versus Indentation Modeling of Multilayered Materials*. International Journal of Solids and Structures, 1992. **29**(20): p. 2471-2492.

106. King, R.B., *Elastic Analysis of Some Punch Problems for a Layered Medium*. International Journal of Solids and Structures, 1987. **23**(12): p. 1657-1664.
107. Bhattacharya, A.K. and W.D. Nix, *Finite-Element Simulation of Indentation Experiments*. International Journal of Solids and Structures, 1988. **24**(9): p. 881-891.
108. Burnett, P.J. and D.S. Rickerby, *The Mechanical-Properties of Wear-Resistant Coatings .2. Experimental Studies and Interpretation of Hardness*. Thin Solid Films, 1987. **148**(1): p. 51-65.
109. Burnett, P.J. and D.S. Rickerby, *The Mechanical-Properties of Wear-Resistant Coatings .1. Modeling of Hardness Behavior*. Thin Solid Films, 1987. **148**(1): p. 41-50.
110. Jonsson, B. and S. Hogmark, *Hardness Measurements of Thin-Films*. Thin Solid Films, 1984. **114**(3): p. 257-269.
111. Stoney, G.G., *The tension of metallic films deposited by electrolysis*. Proceedings of the Royal Society of London Series a-Containing Papers of a Mathematical and Physical Character, 1909. **82**(553): p. 172-175.
112. Mook, W.M., *Compiled Discussions and Notations*, B. Sandoval, Editor. 2016-17.
113. Tehrani, M., *Next Generation Multifunctional Composites for Impact, Vibration and Electromagnetic Radiation Hazard Mitigation*. 2012, Virginia Polytechnic Institute and State University Blacksburg, Virginia.
114. MatWeb, L. *Material Property Data*. 2017 [cited 2017].
115. Idrissi, H., et al., *Point Defect Clusters and Dislocations in FIB Irradiated Nanocrystalline Aluminum Films: An Electron Tomography and Aberration-Corrected High-Resolution ADF-STEM Study*. Microscopy and Microanalysis, 2011. **17**(6): p. 983-990.
116. Uchic, M.D., et al., *Oxide surface films on metal crystals - Response*. Science, 2004. **306**(5699): p. 1134-1135.
117. P. Dumas, J.D.-B., D. Rivi`ere, Yves Levy, J. Corset, *GROWTH OF THIN ALUMINA FILM ON ALUMINIUM AT ROOM TEMPERATURE : A KINETIC AND SPECTROSCOPIC STUDY BY SURFACE PLASMON EXCITATION*. Journal de Physique Colloques, 1983. **44**(C10): p. C10-205-C10-208.
118. Shim, S., W.C. Oliver, and G.M. Pharr, *A comparison of 3D finite element simulations for Berkovich and conical indentation of fused silica*. International Journal of Surface Science and Engineering, 2007. **1**(2-3): p. 259-273.

119. Hay, J.C., A. Bolshakov, and G.M. Pharr, *A critical examination of the fundamental relations used in the analysis of nanoindentation data*. Journal of Materials Research, 1999. **14**(6): p. 2296-2305.
120. Bolshakov, A. and G.M. Pharr, *Inaccuracies in Sneddon's solution for elastic indentation by a rigid cone and their implications for nanoindentation data analysis*. Thin Films: Stresses and Mechanical Properties Vi, 1997. **436**: p. 189-194.
121. Best, J.P., et al., *A comparison of three different notching ions for small-scale fracture toughness measurement*. Scripta Materialia, 2016. **112**: p. 71-74.
122. Di Maio, D. and S.G. Roberts, *Measuring fracture toughness of coatings using focused-ion-beam-machined microbeams*. Journal of Materials Research, 2005. **20**(2): p. 299-302.
123. Iqbal, F., et al., *In situ micro-cantilever tests to study fracture properties of NiAl single crystals*. Acta Materialia, 2012. **60**(3): p. 1193-1200.
124. Jaya, B.N. and V. Jayaram, *Crack stability in edge-notched clamped beam specimens: modeling and experiments*. International Journal of Fracture, 2014. **188**(2): p. 213-228.
125. Jaya, B.N., V. Jayaram, and S.K. Biswas, *A new method for fracture toughness determination of graded (Pt,Ni)Al bond coats by microbeam bend tests*. Philosophical Magazine, 2012. **92**(25-27): p. 3326-3345.
126. Liu, S., et al., *Measuring the fracture resistance of hard coatings*. Applied Physics Letters, 2013. **102**(17).
127. Kiener, D., et al., *FIB damage of Cu and possible consequences for miniaturized mechanical tests*. Materials Science and Engineering a-Structural Materials Properties Microstructure and Processing, 2007. **459**(1-2): p. 262-272.
128. Uchic, M.D. and D.A. Dimiduk, *A methodology to investigate size scale effects in crystalline plasticity using uniaxial compression testing*. Materials Science and Engineering a-Structural Materials Properties Microstructure and Processing, 2005. **400**: p. 268-278.
129. Uchic, M.D., P.A. Shade, and D.M. Dimiduk, *Plasticity of Micrometer-Scale Single Crystals in Compression*. Annual Review of Materials Research, 2009. **39**: p. 361-386.
130. Shim, S., et al., *Effects of focused ion beam milling on the compressive behavior of directionally solidified micropillars and the nanoindentation response of an electropolished surface*. Acta Materialia, 2009. **57**(2): p. 503-510.

131. Hugo, R.C. and R.G. Hoagland, *The kinetics of gallium penetration into aluminum grain boundaries - In situ TEM observations and atomistic models*. Acta Materialia, 2000. **48**(8): p. 1949-1957.
132. Rajagopalan, M., et al., *Atomic-scale analysis of liquid-gallium embrittlement of aluminum grain boundaries*. Acta Materialia, 2014. **73**: p. 312-325.
133. Schmidt, S., et al., *Gallium segregation at grain boundaries in aluminium*. Zeitschrift Fur Metallkunde, 2002. **93**(5): p. 428-431.
134. Kobayashi, M., et al., *Preferential penetration path of gallium into grain boundary in practical aluminium alloy*. Philosophical Magazine, 2006. **86**(28): p. 4351-4366.
135. Motz, C., T. Schoberl, and R. Pippan, *Mechanical properties of micro-sized copper bending beams machined by the focused ion beam technique*. Acta Materialia, 2005. **53**(15): p. 4269-4279.
136. Chawla, N., R.S. Sidhu, and V.V. Ganesh, *Three-dimensional visualization and micro structure-based modeling of deformation in particle-reinforced composites*. Acta Materialia, 2006. **54**(6): p. 1541-1548.
137. Constantinides, G., et al., *Quantifying deformation and energy dissipation of polymeric surfaces under localized impact*. Materials Science and Engineering a-Structural Materials Properties Microstructure and Processing, 2008. **489**(1-2): p. 403-412.
138. Dehnavi, M.Y., et al., *Utilizing digital image correlation to determine stress intensity factors*. Polymer Testing, 2014. **37**: p. 28-35.
139. Galanov, B.A., et al., *Determination of the Hardness and Youngs Modulus from the Depth of Penetration of a Pyramidal Indentor*. Strength of Materials, 1983. **15**(11): p. 1624-1628.
140. Herbert, E.G., et al., *On the measurement of stress-strain curves by spherical indentation*. Thin Solid Films, 2001. **398**: p. 331-335.
141. Pharr, G.M., et al., *Nanoindentation of soft films on hard substrates: Experiments and finite element simulations*. Thin-Films - Stresses and Mechanical Properties Vii, 1998. **505**: p. 109-120.
142. Pharr, G.M., W.C. Oliver, and D.R. Clarke, *The Mechanical-Behavior of Silicon during Small-Scale Indentation*. Journal of Electronic Materials, 1990. **19**(9): p. 881-887.
143. Qidwai, M.A.S., A.C. Lewis, and A.B. Geltmacher, *Using image-based computational modeling to study microstructure-yield correlations in metals*. Acta Materialia, 2009. **57**(14): p. 4233-4247.

144. Swain, M.V. and J. Mencik, *Mechanical Property Characterization of Thin-Films Using Spherical Tipped Indenters*. Thin Solid Films, 1994. **253**(1-2): p. 204-211.
145. Systèmes, D., *Abaqus Analysis User's Guide*. 2014. **v6.14**.
146. Tsui, T.Y., W.C. Oliver, and G.M. Pharr, *Nanoindentation of soft films on hard substrates: The importance of pile-up*. Thin Films: Stresses and Mechanical Properties Vi, 1997. **436**: p. 207-212.
147. Voyiadjis, G.Z.P., R., *Size effects in nanoindentation: an experimental and analytical study*. Acta Mech 2010. **211**: **131**.
148. Whitehead, A.J. and T.F. Page, *Nanoindentation Studies of Thin-Film Coated Systems*. Thin Solid Films, 1992. **220**(1-2): p. 277-283.